The Development of Anti-Cancer Drug Delivery Systems

Jingyi Zong

A thesis submitted for the degree of Doctor of Philosophy

Department of Chemistry

University of Durham

October, 2016

Abstract

Cancer is undoubtedly one of the main threats to global human health and as a result, despite significant advances in the field, new and improved cancer treatments are still in great need. Although chemotherapy (in combination with other therapies) is widely used to suppress the growth of tumours, many of the current anti-cancer drugs suffer from poor selectivity and consequently severe toxicity. In order to conquer these limitations, targeted drug delivery systems have been designed and studied with the primary aim of improving the accuracy of transporting anti-cancer drugs into cancer cells and tissue areas. The overall aim of the work presented in this thesis is to design new anti-cancer drug delivery systems using three different strategies.

In Chapter 2, intelligent stimulus-responsive short elastin-like peptides (ELPs) and elastin-based side chain polymers (ESPs) were synthesised. The conformation and aggregation properties of these ELPs and ESPs were studied in different aqueous buffers (varying pH also) using ultraviolet-visible (UV-Vis) spectroscopy and circular dichroism (CD). Of the ELPs investigated, peptide **10** (*N*-acetylated VPGVG) was found to have the lowest transition temperature at pH 7 (i.e. 45^{o}C). Amongst all the ESPs, PF100-GABA(VPGVG) (**29**) was proven to have the lowest transition temperature (47^{o}C) which was most likely due to the fact that it had the highest molecular weight.

In Chapter 3, gold nanoparticles (GNPs) were synthesised and functionalised with biomolecules including elastin-like peptides (ELPs), elastin-based side chain polymers (ESPs) and the pro-apoptotic peptide $_{D}$-(KLAKLAK)$_2$ (KLA). The hybrids materials, ELP-GNPs and ESP-GNPs were characterized by UV-Vis, CD and transmission electron microscopy (TEM). The hybrids showed the same temperature sensitive properties as the free ELPs and ESPs previously studied, confirming the successful functionalization of GNPs. The KLA-GNPs were found to have increased anti-cancer activity against HeLa cells compared to the free KLA.

In Chapter 4, the pro-apoptotic KLA peptide was conjugated to a series of cell penetrating peptoids (CPPos) to prepare peptoid-peptide hybrids (CPPos-KLA). The anti-cancer, antimicrobial and cell penetrating properties of these peptoid-peptide hybrids were investigated. The results demonstrated an increasing trend in anti-cancer ability of CPPos-KLA hybrids (compared to free KLA) and KLA-CPPo6 (**57**) gave the lowest IC_{50} value (ca.8 μM) against HeLa cells.

Acknowledgements

First and foremost, I would like to thank my academic supervisors, Professor Neil Cameron and Dr. Steven Cobb, for their kind support and guidance over the four years. With their patience and unrelenting help, I have learned not only knowledge and experience, but also an attitude of doing research which will benefit me for life.

I would like to thank Dr. Beth Bromley for her kindly advice in CD experiments and letting me use her lab machines. I would like to thank the staff in the mass spectrometry services (Chemistry Department), in particular Mr Peter Stokes for his advice and help. I would like to thank Dr Aileen Congreve for her kind help and advice on HPLC experiments. I would like to thank Mr. Douglas Carswell for conducting the TGA measurements of my samples and for his support. I would also like to thank Ms Helen Grindley and Mrs Christine Richardson from the Biological and Biomedical Sciences Department for helping me with the preparation of TEM samples and measurements.

I would like to express my grateful thanks to Dr. Wong Ka-Leung and his group in Hong Kong Baptist University, especially Lijun Jiang, for their collaboration on all the experiments of anti-cancer screen of KLA peptide and peptide-peptoid hybrids.

Many thanks to all the Cameron and Cobb group members, past and present, for making my research much more enjoyable: Dr. Sarah Hehir, Dr. Fanny Joubert, Dr. Arturas Kubilis, Dr. Ahmed Eissa, Dr. Adam Hayward, Dr. Paul Thornton, Dr. Matt Disbury, Dr. David Johnson, Ali Abdulkarim, Maria Andela Caballo Gonzalez, Caitlin Langford, Dr Anica Dose, Maria Czyzewska, Dr. Lara Small, Dr. Asahi Cano-Marqués, Dr. Bnar Ahmed, Dr Chris Coxon, Dr Gabriella Eggimann, Alex Webster, Mark Laws, Ambrose Crofton, Caitlin Mooney, Sam Lear, Hannah Bolt, Beatriz Martínez, Diana Giménez and Dr Alex Hudson.

Last but not least, thanks to the Durham University and China Scholarship Council (CSC) for funding my research. I am also very grateful to the Henry Lester and Great Britain China Education awards, for their financial support in my writing-up days.

To conclude, I would like to dedicate this Doctoral Thesis to my family, who I will never be able to give back all the support they have given to me as it is immeasurable. Thanks to my mum, dad, my mother-in-law, father-in-law and my lovely sister, tian tian. To my beloved husband, Xilin, who stands by me and always comforts and cares for me. I am so blessed to have you.

Declaration

This work was conducted in the Department of Chemistry at Durham University between September 2012 and September 2016. The work has not been submitted for a degree in this, or any other university. It is my own work, unless otherwise indicated.

Copyright

Contents

List of Figures

List of Tables

List of Appendices

List of Abbreviation

A (Ala)	alanine
Ac	acetyl
Aib	α-methylalanine
Au	gold
AMPs	antimicrobial peptides
Boc	*tert*-butyloxycarbonyl
BSA	bovine serum albumin
BTV	detect bluetongue virus
C (Cys)	Cysteine
CD	circular dichroism
$CDCl_3$	deuterated chloroform
CH_3CN	acetonitrile
CMC	critical micelle concentration
CMT	critical micellization temperature
CT	Computed Tomography
CPTs	Camptothecins
CPPs	cell penetrating peptides
CPPos	cell penetrating peptoids
D (Asp)	Aspartate
DCM	dichloromethane
DIC	*N*,*N*′-Diisopropylcarbodiimide
DIPEA	*N*,*N*-Diisopropylethylamine
DMF	dimethylformamide
DMSO	dimethyl sulfoxide
DOX	Doxorubicin
3D	three dimensional

DNA	deoxyribonucleic acid
DACH	diaminocyclohexane
ε	molar extinction coefficient
e.g.	exempli gratia (for example)
ESI	electro-spray ionization
Et_2O	diethyl ether
eq	equivalent
EPR	enhanced permeation and retention
E (Glu)	glutamic acid
ELP	elastin-like polypeptide
ESP	elastin-based side chain polymers
F (Phe)	phenylalanine
Fmoc	fluorenylmethyloxycarbonyl
FDA	Food and Drug Administration
G (Gly)	Glycine
g	grams
GNPs	gold nanoparticles
H_2	hydrogen
HOBt	Hydroxybenzotriazole
HPLC	high performance liquid chromatography
HDPs	host defense peptides
HCST	higher critical solution temperature
HIV-1	human immunodeficiency virus 1
HPMA	*N*-(2-hydroxypropyl) methacrylamide
I (Ile)	isoleucine
IR	infrared
iRGD	internalizing RGD
K (Lys)	lysine
L (Leu)	leucine

LCST	lower critical solution temperature
m/z	mass/charge
MALDI	matrix assisted laser desorption/ionization
mM	millimolar
mAb	monoclonal antibody
MS	mass-spectrometry
MW	molecular weight
μM	micromolar
MUA	mercaptoundecanoic acid
MAP	multiple antigenic peptide
N (Asn)	asparagine
NMM	*N*-Methylmorpholine
NMR	nuclear magnetic resonance
NLS	nuclear localization signal
NCI	National Cancer Institute
P (Pro)	Proline
PAAc	poly(acrylic acid)
PMAAc	poly(methacrylic acid)
PEAAc	poly(2-ethyl acrylic acid)
PPAAc	poly(2-propyl acrylic acid)
PBS	phosphate-buffered saline
PBLA	poly (β-benzyl-$_L$-aspartate)
PLGA	poly (lactic-co-glycolic acid)
PCL	poly (ε-caprolactone)
PEG	poly(ethylene glycol)
PDEAAm	poly(N,N-diethylacrylamide)
PEO	poly (ethylene oxide)
PPO	propylene oxide
PGA	poly (glycolic acid)

Ph	phenyl
ppm	parts per million
Pt	platinum
PNIPAAm	poly(N-isopropylacrylamide)
PDMAEMA	Poly(*N*,*N*-dimethyl aminoethyl methacrylate)
PDEAEMA	poly(*N*,*N*-diethyl aminoethyl methacrylate)
PVCL	poly(N-vinyl caprolactam)
PyBOP	(Benzotriazol-1-yloxy)tripyrrolidinophosphonium hexafluorophosphate
PDLLA	poly ($_{D,L}$-lactic acid)
PIC	polyion complex micelles
PEG-P (Asp)	poly (ethylene glycol)-poly (aspartic acid)
PEG-P (Lys)	poly (ethylene glycol)-poly ($_{L}$-Lysine)
P4VP or P2VP	Poly (4 or 2-vinylpyridine)
PDT	photodynamic therapy
Q (Gln)	glutamine
R (Arg)	arginine
r.t.	room temperature
rDNA	recombinant DNA
RP-HPLC	reverse phase high-performance liquid-chromatography
RES	reticuloendothelial system
RAFT	reversible addition-fragmentation chain-transfer
S (Ser)	serine
SPRs	stimuli-responsive polymers
SNP	synthetic responsive polymer
siRNA	short interfering RNA
SPPS	solid phase peptide synthesis
SMH	Shai-Matsuzaki-Huang
SCID	severe combined immunodeficiency disease

*t*Bu	*tert*-butyl
T_b	body temperature
TEM	transmission electron microscopy
TFA	trifluoroacetic acid
TIPS	triisopropylsilane
T_t	transition temperature
TOF	time of flight
TA	thioctic acid
Trt	trityl
UV	ultraviolet
UCST	upper critical solution temperature
V (Val)	valine
Vis	visible
Y (Tyr)	Tyrosine
θ	mean residue ellipticity

Chapter 1: Introduction

1.1 Background

1.1.1 Cancer cases and global health

Over the last century cancer has become one of the main threats to global human health. According to worldwide cancer statistics, around 14.1 million new cases were recorded in 2012 and an estimated 8.2 million people died from cancer. Despite significant improvements in cancer treatments, cancer deaths are still predicted to rise from 8.2 million to 13 million per annum largely due to increasing life expectancies.[1]

According to the 'Global Cancer Facts & Figures', cancer is the second leading cause of death worldwide following cardiovascular diseases.[2] The most common form of cancer often varies from country to country and between the male and female populations. As shown in **Figure 1.1**, in a global context among women breast cancer is the most common form of the disease, while cases of prostate, lung and throat cancer are the highest among men. The specific reasons for geographic differences in cancer occurrences are not clear, but they are most probably due to local environmental and/or lifestyle differences. If one looks, for example, at the range in China, the most common cancers are lung and throat (bronchus & trachea) among both women and men. These data provide strong evidence that cancers are caused by factors related to lifestyle choices and, for example, in China, which has a large smoking population, the incidence rate of lung cancer is relatively high. In addition, air pollution is becoming a major issue in China, and this is likely to also contribute significantly to the expected increase in the number of lung and throat cancer cases.[3]

As indicated in some cases, the occurrence of cancer can largely be attributed to particular factors. However, cancer is a very complex illness and the aetiology of cancer may involve more than one of the following factors: carcinogenic chemicals in

industrial pollution such as tar or soot; tobacco smoke; cancer-causing food; radiation; oncogenic virus; genetic disposition; and the ageing process.

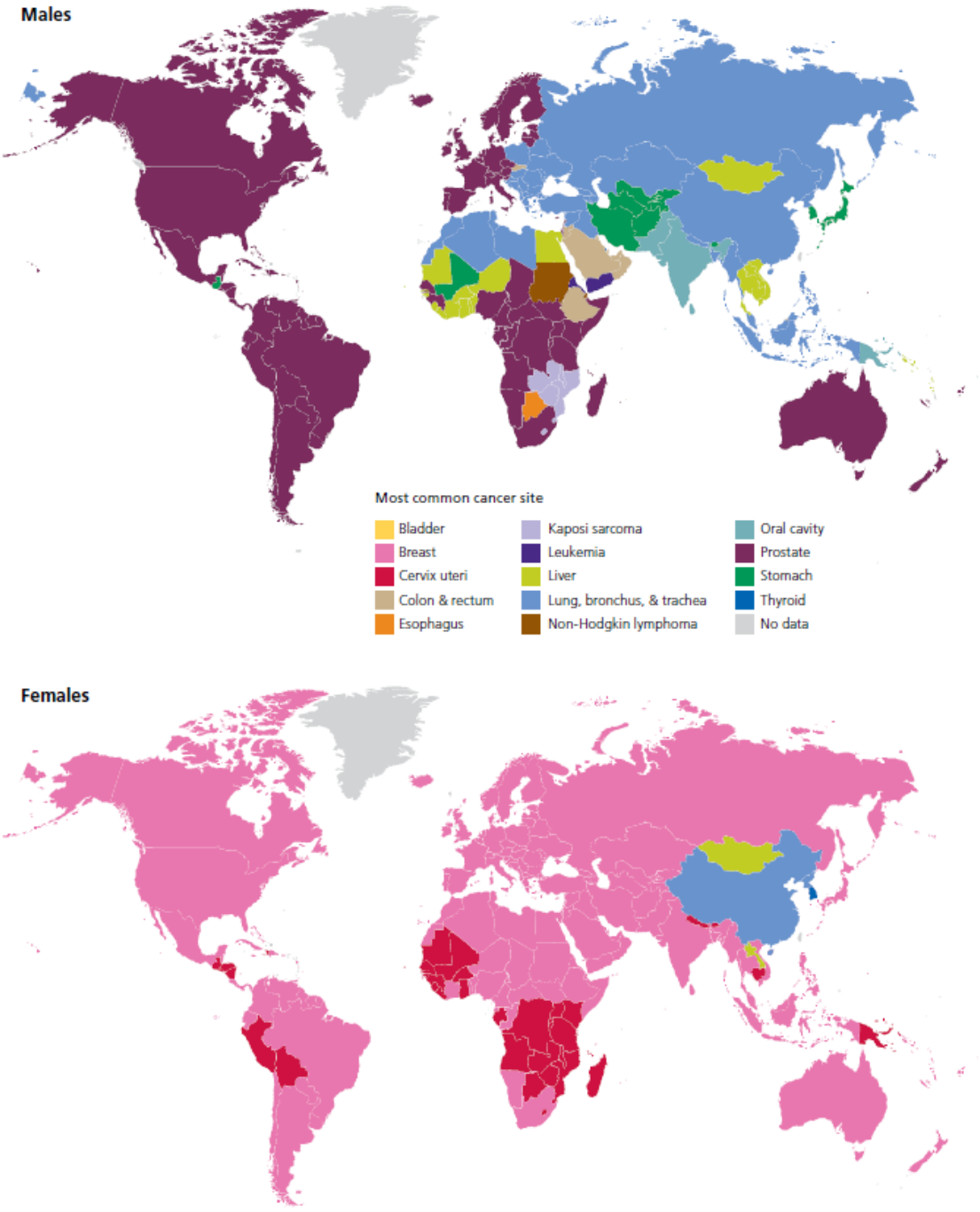

Figure 1.1: Overview of the most common forms of cancers worldwide split by sex, 2012.[2]

Cancer may arise in any part of the body, and cancer cells can migrate inside the body either through the bloodstream or the lymph system. All cancers begin with a change in the function of normal healthy cells. Compared to normal cells, cancer cells have

damaged, lost, or multiple copies of some genes. A gene change is called a mutation, and more than half a dozen different mutations of a gene turns a normal cell into a cancer cell. These mutations will make cells grow and reproduce in an uncontrolled way, resulting in unlimited cell division, leading to maligant tumours, vascularisation and metastasis.[4]

1.1.2 Cancer treatment options

Before the development of modern chemotherapy, traditional methods of cancer treatment were mainly surgery and extended radiotherapy. Even today surgery is still a viable option for many types of cancer where solid tumours can be removed by an experienced surgeon without significant damage to the surrounding tissues or organs. Surgery is most often followed by radiotherapy, which is used to kill any surviving cancer cells missed by surgery. However, where surgery and radiotherapy can often eradicate localised or primary malignant tumours, they are less useful when a cancer has metastasised to different parts of the body. In this case cancer treatment relies heavily on chemotherapy or a combination of treatments depending on the type of cancer. Chemotherapy combined with traditional therapies (surgery or radiotherapy) is commonly called adjuvant therapy.[5] In the following section, we will review these three major treatments briefly.

1.1.2.1 Surgical resection

The first recorded surgery for cancer goes as far back as around 1500 BC. The Ebers Papyrus, a written knowledge of ancient Egyptian medical treatise, contains chapters on surgical treatment of identified tumours.[6] Hippocrates, a famous Greek physician, was the first to identify the cause of cancer as an excess of black bile and described the tumours by the term carcinoma or sarcoma. Hippocrates' discovery and study of cancer was continued by another Greek physician, Galen, who recorded the appearance of some cancers as characteristically crab-like and classified cancer as a systemic disease.[7] Galen was also the first to observe that breast cancer was found to frequently occur among women. He wrote about successful surgical treatments for breast cancer but only in cases where the tumour was at an early stage and was of a notable size. However, it should also be noted that in the time of Galen surgery was still very primitive and patients often died due to complications such as extensive blood loss. [6,8]

It was not until the nineteenth century, that standard surgical resection technique was established and the successful surgical treatment of cancer became possible. With the improvement of anaesthetic techniques in 1846, surgery started to play a very important role in the treatment of malignant diseases like cancer. A new speciality was developed, known as surgical oncology. Generally, a surgical oncologist is a fully qualified surgeon who has undertaken additional training in areas such as pathology, radiology, epidemiology and even clinical psychology.[9] The creation of a multidisciplinary skill set is required to enable a more advanced approach to the diagnosis, treatment and rehabilitation of cancer patients.

In order to describe how much cancer is in the body and where it is located, the staging system was developed. The first classification of malignant tumours (TNM) system was reported by Pierre Denoix in the mid-1940s.[10] The T represents the primary tumour size, N stands for the regional lymph node involvement and the M is for metastasis. The TNM system has proved to be a very effective method for recording the malignant tumour status and for enabling suitable cancer therapy to be tailored to individual patients. Based on the cancer stage, a suitable surgery will be operated and as much as possible of the tumour-related area will be removed. Surgical resection is now a highly established and mature technique for treatment of primary stage cancers, but as previously highlighted even when 99.99999 % of the tumour has been removed, without combination therapy the chance of a new tumour developing is still high.[8]

1.1.2.2 Radiotherapy

In 1895, Wilhelm Conrad Roentgen, a German physicist, first detected an unknown electromagnetic radiation (wavelength from 0.01 to 10 nanometers) and named it X-rays. This exciting discovery brought Roentgen the first Nobel Prize in physics in 1901.[6] It did not take long for researchers to establish that X-ray radiation had destructive effects on healthy cells and could cause carcinogenicity and mutagenicity.[9] However, beyond the negative and harmful effects the discovery of X-ray radiation also opened up new opportunities for cancer diagnosis and therapy.

When high energy X-rays pass through an atom, the atom will absorb the energy resulting in excitation (an electron moves to a higher orbital level) or ionization (remove one electron from an atom). In the human body, bones contain calcium ions that are more likely to absorb X-rays compared with soft tissues (smaller atoms).[11] The

difference between the absorption of X-rays provides doctors with an image (radiograph) which shows the internal structure of the body. The dense materials show up as white areas on a radiograph, while the soft materials are present as varying shadows. A routine X-ray scan has been broadly used for detection of cancerous tumours especially located in the bone, lung and breast. A more powerful detection technique, called X-ray Computed Tomography (CT), has also been used widely since the 1970s. CT scans take many X-ray images from 360^{o} to produce a cross-sectional image and give more detailed information about a tumour, such as the location, size and shape.[12]

Radiation therapy is a therapy using ionizing radiation to shrink tumours and kill cancer cells by damaging DNA directly or indirectly. Compared to surgery, radiotherapy is designed to have several rounds of treatments and only a portion of cancer cells are affected within one cycle. To understand how radiation works, it is also very important to have an understanding of the normal life cycle of a cell. As shown in **Figure 1.2**, the cell cycle has four stages: G_1 (Gap 1) phase during which the proteins and RNA are made and cell size increases; S (Synthesis) phase when the DNA is synthesised; G_2 (Gap 2) phase during which apparatus for mitosis is built; M (Mitosis) phase when the cell divides into two daughter cells. This process is precisely controlled by proteins called cyclins and cyclin-dependent kinases (CDKs).[8] They are associated with each other and control various stages of the cell cycle. For example, there is a distinct restriction point during Gap 1 (**Figure 1.2**), before which extracellular signals are required and after which the cell is committed to preparing for DNA duplication.

The relative sensitivity of cells, tissues or organs to the harmful effect of ionizing radiation is called radiosensitivity.[13] The most effective radiation happens during the dividing phase (M phase) of the cell cycle, then the G_2 phase, then the G_1 phase and S phase. Cancer cells divide more quickly than normal cells, meaning that normal cells that divide slowly are more likely to survive after radiotherapy. However, some normal cells can divide quite quickly (e.g. skin or bone marrow cells) and these can be damaged by radiotherapy. One possibility to improve therapeutic radiosensitivity is to modulate the cell cycle of cancer cells making them even more different to healthy normal cells.

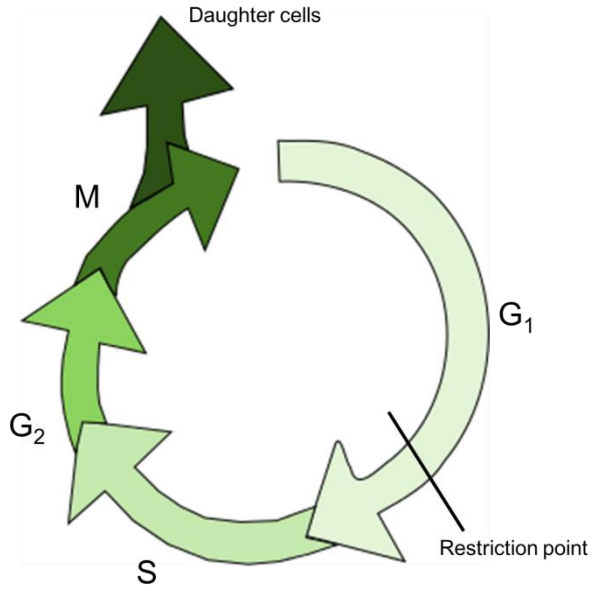

Figure 1.2: A cell life cycle.[8]

1.1.2.3 Chemotherapy

Attempts to treat cancer with chemical entities date back as far as 1800 BC when preparations of plant and herbal medicines were used. Over the years it has been repeatedly shown that natural products isolated from a range of sources can have very potent anti-tumour activities.[14] However, the concept of chemotherapy was first clearly outlined by Paul Ehrlich, a German physician and scientist. Ehrlich pioneered the use of dyes for histological studies and bacterial diagnostics, and this work led him to identify agents which could bind to specific cellular components.[9] In 1908, he was awarded the Nobel Prize in Physiology and Medicine because of his theory of the immune system and discovery of antibodies behaving in a highly specific manners in response to infection.[15] Based on his immune system hypothesis, Ehrlich developed the idea of 'magic bullet' treatment which would go straight to the specific disease-causing organisms to which they targeted.[16] To try and prove his theory, hundreds of chemicals were tested and finally he discovered the arsenic-containing drug, known as Salvarsan, which was developed as the first selective anti-syphilitic drug.[17] Since then, Ehrlich's receptor theory/'magic bullet' treatment hypothesis have been applied and become the main foundations for the design of new selective cancer-targeted medicines.

The first successful systemic anti-cancer drugs were initially developed as chemical weapons. In 1917 the Germans fired shells containing mustard gas (sulfur mustard **1**) into the trenches where soldiers slept overnight, and the next morning they found

themselves with burning eyes and skin.[8] The specific biological effects and subsequently the anti-cancer therapeutic application of mustard gas did not become known until Gilman and Philips published a review in 1946.[18] They synthesised nitrogen mustard analogues (**Figure 1.3**) based on the structure of **1** and studied their cytotoxic actions on cancer tumours. In this study they discovered that the sulfur mustards eliminate a chloride ion and form a cyclic sulfonium ion which reacts with the guanine nucleotides in DNA leading to permanent alkylation and subsequent programmed cell death.[19]

For anti-tumour clinical trials, sulfur mustard itself was found to be too toxic for systemic use, so the less reactive and less toxic nitrogen mustards (*N*-mustard, see **Figure 1.3**) were further developed. The nitrogen mustards' anti-tumour effects were examined by injecting them into lymphomas-bearing mice and almost immediate regression of cancer tumours was seen. Subsequently, clinical trials of mechlorethamine (Mustine **3**) were undertaken on more than 150 patients who suffered from Hodgkin's lymphoma, and positive results were demonstrated by remission of some patients who went on to live up to three years.[8] Nowadays, **3** is still used as an effective anti-cancer drug. Based on the original structure of **3**, many more nitrogen mustards drugs have been developed and used in the treatment of a range of cancers, such as cyclophosphamide **5**, one of the most successful alkylating drugs. The cyclic phosphoramide provides a non-toxic effect as a prodrug, and it needs to be broken down by enzymes in the liver before the active mustard can be revealed. Anti-cancer activity of **5** lasts 1-2 days which is much longer than **3** which only lasts a few minutes.[8]

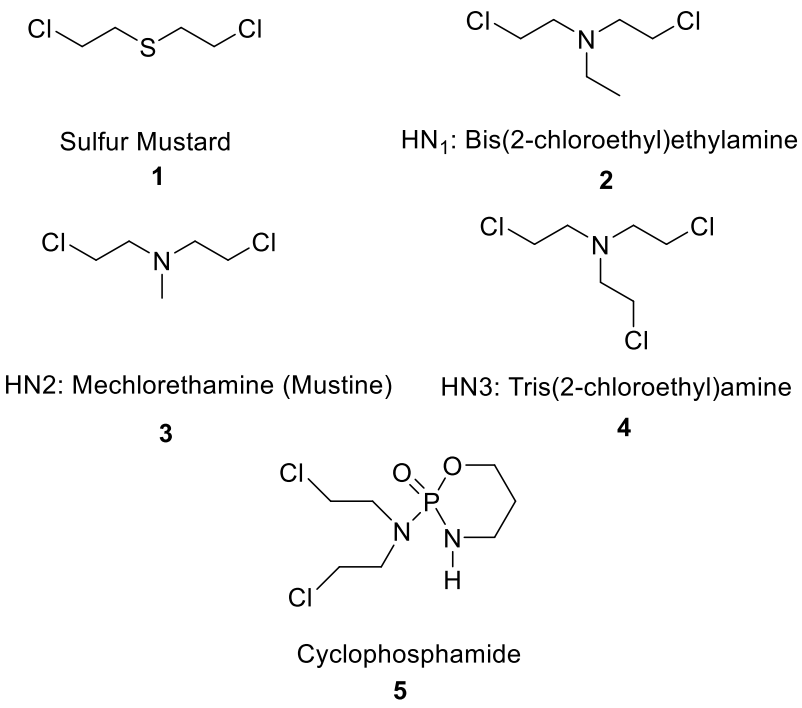

Figure 1.3: Structures of mustard gas and several nitrogen mustards.

Not long after the discovery of the DNA alkylating agents, another successful class of anti-cancer drugs known as the anti-metabolite agents were developed. Generally, the anti-metabolites have a similar structure to naturally occurring metabolites (such as folic acid **6** shown in **Figure 1.4**) and as such they compete for enzyme and receptor binding sites, disrupting natural cellular processes. There are three main types of anti-metabolite: anti-folate, anti-purine and anti-pyrimidine. The first known anti-folate drug is aminopterin **7**, which was investigated with its effects in leukemic children by Sidney Farber in 1947.[20] Remissions occurred among most of the children and this positive effect inspired a search for more efficient and less toxic antagonists to folic acid. Methotrexate **8** was synthesised and proven to be the best anti-folate type drug so far.[21] In 1956, methotrexate was found to be a successful cure for a rare cancer called choriocarcinoma.[22]

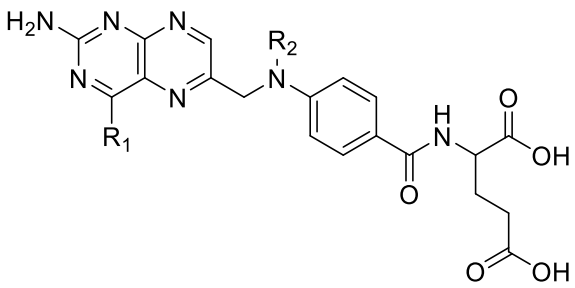

		R1	R2
Folic acid	**6**	OH	H
Aminopterin	**7**	NH2	H
Methotrexate	**8**	NH2	CH3

Figure 1.4: The structure of folic acid, aminopterin and methotrexate.

Over the years, many new anti-cancer drugs have been discovered. Due to the development of a variety of anti-cancer drugs, chemotherapy as a cancer treatment, has become the most promising form of treatment against malignant tumours with high dividing rates. In summary, surgery, radiotherapy and chemotherapy are all effective treatments in cancer therapy. A combination of surgical resection and radiotherapy has enormously improved the first stage of cancer remission, but as mentioned before once the tumour has reoccurred or metastasized, chemotherapy is the only viable option.

1.2 Chemotherapy: Advantages and disadvantages

One of the main aims in the development of new chemotherapies is to be selective for proliferating tumour cells over non-proliferating normal healthy cells. Many commonly used anti-cancer drugs are more targeted and effective against tissue with a higher portion of dividing cells, the proportion which is often called ‘growth fraction’. As discussed in **Section 1.1.2.2**, growth fraction is calculated by the fraction of the active cells in the life cycle (G_1, S, G_2, M) divided by total viable cell population (G_0, G_1, S, G_2, M). Since it is the dividing cells that are targeted by chemotherapeutic drugs, it has been observed that cancer cells and normal tissues with high growth fractions are more susceptible to be affected by anti-cancer drugs. Also, the growth fraction is inversely proportional to the mass doubling times for tumours. It follows that tumours with shorter doubling time are more curable with chemotherapy.

However, when the cancer cells are killed largely by a good and efficient chemotherapy, normal tissues with a high growth fraction, such as bone marrow, hair follicles and

gastrointestinal mucosa, are also damaged by anti-cancer drugs, leading to significant adverse effects. For example, damage of bone marrow, bleeding and infection are some examples of complications of cancer treatment. Thus, the aim of chemotherapy is to enhance the toxicity specifically targeted to cancer cells, at the same time as reducing the side effects on normal cells.

With advances in the development of cancer treatments, more anti-cancer agents have been introduced into chemotherapy, such as proteins, oligo-peptides, antibodies, hormones, nucleic acids, growth factors and so forth. The major problem with chemotherapy in the treatment of cancer is its lack of selectivity when destroying cancer or normal cells. The efficacy of cancer chemotherapy is limited by their poor uptake by cancer cells and high toxicity to normal cells. In addition, most anti-cancer drugs are not water-soluble and thus have poor cellular uptake.

In such circumstances, the development of new anti-cancer drugs aims at addressing the following issues: 1) be safe and non-toxic until within the tumour map; 2) can effectively target the tumour site; 3) can kill cancer cells without affecting normal cells and tissues; 4) achieve good permeability in tumour tissue; 5) maintain long lasting *in vivo* stability and metabolism in blood; 6) capture and kill free cancer cells, restraining recurrence. Therefore, the development of novel anti-cancer drug delivery systems that specifically target cancer cells is urgently required.

1.3 Anti-cancer drug delivery systems

For therapeutic applications, advanced drug delivery systems have been designed and studied to improve the efficacy and accuracy of transporting anti-cancer drugs into the cancer area. Different delivery systems have been developed in order to improve the specific targeting ability, such as loading drugs into liposomes, degradable polymers and novel nanoparticles. In the following section, several common drug delivery systems will be summarized and their applications in the field of cancer therapy discussed.

1.3.1 Polymers

The well-studied field of polymer chemistry provides a solid foundation for discovering new approaches by which anti-cancer drugs can be conjugated to polymers or captured within polymeric micelles.[23] Polymeric materials have great advantages in the

application of drug delivery systems due to their biocompatibility and stable mechanical properties. During the past 40 years, polymers have played a significant role as inert carriers to which therapeutic agents can be covalently linked. Examples include polymer-protein conjugates, polymer-drug conjugates, polymer-DNA complexes and polymeric micelles as shown in **Figure 1.5**.[24] These approaches have developed into a new area of research which is known as polymer therapeutics. Many studies on polymer-drug conjugates have demonstrated clear improvements in pharmacokinetic and pharmacodynamic properties. For example, longer plasma half-life, increased stability of proteins, enhanced solubility of lipophilic drugs, decreased immunogenicity response and the potential for target delivery.[23-25] The majority of these polymer conjugates are designed for anti-cancer chemotherapy, although they can be also designed for other diseases, such as diabetes, arthritis and ischemia.[26,27]

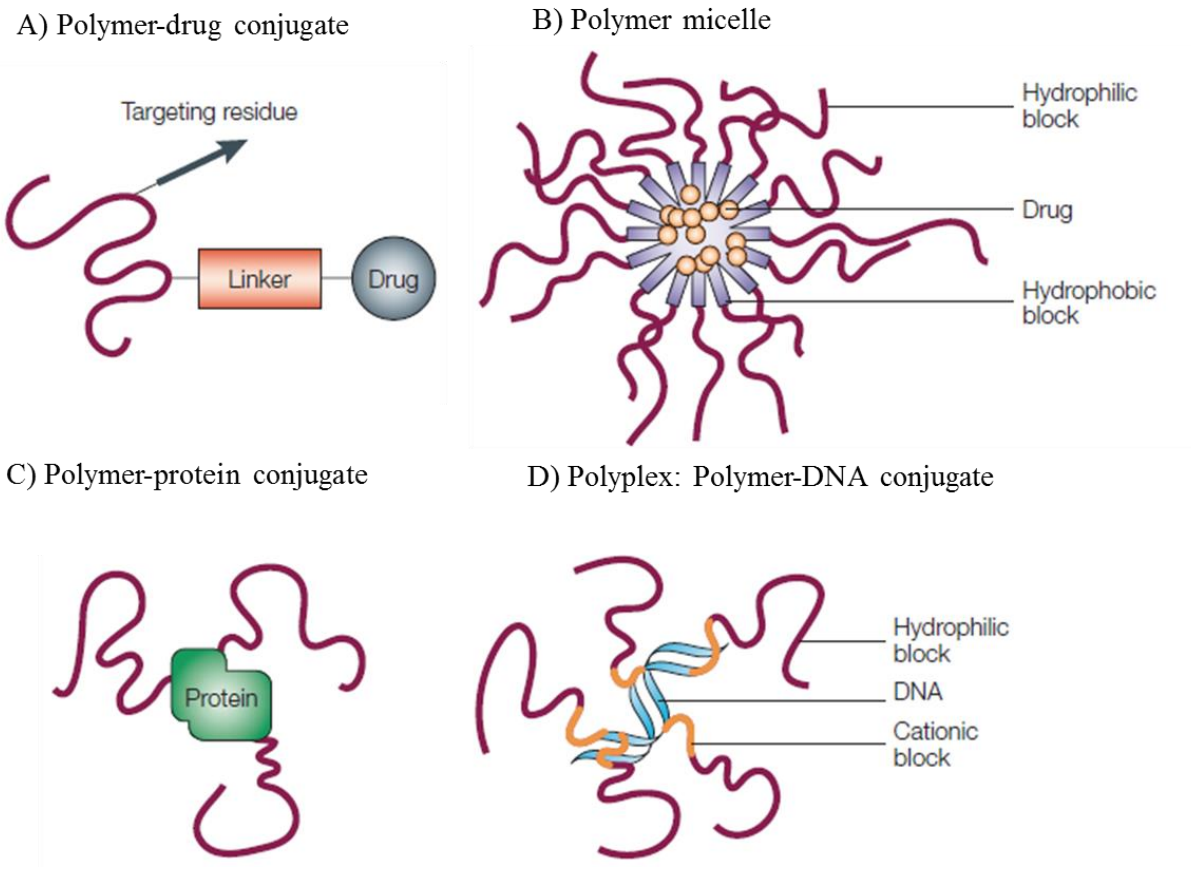

Figure 1.5: Schematic representations of polymer therapeutics: (a) polymer-protein conjugate; (b) polyplex: polymer-DNA conjugate; (c) polymer-drug conjugate; (d) polymer micelle. Reproduced from [24] with permission from Nature Publishing Group, copyright © 2003.

1.3.1.1 Polymer-drug conjugates

Polymer therapeutics have been studied for over four decades and one of the most studied approaches for polymer therapies is polymer-drug conjugates. The pioneering work carried out by Ringsdorf in 1975 on water soluble polymers demonstrated that they were an efficient platform for the delivery of low molecular weight drugs.[28] Further pioneering work by Duncan *et al*. focused on the design of a series of HPMA (*N*-(2-hydroxypropyl) methacrylamide) copolymer-anticancer drug conjugates.[29,30] It has been proven that polymer-drug conjugates have several advantages compared with using anti-cancer drugs alone in chemotherapy such as fewer side effects, enhanced uptake efficiency, longer circulation time, improved patient compliance and easier passive targeting to the tumour site via the enhanced permeation and retention (EPR) effect.[31]

This EPR effect was first found by Matsumura and Maeda when they were studying macromolecular systems (polymer conjugates, nanoparticles and liposomes) and they observed that such systems tend to be selective and accumulate in tumour tissues rather than normal healthy tissues.[32] Tumour vessels, which are normally used as cancer cells' blood and oxygen supplies, are abnormal in formation with a lack of smooth muscle. In addition, tumour tissues have imperfect lymphatic drainage. These defective characteristics of tumour vessels make it easier to retain macromolecular systems in the interstitium, leading to effective tumour targeting.[33] In addition, the high molecular weight of the polymer carriers slows the clearance of conjugates and allows the drug to have a longer systemic circulation time. Furthermore, because of the EPR effect, the polymer-drug conjugate accumulates more in the tumour area leading to a maximised anti-cancer activity.[34]

In general, the rational design of polymer-drug conjugates is composed of three parts: a water soluble polymeric carrier, a small molecule anti-cancer agent and a biodegradable linker between them which is usually a peptidyl or ester linkage.[33] The first reported synthetic polymer-anti-cancer drug complexes were HPMA copolymer-doxorubicin conjugates named PK1.[35] The linkage between the drug and the polymer is a tetrapeptide chain with a sequence of Gly-Phe-Leu-Gly which can be broken by the action of lysosomal enzymes to release the drug. The pharmacokinetic behaviour of PK1 was significantly enhanced compared to free DOX, with a longer half-life of 2.7 h

(0.13 h of DOX) and an elimination half-life of 49 h (85 h for DOX). In addition, the tumour targeting ability increased over 10-100 fold compared to free doxorubicin, depending on the tumour size, and this suggested that the complex was a potent anti-cancer agent.[36,37] Another example of a polymer-drug conjugate is the HPMA copolymer-camptothecin complex. Camptothecins (CPTs) are a family of synthetic anti-cancer agents that inhibit topoisomerase I activity. The water-insolubility and instability of CPTs limit their therapeutic efficacies in patients. Conjugation of CPT-HPMA has improved the drug solubility and stability of the lactone ring.[31,38]

Since the first example of a HPMA copolymer conjugated with DOX was applied as a polymer therapy in cancer treatment, more than twelve polymer-drug conjugates have entered early clinical trials as shown in **Table 1.1**.[23,25]

Table 1.1: Polymer-drug conjugates summary.[23]

Compound	**Name**	**Clinical trial status**	**Target**
Polyglutamate-pacliatxel	CT02103; Xyotax	Phase III	Non-small-cell lung cancer; ovarian cancer
Polyglutamate-camptothecin	CT-2106	Phase I	Various cancers
HPMA-doxorubicin	PK1; FCE28068	Phase II	Lund and breast cancers
HPMA-doxorubicin-galactosamine	PK1; FCE28069	Phase I/II	Hepatocelular carcinoma
HPMA-paxlitaxel	PNU166945	Phase I	Various cancers
HPMA-camptothecin	MAG-CPT	Phase I	Various cancers
HPMA-carboplatin platinate	AP5280	Phase I/II	Various cancers
HPMA-DACH-platinate	AP5346; ProLindac	Phase I/II	Various cancers
Dextran-doxorubicin	AD-70, DOX-OXD	Phase I	Various cancers
Modified dextran-camptothecin	DE-310	Phase I	Various cancers
PEG-camptothecin	Prothecan	Phase II	Various cancers

DACH: diaminocyclohexane; HPMA: *N*-(2-hydroxypropyl)methacrylamide; PEG: poly(ethyleneglycol).

1.3.1.2 Polymer micelles

Polymer micelles are macromolecular assemblies that are formed from AB type or ABA type amphiphilic block polymers. They have many advantages to support their biological applications, such as being biodegradable, non-toxic, biocompatible and non-immunogenic. Generally, polymer micelles are spherical nanostructures and they consist of a hydrophobic inner core and a hydrophilic outer shell. The sizes of these polymer micelles are on average 10-200 nm in diameter, which also categorise them as nanoparticle delivery systems. Water-insoluble drugs can be encapsulated inside the hydrophobic core physically via self-assembly or chemically linked through covalent bonds. Due to the hydrophilicity of the outer shell and biodegradability of the polymer micelle, this drug delivery system can maximize tissue compatibility, increase the half-life in plasma and minimizing the cytotoxicity of the hydrophobic drug.[39]

The major contribution of polymer micelles as drug carriers is to stabilize the drug in the body with a longer circulation time. The large molecular weight of polymer micelles above a threshold molecular weight (42000-5000 Da) means that they can escape glomerular filtration. In addition, the polymer micelle with good biocompatibility can avoid being recognized by the reticuloendothelial system (RES) which is located in the spleen, liver and lung, and thus escape elimination from blood circulation.[40] In order to obtain good biocompatibility, the structure of polymers should have high flexibility, a high degree of hydration and display low immunogenicity. Poly(ethylene oxide) (PEO) is a commonly used hydrophilic polymer of amphiphilic block polymers that has been approved by the FDA.[41] The hydrophobic core of the copolymers can be poly(propylene oxide) (PPO), poly($_{D,L}$-lactic acid) (PDLLA), poly(ε-caprolactone) (PCL) or poly(β-benzyl-$_{L}$-aspartate) (PBLA). Thus, the polymer micelles can be prepared from copolymers PEO-PPO-PEO, PEO-PDLLA or PEO-PBLA and so on.[42] The micelle formation process is affected by many factors, such as the chain ratio of hydrophobic and hydrophilic domains, concentration, temperature and solvents. When the hydrophilic domain volume fraction of the copolymer is more than 45%, polymeric micelle morphologies are formed from self-assembly.[43] The minimum concentration of the self-association of copolymers is known as the critical micelle concentration (CMC). Below the CMC, the amphiphilic copolymer cannot form polymer micelles. The lowest temperature and the highest temperature that polymer micelles can exist in the solution are both named the critical micellization temperature (CMT).[44]

The encapsulation of a hydrophobic drug by copolymers can be carried out using either the dialysis method or the oil/water emulsion method.[45] In the dialysis method, the drug and polymers are first dissolved in an organic solvent and then dialysed against another solvent, most commonly distilled water. The polymer micelles are formed during the dialysis process with the hydrophobic drug being incorporated into the hydrophobic core at the same time. In the other method, the drug is first dissolved in an organic solvent with a low volatile point and then added dropwise to the polymer micelle solution in water to form the oil/water emulsion. The emulsion is kept overnight in an open atmosphere to allow evaporation of the organic solvent with the drug entrapped inside the hydrophobic core. The free drug can be removed by ultrafiltration. For example, doxorubicin is loaded inside the PEO-PBLA polymer micelles with a highest incorporation ratio of 22% (w/w).[46] Drug loading and release have been investigated through many polymer micelles examples. [47,48] The loading efficacy of polymeric micelles is increased when the hydrophobic chain length is increased. In addition, the rate of drug release from polymeric micelles is related to the hydrophobicity of the inner core, the less hydrophobic the faster the drug release due to the weaker interaction between the inner core and the drug. Therefore, it can be concluded that the drug loading and release is dependent on the chemical structure of the amphiphilic polymer micelles.[49]

During the last decade, many types of copolymer micelles have been formed and investigated. Polyion complex micelles (PIC) are formed via electrostatic interactions between two oppositely charged copolymers. For example, when the negatively charged poly(ethylene glycol)-poly(aspartic acid) PEG-P(Asp) and the positively charged poly(ethylene glycol)-poly($_L$-Lysine) PEG-P(Lys) are mixed in stoichiometric charged ratios in aqueous solution they form narrowly distributed PIC micelles with sizes in the range of 30-50 nm.[50] Furthermore, polymer micelles can be designed to have environmental responses, such as to pH, temperature and light. Thus, the drug can be released from the polymeric micelles by physical stimuli which can enhance the specific targeting ability.

1.3.1.3 Polymer-protein Conjugate

The development of recombinant DNA (rDNA), monoclonal antibody (mAb) and solid phase peptide synthesis techniques has introduced new classes of anti-cancer drugs that

are protein, peptide and antibody-based drugs.[51] Over the past decade, more than 350 protein-based drugs have been entered into clinical trials.[52] However, the short half-lives and low enzymatic stabilities of protein and peptide drugs limit their therapeutic applications. In order to achieve the desired effects in a relatively low dose, hydrophilic polymers have been used to modify protein drugs. The polymer-protein conjugates improve the *in vivo* stability thus increasing the biological half-life and also in many cases offer an EPR effect.[24]

Davis *et al.* conjugated a water-soluble polymer polyethylene glycol (PEG) to bovine serum albumin (BSA).[53] This strategy of covalent combination between the selected drug and PEG has now become widely used and is known as PEGylation.[54] PEG is a polymer formed from the repeating ethylene glycol units and the structure of PEG can be chosen as linear or branched with certain molecular masses. Each unit of PEG is tightly bound to two or three water molecules and this becomes much larger in water. This is confirmed by size-exclusion chromatography and gel electrophoresis.[55] The binding water property of PEG can protect the drug from enzyme degradation, slow renal clearance and decrease the immunological effects of the protein drugs. In order to maximize the stability of the PEGylated protein drug, stable chemical bonds between the protein drug and the PEG polymer are needed. Modification of PEG with a variety of functional groups to prepare a more active PEG derivative is the most common method and these include PEG carbonate, PEG ester or PEG aldehyde. Generally, the PEG derivatives are reacted with the amino groups of lysine or N-terminal amino groups.[56]

In 1990, PEG-adenosine deaminase (Adagen®) was approved by the FDA in the treatment of severe combined immunodeficiency disease (SCID) as the first PEGylated protein drug. Subsequently, more PEGylated protein drugs have been designed, and evaluated in clinical trials with some progressing to the market. For example, PEGylated L-asparaginase (Oncaspar®, approved by the FDA in1994) has been used as a chemotherapeutic agent in the treatment of acute lymphocytic leukaemia. This enzyme drug breaks down L-asparagine to aspartic acid and ammonia, which deprives the leukemic cells of asparagine, leading to cell death. PEG-L-asparaginase has been shown to increase the plasma half-life and most importantly decrease hypersensitivity reactions.[57] Although there are many improvements obtained from PEGylation, there

are still some problems left to solve. For example, the size, structure and the active functional groups of PEG need to be carefully designed and controlled. Even small changes can affect the biological activity of the PEGylated protein drugs.

In summary, the polymer therapeutic approach has made some great achievements in delivering potent anti-cancer drugs. Nowadays, four polymers including HPMA copolymer, poly-L-glutamic acid, PEG and Dextran have been conjugated with anti-cancer drugs (DOX, paclitaxel, camptothecin and *cis*-platin) and tested in clinical trials. The key point of successful medical application is to optimize polymer structures based on the multi-disciplinary knowledge of biology, cancer pathophysiology and clinical rules. More polymers with specified structures, responsivenesses and biological activities have been designed and synthesised, the combinations between newly designed polymers and drugs will also be explored. It is believed that polymer therapies have potential for providing improved treatments in the future.

1.3.2 Nanoparticles

Generally, nanoparticle drug delivery systems can transport pharmaceutically active agents into cells/tissues via conjugation to nanometeric carriers. The nanometeric carrier typically consists of sub-particles within the size range of 2-1000 nm and they can have various morphologies, including nanospheres, nanoliposomes and nanocapsules (**Figure 1.6**).[58,59]

Nanoparticles, due to their relatively small size, can enhance cargo retention time in the bloodstream. For anti-cancer drug delivery, using nanoparticles as a method of transportation enhances the ability of targeting cancer cells in a passive or an active manner.

There are many advantages of nanoparticle based drug delivery systems. 1) Due to the small size of the nanoparticle, usually smaller than a tissue cell, drugs can be administered in a flow form, such as injection into a vein. Nanoscale carriers can enter the blood capillary tubes through the free flow of blood in the circulatory system and are taken up through the cells via endocytosis, which improves the absorption and bioavailability of drugs. 2) Nanoparticle can pass through natural biological barriers in the body, such as the cell membrane barrier, blood-brain barrier to reach the cancer site. 3) The large surface area of nanoparticles can increase the solubility of poor

water-soluble drugs, which means that they can overcome conventional formulation problems of low utilization. 4) The nanoparticles may also be designed as a targeting system, more precisely for a particular tissue, organ or cells. 5) Nanocarrier systems can achieve active targeting effects by introducing a specific targeting ligand to seek tumour cells.

When nano-drug carriers enter into the blood by intravenous injection, they can be excreted from the body before they reach their target tissue. The major challenge therefore is to extend the circulation time of nanocarriers in the blood, which can be affected by the anti-cancer drug, the materials of nanoparticles and modification method of the nanoparticles.

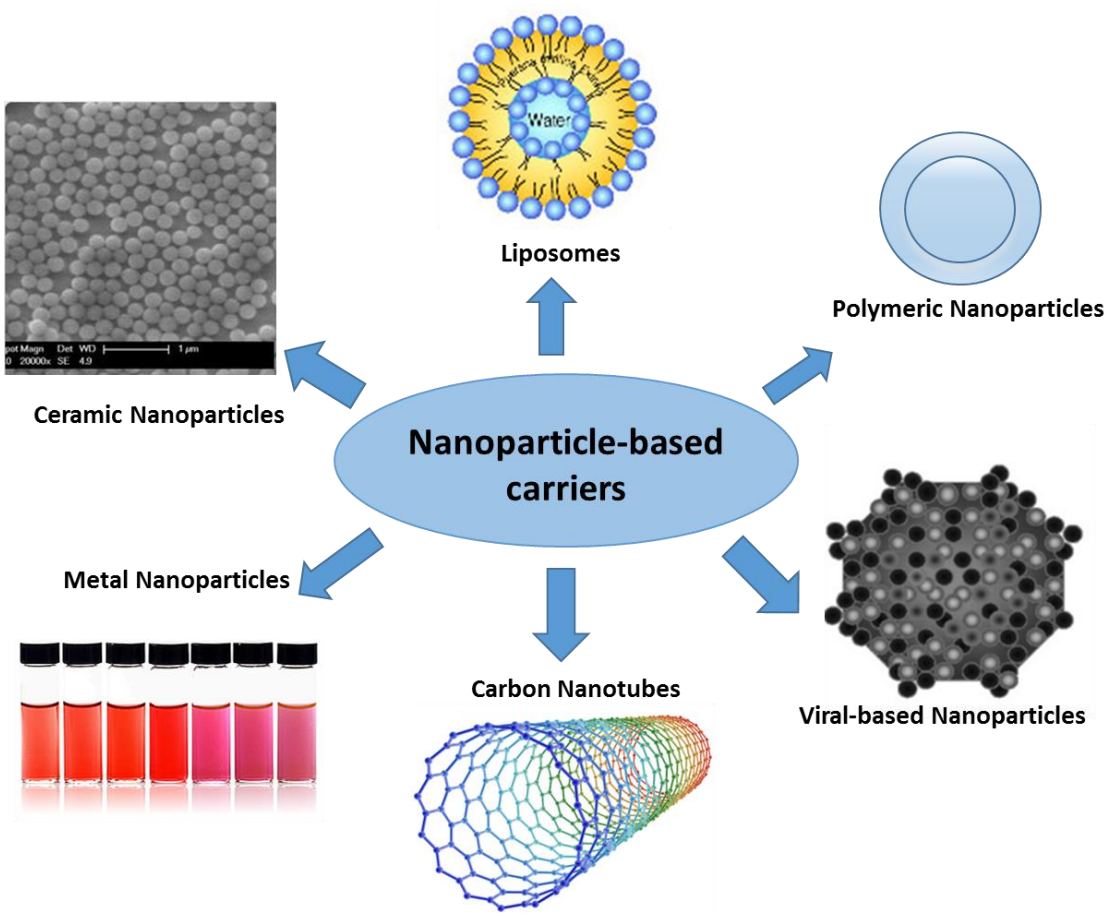

Figure 1.6: Different type of nanoparticle-based carriers.

1.3.2.1 Polymeric nanoparticles

Polymeric nanoparticles are made from biodegradable polymers and they form solid colloidal carriers with sizes smaller than 1 μm. These polymeric nanoparticles can target cancer cells through surface functionalization, and can enhance the therapeutic

efficiency of anti-cancer agents by increasing the systemic circulation half-life.[60] For example, polyethylene glycol (PEG) has been used to functionalize the surfaces of polymeric nanoparticles to increase their stability.[60]

Compared with other solid colloidal carriers, polymeric nanoparticles have been considered as highly promising materials for cancer treatments, because of their biocompatibility, stability and efficacy of high loading. Natural and synthetic polymers are both good candidates. Examples of natural polymers have been investigated to form nanoparticles including gelation, alginate, and chitosan.[61-63] For synthetic polymers, poly(lactic-co-glycolic acid) (PLGA) is one of the most widely studied copolymers for delivery due to its great biodegradability.[64] PLGA undergoes hydrolysis in the body and the products are lactic acid and glycolic acid which are non-toxic. Some other polymers like PEG, PLGA, poly (glycolic acid) (PGA), PCL can also degrade inside the body via normal metabolic pathways and have been approved by the FDA.[65]

By varying the preparation method, nanospheres with a dense matrix or nanocapsules with a liquid core can be obtained. There are two classes of polymeric nanoparticle preparation methods. One is based on the polymerization of monomers carried out by emulsion or interfacial polymerization. The other is a polymer dispersion method, including particle precipitation and double emulsification methods.[66] For the preparation of drug loaded nanoparticles, higher entrapment efficiency can be obtained when the drug is incorporated during the polymerization of monomers rather than absorbed on prepared polymeric nanoparticles.[67]

The polymeric nanoparticles prepared from amphiphilic block copolymers can be considered as core/shell structures, but they are different from polymeric micelles. First, preformulated nanoparticles is controlled kinetically while micelles is controlled thermodynamically. The formation of nanoparticles is controlled by several factors including pH level, temperature and solvents, etc. The formation of micelles is based on the self-assembly of the block polymer unit above CMC. Second, the inner core of nanoparticles is presented in a ‘frozen’ state due to the entanglement of the hydrophobic domain. Once formed, the polymeric nanoparticles can be stabilized in the solvent by steric or electrostatic repulsion.[68]

Both hydrophobic and hydrophilic drugs can be delivered by polymeric nanoparticles. In addition, by functionalization of the nanoparticles with specific targeting domains, the polymeric nanoparticle drug delivery system can then release the drug only in the cancer site. For example, biodegradable PLGA-b-PEG copolymer encapsulated hydrophilic anti-cancer drug docetaxel was used to form polymeric nanoparticles via the nanoprecipitation method. Then, the surface of the formed nanoparticles were functionalized with A10 aptamers which has preloaded DOX via intercalation.[69] The targeted bioconjugate carrier of polymeric nanoparticle and aptamer can release both drugs only in cancer cells that have specific membrane antigens which aptamers bind to. This novel targeted drug delivery system may allow co-delivery in future cancer treatments.

1.3.2.2 Gold nanoparticles (GNPs)

Gold nanoparticles (GNPs) have a long history of being used in biomedical research. The interest in studying GNPs has been stimulated by their ability to be easily functionalized with a wide range of molecules, low levels of cytotoxicity and their size related optical properties. Functionalization of GNPs with different biological molecules has many applications in biomedical imaging, clinical diagnosis and therapy. GNPs are good candidates for medical processes such as labelling, sensing and imaging, drug delivery, and cancer therapeutics due to their unique optical and photothermal properties.[70-72]

One of the early examples of how the optical aspects of spheroidal GNPs can be usefully applied was demonstrated by Mirkin *et al.* in 1996. They showed that DNA-capped gold nanoparticles can assemble into controlled aggregates through DNA hybridization, leading to a distinct shift in surface plasmon properties which can be detected by the naked eye.[73,74] This concept can be useful in the detection of nucleic acids and pathogen nuclear materials in clinical samples. Nanosphere Inc. has developed a concept which uses gold nanoparticles conjugated with oligonucleotides (DNA or RNA) combined with multiplex array analysis and microfluidics for diagnostic tests to detect nucleic acids. Conjugates of functionalized GNP-DNA have also been applied in therapeutics that are reliant upon efficient delivery. For example, remotely controlled GNPs with near-infrared illumination have shown their potential application as optical switches for gene delivery with gene-interfering DNA oligonucleotides.[75] UV

light can be used as a means for illumination as well, activating the release of an inhibiting group from a GNP-peptide conjugate and thus permitting the nanocomplex to bind to a cell.[76,77]

GNP-DNA conjugates can also be used for gene silencing. Gene silencing is well known for its ability to specifically abolish a molecular pathway and *in vivo* delivery could make a considerable impact on genetic diseases such as cancer. GNP-DNA conjugates have been tested as vehicles for gene silencing DNA or RNA transcripts.[78,79] Although this technology has not been demonstrated *in vivo*, it clearly showed that designed GNPs are favourable candidates for biomedical applications. Other interesting uses of GNPs include molecular sensing based on Raman spectroscopy and the enhancement of Raman signatures by surface plasmons. Raman imaging holds significant potential as a strategy for biomedical imaging of living subjects. The Raman images of methylene blue molecules that adsorbed on gold nanospheres have been studied.[80] Dye molecules attached to the GNPs and localized in the hotspots, leading to the enhancement of their vibrational state. In this report, Raman imaging was tested in cells but not within living organisms.[81] Recently, this spectroscopic method of detection has been applied for *in vivo* sensing.[82]

In recent years, GNPs have been widely used in biomedical applications, such as targeting probes or drug carriers due to their small size, biocompatibility and ease of synthesis and modification. Chan *et al.*[83] studied the uptake of GNPs in HeLa cells and found that particles with diameters between 20-60 nm have the highest cellular uptakes. Functionalization of GNPs with cell penetrating peptides can be carried out to help improve the efficiency of living cell uptake. In 2008, Sun *et al.*[84] utilised CALNN and its derivative CALNNGGRRRRRRRR ($CALNNR_8$) to functionalize GNPs to prepare nanomaterials that could target intracellular components. In this study, GNPs of different sizes (13nm, 30nm, 60nm) were synthesised by using the Frens-Turkevich method.[85,86] Then, peptide-capped GNPs were prepared by a one-step gold-thiol reaction. The ratio of the $CALNNR_8$ to CALNN on the surface of the GNPs was 1:9 respectively. After incubation with HeLa cells, it was found that the peptide-GNPs had translocated into the cell nucleus.

1.3.3 Cell penetrating peptides

Recently, therapeutic peptides have been found to be useful in drug delivery due to their biocompatibility, biodegradability and non-immunogenicity. Among polypeptides, cell penetrating peptides (CPPs) are promising drug delivery systems that are capable of transferring molecules into, cytosol and even to reach intracellular targets.[87] During the last decade, cell penetrating peptides (CPPs) have been developed extensively and applied to CPP-based drug delivery strategies. Firstly, Frankel and Pabo[88] discovered that the purified Tat protein which is derived from the human immunodeficiency virus 1 (HIV-1) can be taken up by cells and localized into the nucleus. Later, Derossi *et al.*[89] found that a 16 amino acid peptide (pAntp or penetratin) derived from the third helix of the homeodomain protein[90] is also capable of internalizing into nuclei through plasma membranes. Based on the discovery of these two types of CPPs, additional examples have been identified that are generally rich in basic cationic residues (Lys, Arg). This is due to the interaction between the polycations and the negatively charged molecules on the cell surface. It is now known that CPPs are normally made of short polycationic peptide sequences, in the range of 10-30 amino acids. There are three subgroups of CPPs as defined by their origin or sequence characteristics: protein derived, chimeric and synthetic as listed in **Table 1.2**.[91]

Table 1.2: Categories of cell-penetrating peptides with a few examples.[91]

Category	Name and sequence	Origin
Protein derived CPP	Penetratin RQIKIWFQNRRMKWKK-NH_2	*Drosophila* homeoprotein Antennapedia
	Tat (48-60) GRKKRRQRRRPPQ	Human immunodeficiency virus type 1 (HIV-1) Tat
Chimeric CPP	MPG GALFLGFLGAAGSTMGA-cya*	A hydrophobic domain from the fusion sequence of HIV gp41 and NLS of SV40 T-antigen
	Pep-1 KETWWETWWTEWSQPKKKRKV-cya*	NLS from Simian Virus 40 large antigen T and reverse transcriptase of HIV
Synthetic CPP	MAP KLALKLALKALKAALKLA	Amphipathic model peptide
	Octa / Nona-Arginine RRRRRRRR/R	Positively charged sequence

* -cya : N-terminal cysteamide

CPPs have been shown to improve the intracellular delivery of a variety of biomolecules, including DNA and short interfering RNA (siRNA).[92] In the field of cancer drug delivery research, CPPs have been used to increase the therapeutic efficiency of commonly used cancer drugs, such as doxorubicin and methotrexate.[93,94] For example, the Tat-Doxorubicin conjugates have demonstrated an increased killing ability on drug resistant tumour MCF-7cells (MCF-7/ADR). Although combining anti-cancer agents with CPPs has improved cellular uptake, CPPs suffer like all peptides from poor stability *in vivo* and have no intracellular specificity.[95] In response to this tumour specificity problem, adding a home targeting domain to the sequence of CPPs to containing both tumour targeting properties and cell penetrating ability has been carried out. For example, a folate acid receptor as a homing domain has been conjugated to a CPP-modified liposomal nanocarrier which demonstrated an enhanced cellular uptake in folate receptor-responsive cell lines.[96] It has been discovered that folate receptors are highly expressed in cervical, breast, lung and brain tumours.[97] Another example of modulated CPP delivery is RGD. The internalizing RGD (iRGD) has demonstrated the ability to target many types of tumour *in vivo* and can be detected throughout the

tumour substance, not limited to the tumour vasculature.[98] Liu *et al.* designed a multifunctional peptide R8-RGD, a modified RGD peptide conjugated to a cell penetrating peptide R8, which increased the cellular uptake of liposomes in C6 glioma cells by nearly 30-fold.[99] Moreover, this modified CPP-conjugated liposome efficiently delivered the anti-cancer drug paclitaxel to specific tumour areas.

1.4 Stimuli responsive drug delivery

Compared to normal tissues, tumour areas have a high temperature (about 39-42 ℃) and a low pH (pH = 6.5-7.2).[100] In cancer treatment studies, attempts are often made to exploit these properties to design target treatments. Intelligent stimulus-responsive materials, especially temperature and pH-responsive materials are widely used in biomedical research due to their spontaneous changeable properties under variable conditions.

It is well known that biopolymers such as proteins or nucleic acids can react sensitively to changes in the environment. Using chemistry to create mimics of biopolymers and biological systems is a significant area of research. During the past decades, stimuli-responsive novel materials have proved to be effective for targeted drug delivery.

The nature of the environmental stimulus can be classified into three categories: physical, chemical, and biomedical (**Table 1.3**).[101] Stimuli-responsive delivery systems can be made of polymers, liposomes or nanoparticles. Here, we will mainly focus on the discussion of stimuli-responsive polymers (SPRs) applied in drug delivery areas. SPRs are known as smart polymers or environmentally responsive polymers and can respond to a variety of signals that include temperature, ionic strength, environmental pH and chemical agents including ligands and enzymes.

Table 1.3: Environmental stimuli categories.

Physical	Chemical	Biomedical
Temperature	pH	Enzyme substrate
Ionic strength	Specific ions	Affinity ligands
Solvents	Chemical agents	other biochemical agents
Electromagnetic radiation (UV, light)		
Electric fields		
Mechanical stress, strain		
Sonic radiation		
Magnetic fields		

Physical stimuli have an effect on the interaction between the polymer molecules themselves or between the polymer chains and the solvent molecules as well as chemical and biomedical stimuli. Physical stimuli, such as temperature, can change molecular interactions at a certain point which creates a phase transition. These changes, which can be observed by microscopy, can explain the smart behaviour.

With respect to possible applications in biomedicine or biotechnology, the main focus is based on smart polymers with transitions triggered by temperature, pH and light. Many materials have been widely studied in drug targeting delivery and controlled release, such as poly(N-isopropylacrylamide) (PNIPAAm).[102] In the following section, aspects of temperature, pH and light responsiveness will be introduced.

1.4.1 Temperature sensitive targeting

Temperature responsive polymers undergo inverse temperature phase transitions. Below their transition temperature (T_t) thermally-responsive SRPs are soluble in aqueous solution, but upon raising their temperature above the T_t, SRPs become insoluble and aggregate in solution. In this case, the transition temperature is called a lower critical solution temperature (LCST). Otherwise, if aggregation is observed below a critical temperature the polymer shows an upper critical solution temperature (UCST) or higher

critical solution temperature (HCST) behaviour. However, most research is conducted on polymers with LCST behaviour.

The most studied synthetic responsive polymer (SNP) is PNIPAAm. It undergoes a transition temperature in water at 32-34 ℃, changing from a hydrophilic state below this temperature to a hydrophobic state above it.[103] The sharp phase transition of PNIPAAm is attributed to the balance between hydrophilic and hydrophobic interactions. The phase change of an aqueous PNIPAAm solution is from coil to globule when raising the temperature. The phase transition, as shown in **Figure 1.7**, arises because the water molecules bonded to the side-chain isopropyl moieties are released into the aqueous phase when temperature exceeds the critical point.[104] The balance between segment-segment interactions and segment-solvent intermolecular interactions can be shifted by temperature changes. The phase separation can also be explained thermodynamically in terms of the change of the free energy (ΔG). The free energy of polymer systems can be described as: $\Delta G = \Delta H - T\Delta S$ with the ΔH representing enthalpic energy and ΔS standing for entropy change. Below the LCST, the polymer and the solvent molecules form a homogeneous mixture supported by hydrogen-bonding to the polymer chain and this has a favourable free energy ($\Delta G<0$). When the temperature is raised above LCST, the occurrence of phase separation is due to the enthalpic contribution that overcomes the entropic part resulting in an unfavourable free energy of the system ($\Delta G>0$).[105]

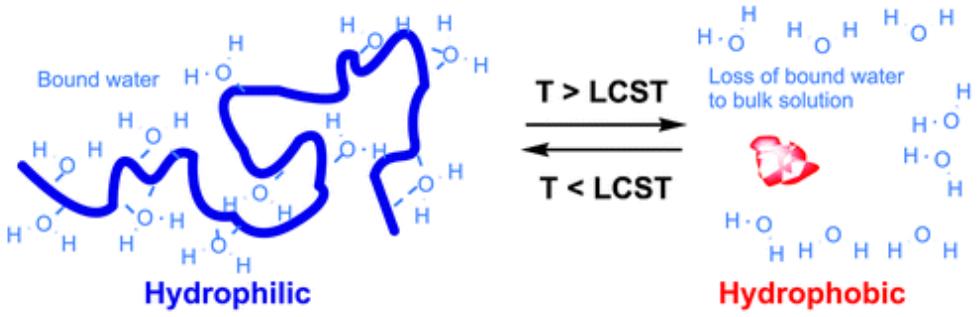

Figure 1.7: Schematic of 'smart' polymer conformation change with temperature. Reproduced from [104] with permission from Royal Society of Chemistry, copyright © 2005.

According to the theory above, the LCST of a given polymer can be adjusted by changing the hydrophilic or hydrophobic moieties in the polymer chain. Raising the hydrophobicity will cause a decrease in LCST. On the other hand, more hydrophilic

domains will increase the LCST. This temperature shift can be affected by many possibilities. PNIPAAm contains a hydrophobic isopropyl group and a hydrophilic amide group. The balance mainly depends on the N-substituent. Many PNIPAAm-based materials that have the LCST close to body temperature (37 ℃) have been reported for biomedical applications.[106-108] Except for PNIPAAm, there are some other important temperature sensitive polymers. They are poly(*N*,*N*-diethylacrylamide) (PDEAAm), poly(N-vinyl caprolactam) (PVCL), poly(ethylene glycol) (PEG), poly(propylene oxide) (PPO) and poly(VPGVG) as shown in **Figure 1.8**.[104]

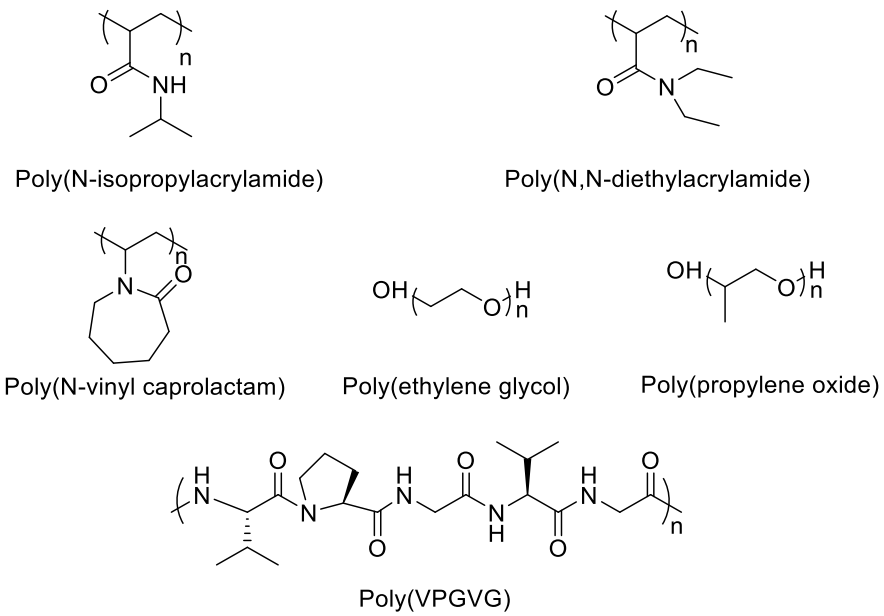

Figure 1.8: Structures of commonly used responsive polymer systems.

PDEAAm has a lower enthalpy value of phase transition than PNIPPAm which means its LCST is 32 ℃.[109] PVCL is water soluble at room temperature gradually becoming insoluble from 32-40 ℃.[110,111] PEG polymers in pure water have a high LCST of 96 ℃, while in aqueous salt solution, the critical temperature decreases.[112] Copolymerization is the most common way of adjusting the LCST. For example, PPO itself is hydrophobic, but PPO-PEG copolymers can lead to a wide range of hydrophilic-lipophilic properties when the composition is varied.[113] A number of PEO-PPO-PEO block polymers have been shown to aggregate in the form of micelles or even in the form of gels at high concentrations with increasing temperature.[114] As is well known, PEO and PPO block copolymers like Poloxamers and Pluronics are commercially available and exhibit phase transition varying from 20 ℃ to 85 ℃.[115] All the materials currently mentioned

can be also classified as multiple-responsive polymers because they are not only temperature sensitive but also respond to pH, salts or electromagnetic radiation.[112,116]

1.4.2 pH targeting

Polymers containing ionizable functional groups that respond to pH variations are called pH-sensitive polymers. Their structure and solubility change in response to pH change. This is a common feature of biopolymers. For example, the conformation of peptides mainly depends on intramolecular or intermolecular interactions such as hydrogen bonds or charge attractions.[117] As the environmental pH varies, the transition point within this equilibrium of accepting and donating protons at a specific pH is the so-called pK_a value. If the solution has a pH value close to the pK_a, the degree of ionization will be changed dramatically. When the polymers' pendant groups become charged in aqueous solution, they become polyelectrolytes and the conformation is expanded. But when the pH changes, the polymer turns into an uncharged macromolecule and has a transition from an expanded state to a collapsed state. This is explained by the osmotic pressure applied by mobile counter ions neutralizing the network charges.[118] There are two types of pH-responsive polyelectrolytes: weak polyacids and weak polybases.

Polyacids

The presence of carboxylic groups in polymers is the most common feature of pH-responsive polyacids (**Figure 1.9**). The pK_a values of the carboxylic groups are usually between 5 and 6. At a higher pH, the pendant carboxylic group is deprotonated forming polyelectrolytes. On the other hand, the carboxylic groups accept protons forming an uncharged and hydrophobic molecule at a lower pH.

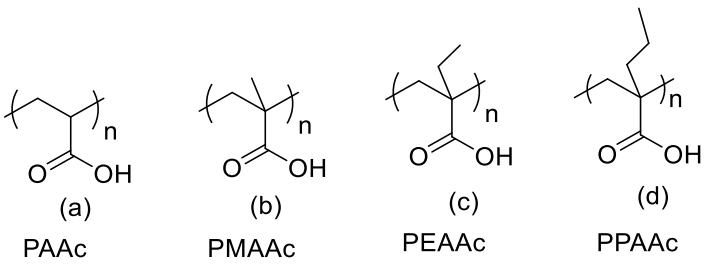

Figure 1.9: Structures of pH-responsive polyacids: (a) poly(acrylic acid) (PAAc); (b) poly(methacrylic acid) (PMAAc); (c) poly(2-ethyl acrylic acid) (PEAAc); (d) poly(2-propyl acrylic acid) (PPAAc).[119]

Poly(acrylic acid) (PAAc) and poly(methacrylic acid) (PMAAc) are typical examples of pH-sensitive polyacids.[119-122] According to the theory above, PAAc and PMAAc are polyelectrolytes at high pH because of electrostatic repulsion forces between the molecular chains. Their carboxylic groups accept protons at low pH and release them at high pH. PMAAc has an additional hydrophobic methyl group than PAAc which means it shows a more compact conformation and an abrupt phase transition compared with the relatively continuous phase transition of PAAc. This compact conformation of uncharged PMAAc is sometimes referred as a 'hypercoiled' conformation. Following this trend, adding a more hydrophobic moiety can offer a more compact conformation and a sharper phase transition. Therefore, poly(2-ethyl acrylic acid) (PEAAc) and poly(2-propyl acrylic acid) contain more hydrophobic moieties and provide more hypercoiling behaviour at low pH.[118,123] This behaviour of polymers, changing from a charged extended chain to an uncharged coil structure, can act as a simple switch between 'on' and 'off' state which can be applied in pharmaceutical areas.[118]

Polybases

Figure 1.10 shows some representatives of weak polybases. The amine groups of these polymers accept protons at low pH values forming polyelectrolytes, while releasing protons at higher pH resulting in uncharged macromolecules. Poly(*N*,*N*-dimethyl aminoethyl methacrylate) (PDMAEMA) and poly(*N*,*N*-diethyl aminoethyl methacrylate) (PDEAEMA) are the most frequently investigated pH-responsive polybases. As for the theory of polyacids, a polymer that has a longer hydrophobic group at the end of the pendant group causes stronger hydrophobic interactions at high pH. PDEAEMA has a more compact structure at high pH than PDMAEMA, therefore also leading to a 'hypercoiled' conformation. When the pH is 7.5, PDEAEMA shows an abrupt precipitation due to the deprotonation of amino groups.[124] PDMAEMA was reported to have similar sensitive properties as PNIPAAm that has not only pH sensitivity but also temperature sensitivity.[125] Poly(4 or 2-vinylpyridine) (P4VP or P2VP) have aromatic amines and offer a critical pH at 5 due to the process of deprotonation of pyridine groups.[126,127] Poly(vinyl imidazole) (PVI) is another pH-sensitive polybase that has the imidazole group.

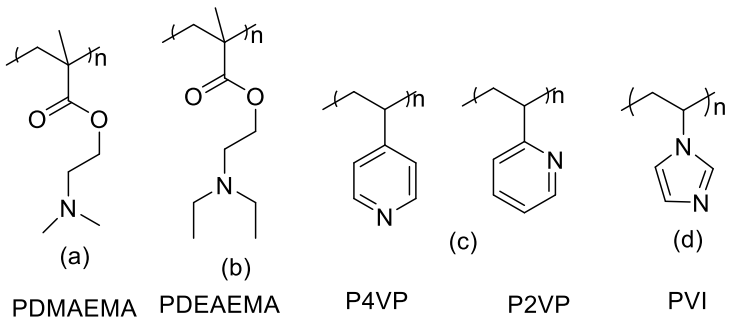

Figure 1.10: Structures of pH-responsive polyabases: (a) poly(*N*,*N*-dimethyl aminoethyl methacrylate) (PDMAEMA); (b) poly(*N*,*N*-diethyl aminoethyl methacrylate) (PDEAEMA); (c) poly(4 or 2-vinylpyridine) (P4VP or P2VP); (d) poly(vinyl imidazole) (PVI).[128]

For different applications, sometimes it is required to adjust the critical pH of certain polymers, at which phase transitions happen as well as conformation changes. This usually can be modified by copolymerization with hydrophilic or hydrophobic co-monomers.[123,129]

1.4.3 Light activation

Light as an easily controlled stimulus is very important and attractive. It has been used broadly in smart materials as it offers a wide range of adjustable parameters such as wavelength, intensity and duration.[129,130] Azobenzene and spyrobenzopyran moieties in macromolecules can lead to photoresponsive polymers that undergo an efficient and reversible photo-isomerization reaction upon irradiation with UV-Vis light.[131] For example, Nalluri and co-workers reported a light-responsive interaction of vesicles that are composed of amphiphilic with bifunctional guest molecules containing azobenzene groups. Only the *trans*-azobenzene can bind to the cyclodextrins, the *cis*-azobenzene adopts a conformation that prevents it from acting as a guest. When UV light (350 nm) irradiation was used excite molecules, the *trans*-azobenzene induces rapid aggregation and adhesion of vesicles. This photoresponsive supramolecular system is highly selective and fully reversible.[132]

1.5 Summary and project aims

The overall aim of this thesis is to combine different components to develop three delivery systems that have potential applications in drug delivery and specifically cancer therapy.

The first aim of the work is to design and synthesise stimuli-responsive polymers based on the structure of natural elastin-like polypeptide (ELP). Solid-phase peptide synthesis and reversible addition-fragmentation chain-transfer (RAFT) polymerisation techniques will be used to prepare novel elastin-based side chain polymers (ESPs).

The second aim of the work is to focus on preparing peptide-functionalized GNPs including thermo-responsive polymers and anti-cancer peptide ($_D$-KLA). GNPs can improve the stability of peptides and permeability in cancer cells, and their fluorescence properties can be used as *in vivo* tracking molecules. Here we are looking to develop a novel system which can deliver the anti-cancer peptide $_D$-KLA into cancer cells for application in cancer diagnosis and therapy. Under normal physiological conditions, the nanoparticles will be coated with polymers that will 'hide' the peptide prior to it reaching the tumour tissue. The elastin-like polymers (ESPs) can protect the nanoparticle constructs from degradation *in vivo* (so-called 'stealth' behaviour). While in the extra-cellular space of tumour tissue (higher temperature 42^{o}C), the ESPs' aggregation behaviours will lead to the exposure of anti-cancer KLA peptide. The surface of GNPs will be modified with temperature-sensitive ESPs and anti-cancer KLA peptide via thiol-gold linkages. Temperature-responsiveness of ESP functionalized GNPs will be studied using UV-Vis spectroscopy and circular dichroism measurements. KLA peptide conjugated GNPs will be synthesised and their cytotoxicities and cellular uptake abilities will be studied. Then, GNPs nanocomposites functionalized by both ESPs and KLA peptide will be synthesised and temperature related cytotoxicities will be tested.

Finally we will study delivery of mitochondrial pro-apoptotic peptide ($_D$-KLA) into cell with organelle specificity using cell penetrating peptoids (CPPos). CPPos are very promising candidates, as they not only have the same penetrating ability of cell penetrating peptides (CPP), but also highly resistant to proteolysis. Based on this, we will conjugate anti-cancer peptide $_D$-KLA to a series of cell penetrating peptoids (CPPos) to obtain better $_D$-KLA delivery systems. KLA-peptoid hybrids cytotoxicity will be tested in HeLa cervical cancer cells.

1.6 References

1. WHO. *World Cancer Report 2014*, 2014. http://www.who.int/mediacentre/factsheets/fs297/en/, (accessed 2014).

2. *Atlanta: American Cancer Society*, 2015. http://www.cancer.org/acs/groups/content/@research/documents/document/acspc-044738.pdf, (accessed 2015)
3. W. Chen, R. Zheng, H. Zeng and S. Zhang, *Thoracic Cancer*, 2015, **6**, 209-215.
4. B. Vogelstein and K. W. Kinzler, *Nat. Med.*, 2004, **10**, 789-799.
5. I. M. Ariel, *High-Risk Breast Cancer*, Springer, 1991.
6. *American cancer society*, 2014 http://www.cancer.org/acs/groups/cid/documents/webcontent/002048-pdf.pdf, (accessed 2014)
7. A. R. David and M. R. Zimmerman, *Nat. Rev. Cancer*, 2010, **10**, 728-733.
8. J. Mann, *Life Saving Drugs: The Elusive Magic Bullet*, Royal Society of Chemistry, 2004.
9. Y. H. Bae, R. J. Mrsny and K. Park, *Cancer Targeted Drug Delivery: An Elusive Dream*, Springer Science & Business Media, 2013.
10. M. Gospodarowicz, L. Benedet, R. V. Hutter, I. Fleming, D. E. Henson and L. H. Sobin, *Cancer Prev Control*, 1998, **2**, 262-268.
11. J. T. Bushberg and J. M. Boone, *The essential physics of medical imaging*, Lippincott Williams & Wilkins, 2011.
12. D. J. Brenner and E. J. Hall, *N. Engl. J. Med.*, 2007, **357**, 2277-2284.
13. T. M. Pawlik and K. Keyomarsi, *Int. J. Radiat. Oncol. Biol. Phys.*, 2004, **59**, 928-942.
14. A. Charles and A. Ramani, *J. Chem. Pharm. Res.*, 2011, **3**, 205-211.
15. P. Ehrlich, *Nobel lecture* 1908.
16. K. Strebhardt and A. Ullrich, *Nat. Rev. Cancer*, 2008, **8**, 473-480.
17. V. T. DeVita and E. Chu, *Cancer Res.*, 2008, **68**, 8643-8653.
18. A. Gilman and F. S. Philips, *Science*, 1946, **103**, 409-436.
19. G. P. Wheeler, *Cancer Res.*, 1962, **22**, 651-688.
20. S. Farber, L. K. Diamond, R. D. Mercer, R. F. Sylvester Jr and J. A. Wolff, *N. Engl. J. Med.*, 1948, **238**, 787-793.
21. D. R. Seeger, D. B. Cosulich, J. M. Smith and M. E. Hultquist, *J. Am. Chem. Soc.*, 1949, **71**, 1753-1758.
22. M. C. Li, R. Hertz and D. M. Bergenstal, *N. Engl. J. Med.*, 1958, **259**, 66-74.
23. R. Duncan, *Nat. Rev. Cancer*, 2006, **6**, 688-701.
24. R. Duncan, *Nat. Rev. Drug Discov.*, 2003, **2**, 347-360.
25. R. Satchi-Fainaro, R. Duncan and C. M. Barnes, *Polymer Therapeutics II*, Springer, 2006.
26. M. J. Vicent, L. Dieudonné, R. J. Carbajo and A. Pineda-Lucena, *Expert Opin. Drug Deliv.*, 2008, **5**, 593-614.
27. W. B. Liechty, D. R. Kryscio, B. V. Slaughter and N. A. Peppas, *Annu. Rev. Chem. Biomol. Eng.*, 2010, **1**, 149.
28. H. Ringsdorf, *J. Polym. Sci., C*,1975,**51**,135-153
29. R. Duncan and J. Kopeček, *Polymers in medicine*, Springer, 1984.
30. R. Duncan, J. B. Lloyd and J. Kopeček, *Biochem. Biophys. Res. Commun.*, 1980, **94**, 284-290.
31. C. Li and S. Wallace, *Adv. Drug Deliv. Rev.*, 2008, **60**, 886-898.
32. Y. Matsumura and H. Maeda, *Cancer Res.*, 1986, **46**, 6387-6392.
33. R. Duncan, M. J. Vicent, F. Greco and R. I. Nicholson, *Endocr. Relat. Cancer*, 2005, **12**, S189-S199.
34. P. Chytil, T. Etrych, Č. Koňák, M. Šírová, T. Mrkvan, J. Bouček, B. Říhová and K. Ulbrich, *J. Control. Release*, 2008, **127**, 121-130.

35. P. A. Vasey, S. B. Kaye, R. Morrison, C. Twelves, P. Wilson, R. Duncan, A. H. Thomson, L. S. Murray, T. E. Hilditch and T. Murray, *Clin. Cancer Res.*, 1999, **5**, 83-94.
36. R. Sinha, G. J. Kim, S. Nie and D. M. Shin, *Mol. Cancer Ther.*, 2006, **5**, 1909-1917.
37. L. W. Seymour, D. R. Ferry, D. Anderson, S. Hesslewood, P. J. Julyan, R. Poyner, J. Doran, A. M. Young, S. Burtles and D. J. Kerr, *J. Clin. Oncol.*, 2002, **20**, 1668-1676.
38. N. E. Schoemaker, C. Van Kesteren, H. Rosing, S. Jansen, M. Swart, J. Lieverst, D. Fraier, M. Breda, C. Pellizzoni and R. Spinelli, *Br. J. Cancer*, 2002, **87**, 608-614.
39. S. M. Moghimi, A. C. Hunter and J. C. Murray, *FASEB J.*, 2005, **19**, 311-330.
40. S. Stolnik, L. Illum and S. S. Davis, *Adv. Drug Deliv. Rev.*, 2012, **64**, 290-301.
41. J. M. Harris, *Poly (ethylene glycol) Chemistry*, Springer, 1992.
42. M.-C. Jones and J.-C. Leroux, *Eur. J. Pharm. Biopharm.*, 1999, **48**, 101-111.
43. R. Erhardt, A. Böker, H. Zettl, H. Kaya, W. Pyckhout-Hintzen, G. Krausch, V. Abetz and A. H. E. Müller, *Macromolecules*, 2001, **34**, 1069-1075.
44. G. B. Dutt, *J. Phys. Chem. B*, 2005, **109**, 4923-4928.
45. S. B. La, T. Okano and K. Kataoka, *J. Pharm. Sci.*, 1996, **85**, 85-90.
46. G. Kwon, M. Naito, M. Yokoyama, T. Okano, Y. Sakurai and K. Kataoka, *J. Control. Release*, 1997, **48**, 195-201.
47. S. C. Kim, D. W. Kim, Y. H. Shim, J. S. Bang, H. S. Oh, S. W. Kim and M. H. Seo, *J. Control. Release*, 2001, **72**, 191-202.
48. H. S. Yoo and T. G. Park, *J. Control. Release*, 2004, **96**, 273-283.
49. O. M. Koo, I. Rubinstein and H. Onyuksel, *Nanomedicine*, 2005, **1**, 193-212.
50. A. Harada and K. Kataoka, *Macromolecules*, 1995, **28**, 5294-5299.
51. T. Nagle, C. Berg, R. Nassr and K. Pang, *Nat. Rev. Drug Discov.*, 2003, **2**, 75-79.
52. J. A. Cavagnaro, *Nat. Rev. Drug Discov.*, 2002, **1**, 469-475.
53. F. F. Davis, A. Abuchowski, T. Van Es, N. C. Palczuk, R. Chen, K. Savoca and K. Wieder, *Enzyme Engineering*, Springer, 1978.
54. O. H. Brekke and I. Sandlie, *Nat. Rev. Drug Discov.*, 2003, **2**, 52-62.
55. A. Kozlowski and J. M. Harris, *J. Control. Release*, 2001, **72**, 217-224.
56. J. M. Harris and R. B. Chess, *Nat. Rev. Drug Discov.*, 2003, **2**, 214-221.
57. T. C. Abshire, B. H. Pollock, A. L. Billett, P. Bradley and G. R. Buchanan, *Blood*, 2000, **96**, 1709-1715.
58. T. Jung, W. Kamm, A. Breitenbach, E. Kaiserling, J. X. Xiao and T. Kissel, *Eur. J. Pharm. Biopharm.*, 2000, **50**, 147-160.
59. C. P. Reis, R. J. Neufeld, A. J. Ribeiro and F. Veiga, *Nanomedicine*, 2006, **2**, 8-21.
60. R. Gref, M. Lück, P. Quellec, M. Marchand, E. Dellacherie, S. Harnisch, T. Blunk and R. Müller, *Colloids Surf., B*, 2000, **18**, 301-313.
61. C.-Y. Yu, L.-H. Jia, B.-C. Yin, X.-Z. Zhang, S.-X. Cheng and R.-X. Zhuo, *J. Phys. Chem. C*, **2008**, *112*, 16774-16778.
62. J. Wang, B. Chen, D. Zhao, Y. Peng, R.-X. Zhuo and S.-X. Cheng, *Int. J. Pharm.*, **2013**, *446*, 205-210.
63. G. Kaul and M. Amiji, *Pharm. Res.*, **2005**, *22*, 951-961.
64. H. K. Makadia and J. Siegel, *Polymers*, **2011**, *3*, 1377-1397.
65. F. Alexis, J.-W. Rhee, J. P. Richie, A. F. Radovic-Moreno, R. Langer and O. C. Farokhzad, *Urol. Oncol.*, 2008, **26**, 74-85.
66. B. Mishra, B. B. Patel and S. Tiwari, *Nanomedicine*, 2010, **6**, 9-24.

67. M. J. Alonso, C. Losa, P. Calvo and J. Vila-Jato, *Int. J. Pharm.*, 1991, **68**, 69-76.
68. H. K. Cho, I. W. Cheong, J. M. Lee and J. H. Kim, *Korean J. Chem. Eng.*, 2010, **27**, 731-740.
69. L. Zhang, A. F. Radovic-Moreno, F. Alexis, F. X. Gu, P. A. Basto, V. Bagalkot, S. Jon, R. S. Langer and O. C. Farokhzad, *ChemMedChem*, 2007, **2**, 1268-1271.
70. P. Ghosh, G. Han, M. De, C. K. Kim and V. M. Rotello, *Adv. Drug Deliv. Rev.*, **2008**, *60*, 1307-1315.
71. N. R. Jabir, S. Tabrez, G. M. Ashraf, S. Shakil, G. A. Damanhouri and M. A. Kamal, *Int. J. Nanomedicine*, **2012**, *7*, 4391.
72. V. P. Pattani and J. W. Tunnell, *Lasers Surg. Med.*, **2012**, *44*, 675-684.
73. C. A. Mirkin, R. L. Letsinger, R. C. Mucic and J. J. Storhoff, *Nature*, 1996, **382**, 607-609
74. J. Storhoff and C. Mirkin, *Chem. Rev.*, 1999,**99**, 1849-1862.
75. S. E. Lee, G. L. Liu, F. Kim and L. P. Lee, *Nano Lett.*, 2009, **9**, 562-570.
76. R. Lévy, N. T. Thanh, R. C. Doty, I. Hussain, R. J. Nichols, D. J. Schiffrin, M. Brust and D. G. Fernig, *J. Am. Chem. Soc.*, 2004, **126**, 10076-10084.
77. T. Dvir, M. R. Banghart, B. P. Timko, R. Langer and D. S. Kohane, *Nano Lett.*, 2009, **10**, 250-254.
78. M. D. Massich, D. A. Giljohann, D. S. Seferos, L. E. Ludlow, C. M. Horvath and C. A. Mirkin, *Mol. Pharm.*, 2009, **6**, 1934-1940.
79. A. E. Prigodich, D. S. Seferos, M. D. Massich, D. A. Giljohann, B. C. Lane and C. A. Mirkin, *Acs Nano*, 2009, **3**, 2147-2152.
80. W. Cai, T. Gao, H. Hong and J. Sun, *Nanotechnol Sci Appl*, 2008, **2008**, 17-32.
81. G. Laurent, N. Fédidj, S. L. Truong, J. Aubard, G. Lévi, J. Krenn, A. Hohenau, A. Leitner and F. Aussenegg, *Nano Lett.*, 2005, **5**, 253-258.
82. X. Qian, X.-H. Peng, D. O. Ansari, Q. Yin-Goen, G. Z. Chen, D. M. Shin, L. Yang, A. N. Young, M. D. Wang and S. Nie, *Nat. Biotechnol.*, 2008, **26**, 83-90.
83. B. D. Chithrani and W. C. Chan, *Nano Lett.*, 2007, **7**, 1542-1550.
84. L. Sun, D. Liu and Z. Wang, *Langmuir*, 2008, **24**, 10293-10297.
85. J. Turkevich, P. C. Stevenson and J. Hillier, *Discuss. Faraday Soc.*, 1951, **11**, 55-75.
86. G. Frens, *Nature*, 1973, **241**, 20-22.
87. V. Bulmus, *Aust. J. Chem.*, 2005, **58**, 411-422.
88. A. D. Frankel and C. O. Pabo, *Cell*, 1988, **55**, 1189-1193.
89. D. Derossi, A. H. Joliot, G. Chassaing and A. Prochiantz, *J. Biol. Chem.*, 1994, **269**, 10444-10450.
90. W. J. Gehring, M. Affolter and T. Burglin, *Annu. Rev. Biochem.*, 1994, **63**, 487-526.
91. M. Lindgren and Ü. Langel, *Cell-Penetrating Peptides: Methods and Protocols*, Springer, 2011.
92. D. Raucher and J. S. Ryu, *Trends Mol Med*, 2015, **21**, 560-570.
93. M. Lindgren, K. Rosenthal-Aizman, K. Saar, E. Eiríksdóttir, Y. Jiang, M. Sassian, P. Östlund, M. Hällbrink and Ü. Langel, *Bioche. Pharmacol.*, 2006, **71**, 416-425.
94. J. F. Liang and V. C. Yang, *Bioorg. Med. Chem. Lett.*, 2005, **15**, 5071-5075.
95. T. A. Aguilera, E. S. Olson, M. M. Timmers, T. Jiang and R. Y. Tsien, *Integr. Biol.*, 2009, **1**, 371-381.
96. M. J. Kang, S. H. Park, M. H. Kang, M. J. Park and Y. W. Choi, *Int. J. Nanomedicine*, 2013, **8**, 1155.

97. N. Parker, M. J. Turk, E. Westrick, J. D. Lewis, P. S. Low and C. P. Leamon, *Anal. Chem.*, 2005, **338**, 284-293.
98. K. N. Sugahara, T. Teesalu, P. P. Karmali, V. R. Kotamraju, L. Agemy, O. M. Girard, D. Hanahan, R. F. Mattrey and E. Ruoslahti, *Cancer Cell*, 2009, **16**, 510-520.
99. Y. Liu, R. Ran, J. Chen, Q. Kuang, J. Tang, L. Mei, Q. Zhang, H. Gao, Z. Zhang and Q. He, *Biomaterials*, 2014, **35**, 4835-4847.
100. D. Schmaljohann, *Adv. Drug Deliv. Rev.*, 2006, **58**, 1655-1670.
101. A. Hoffman and P. Stayton, *J. Biomed. Mater. Res.*, 2000, **52**, 577-586.
102. Y. Qiu and K. Park, *Adv. Drug Deliv. Rev.*, 2001, **53**, 321-339.
103. J. Zhang and N. Peppas, *Macromolecules*, 1999, **33**, 102-107.
104. A. de las Heras and S. Pennadam, *Chem. Soc. Rev.*, 2005, **34**, 276-285.
105. F. Liu and M. Urban, *Prog. Polym. Sci.*, 2010, **35**, 3-23.
106. S. B. Turturro, M. J. Guthrie, A. A. Appel, P. W. Drapala, E. M. Brey, V. H. Pérez-Luna, W. F. Mieler and J. J. Kang-Mieler, *Biomaterials*, 2011, **32**, 3620-3626.
107. J. Zhang, R. Srivastava and R. Misra, *Langmuir*, 2007, **23**, 6342-6351.
108. D. J. Kim, S. M. Kang, B. Kong, W. J. Kim, H. j. Paik, H. Choi and I. S. Choi, *Macromol. Chem. Phys.*, 2005, **206**, 1941-1946.
109. I. Idziak, D. Avoce, D. Lessard, D. Gravel and X. Zhu, *Macromolecules*, 1999, **32**, 1260-1263.
110. E. E. Makhaeva, L. T. M. Thanh, S. G. Starodoubtsev and A. R. Khokhlov, *Macromol. Chem. Phys.*, 1996, **197**, 1973-1982.
111. F. Meeussen, E. Nies, H. Berghmans, S. Verbrugghe, E. Goethals and F. Du Prez, *Polymer*, 2000, **41**, 8597-8602.
112. M. Ataman, *Colloid Polym. Sci.*, 1987, **265**, 19-25.
113. P. Alexandridis, T. Nivaggioli and T. A. Hatton, *Langmuir*, 1995, **11**, 1468-1476.
114. F. Cellesi, N. Tirelli and J. A. Hubbell, *Macromol. Chem. Phys.*, 2002, **203**, 1466-1472.
115. P. Alexandridis and T. Alan Hatton, *Colloids Surf., A*, 1995, **96**, 1-46.
116. M. M. Vorob'ev and N. G. Faleev, *Mendeleev Commun.*, 2005, **15**, 259-261.
117. V. P. Torchilin, F. Zhou and L. Huang, *J. Liposome Res.*, 1993, **3**, 201-255.
118. S. Tonge and B. Tighe, *Adv. Drug Deliv. Rev.*, 2001, **53**, 109-122.
119. E. S. Gil and S. M. Hudson, *Prog. Polym. Sci.*, 2004, **29**, 1173-1222.
120. L. A. Connal, Q. Li, J. F. Quinn, E. Tjipto, F. Caruso and G. G. Qiao, *Macromolecules*, 2008, **41**, 2620-2626.
121. E. He, C. Yue and K. Tam, *Langmuir*, 2009, **25**, 4892-4899.
122. O. E. Philippova, D. Hourdet, R. Audebert and A. R. Khokhlov, *Macromolecules*, 1997, **30**, 8278-8285.
123. N. Murthy, J. R. Robichaud, D. A. Tirrell, P. S. Stayton and A. S. Hoffman, *J. Control. Release*, 1999, **61**, 137-143.
124. A. S. Lee, V. Bütün, M. Vamvakaki, S. P. Armes, J. A. Pople and A. P. Gast, *Macromolecules*, 2002, **35**, 8540-8551.
125. M. Okubo, H. Ahmad and T. Suzuki, *Colloid Polym. Sci.*, 1998, **276**, 470-475.
126. J.-F. Gohy, B. G. Lohmeijer, S. K. Varshney, B. Decamps, E. Leroy, S. Boileau and U. S. Schubert, *Macromolecules*, 2002, **35**, 9748-9755.
127. V. Pinkrah, M. Snowden, J. Mitchell, J. Seidel, B. Chowdhry and G. Fern, *Langmuir*, 2003, **19**, 585-590.
128. E. Gil and S. Hudson, *Prog. Polym. Sci.*, 2004, **29**, 1173-1222.

129. D. Liu, Y. Xie, H. Shao and X. Jiang, *Angew. Chem. Int. Ed.*, 2009, **48**, 4406-4408.
130. C. Brieke, F. Rohrbach, A. Gottschalk, G. Mayer and A. Heckel, *Angew. Chem. Int. Ed.*, 2012, **51**, 8446-8476.
131. H. Bandara and S. Burdette, *Chem. Soc. Rev.*, 2012, **41**, 1809-1825.
132. S. K. M. Nalluri and B. J. Ravoo, *Angew. Chem. Int. Ed.*, 2010, **49**, 5371-5374.

Chapter 2: Synthesis of elastin-like peptide and elastin-based side chain polymers

2.1 Introduction

Elastin is a protein, which helps provide structural integrity to tissues and organs, such as the lungs, the dermis and larger blood vessels.[1] This highly crosslinked insoluble protein is a main component of the extracellular matrix and it is an essential element of elastic fibres, which provide elasticity to tissues within the human body.[2] One of the most interesting properties of elastin (and tropoelastin, the precursor protein of elastin) is its ability to self-assemble and form a coacervate phase when the temperature is increased above their transition temperature (T_t).[3] This thermodynamic inverse phase transition is completely reversible. This particular property has led to the development of a new family of synthetic proteinaceous polymers, the elastin-like polypeptides (ELPs).

2.1.1 Properties of elastin-like polypeptides

Elastin-like polypeptides (ELPs) are artificial biopolymers, derived from hydrophobic domains of tropoelastin. ELPs are composed of repeating pentapeptide sequences Val-Pro-Gly-Xaa-Gly (VPGXG), where the guest residue Xaa can be any amino acid except proline.

Usually, ELPs are described using the notation ELP [$X_iY_jZ_k$-n], as this can distinguish between two different ELP constructs. The bracketed capital letters indicate the single letter amino acid code specifying the guest residues in the pentapeptide sequence VPGXG, the subscripts designate the ratio of the Xaa replacement residue and n represents the total length of the ELP in number of pentapeptides.[4] For example, ELP [$V_1A_3G_4$-160] represents an ELP of 160 unit pentapeptides which has a repeat sequence composed of 8 pentapeptides with the guest residues Val, Ala and Gly in a 1:3:4 ratio. If n is not given, the notation only shows the sequence of a given ELP without a specific

chain length. The most common structure of studied ELPs is poly(VPGVG) or alternatively poly(GVGVP). The structure of poly(VPGVG) is shown in **Figure 2.1**.

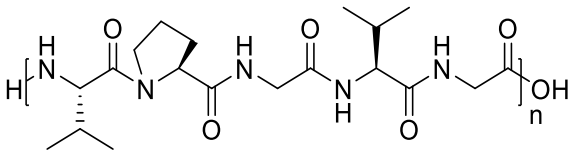

Figure 2.1: Chemical structure of poly(Val-Pro-Gly-Val-Gly).

Urry and co-workers[5-7] were the first to synthesise a large number of ELPs, and they looked at both oligomers and also elastin-like polymers. They studied the biophysical properties of the ELPs in solution and they investigated their potential medical applications as cross-linked elastomeric materials. Urry also found that ELPs have a distinctive property which is known as inverse phase transition behaviour.[5] At low temperatures, ELPs are soluble in solution, but when the solution temperature is increased, they become insoluble and aggregate. Aggregation occurs at a critical temperature, termed the inverse transition temperature (T_t). The coacervation of solution is due to the conformational change of the ELPs, including loss of water from hydrophobic domains and the thermodynamic driving force provided by the increased temperature. Above the T_t, the ELP forms an ordered structure and the entropy of the ELPs is decreased, but the loss of entropy is compensated by the released water from the hydrophobic hydration.[8] This coacervation process is typically reversible; when the temperature is cooled down to below the T_t, the ELPs become soluble again. For example, high molecular weight poly(VPGVG), which has a series of β-turns as shown in **Figure 2.2a**, is soluble in water below 25 ℃. When the temperature is increased above the T_t, the chain undergoes a conformational change to a β-spiral (**Figure 2.2b**) causing a phase transition and macroscopic aggregation.[6]

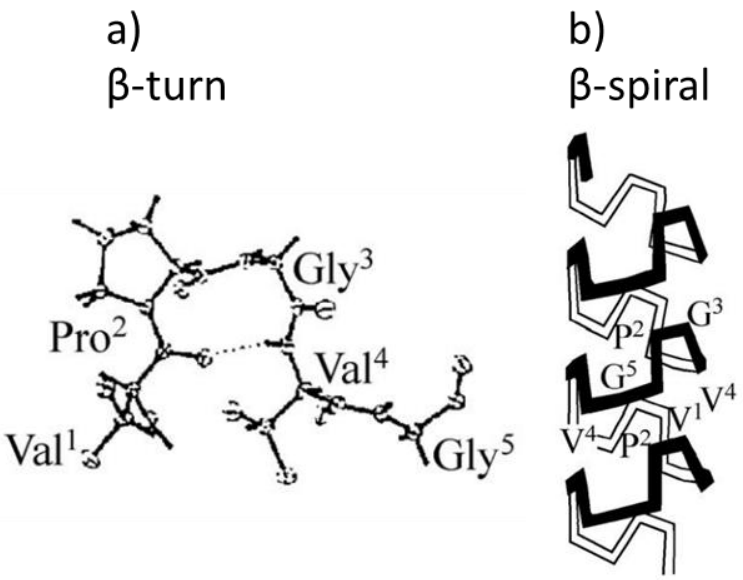

Figure 2.2: (a) Recurring β-turn found in poly(VPGVG); (b) β-spiral structure of poly(VPGVG) when the temperature is above the transition temperature (T_t). Reproduced from [6] with permission from Elsevier, copyright © 1992.

Urry discovered that the T_t has a quantitative relationship with the primary amino acid sequence, the hydrophobicity of the guest residue (Xaa) and the overall peptide chain length.[9] Subsequently, a more accurate and complete description of the ELP transition behaviour was given by Meyer and Chikoti.[10] They demonstrated that the transition temperature can be modulated by the ELP sequence, concentration, peptide chain length and nature of the guest residue. For example, T_t was found to have an approximately linear relationship with the natural log of molecular weight in the range of 1,000 Da to 100,000 Da, where a reduction in molecular weight (MW) causes an increase in T_t. Within the ELP sequence, the main parameter that can modulate the T_t is the hydrophobicity of the fourth 'guest' residue. The hydrophobicity scales for amino acid residues in proteins is presented as: Phe > Leu ≈Ile > Val > Ala > Gly. If the guest residue is Val which is more hydrophobic than Gly, the T_t will be lower. The inverse phase transition can be also influenced by peptide concentration, the addition of NaCl, and pH.[11, 12] Although the effects of many of the parameters that effect T_t have been evaluated, it is still very challenging to rationally design an ELP which has an accurate targeted transition temperature.

2.1.2 Synthesis of elastin-like polypeptides

ELPs can be produced by either biosynthesis or chemical synthesis. Short elastin-like polypeptides can easily be prepared via chemical synthesis, usually using solid phase peptide synthesis (SPPS). However, the SPPS approach can only produce polypeptides with limited chain lengths of up to 50 amino acids. Given this, the biosynthetic approach is more suitable to access longer ELPs when a defined polymer length is required.

2.1.2.1 Elastin biosynthesis

Protein engineering methods have been used for the design and modification of proteins for many years, enabling the preparation of long polypeptides with a defined chain length. **Figure 2.3** outlines the basic approach for producing polypeptides via protein engineering.[13]

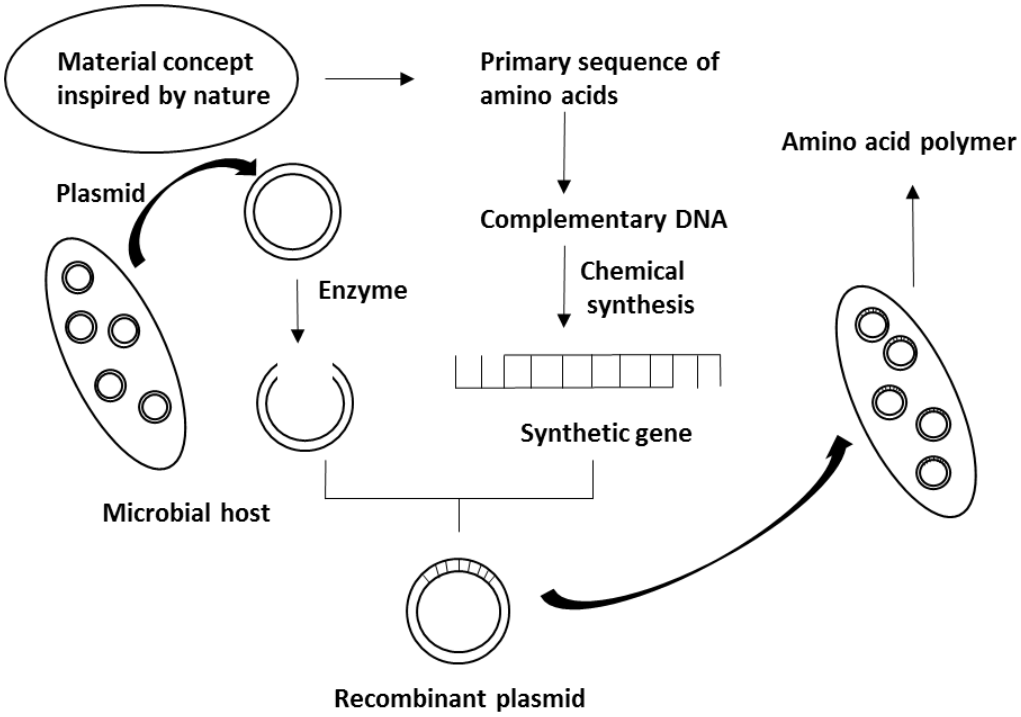

Figure 2.3: Overview of the protein engineering methodology. Adapted from Ref [13].

As elastin is characterized by a repetitive amino acid sequence; it is easier to make a smaller oligonucleotide sequences to prepare an artificial gene which codes for high molecular weight elastin. After constructing the artificial gene library, each gene is incorporated into plasmid DNA, which can be applied to transform a bacterial host. The plasmids are replicated through the bacterial cells. After verifying the sequence of the

selected artificial gene, it is cloned into a second plasmid which allows protein expression. The expression plasmid is re-introduced into the host, and the host cells are cultured to grow to high density. After expression, the target protein needs to be separated from other proteins to obtain the pure product.

Elastin based materials have been made by protein engineering, which is ideally suited for the synthesis of higher molecular weight elastin-like polypeptides. Conticello *et al*.[14] have used this approach to prepare ELP block copolymers which comprise hydrophilic and hydrophobic blocks. Protein engineering can completely control the sequence, composition and chain length of the blocks. Therefore, carefully designed elastin-like biopolymers which may be good candidates for drug delivery or tissue engineering can be produced. There are several other examples where ELPs were expressed in *Escherichia coli* or yeast.[15-17] ELPs can be readily purified from other proteins in cell lysates by exploiting their inverse temperature phase transition without the need to use chromatography.[18]

2.1.2.2 Solid phase peptide synthesis (SPPS)

In 1902, Emil Fisher first introduced peptide chemistry by synthesizing a glycine-glycine dipeptide. Then, another milestone was achieved by Merrifield who won the 1984 Nobel Prize in chemistry for his development of methodology for chemical synthesis on a solid matrix.[19] Since then, most peptides are synthesised by applying the SPPS developed by Merrifield.

As shown in **Figure 2.4**, the basic principle of SPPS is to couple the C-terminus of the first amino acid to an insoluble support and then to build up the polymer chain by coupling the C-terminus of another amino acid continuously. After each coupling, the peptide chain is washed by solvents which can release byproducts. Finally, the designed peptide is cleaved from the polymeric support using a cleavage cocktail. Compared to traditional solution-phase methods, the solid phase approach is simpler and more efficient. Now automated synthesisers based on the Merrifield synthesis are available, which can assemble sequences of more than 50 amino acids in around two days.[20, 21] However, the reactivity between the amino acid and the resin is the main disadvantage of solid phase peptide synthesis. Even though the yield of each coupling step is very high, almost close to 99%, at the end of the whole sequence the yield could become

only 60% if there are 50 amino acids in the chain. The longer the polypeptide chain, the lower the yield.[22]

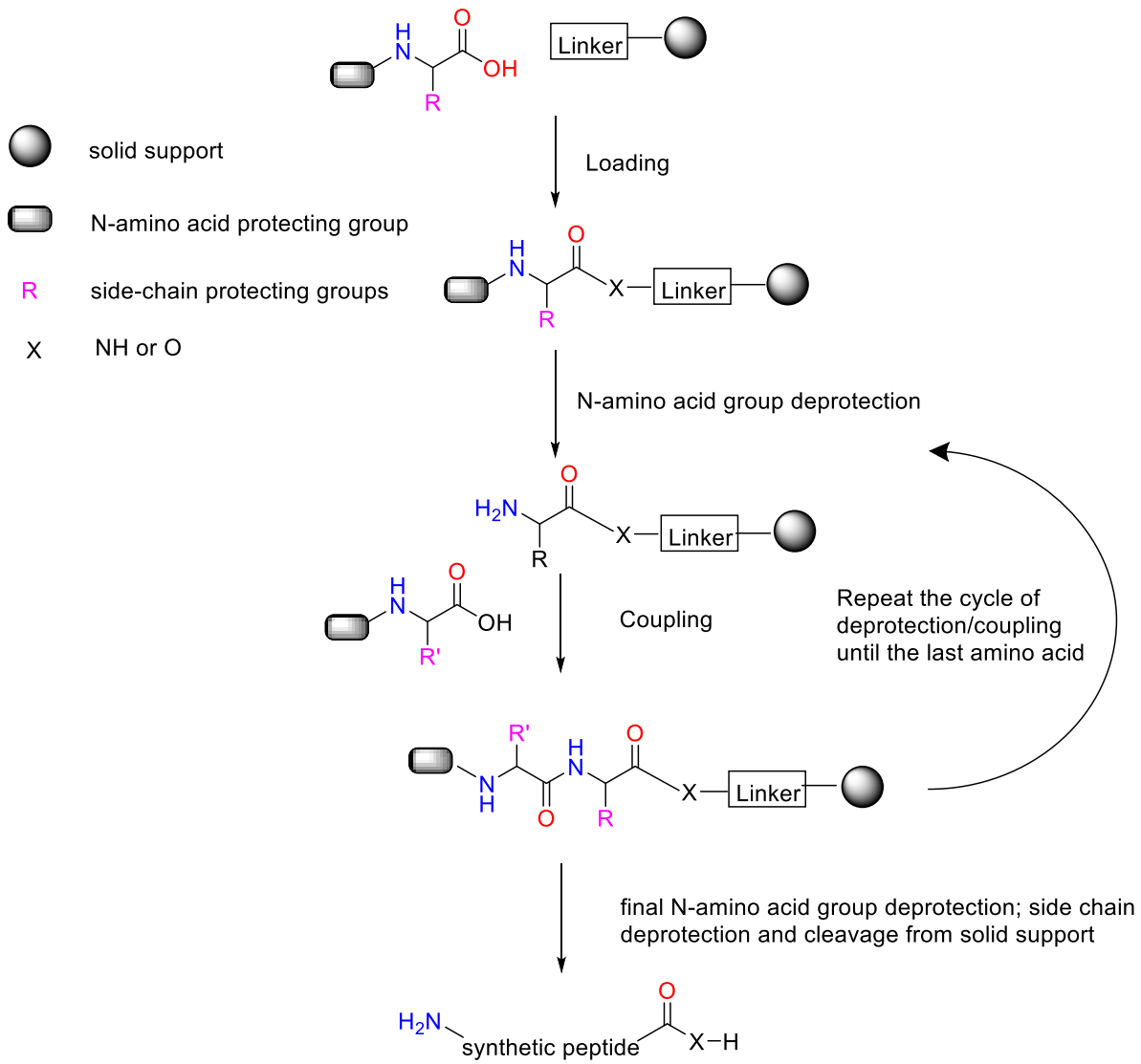

Figure 2.4: The solid-phase peptide synthesis (SPPS) principle.

2.1.3 Applications of elastin-like polypeptides (ELPs)

ELPs have shown considerable potential as drug delivery vehicles in cancer therapy. Soluble polymeric ELP carriers can help to improve drug pharmacokinetics for systemic tumour therapy.[23] ELP carriers have been shown to display enhanced permeability and retention (EPR) effects leading to increased tumour accumulation over the free drug.[24] ELP polymeric carriers can also be used for hyperthermia treatment due to their LCST behaviour. Hyperthermia can synergistically enhance cytotoxicity when applied in solid tumour therapy.[25] Moreover, hyperthermia can further enhance the drug delivery to

tumour infected areas due to the increased permeability of the tumour vasculature.[26] Finally, ELPs with defined chain lengths and sequences can adopt complicated secondary structures through self-assembly and they can be used to encapsulate drugs by forming micelles and vesicles.[27, 28]

One example of a targeting strategy is to design an ELP that has a transition temperature between body temperature and clinical hyperthermia temperature (42^{o}C). Chilkoti and co-workers[29, 30] synthesised two ELPs by protein engineering to make a comparison. One had a guest residues ratio of Val, Gly and Ala of 5:3:2, while the other had a ratio of 1:7:8. ELP[$V_5G_3A_{2\text{-}150}$] has a T_t of 41^{o}C and the control ELP[$V_1G_7A_{8\text{-}160}$] has a T_t of 67^{o}C, which is considerably above the hyperthermia temperature. These two biopolymers were studied by *in vivo* fluorescence microscopy in nude mice with implanted human tumours. The accumulation of these two ELPs in tumours was quantified by analysis of fluorescence intensity across a broad spectral window. The results showed that the accumulation of ELP[$V_5G_3A_{2\text{-}150}$] was about two-fold greater than ELP[$V_1G_7A_{8\text{-}160}$] in the tumour area when heated to 42^{o}C. It is important to note that thermally responsive ELPs can lead to an increase in tumour localization compared to the control ELP without hyperthermia. In addition, the uptake of the thermally responsive ELP was studied to confirm the results which showed a similar 2-fold enhancement in the uptake of the ELP by heated cancer cells compared with unheated cells.[31]

Chilkoti *et al.* also exploited thermally responsive ELPs to deliver the conventional anti-cancer drug, doxorubicin (DOX), to tumours.[32] They synthesised ELP-DOX conjugates, which can self-assemble to form nanoparticles of about 40 nm diameter, in the treatment of solid tumours in mice. The structure of ELP-DOX consists of two parts, a hydrophilic ELP and a short repeated segment attached to doxorubicin via a pH-labile linker as shown in **Figure 2.5**. It was found that the concentration of ELP-DOX conjugates had a 14-fold higher efficacy than the free drug at pH 5.0, and tumour regression showed after a single dose which led to a substantial increase in cell survival.

The properties of ELPs enable them to be used as drug delivery vehicles in different ways (**Figure 2.6**). The first one, known as 'passive targeting' is the simplest. Hydrophobic drugs are attached to a hydrophilic ELP, which has a T_t much higher than body temperature (T_b), to trigger the self-assembly of micelles. These micelles

accumulate in the tumour area by passive targeting due to the EPR effect (**Figure 2.6** (**a**)).[33] The second one is a 'thermal targeting' strategy which builds on the first approach. ELPs are designed to exhibit a T_t between 37°C and 42°C. Then ELP-drug conjugates can be applied to a heated tumour area by using mild hyperthermia to trigger micro-sized aggregates of ELP that adhere to the tumour vasculature. During the return to normothermia, the aggregates dissolve, leading to a large concentration gradient that drives the ELP to dissolve from the aggregates into the tumour (**Figure 2.6** (**b**)).[29] This approach can increase the tumour accumulation compared to an ELP control that does not have phase transition between 37°C and 42°C. Third, ELP block copolymers form micelles in response to hyperthermia, and present multivalent ligands on the micelle corona (**Figure 2.6** (**c**)).[27] In this approach, the block copolymers were also triggered by hyperthermia in the tumour area, resulting in a multivalent display of ligands on a self-assembled drug delivery vehicle. The last strategy is to use ELPs as vehicles for local delivery of drugs by injection (**Figure 2.6** (**d**)). In this method, ELPs that are soluble and injectable at room temperature, but which aggregate at body temperature, are required. An ELP with T_t below body temperature can be injected directly into a tumour area to form an in situ ELP depot, which extends the length of exposure of the tumour to conjugated radiotherapeutics. This approach is supposed to delay the tumour growth significantly.[34]

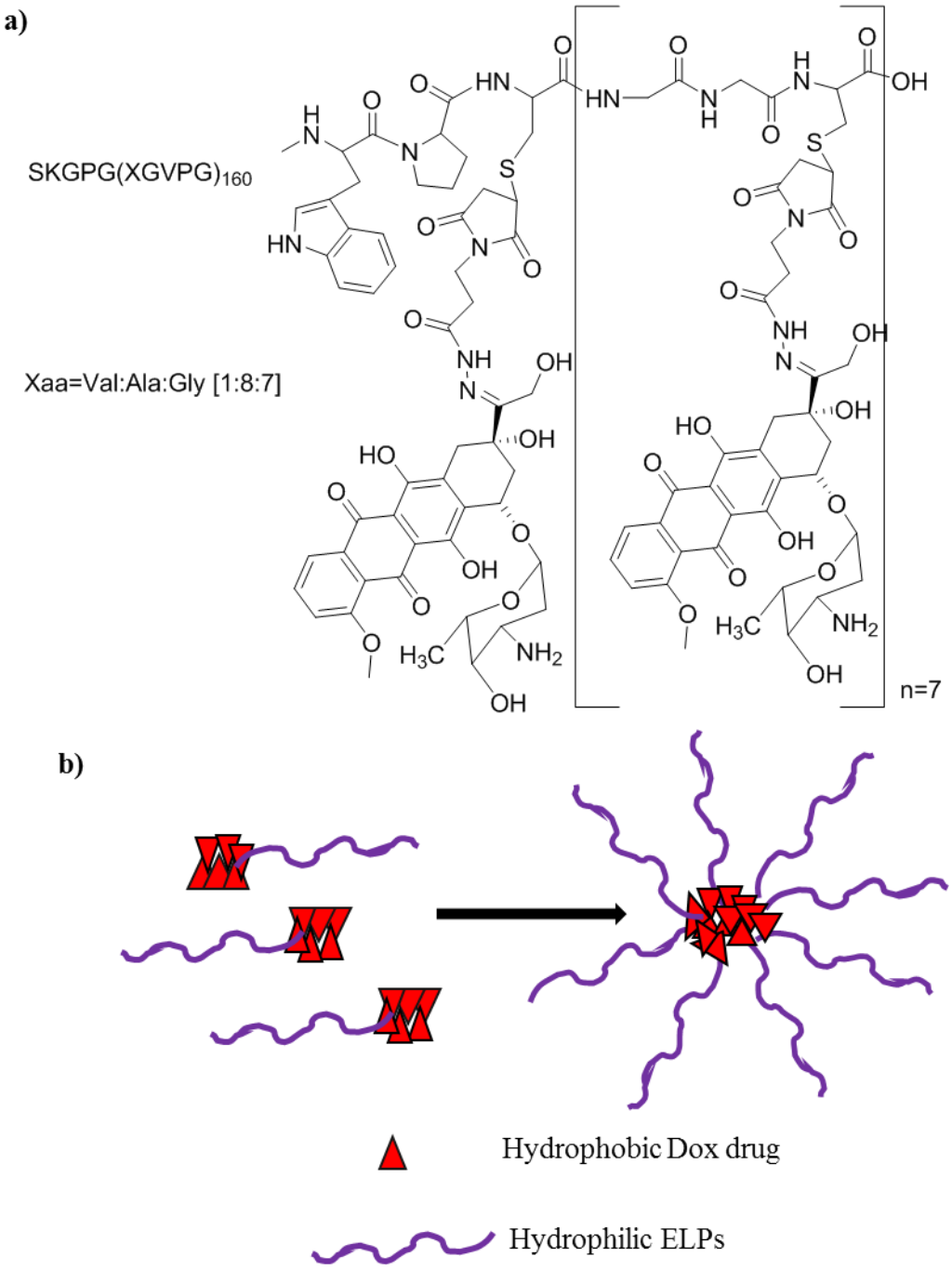

Figure 2.5: ELP–DOX structure: (a) high molecular weight ELPs were conjugated to DOX at cysteine residues via a heterobifunctional linker; (b) the hydrophobic drug block triggers self-assembly of chimeric polypeptide nanoparticles with a drug core surrounded by a hydrophilic polypeptide corona. Reproduced from [32] with permission from Nature, copyright © 2009.

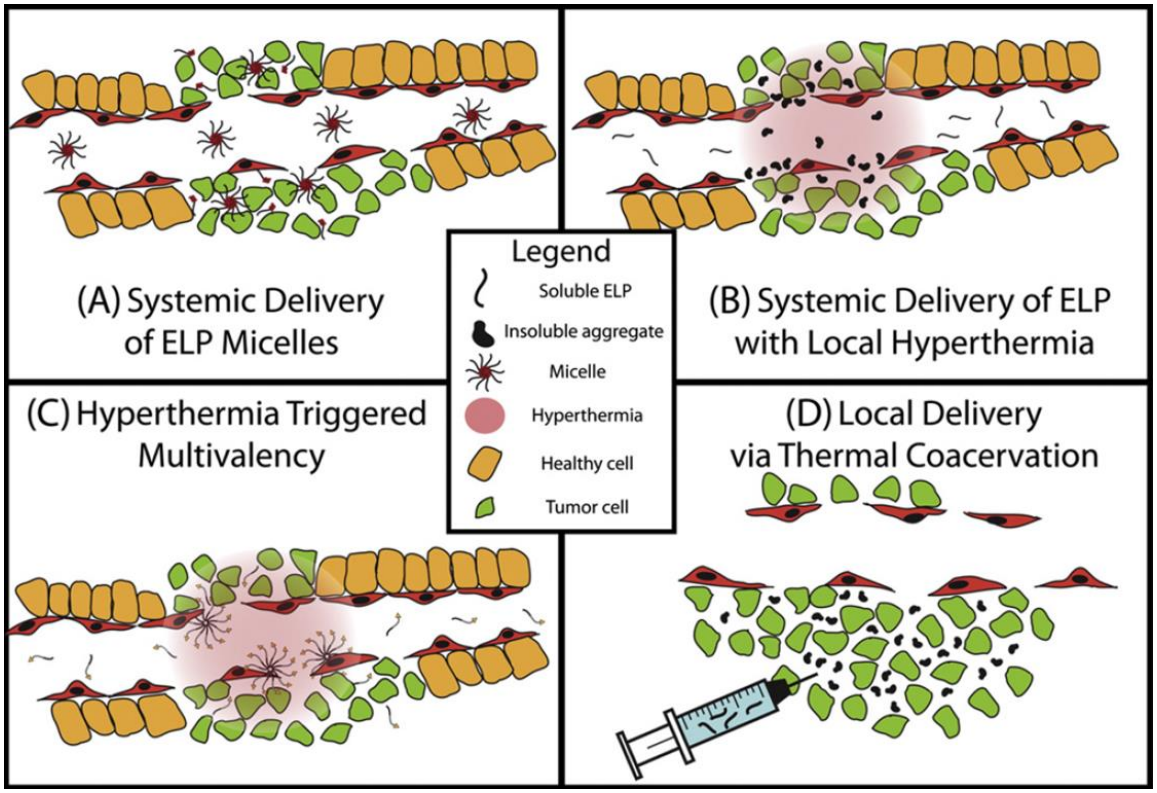

Figure 2.6: ELP–drug delivery strategies: (a) passive targeting (Tt>>Tb); (b) thermal targeting (Tt between 37-42^{o}C); (c) ELP block copolymers form nanoparticle micelles; (d) ELP vehicles (Tt is physiological temperature). Reproduced from [34] with permission from Elsevier, copyright © 2010.

2.1.4 Chapter aims

In this chapter, we aimed to synthesise stimuli-responsive elastin-like peptides and elastin-based side chain polymers. Firstly, the synthesis of short repeated sequences of elastin-like peptides and a study of their properties were carried out. Secondly, the design and synthesis of novel thermo-responsive elastin-based side chain polymers (ESP) were undertaken.

The short elastin-like peptides (ELPs) with different end groups were prepared via the SPPS approach, then the transition temperature of the short ELPs in aqueous buffer solution were examined using ultraviolet-visible (UV-Vis) spectroscopy. In addition, the secondary structure of the ELPs was studied by circular dichroism (CD). The elastin-based side chain polymers (ESP) were prepared by the reversible addition fragmentation chain transfer (RAFT) technique. ESPs with different chain lengths were synthesised and characterized. The influence of the length of chain length, side chain length and buffer concentration on the LCST behaviour was discussed.

2.2 Synthesis of short elastin-like peptides

In order to examine the thermodynamic behaviour of a single unit of VPGVG sequence, peptide **9** was chosen to be synthesised first; Rink Amide resin was used to provide an amide at the C-terminus. Peptide **10** was synthesised to prove how *N*-acetylation affects the conformation transition property at various pH values. Peptide **11** was designed for conjugation to GNPs. These short elastin-like peptides were synthesised via Fmoc-SPPS, and their sequences are shown in **Table 2.1**.

Table 2.1: Sequences and chemical structures of synthesised short elastin-like short peptides.

Sequence	Structure
H-VPGVG-NH_2 (**9**)	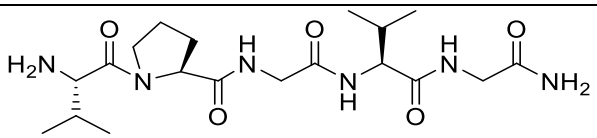
Ac-VPGVG-NH_2 (**10**)	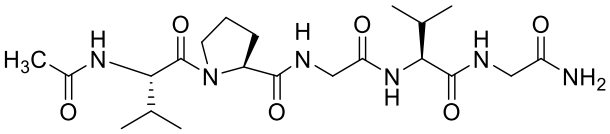
HS-VPGVG-NH_2 (**11**)	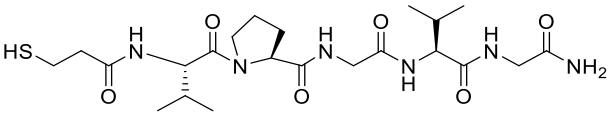

2.2.1 Synthesis of peptide H-VPGVG-NH_2 (9)

The synthesis of **9** is shown in **Figure 2.7**. In solid phase peptide synthesis, the sequence of amino acids added on the resin starts from right to left.

For peptide **9**, Fmoc-Gly-OH was first added with PyBOP and NMM to the Rink Amide resin (loading 0.74 mmol g^{-1}). In order to achieve a high coupling efficiency, each amino acid reaction was repeated to ensure complete functionalization. For cleavage of the peptide from the Rink Amide resin, a TFA solution in the presence of water and triisopropylsilane (TIPS) in a 1:1 ratio was employed. The cleavage cocktail was reduced by rotary evaporation and the condensed solution was added into cold diethyl

ether to obtain the crude peptide. Then the crude peptide was dissolved in deionised water and lyophilised.

For purification process, 10 mg of crude peptide was dissolved in H_2O (containing 0.1% TFA) and purified by semi-preparative reverse phase HPLC. The peptide **9** was the main peak at RT= 16.5-20.2 min, which has an asterisk on it in the chromatogram illustrated in **Figure 2.8**. A small sample of purified **9** was dissolved in water and analyzed by LC-MS. The obtained spectrum is shown in **Figure 2.9**. The peak at 1.5 min is the main product. The mass is 427.2 which represents $[M+H]^+$. The small peaks that appear at 0.5 min and 2.8 min are solvent peaks which also appear in a blank sample. Analytical HPLC analysis of **9** was carried out and the trace is shown in **Figure 2.10**.

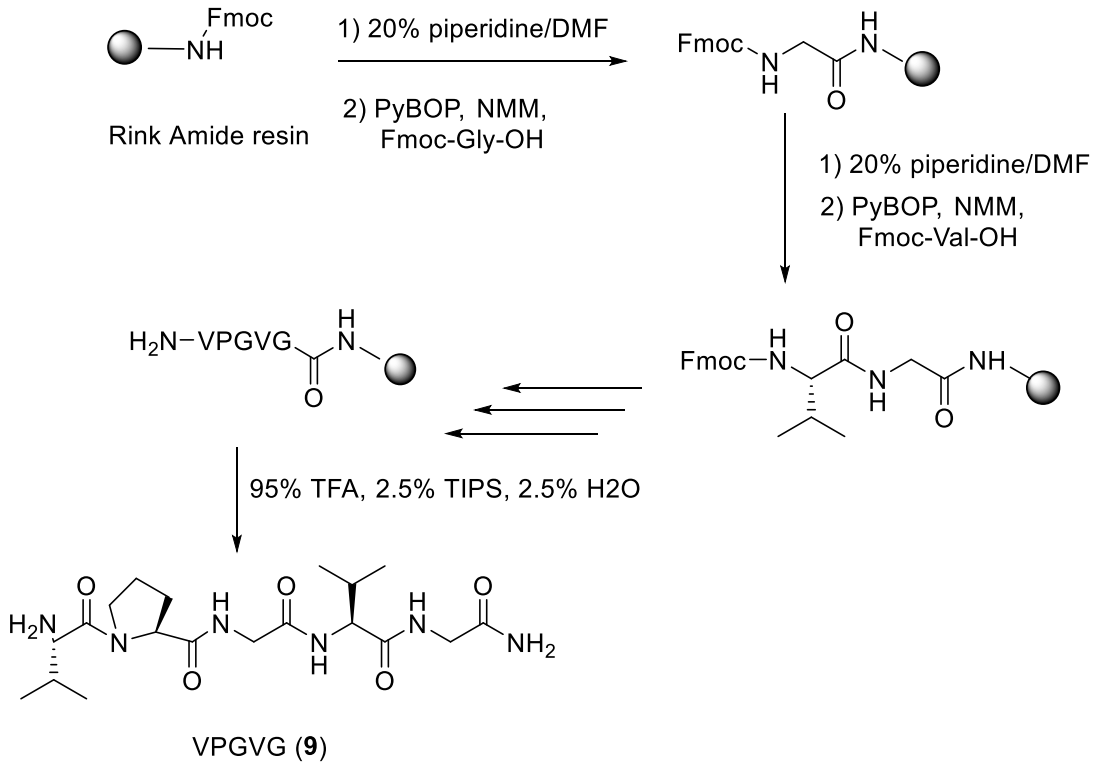

Figure 2.7: Solid phase peptide synthesis of peptide **9**.

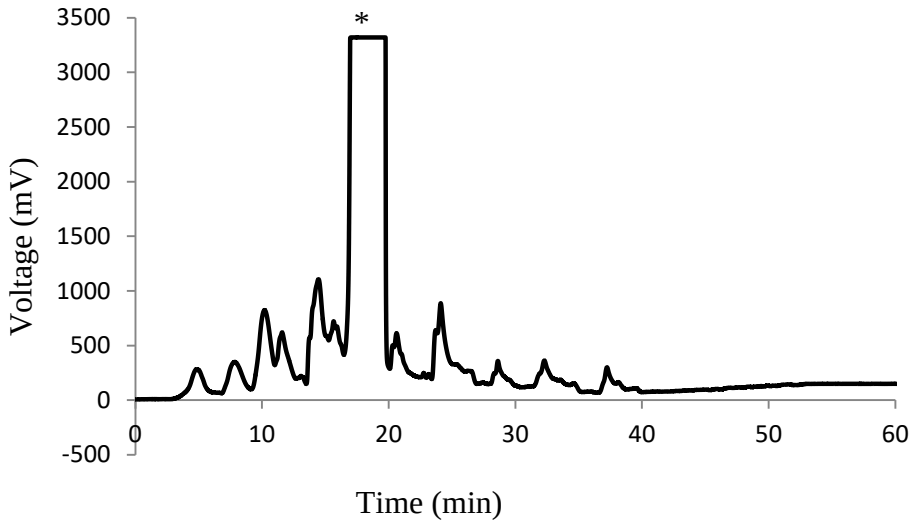

Figure 2.8: Semi-preparative HPLC chromatogram for peptide **9**. 45 min from 0-100% B, retention time range from 16.5-20.2 min.

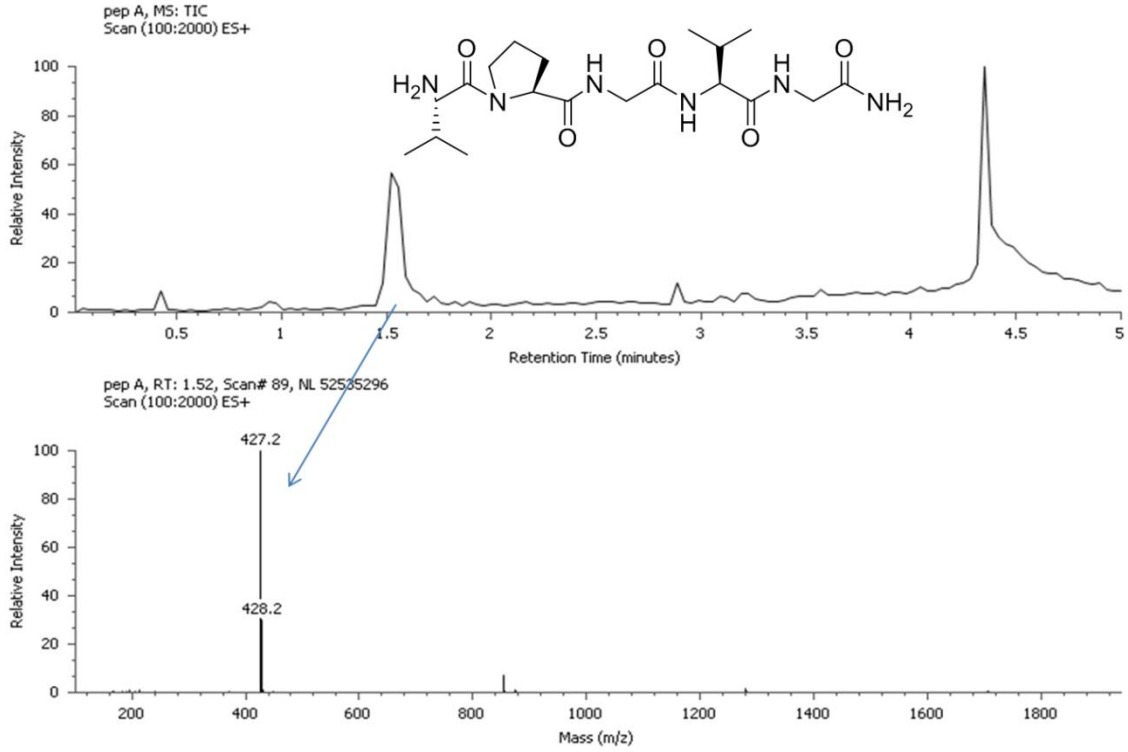

Figure 2.9: LC-MS spectrum of purified peptide **9** (VPGVG-NH_2).

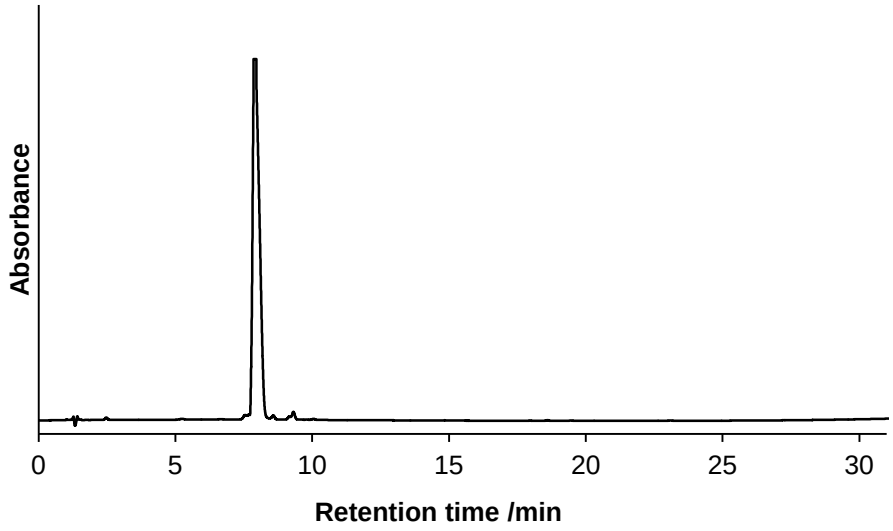

Figure 2.10: Analytical HPLC trace of purified peptide **9** (VPGVG). This pentapeptide was synthesised on a solid resin. HPLC was carried out on an analytical column (C18, 4.6 x 100 mm, 3.5 μm particle size). Peptides were eluted in H_2O/MeCN + 0.05 % trifluoroacetic acid. Retention time = 7.8 min.

2.2.2 Synthesis of acetylated peptide Ac-VPGVG-NH2 (10)

The same synthetic strategy was used to prepare peptide **10**. In order to cap the N-terminus, acetic anhydride in DMF (20% v/v acetic anhydride in DMF) was used as the capping reagent. When the capping reaction was completed, the peptide was cleaved from the resin.

A sample of the crude peptide **10** was purified by semi-perparative reverse phase HPLC. The peptide **10** was the main peak at RT=19.8-23.2 min, which has an asterisk on it. The HPLC chromatogram is shown in **Figure 2.11**. A small sample of purified peptide **10** was dissolved in water and analyzed by LC-MS. The obtained spectrum is shown in **Figure 2.12**. The peak at 2.0 min is the main product. The mass is 469.2 which represents $[M+H]^+$. The small peak that appears at 2.7 min is a solvent peak which also appears in the blank sample. Analysis by analytical HPLC was carried out to confirm peptide purity (**Figure 2.13**).

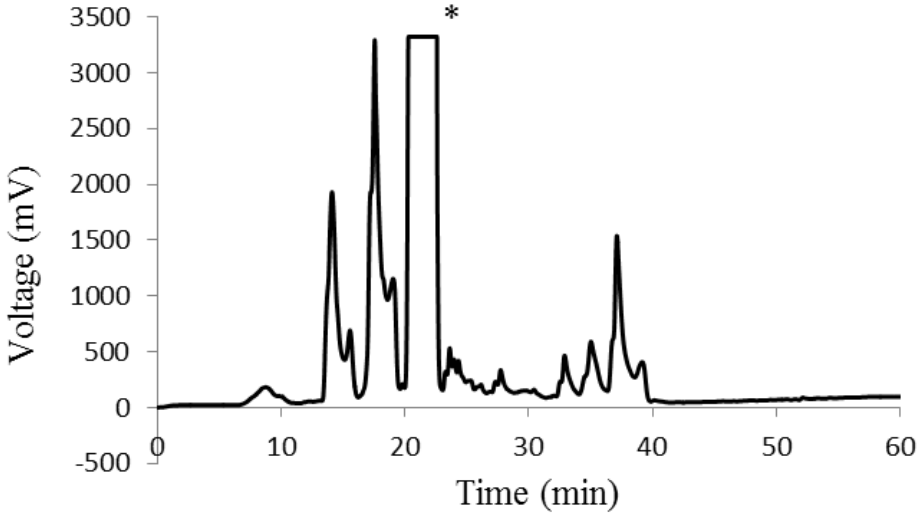

Figure 2.11: Semi-preparative HPLC chromatogram for peptide **10**. 45 min from 0-100% B, retention time range from 19.8-23.2 min.

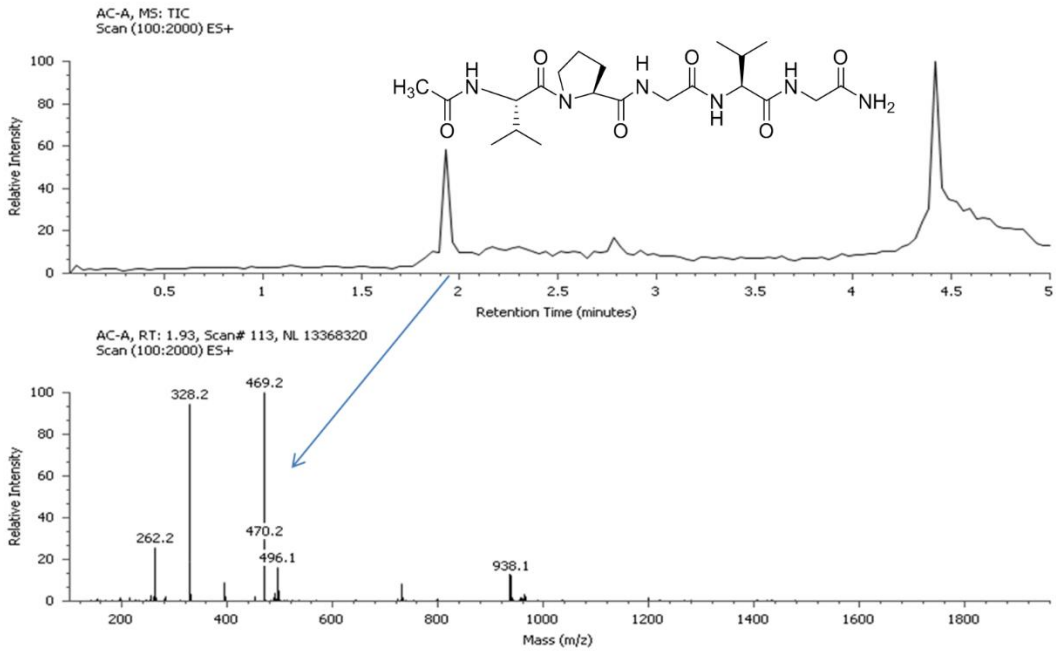

Figure 2.12: LC-MS spectrum of acetylated peptide **10**.

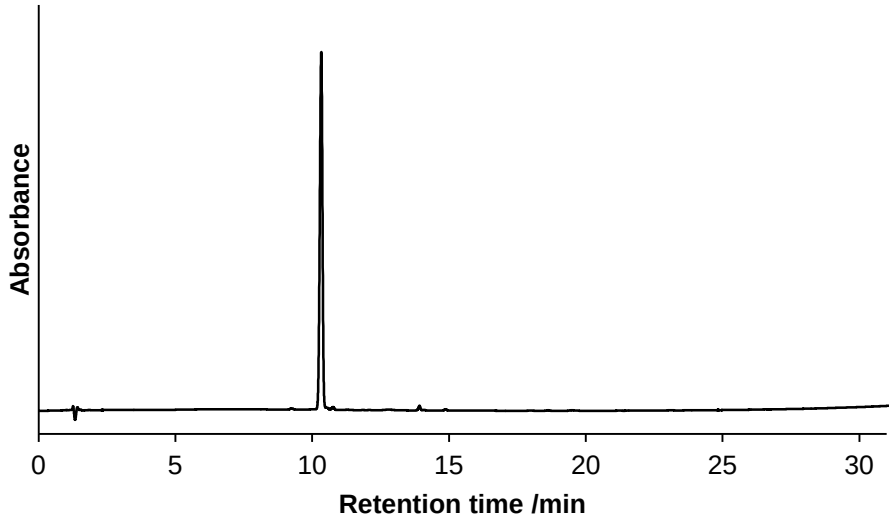

Figure 2.13: Analytical HPLC trace of peptide **10**. HPLC was carried out on an analytical column (C18, 4.6 x 100 mm, 3.5 μm particle size). Peptides were eluted in H_2O / MeCN + 0.05 % trifluoroacetic acid. Retention time = 10.3 min.

2.2.3 Synthesis of thiol-functionalised peptide HS-VPGVG-NH_2 (11)

In order to thiol-functionalize the *N*-terminus, 3-tritylsulfanyl-propionic acid was used. This reagent rather than 3-mercaptopropionic acid was chosen to avoid the disulfide reaction between free thiol groups. In 3-tritylsulfanyl-propionic acid, the trityl group can protect the thiol and also can be easily cleaved by TFA. After synthesizing the sequence VPGVG, the exposed amino acid valine was coupled by adding a mixture of 3-tritylsulfanyl-propionic acid with PyBOP and NMM in DMF. At first, two equivalents were used but the yield was poor. Thus, the amounts of the reagents and 3-tritylsulfanyl-propionic acid were increased to five equivalents which helped to obtain a higher yield. The cleavage cocktail was the same as used for peptide **9**.

The product was purified by semi-preparative HPLC. A sample of the peptide was dissolved in water and analysed using a gradient of 0-100% solvent B in 55 min. The peptide was the main peak at RT=29.90 min, which has an asterisk on it in the chromatogram given in **Figure 2.14**.

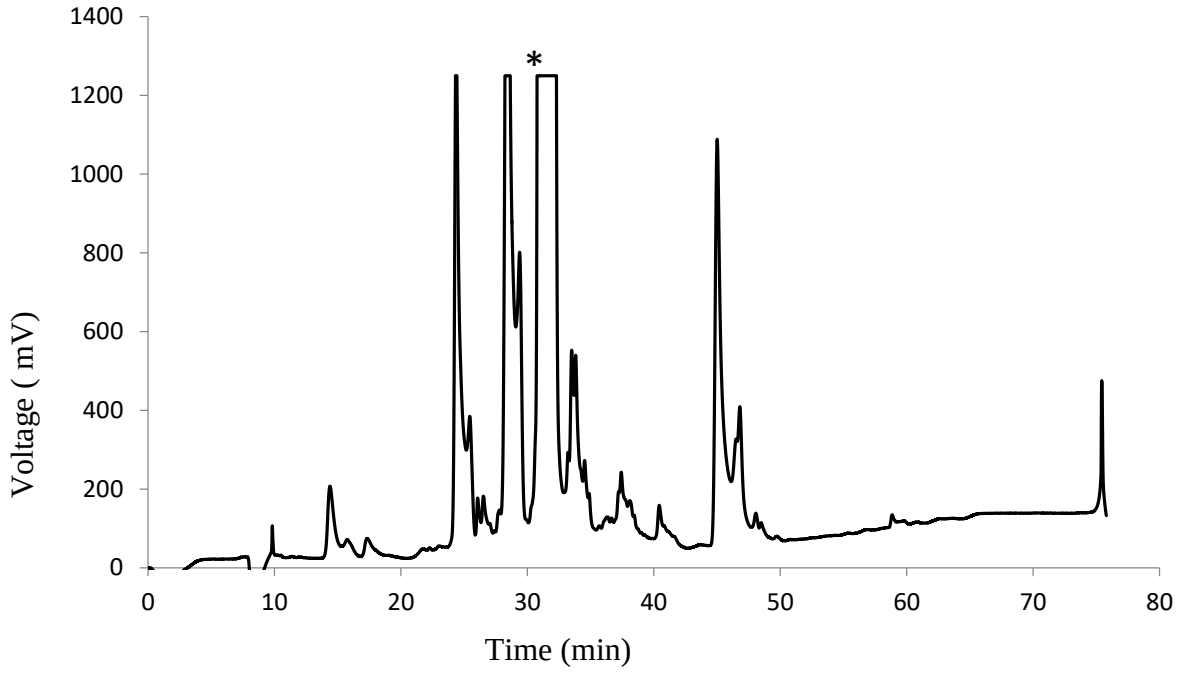

Figure 2.14: Semi-preparative HPLC chromatogram of crude product of peptide **11**. The peak with an asterisk represents the target peptide peak.

After purification, a small sample of the peptide was dissolved in water and analyzed by LC-MS. The obtained trace is shown in **Figure 2.15**. The peak at 2.0 min is the main product. The mass is 515.1 which represents $[M+H]^+$. The other peaks that appear at 2.7 min and 4.5 min are solvent peaks which also appear in the blank sample. Analysis by analytical HPLC was carried out to confirm the purity of peptide **11** (**Figure 2.16**).

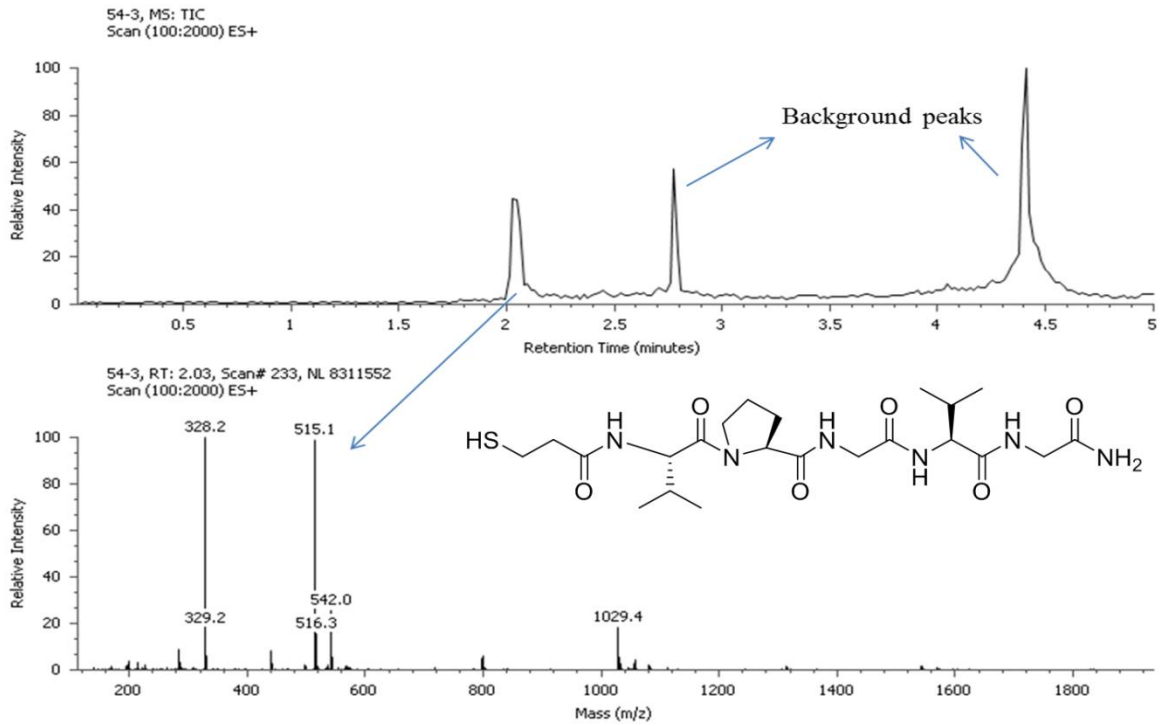

Figure 2.15: LC-MS spectrum of purified thiol-peptide **11**.

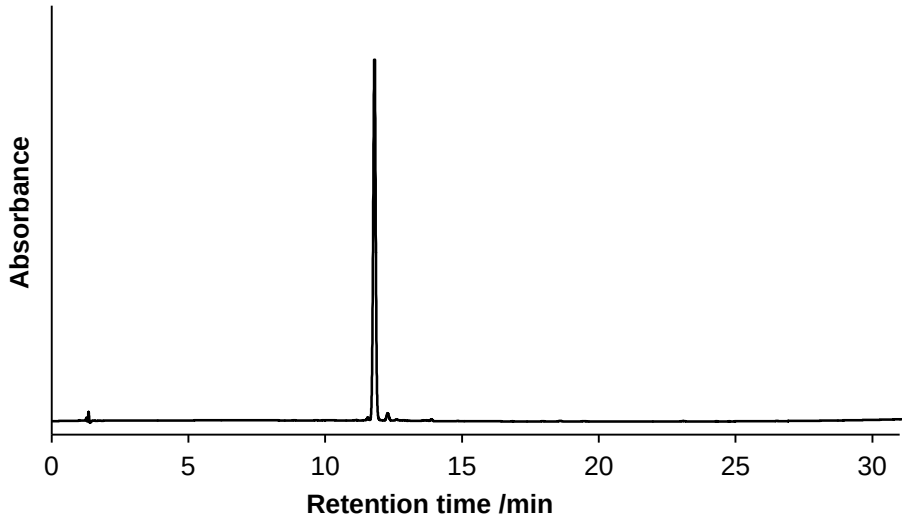

Figure 2.16: Analytical HPLC trace of peptide **11**. HPLC was carried out on an analytical column (C18, 4.6 x 100 mm, 3.5 μm particle size). Peptides were eluted in H_2O / MeCN + 0.05 % trifluoroacetic acid. Retention time = 11.7 min.

2.3 Lower critical solution temperature (LCST) and circular dichroism (CD) studies of short elastin-like peptides

2.3.1 LCST behaviour of short elastin-like peptides

Normally, the LCST value of a polymer depends greatly on its hydrophobicity or hydrophilicity. In other words, the hydrophilic and hydrophobic interactions between the polymer chains play a vital role in influencing the LCST value. These interactions are related to the hydrophobic interaction among polymers and hydrophilic interaction (hydrogen bonding) between hydrophilic groups of the polymer and water. The conformation and solubility of ELP changes in response to a pH change. The conformation of peptides mainly depends on intra- and intermolecular interactions, such as hydrogen bonds or electrostatic interactions.[35] As the environmental pH changes, the hydrophobic or hydrophilic nature of peptides also changes and thus affects the LCST value. The more hydrophilic the peptide, the higher will be the LCST value.

2.3.1.1 LCST behaviour at different concentrations

Figure 2.17 a) shows typical turbidimetry plots obtained for peptide **9** solutions with different concentrations in phosphate buffered saline (PBS) at pH=9. There is an increase in light absorption as the solution is heated. The values of LCST of the peptide **9** were evaluated in the concentration range of 0.5-2 mg mL^{-1}, which was the lower limit of sensitivity of the equipment used. At the lowest concentration (0.5 mg mL^{-1}), the LCST of the solution arrived at 42^{o}C; while at the highest concentration (2 mg mL^{-1}), the LCST decreased to 39^{o}C. This shows that the concentration can affect the LCST to some extent: decreasing the concentration gave an increase in the observed LCST. However, the transition temperature of the peptide **9** solution (1 mg mL^{-1}) is 44^{o}C, which is higher than the transition temperature with a lower concentration (0.5 mg mL^{-1}).

LCST behaviour of acetylated peptide **10** solutions with different concentrations at pH=7 was also detected. The curves in **Figure 2.17** b) show that the LCST of acetylated peptide **10** in the concentration range of 0.5-2 mg mL^{-1} are all 45^{o}C, which means the concentration does not affect the transition temperature. These data illustrate that concentration has a very little influence on LCST in the range of 0.5-2 mg mL^{-1}.

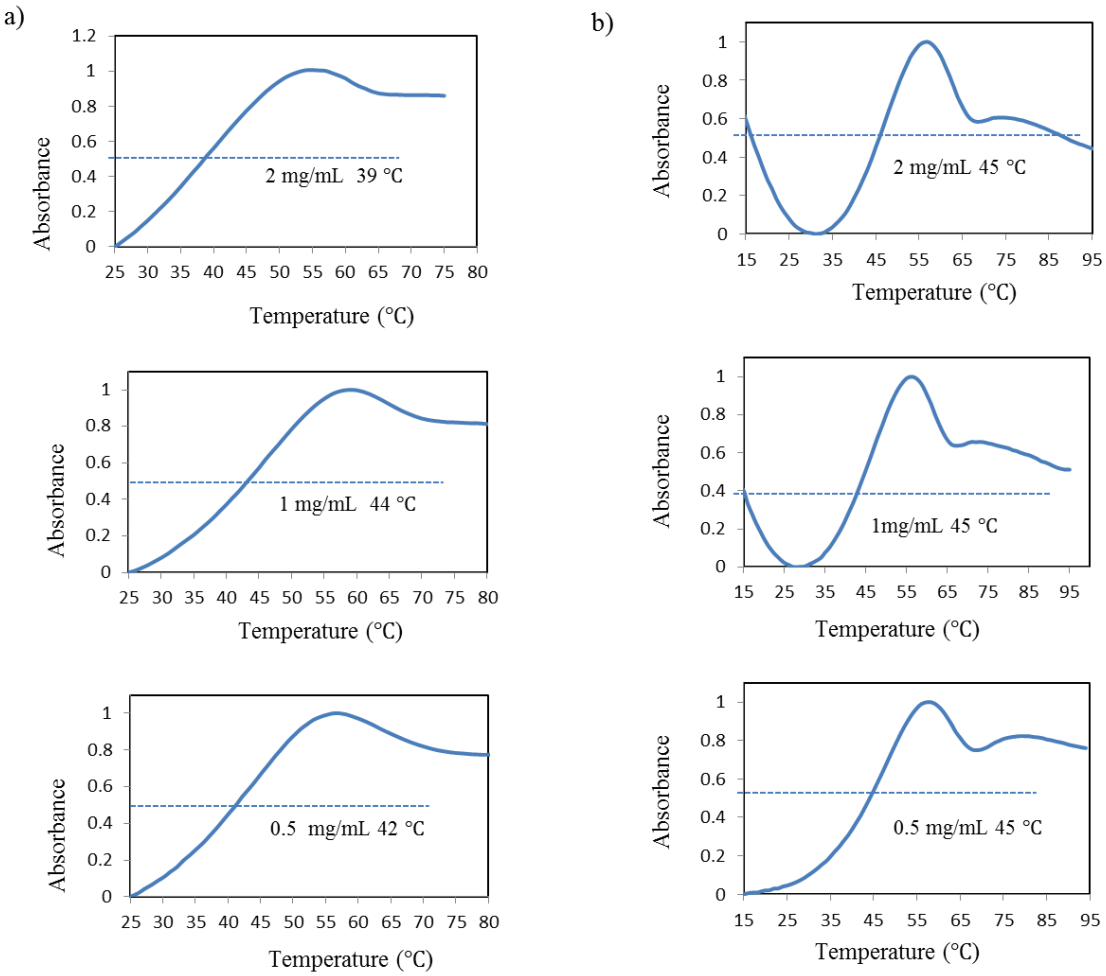

Figure 2.17: (a) The LCST behaviours of peptide **9** solutions with different concentrations at pH=9 as observed by UV-Vis absorbance at 300 nm; (b) the LCST behaviour of peptide **10** solutions with different concentrations at pH=7 as observed by UV-Vis absorbance at 300 nm.

2.3.1.2 LCST behaviour at different pH

Peptide **9** in neutral solutions showed no LCST behaviour, which is the same at a lower pH. This was anticipated since peptide **9** bears a free amine (pK_{aH} ~ 9.2) at the N-terminus, which was expected to be protonated when pH is 7 or lower than 7. At high pH, such as at pH=9, the end-group free amine is not protonated, giving the peptide **9** more hydrophobic character as shown in **Figure 2.18** a).

We also studied the LCST behaviour of peptide **10** at various pH conditions as shown in **Figure 2.18** b). The concentration of all the solutions was 1 mg mL^{-1}. Compared to peptide **9**, peptide **10** has a hydrophobic end group which allowed LCST behaviour to be observed under neutral solutions. At pH=7 it exhibits a transition temperature of

45°C, where at pH=9 the transition temperature decreases to 39°C. This is because the pK_{aH} of the amine group is around 9, therefore peptide **10** becomes a less charged molecule, which has more hydrophobic character, at pH=9. At pH=3, there is no LCST. This may be due to the hydrolysis of the C-terminalus amide. This experiment was repeated three times and still no LCST was observed.

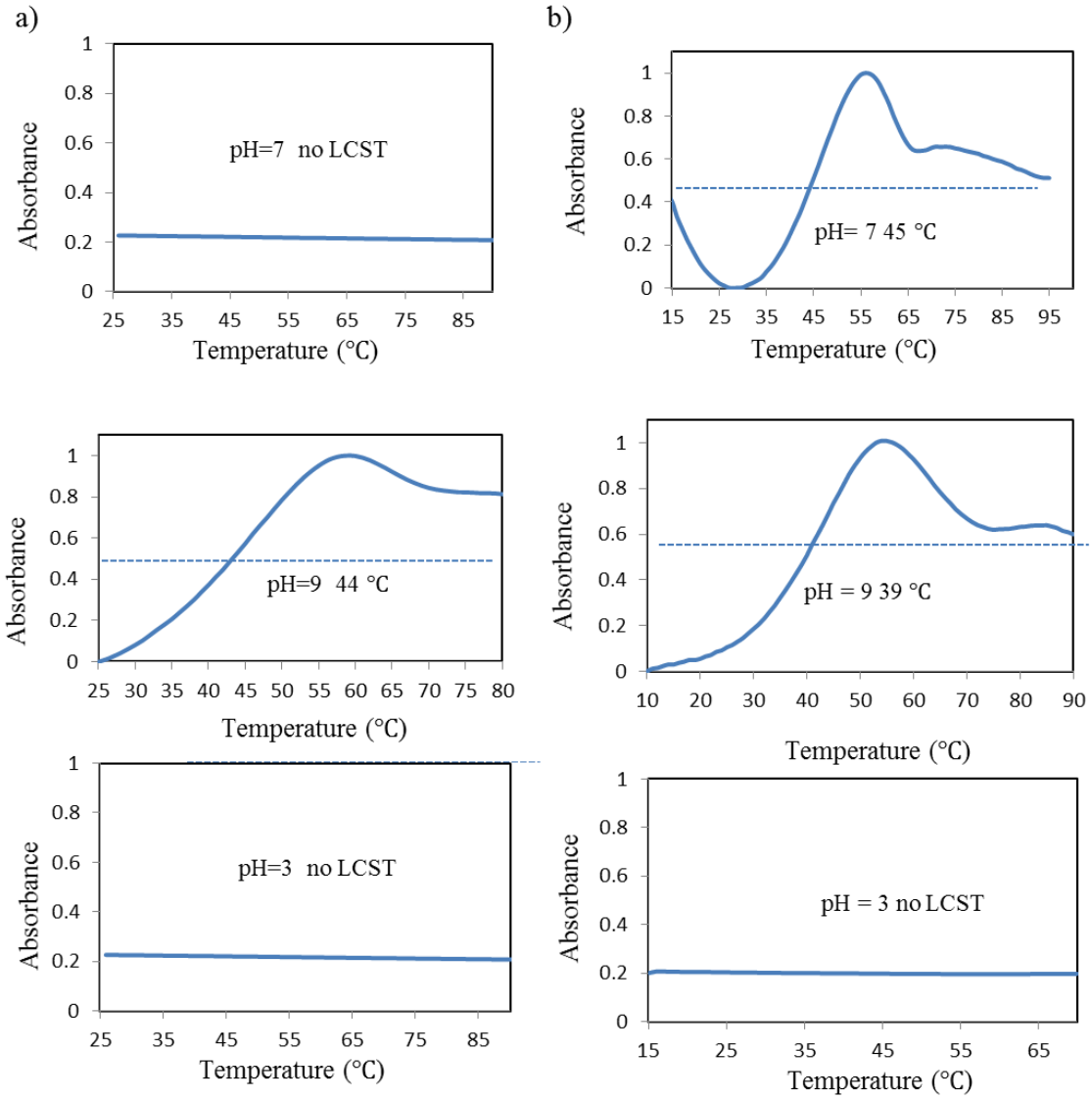

Figure 2.18: (a) The LCST behaviours of peptide **9** solutions (1 mg mL^{-1}) at various pH values as observed by UV-Vis absorbance at 300 nm; (b) the LCST behaviours of peptide **10** solutions (1 mg mL^{-1}) at various pH values as observed by UV-Vis absorbance at 300 nm.

2.3.1.3 Summary of LCST behaviours of Rink Amide peptides

Neutral solutions of peptide **9** (VPGVG) showed no LCST behaviour, also at a lower pH. At a higher pH, such as at pH=9, the free amino end group was not protonated,

giving peptide **9** a more hydrophobic character. At pH=9, a clear phase transition at 44°C was observed as shown in **Figure 2.19**.

The LCST behaviours of peptide **10** solutions at various pH values are shown in **Figure 2.19** as well. Compared to peptide **9**, the *N*-acetylated peptide **10** has a hydrophobic end group, therefore it showed LCST behaviour in neutral solution. The LCST of peptide **10** at pH=7 is 45°C, while at pH=9, the transition temperature decreases to 39°C. This is because the pK_{aH} of the amine group is around 9, peptide **10** becomes more hydrophobic at pH=9. At pH=6, the transition temperature increased to 50°C. When pH decreased to pH=3, it shows that there is no LCST. This may because of hydrolysis of the amide.

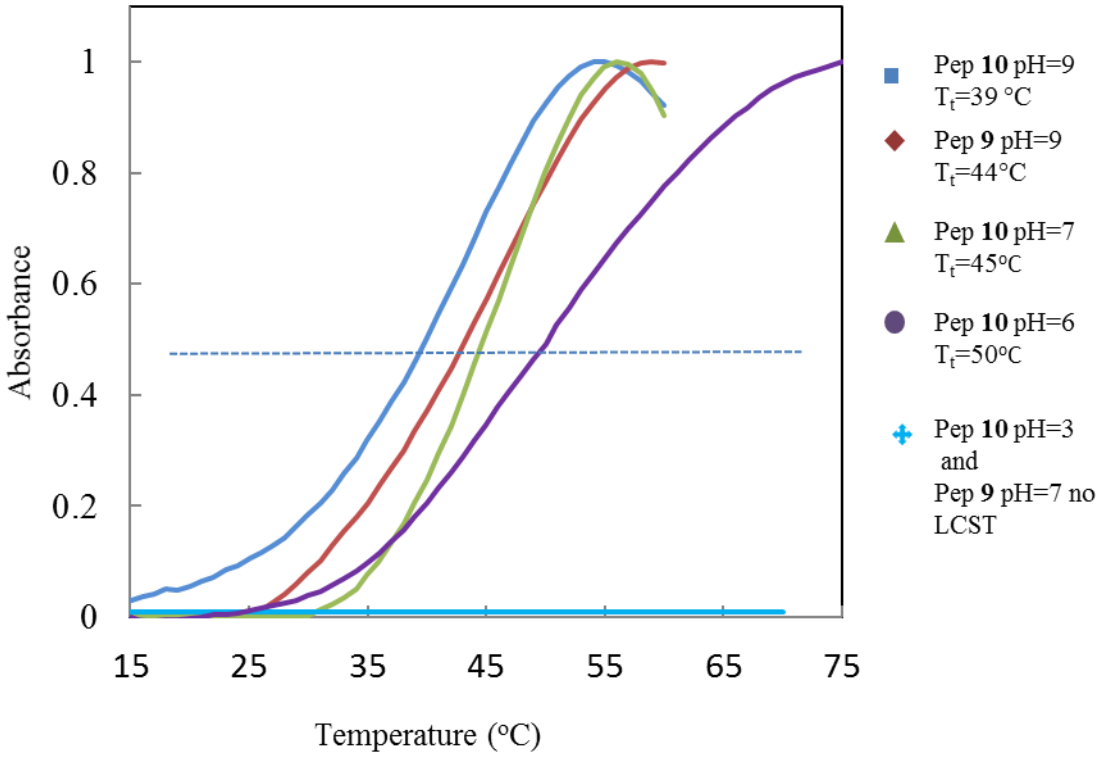

Figure 2.19: The LCST behaviours of peptide **9** and peptide **10** solutions (1 mg mL^{-1}) at different pH values, absorbance at 300 nm.

From the above turbidimetry data in **Figure 2.19**, only peptide **10** shows a transition temperature which is close to ideal (38-42°C) at pH 7. Peptide **10** has a similar structure to thiol-functionalized peptide **11** as shown in **Figure 2.20**. This means that peptide **11** should have a similar LCST behavior as peptide **10**. As peptide **11** will be conjugated to

GNPs to endow the LCST property to the ELP-GNP conjugates, it is important for peptide **11** to have a transition temperature close to 42°C.

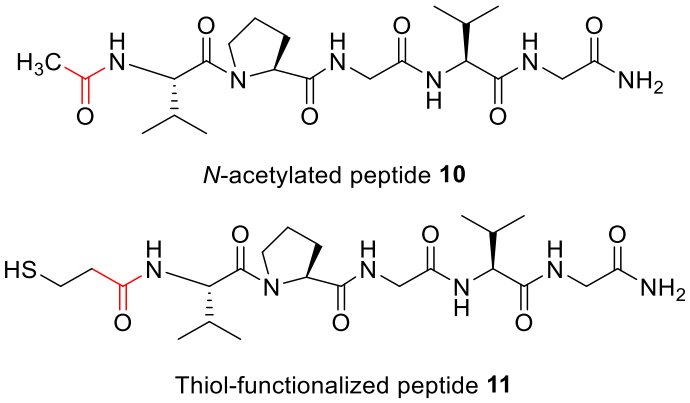

Figure 2.20: Structure of peptide **10** and thiol-functionalized peptide **11**.

2.3.2 CD of short elastin-like peptides

The temperature dependence of the secondary structure of peptide **10** in dilute solution (0.2 mg mL^{-1}) was evaluated using CD spectroscopy. The CD spectra obtained in PBS buffer (pH 7.4) at different temperatures are shown in **Figure 2.21**.

At low temperature (4°C), the CD spectrum obtained had a large negative peak at approximately 197 nm, which is characteristic of a random coil.[36] With increasing temperature, the mean residue ellipticity (MRE) at 197 nm decreased in magnitude which supports increasing β-turn content.[37] In addition with increasing temperature, a small increase in magnitude in the [θ] value at 222 nm was observed. This peak is associated with type I/III β-turn.[38] These are indications of transforming from random coil to a more stable conformation. The most convincing change is the decreased intensity of the negative peak at 197 nm, which is the same trend for long chain elastin-like peptides when temperature is increased.[7] The conformational transition from random coil towards β-turn occurred gradually over a wide temperature range from 4°C to 60°C. The [θ] value change at 200 and 222 nm are plotted respectively in **Figure 2.22 and 2.23**, which both show the same trends when temperature increases.

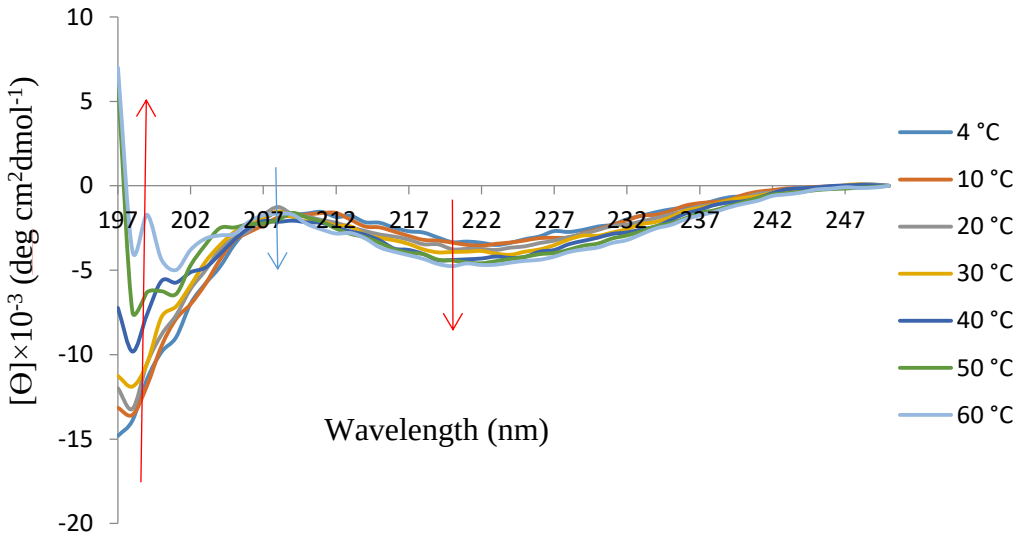

Figure 2.21: Temperature dependence circular dichroism (CD) spectra of peptide **10** (0.2 mg mL^{-1}) in PBS buffer at pH 7.4 between 4°C and 60°C.

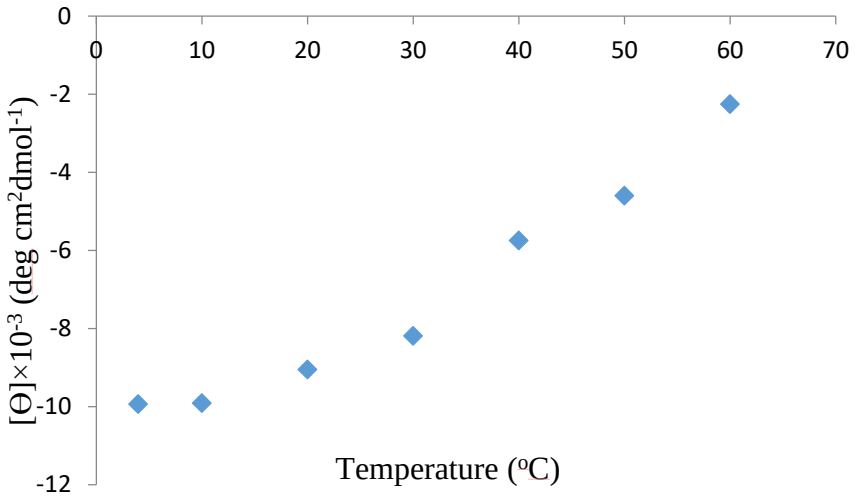

Figure 2.22: Temperature profile of $[\theta]_{200}$ values for peptide **10** (0.2 mg mL^{-1}) in PBS buffer at pH 7.4 between 4°C and 60°C.

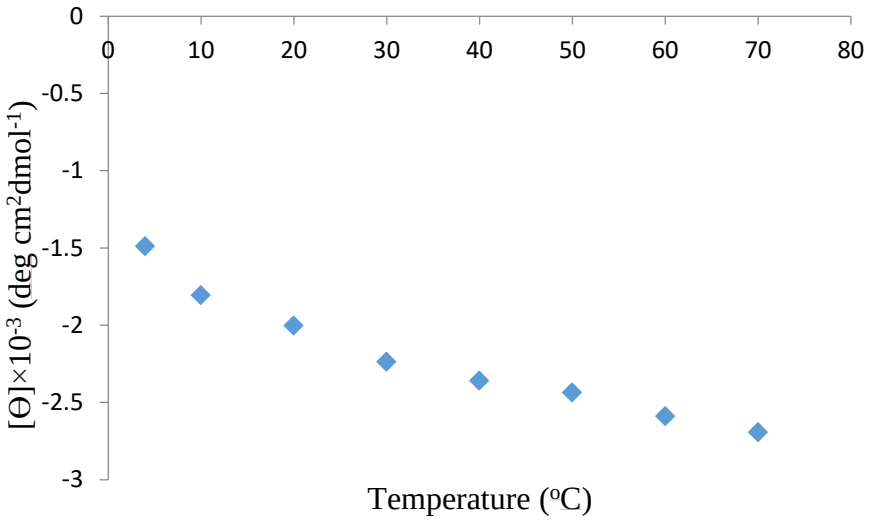

Figure 2.23: Temperature profile of $[\theta]_{222}$ values for peptide **10** (0.2 mg mL^{-1}) in PBS buffer at pH 7.4 between 4°C and 60°C.

As discussed in **Section 2.3.1.3**, the structure of thiol-end peptide **11** is similar to the structure of peptide **10**. The temperature dependence of the secondary structure of purified peptide **11** in dilute solution (0.2 mg mL^{-1}) was also evaluated using CD spectroscopy. The spectra obtained in a PBS buffer (pH 7.4) from 10°C to 70°C are shown in **Figure 2.24**.

The CD spectra was found to exhibited an obvious increase in MRE at 195 nm to 200 nm and a very small increase at 206 nm to 212 nm, which are signatures of β-turn formation. At the lowest temperature (10°C), the spectrum yielded a large negative peak at approximately 195 nm, which is characteristic of a random coil. With increasing temperature, there exists a small decrease in MRE at 222 nm. This peak is associated with a type I/III β-turn. The spectra are characterized by a high proportion of random coils and a low proportion of β-turn at low temperature. This distribution is gradually inverted with increasing temperature. With increasing temperature, the random coil signal becomes less pronounced at 195 nm to 200 nm, while the β-turn increases at 222 nm.

The trends at 200 nm and 222 nm discussed above are both indications of a transition from a less-ordered state toward a more ordered secondary structure. The conformational transition from random coil to β-turn occurred gradually over a wide temperature range from 10°C to 70°C. This shows that the peptide has a more stable

status at higher temperature. When the temperature is increased, the thiol-peptides became more hydrophobic and had a structure change from random coil to β-turn.

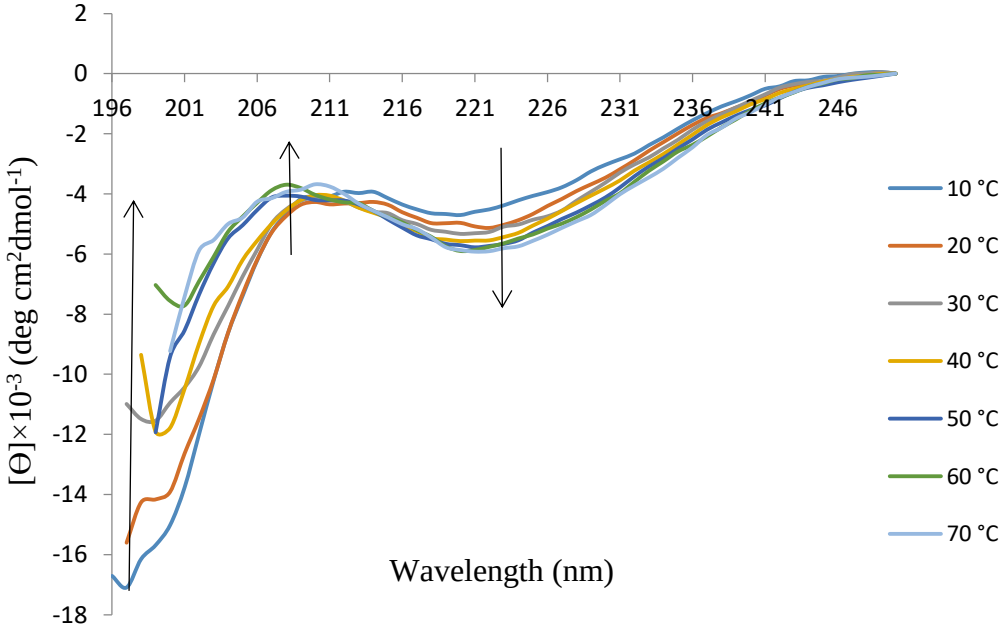

Figure 2.24: Temperature dependence CD spectra of thiol-peptide **11** (0.2 mg mL^{-1}) in PBS buffer at pH 7.4 between 10°C and 70°C.

The changes in MRE at 200 and 222 nm when the temperature was increased are plotted respectively in **Figure 2.25** and **2.26**, which both show the same trend. In **Figure 2.25**, the MRE increased slowly with increasing temperature at 200 nm. In **Figure 2.26**, the MRE decreased smoothly with increasing temperature at 222 nm. In **Figure 2.27**, the temperature of the CD spectrometer was changed from 10°C to 50°C in 3 cycles and the CD signal of thiol-peptide **11** at 200 nm was measured. When the temperature was lowered to 10°C, the MRE decreased, which indicates aggregate dissociation. Multiple cooling and heating cycles were executed and showed little effect on the particles' properties. The data showed the reversibility of thiol-peptide **11** under thermal conditions.

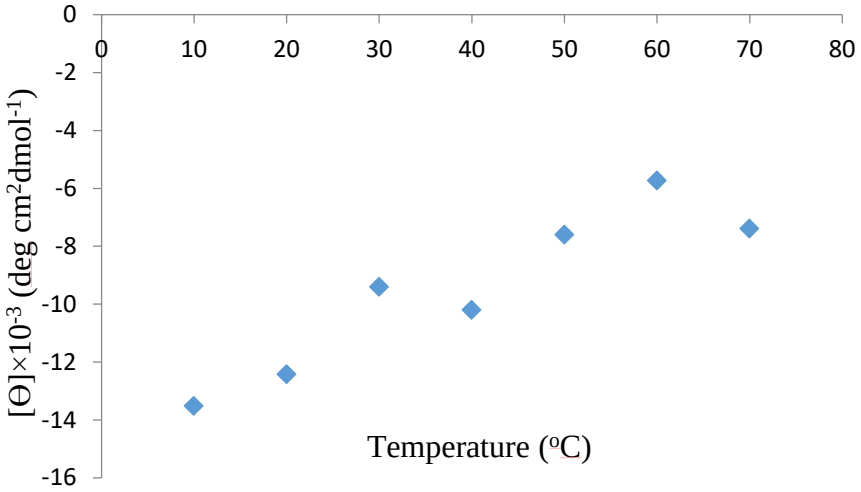

Figure 2.25: Temperature profile of $[\theta]_{200}$ values for thiol-peptide **11** (0.2 mg mL^{-1}) in PBS buffer at pH 7.4 between 10°C and 70°C.

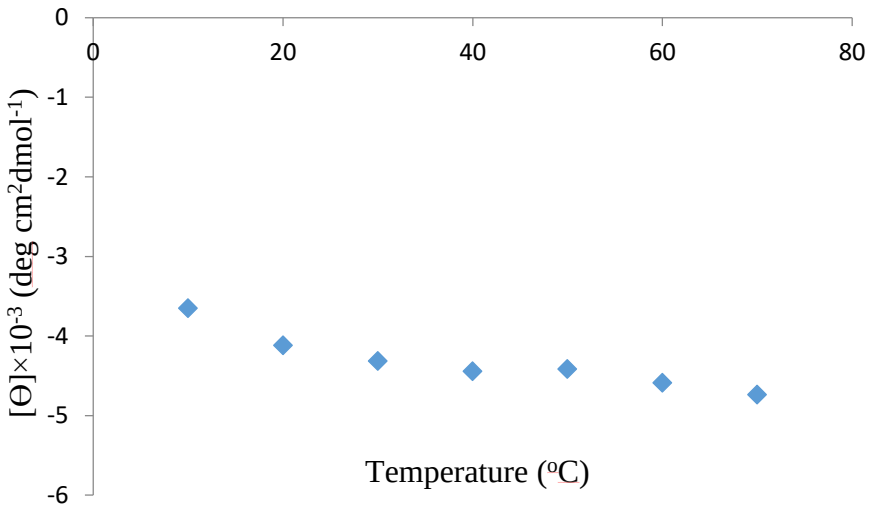

Figure 2.26: Temperature profile of $[\theta]_{222}$ values for thiol-peptide **11** (0.2 mg mL^{-1}) in PBS buffer at pH 7.4 between 10°C and 70°C.

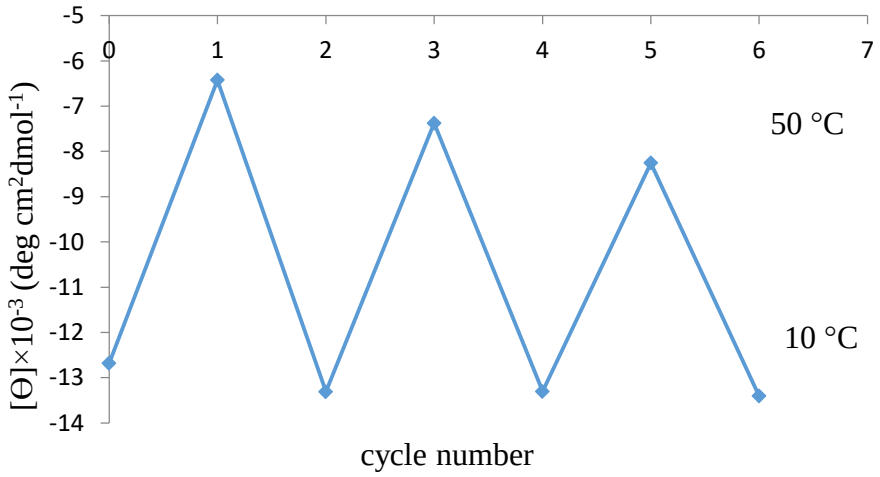

Figure 2.27: The CD signal at 200 nm of thiol-peptide **11** (0.2 mg mL^{-1}) in PBS buffer at pH 7.4 when alternating the temperature 3 times between $10^{o}C$ and $50^{o}C$.

2.4 Synthesis of elastin-based side chain polymers

2.4.1 Synthesis of pentafluorophenyl acrylate (14) monomer

In order to modify the transition temperature of short elastin-like peptides to the ideal range, elastin-based side chain polymers have been introduced in this study. Here, reversible addition fragmentation chain transfer (RAFT) polymerization was used to polymerize monomer pentafluorophenyl acrylate (PFPA). RAFT is an important technique for tailoring well-defined macromolecular architectures. In addition, monomer PFPA is an activated ester with fewer cytotoxic effects which has been widely applied in the synthesis of biologically active polymers.[39, 40]

The reaction of the monomer was performed in a two-necked round bottomed flask under a nitrogen atmosphere. In the first step, the ratio of the triethylamine (TEA) to pentafluorophenol (PFP) (**12**) was 1.2:1 in order to give full conversion to the pentafluorophenolate anion. Acryloyl chloride (**13**) was then added drop-wise in the presence of TEA and PFP as shown in **Figure 2.28**.

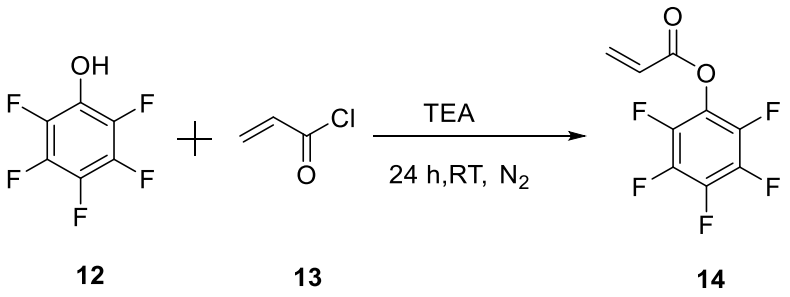

Figure 2.28: Synthesis of pentafluorophenyl acrylate (PFPA) (**14**).

Purified **14** was characterized by ^{1}H NMR, ^{13}C-NMR and ^{19}F NMR spectroscpies which are shown in **Figures 2.29** to **2.31**. In the ^{1}H-NMR spectrum (**Figure 2.29**), the set of signals at 6.70 ppm, 6.35 ppm and 6.16 ppm are respectively correlated to protons c, a and b. In the ^{13}C-NMR spectrum (**Figure 2.30**), the signals at 125.34, 135.42 and 161.65 respectively represent C-H, CH_2 and –C=O. In the ^{19}F NMR spectrum (**Figure 2.31**), there are three signals at -162 ppm, -158 ppm and -153 ppm which are due to three types of aromatic fluorine environment.

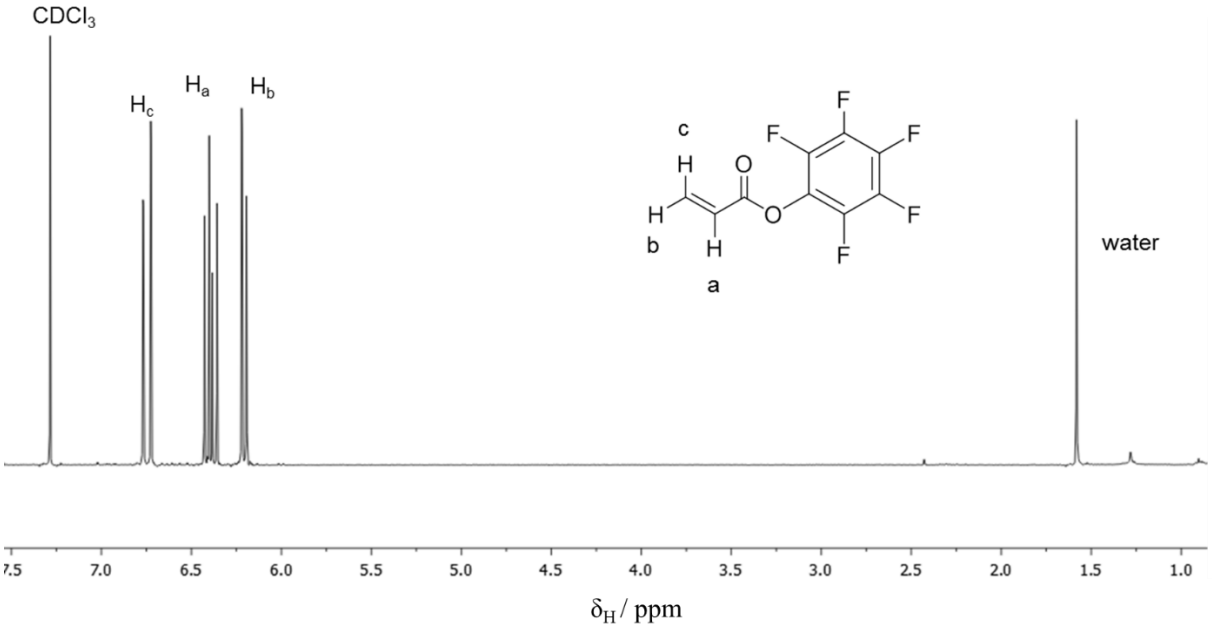

Figure 2.29: ^{1}H-NMR spectrum of monomer PFPA in $CDCl_3$.

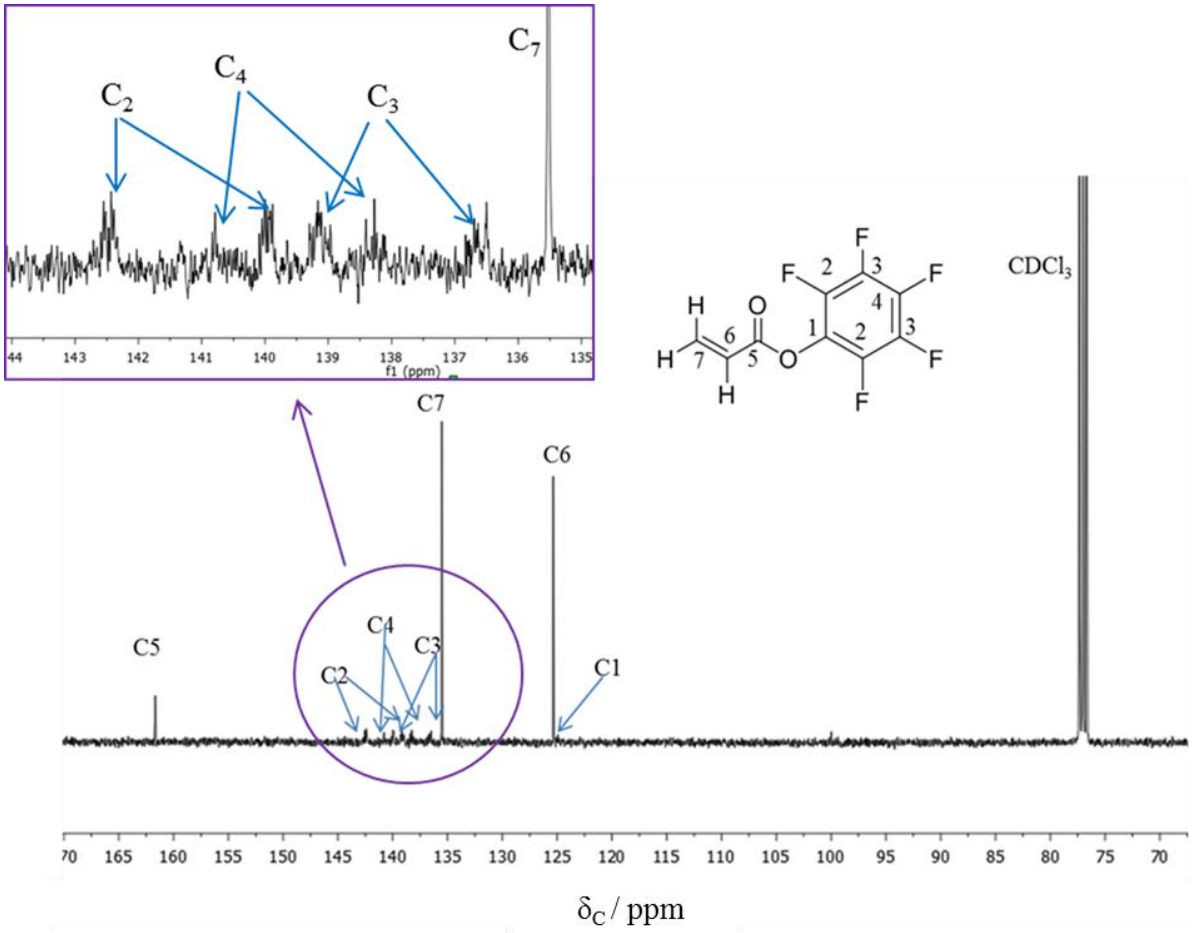

Figure 2.30: ^{13}C-NMR spectrum of monomer PFPA in $CDCl_3$.

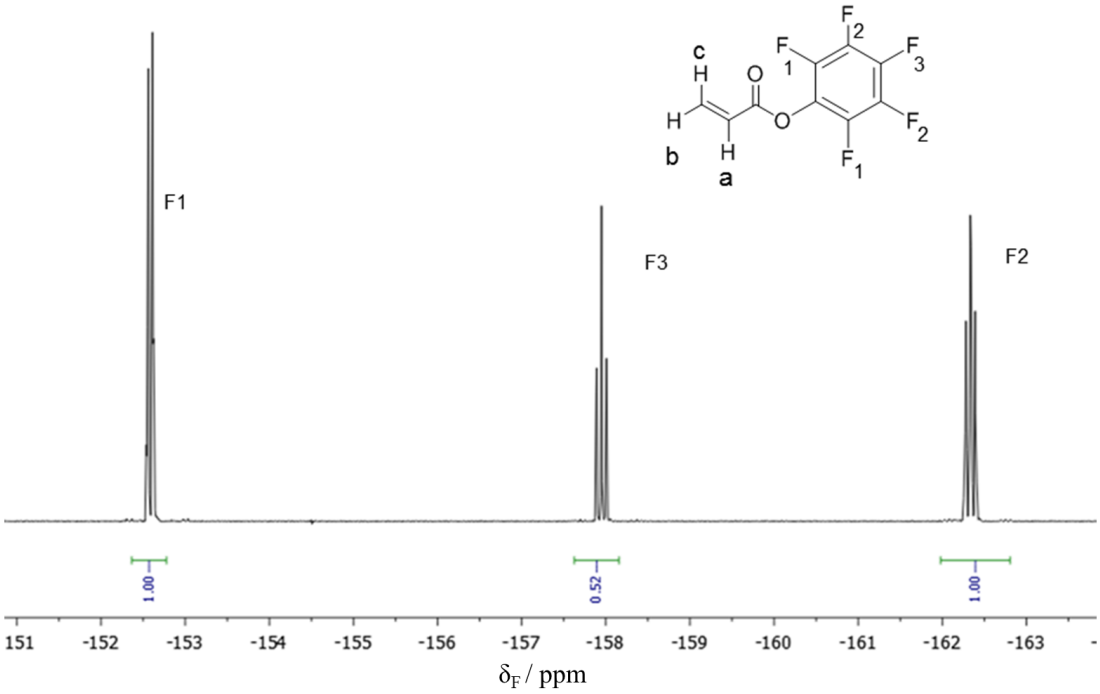

Figure 2.31: ^{19}F-NMR spectrum of monomer PFPA in $CDCl_3$.

2.4.2 Synthesis of poly(pentafluorophenyl acrylate) polymers

RAFT polymerization is one of the most convenient and versatile polymerization methods. The RAFT mechanism provides a controlled living radical polymerization that gives well defined polymers with a narrow molecular weight distribution.[41]

In our work, pentafluorophenyl acrylate (**14**) was polymerized in the presence of benzyl 2-hydroxyethyl carbonotrithioate (**15**) as a RAFT agent in benzene at 70^{o}C. Pentafluorophenyl acrylate (**14**) has been discovered to be a good candidate for RAFT polymerization.[41] One of the advantages of poly(pentafluorophenyl acrylate) (PPFPA) is its excellent solubility in common organic solvents and high reactivity compared to conventional activated esters. Furthermore, by using ^{19}F NMR spectroscopy, it is easy to monitor the reaction of the PFP ester groups. We used benzyl 2-hydroxyethyl carbonotrithioate (**15)** as a RAFT agent and it resulted in a trithiocarbonate end group on the polymer. This end group can be converted to a thiol through a reductive aminolysis, which has advantageous properties for attachment to gold nanoparticle surfaces. The reaction scheme is shown in **Figure 2.32**.

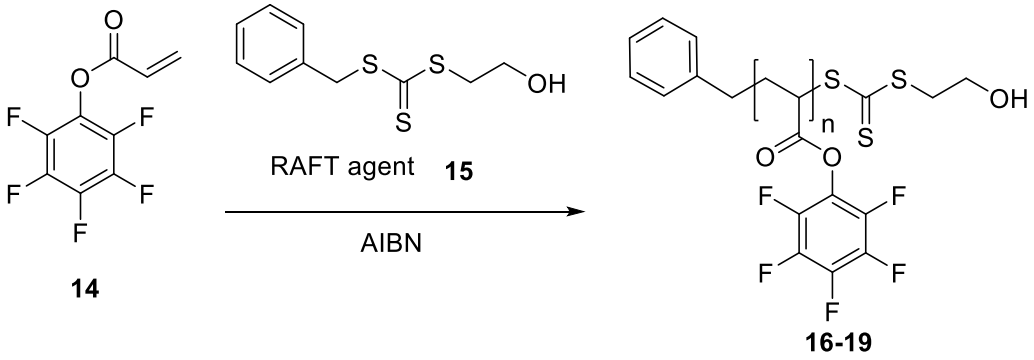

Figure 2.32: Synthesis of poly(pentafluorophenyl acrylate) poly (PFPA) (**16-19**).

We synthesised different molecular weights of P(PFPA), from P(PFPA)-25 to P(PFPA)-100 (**16-19**). The data of all the polymers synthesised are summarized in **Table 2.2**. For the lower molecular weight reaction, the ratio of [RAFT]/[I] was 1:0.2; while for P(PFPA)-100 reaction, the best ratio of [RAFT]/[I] was 1:0.5.

Table 2.2: Summary of all the polymerization reactions.

Runs	[M]/[RAFT]/[I]	$M_{n,theor}$ g.mol^{-1}	$M_{n,GPC}$ g.mol^{-1}	$Đ_M$	$M_{n,NMR}$ g.mol^{-1}	Yield %
P(PFPA)-25 (**16**)	25/1/0.2	6,194	8,200	1.26	6,200	65
P(PFPA)-50 (**17**)	50/1/0.2	12,144	15,700	1.27	10,700	60
P(PFPA)-75 (**18**)	75/1/0.2	18,094	16,300	1.26	14,500	70
P(PFPA)-100 (**19**)	100/1/0.5	24,044	23,500	1.19	19,500	69

Here, we discuss the experimental results of P(PFPA)-100 (**19**) as an example. The conversion of this RAFT polymerization is quite high (83%) which proves that it worked very well. The calculation is based on the comparision of the integral (I) of monomer peak and polymer peak by ^{1}H NMR spectroscopy as shown in **Figure 2.33** and the equation can be found in **Section 6.3.3**. Then **19** was purified and was analyzed by THF GPC, ^{1}H NMR and ^{19}F NMR spectroscopies (**Figure 2.34**) in CD_2Cl_2.

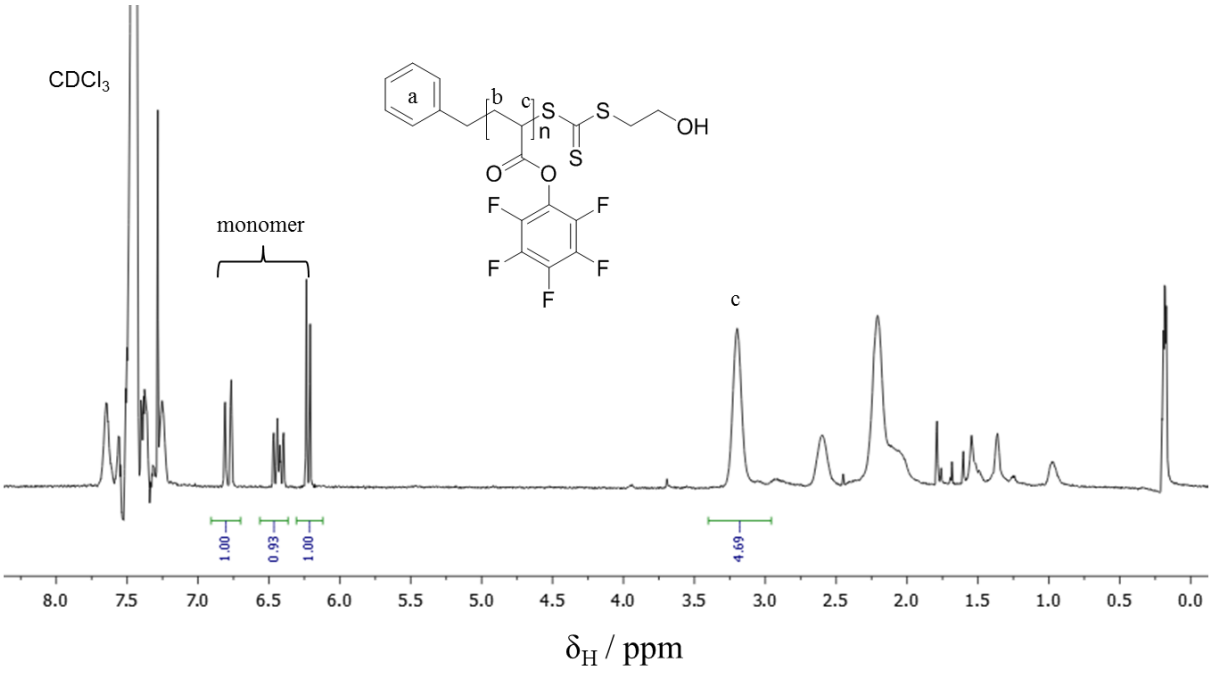

Figure 2.33: ^{1}H NMR spectrum of P(PFPA)-100 (**19**) in $CDCl_3$.

The molecular weight obtained by THF GPC (23,500 g.mol^{-1}) is in very good accord with the theoretical molecular weight (24,044 g.mol^{-1}) as shown in **Table 2.2**. The GPC

also indicated monomodal distributions with low dispersity ($Đ_M$ =1.19). The ^{1}H NMR spectrum of purified P(PFPA)-100 (**19**) showed characteristic signals from backbone protons (peak b and c) around 2.0 and 3.0 ppm as shown in **Figure 2.34**. The aromatic ring signal (peak a), which is at 7.2 ppm, verified the presence of the RAFT agent (**15**). By comparing the phenyl protons (5H, 7.2 ppm) and backbone proton (1H, 3.0 ppm) integrals, the degree of polymerization (DP) can be determined. From the ^{1}H NMR spectrum, we calculate a DP of 81 and the molecular weight of P(PFPA)-100 (**19**) is 19,300 g.mol$^{-1.}$ The ^{19}F NMR analysis confirmed the expected structure with three signals at -153, -158 and -162 ppm attributed to the pentafluorophenyl group. Complementary FT-IR showed a carbonyl absorption peak of pentafluorophenyl ester at 1782 cm^{-1} and a C=C bond of aromatic band absorption peak at 1516 cm^{-1} as shown in **Figure 2.35**.

For **16**, **17** and **18**, the same method was used and the experimental ^{1}H NMR and ^{19}F NMR results can be found in **Appendices 2.1, 2.2** and **2.3**. The DPs calculated from ^{1}H NMR spectroscopies were 25, 44 and 60 respectively.

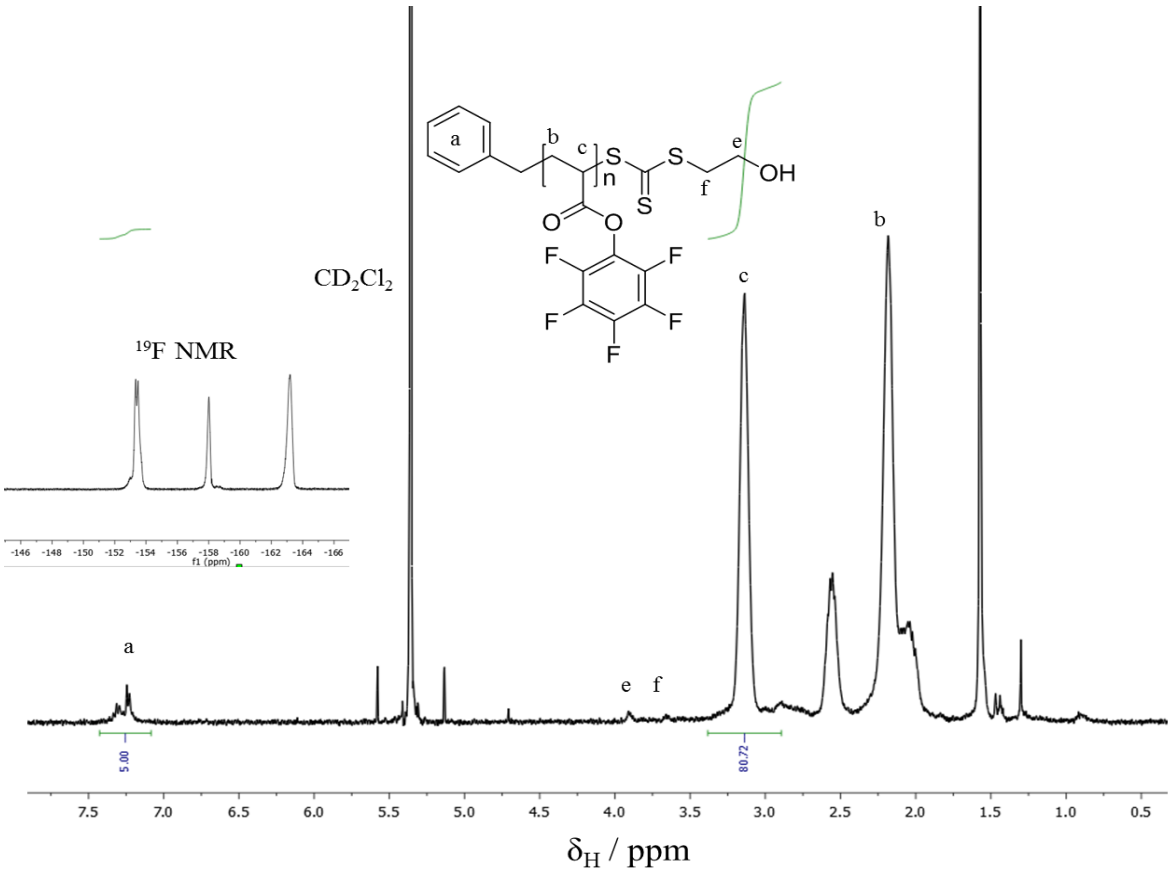

Figure 2.34: ^{1}H NMR spectrum of purified P(PFPA)-100 (**19**) in CD_2Cl_2.

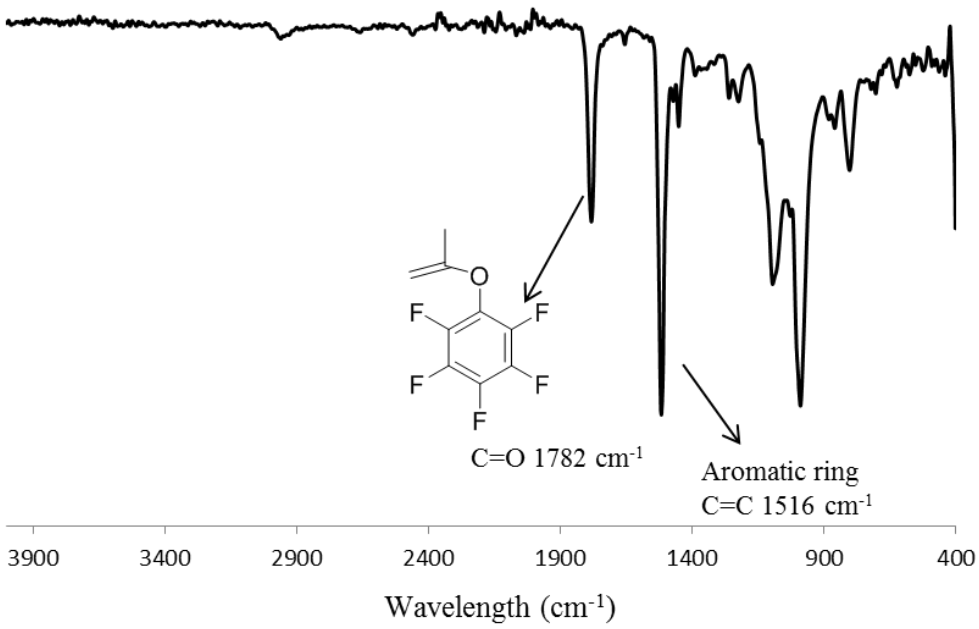

Figure 2.35: ATR-FTIR spectrum of P(PFPA)-100 (**19**).

2.4.3 Synthesis of elastin-like peptides for coupling to P(PFPA)

As for the synthesis of side chain peptides (**9**, **20**-**21**), solid-phase peptide synthesis with a Fmoc-protecting group strategy and Rink Amide resin was employed in the preparation of peptides **9**, **20** and **21** (**Table 2.3**).

Table 2.3: Summary of all the peptides synthesised.

Sequence	Structure
H-VPGVG-NH_2 (**9**)	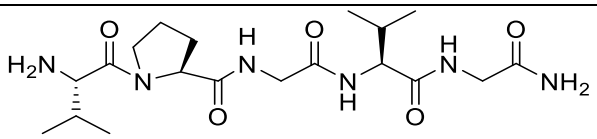
H-GVPGVG-NH_2 (**20**)	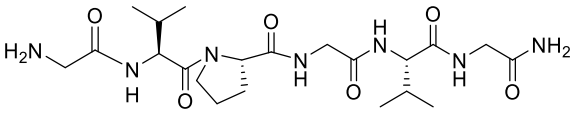
GABA-VPGVG-NH_2 (**21**)	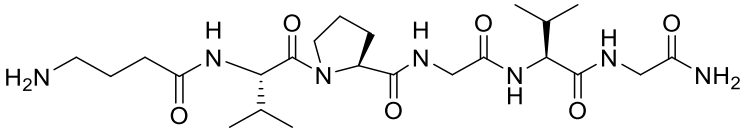

As for peptide **9** (VPGVG), the same preparation method was used and the discussion can be found in **Section 2.2.1**. The same method was applied to **20** and **21**. Crude products were purified by semi-preparative HPLC (**Appendix 2.4**) using the same conditions as discussed in **Section 2.2.3**. After purification, 53% of pure peptide **20** (GVPGVG) was obtained.

After purification, a small sample of peptide **20** was dissolved in water and analyzed by LC-MS. The obtained spectrum is shown in **Figure 2.36**. The peak eluting at 2 min is the main product. The mass is 484.0 which represents $[M+H]^+$. The other peaks that appear at 3.0 min and 4.5 min are solvent peaks which also appear in the blank sample. Analysis by analytical HPLC was carried out to confirm the purity of peptide **20** (**Figure 2.37**).

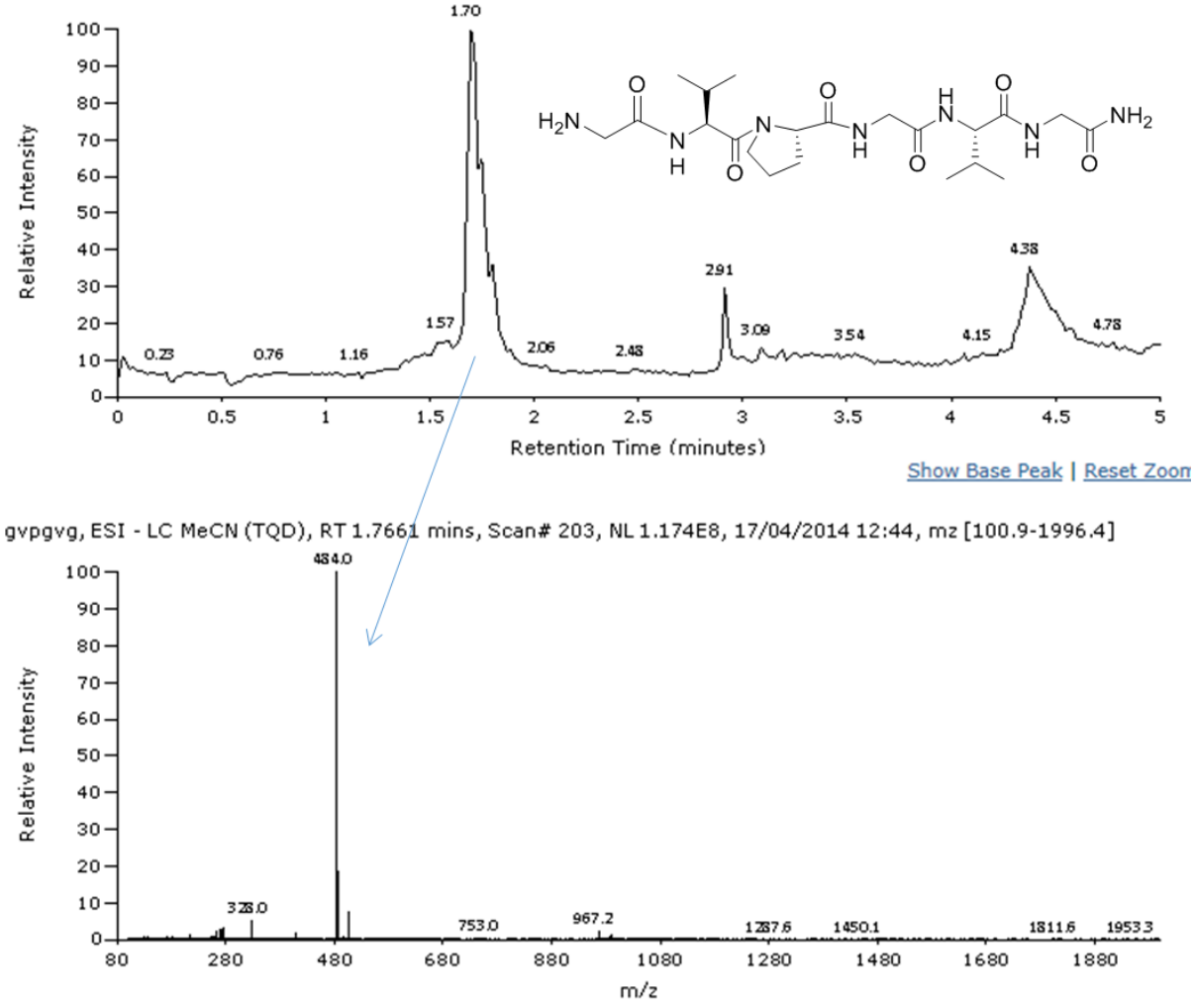

Figure 2.36: LC-MS spectrum of purified peptide **20**.

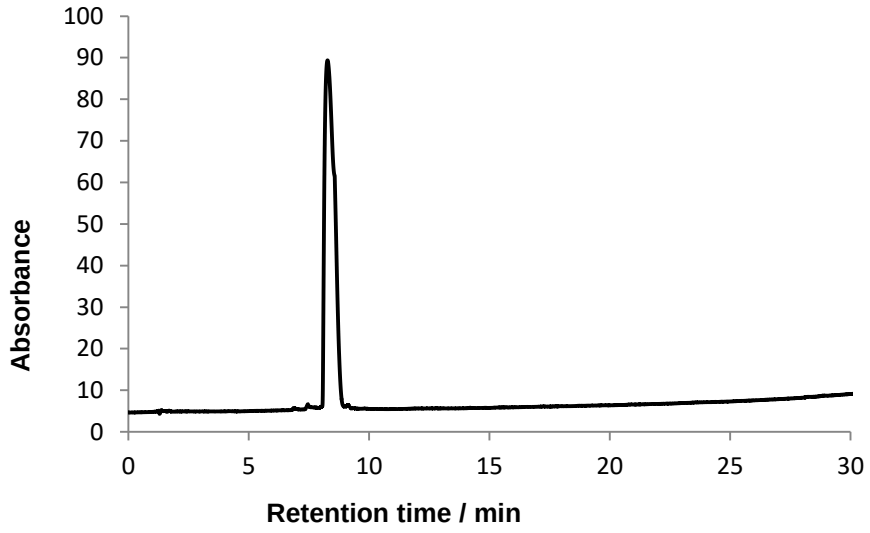

Figure 2.37: Analytical HPLC trace of purified **20**. HPLC was carried out on an analytical column (C18, 4.6 x 100 mm, 3.5 μm particle size). Peptides were eluted in H_2O / MeCN + 0.05 % trifluoroacetic acid.Retention time = 8.3 min.

For peptide **21,** the same HPLC purification method was used as that for peptide **20** (**Appendix 2.5**). After purification, 55% of purified **21** was obtained. The LC-MS spectrum of **21** is shown in **Figure 2.38**. The peak that elutes at 1.7 min is the main product. The mass is 511.9, which represents $[M+H]^+$. The other peaks that appear at 2.7 min and 4.5 min are solvent peaks which also appear in the blank sample. The analytical HPLC trace of **21** was carried out and the spectrum is shown in **Figure 2.39**.

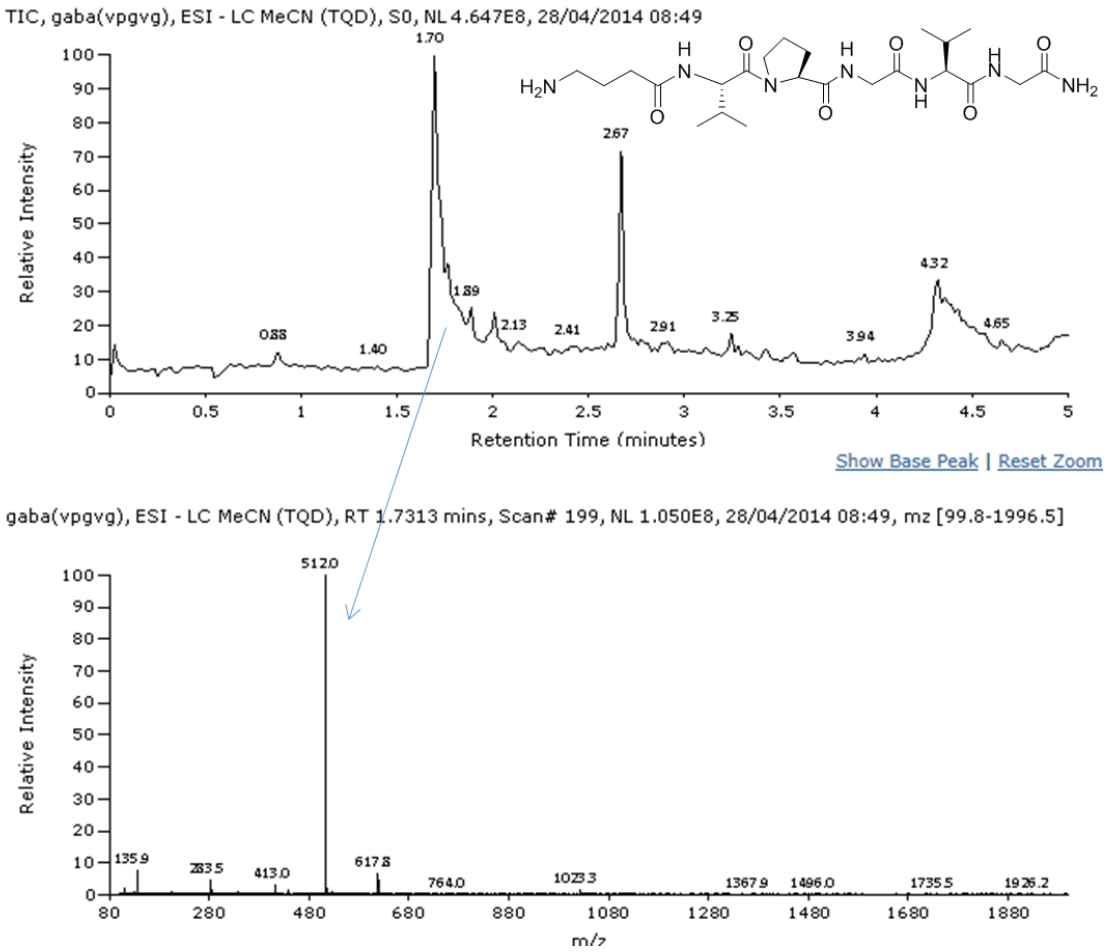

Figure 2.38: LC-MS spectrum of purified peptide **21**.

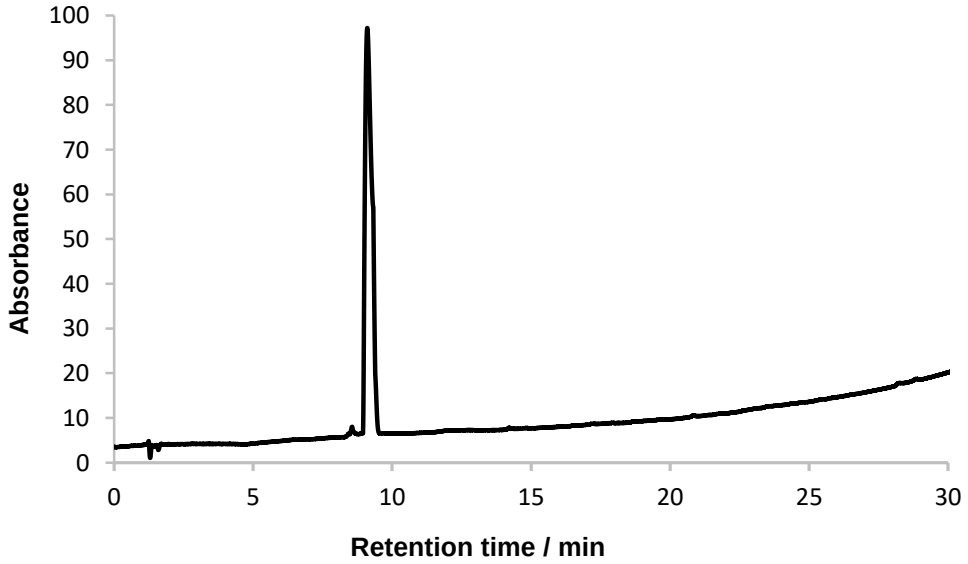

Figure 2.39: Analytical HPLC trace of purified **21**. HPLC was carried out on an analytical column (C18, 4.6 x 100 mm, 3.5 μm particle size). Peptides were eluted in H_2O / MeCN + 0.05 % trifluoroacetic acid.Retention time = 9.1 min.

2.4.4 Synthesis of elastin-based side chain polymers

P(PFPA) was modified by reaction with the amine end of the short elastin-like peptide (ELPs). P(PFPA) was dissolved in *N*,*N*-dimethyl formamide (DMF) and the solution of peptide dissolved in dimethyl sulfoxide (DMSO) in the presence of 1.5 equivalents of trimethylamine, which was added slowly. Here, we chose DMSO as the solvent rather than water to avoid precipitation of the polymer. The ratio of [NH_2-peptide]/[PPFPA] was chosen as 1.4:1 to ensure a full conversion of activated ester. The larger ratio will not have a significant impact on the yield.[40] To ensure the total consumption of pentafluorophenyl ester, the reaction was carried out overnight at 30^{o}C. When the reaction was finished, the solution was dialyzed against water for 3 days using a membrane with a cut-off of 3500 Daltons. The purpose of dialysis was to remove any unreacted peptides. As proof of a successful reaction, the solubility of the polymer was transformed from hydrophobic P(PFPA) to hydrophilic elastin-based side chain polymer (ESP). After freeze drying, a white fluffy powder was obtained. The reaction scheme is shown in **Figure 2.40**. **Table 2.4** shows the characterisation data for all the ESP **22**-**29**.

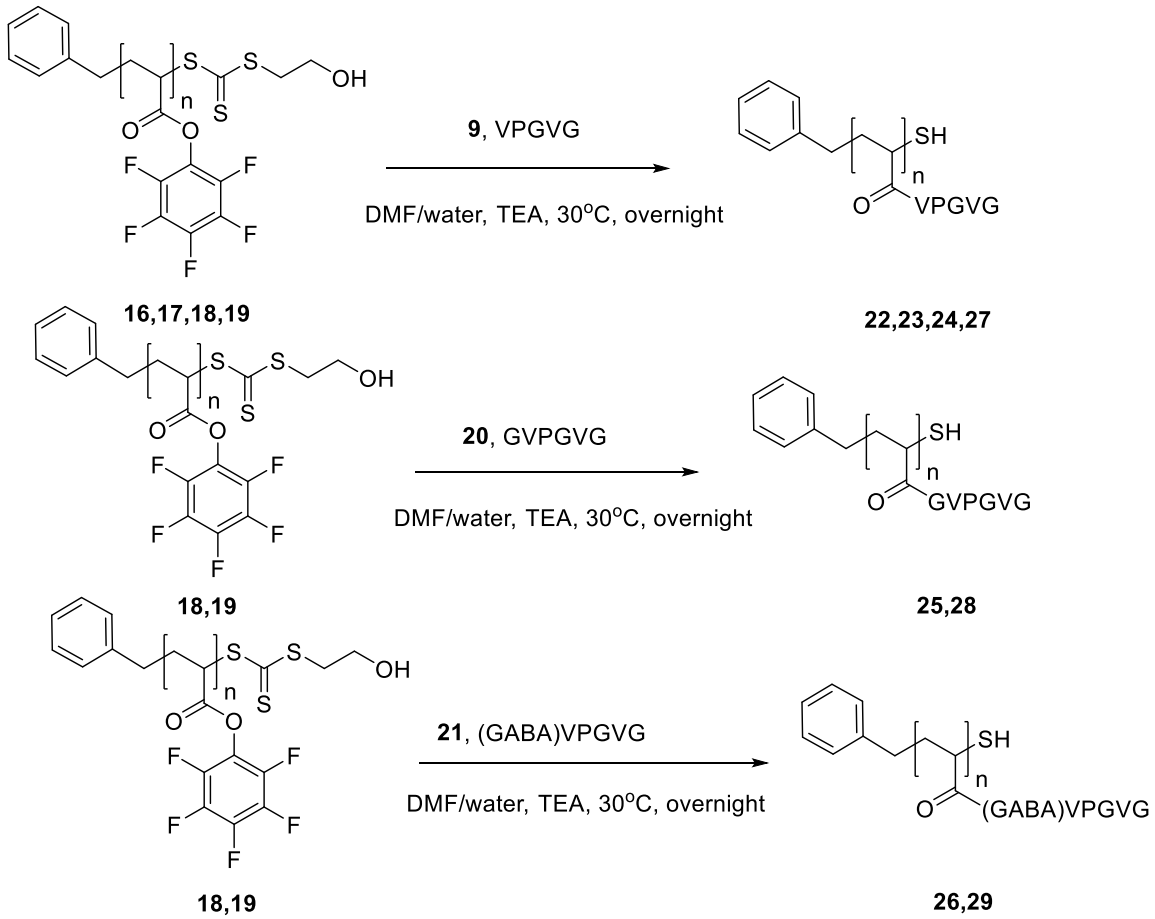

Figure 2.40: Chemical modification of PFPA in the presence of peptide.

Table 2.4: Characterisation date for peptide-polymer hybrids **22-29**.

Runs	[Polymer]/[Peptide]/[TEA]	$M_{n,theor}$ g.mol^{-1}	$M_{n,GPC}$ g.mol^{-1}	$Đ_M$	Yield %
PF25-VPGVG (**22**)	1/1.4/1.4	12,125	5,600	1.31	71
PF50-VPGVG (**23**)	1/1.4/1.4	21,245	6,400	1.46	87
PF75-VPGVG (**24**)	1/1.4/1.4	28,925	10,100	1.30	83
PF75-G(VPGVG) (**25**)	1/1.4/1.4	32,345	10,600	1.22	81
PF75-GABA(VPGVG) (**26**)	1/1.4/1.4	34,025	11,300	1.23	79
PF100-VPGVG (**27**)	1/1.4/1.4	39,005	11,500	1.26	80
PF100-G(VPGVG) (**28**)	1/1.4/1.4	43,622	13,000	1.25	80
PF100-GABA(VPGVG) (**29**)	1/1.4/1.4	45,890	13,400	1.27	76

The elastin-based side chain polymers were analysed by ^{1}H NMR and ^{19}F NMR in d_6-DMSO and FT-IR spectroscopies. The ^{19}F NMR spectrum can be used to easily determine whether the pentafluorophenyl ester has fully reacted or not. For low molecular weight PF25-VPGVG (**22**) and PF50-VPGVG (**23**), the ^{19}F NMR spectrum showed no signals at -153, -158 and -162 ppm from pentafluorophenyl group, as shown in **Appendix 2.6** and **2.7**. However, for the larger molecular weight PF75-VPGVG (**24**) and PF100-VPGVG (**27**), the reactions were not complete because the ^{19}F NMR spectrum showed a very small peak in this area as shown in **Appendix 2.8** and **2.9**. In support, ATR-FTIR spectra of **24** and **27** both showed a small carbonyl absorption peak at 1782 cm^{-1} while no such peaks were seen in ATR-FTIR spectra of **22** and **23**. The comparison ATR-FTIR data can be found in **Appendix 2.10**.

These results showed that longer the polymer, the more difficult the reaction. Also because of the structure of peptide VPGVG, the amine of amino acid valine is quite hindered and slow to react with pentafluorophenyl ester. Therefore, we synthesised peptide **20** and peptide **21** which had a short linker glycine and longer linker 4-aminobutanoic acid to react with P(PFPA)-75 (**18**) and P(PFPA)-100 (**19**).

An example of the ^{1}H NMR and ^{19}F NMR spectra (in d_6-DMSO) of the PF75-GVPGVG (**25**) is given in **Figure 2.41**. The absence of the backbone proton signal at 3.0 ppm indicates an efficient modification of pentafluorophenyl ester. Moreover, the signal at 0.85 ppm attributed to the protons which belong to methyl

group from amino acid valine confirms a successful modification. The presence of the RAFT agent can be found by the signal at 7.2 ppm attributed to the aromatic ring. From the ^{19}F NMR spectrum, it is easy to tell that the reaction of the ester groups is highly efficient from the absence of any signals. In **Figure 2.42**, ATR-FTIR shows a carbonyl absorption shift from 1782 cm^{-1} to 1654 cm^{-1} corresponding to a change of the carbonyl functionality from being adjacent to pentafluorophenyl to carbonyl in an amide bond. The absence of a band at 1715 cm^{-1} confirms the absence of any free carboxylic acid group due to the prior hydrolysis of the pentafluorophenyl group. DMF GPC result showed only one peak and the dispersity $Đ_M$ is reasonable (1.26). The molecular weight obtained from GPC measurement was based on PEO standards and it is not accurate. Since the ^{19}F NMR as well as the ATR-FTIR spectrum supported the full functionalisation of pentafluorophenyl ester, we used the same DP for PF75-GVPGVG (**25**) as for P(PFPA)-75 (**18**).

For **26**, **28** and **29**, the same method was used and the experimental results of ^{1}H NMR and ^{19}F NMR spectroscopy can be found in **Appendix 2.11, 2.12** and **2.13**.

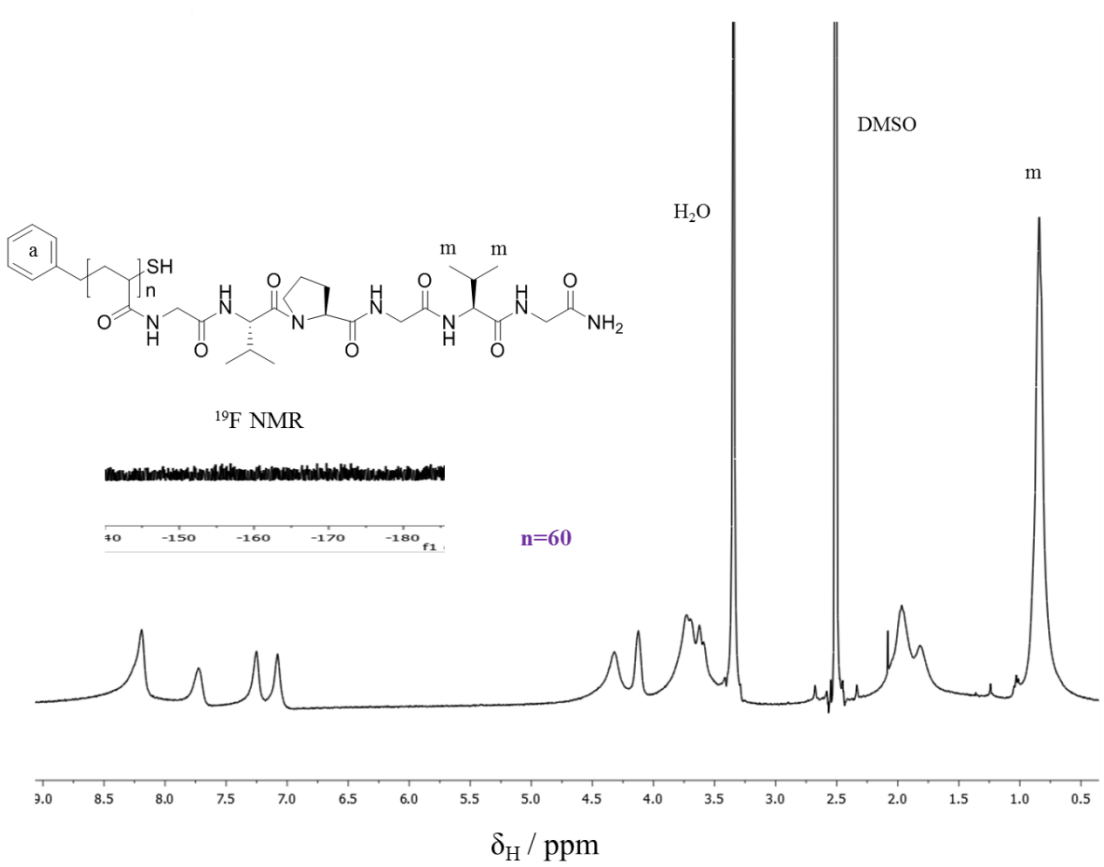

Figure 2.41: ^{1}H NMR and ^{19}F NMR spectra of PF75-GVPGVG (**25**) in d_6-DMSO.

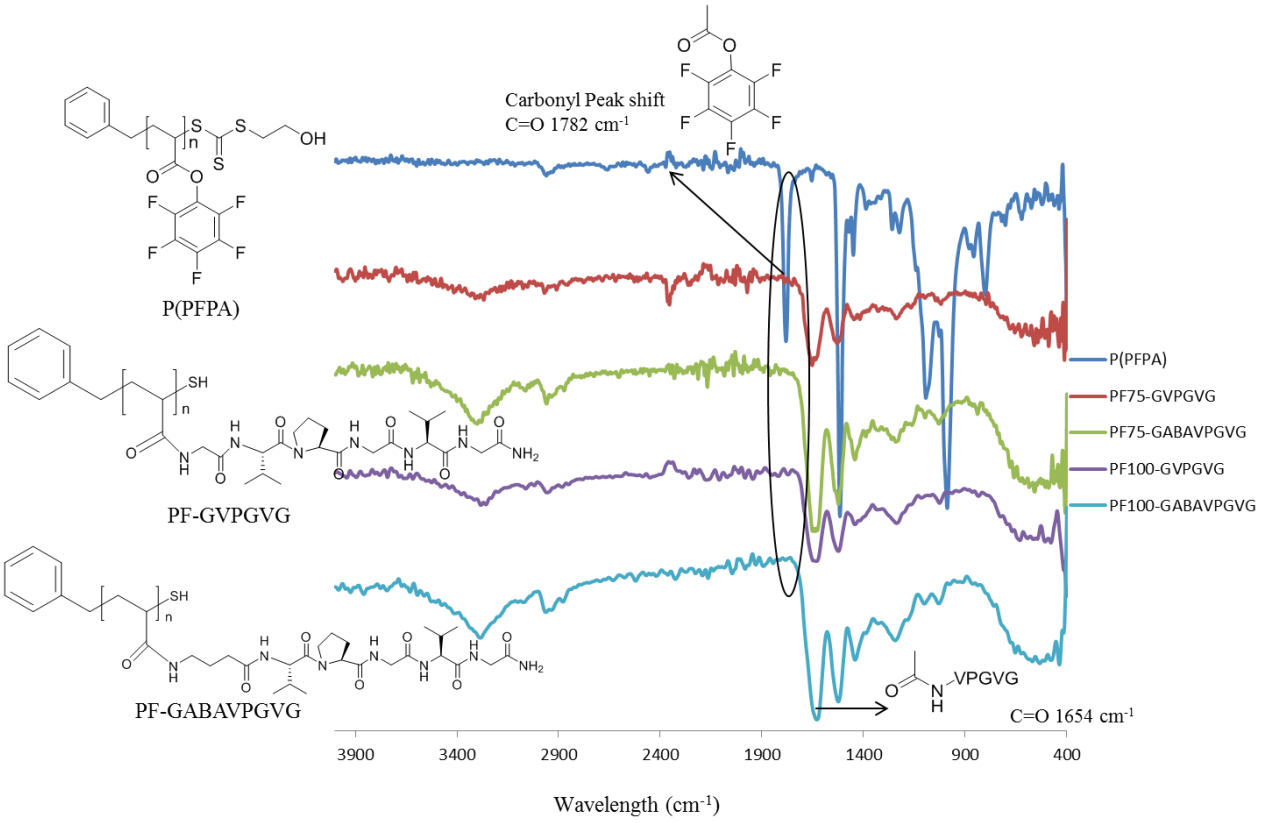

Figure 2.42: ATR-FTIR spectra of P(PFPA) (**16**) and PF(75,100)-GVPGVG (**25**,**28**) and PF(75,100)-GABA(VPGVG) (**26**,**29**).

2.5 LCST and CD experiments of elastin-based side chain polymers

2.5.1 LCST behaviour of elastin-based side chain polymers (ESPs)

In the following part, we will describe our investigations of the influence of the length of the side chain, polymer weight and NaCl concentration on the LCST behaviour of the elastin-based side chain polymers.

2.5.1.1 Chain length and molecular weight

It has been shown that, as the molecular weight of linear poly(VPGVG) is increased, the transition temperature is decreased.[7, 10] To investigate whether elastin-based side chain polymers (ESP) were also affected in the same way, four different chain length polymers were synthesised and studied as shown in **Table 2.5**. The degree of polymerization was determined by ^{1}H NMR spectroscopy of the poly(PFPA).

Each polymer was dissolved in pH=7.4 phosphate buffer at a concentration of 1mg mL^{-1}. When the number of VPGVG units (DP_n) in the polymer is increased from 25 to 80, we see a change in LCST from higher than 100^oC to 42^oC. However, as was discussed in **Section 2.4.4**, the reactions of PF75-VPGVG (**24**) and PF100-VPGVG (**27**) were not complete because the ^{19}F NMR spectra showed small peaks in the range of -150 to -165 ppm. Therefore, **24** and **27** were not 100 % pure with VPGVG side chains, which means the LCST of pure **24** and **27** should be higher than what was observed. As the reaction temperature, time and ratios of reagents as well as polymer synthesis were the same, we assume that the purities of **24** and **27** were similar. Here, we only use the data to discuss the effect of chain length on transition temperature as a qualitative analysis.

For **22** and **23**, the absorbance value increased when temperature increased (15^oC-95^oC) in a liner relationship. The transition temperature of the **22** and **23** could not be detected because it is above the highest temperature that could be measured. For **24** and **27**, the transition temperature was 49^oC and 42^oC as shown in **Figure 2.43**. The turbidity measurements clearly showed a decrease in the transition temperature as the chain length was increased. It has been proven by Fernandez-Trillo *et al.*[42] that transition temperature is decreased when the chain length of elastin-based side chain polymers (ESPs) is increased. This is because longer chain lengths increase overall molecular weights, which will reduce phase transition temperatures.

Table 2.5: Molecular weight data and transition temperatures for elastin-based side chain polymers.

Polymer	**DP_n**	**$M_{n,theor}$ kg.mol^{-1}**	**Transition temperature (^oC)**
PF25-VPGVG (**22**)	25	12.1	/
PF50-VPGVG (**23**)	44	21.2	/
PF75-VPGVG (**24**)	60	28.9	49
PF100-VPGVG (**27**)	81	39.0	42

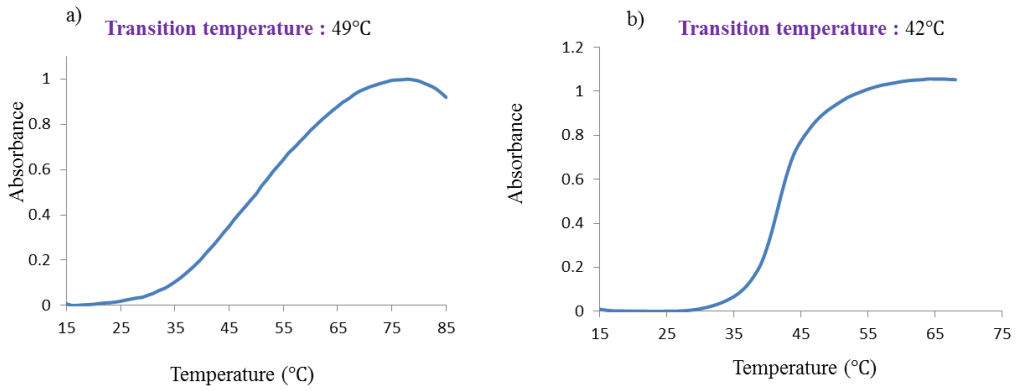

Figure 2.43: Turbidity measurements of different polymers (1 mg mL^{-1}) as observed by UV-Vis absorbance at 300 nm: (a) PF75-VPGVG (**24**) and (b) PF100-VPGVG (**27**).

We also investigated whether the peptide sequence affected the transition temperature. Four polymers with different peptide side chains were synthesised and studied as shown in **Table 2.6**. The polymers were dissolved in a phosphate buffer of pH 7.4 and at a concentration of 1 mg mL^{-1}. The first two polymers have the same chain length (60), but the side chain is different. The transition temperatures of the first two polymers were 76°C and 68°C as shown in **Table 2.6**. And the last two polymers have longer chain length (81), and the transition temperatures were 49°C and 47°C, which are much lower than the first two polymers. The molecular weight was different proving that the larger the molecular weight, the lower the transition temperature. Comparing the peptide G(VPGVG) **20** and GABA(VPGVG) **21**, the longer linker produces a lower transition temperature. This is because the longer linker distances the peptides from the polymer.

Table 2.6: Molecular weight data and transition temperature for elastin-based side chain polymers.

Polymer	**DP_n**	**$M_{n,theor}$ kg.mol^{-1}**	**Transition temperature (°C)**
PF75-GVPGVG (**25**)	60	32.3	76
PF75-GABA(VPGVG) (**26**)	60	34.0	68
PF100-GVPGVG (**28**)	81	43.6	49
PF100-GABA(VPGVG) (**29**)	81	45.9	47

2.5.1.2 Effect of concentration on polymer 28 and 29

The second physical parameter of interest is the concentration of the polymer solution. It has been shown that as the concentration is increased, the transition temperature decreases.[10] To investigate the effect of concentrations on polymer PF100-GVPGVG (**28**) and PF100-GABA(VPGVG) (**29**), three different concentrations in PBS solution were prepared and their transition temperatures measured.

As shown in **Figure 2.44**, the turbidity measurements clearly confirmed that as the concentration increases, the transition temperature decreases which is the same trend that is observed for linear VPGVG. For linear VPGVG, Urry *et al.*[3,43] discussed that this concentration effect is caused by the fact that the transition of the secondary structure is a cooperative process. This means that when concentration is increased, this cooperative effect increased as well, and the transition temperature decreased. This explanation could also apply to the elastin-based side chain polymers. For polymer PF100-GVPGVG (**28**), when the concentration increased from 0.5 mg mL^{-1} to 2 mg mL^{-1}, the transition temperature changed from 52°C to 47°C. For the polymer PF100-GABA(VPGVG) **29**, the transition temperature decreased from 48°C to 46°C when the concentration was increased.

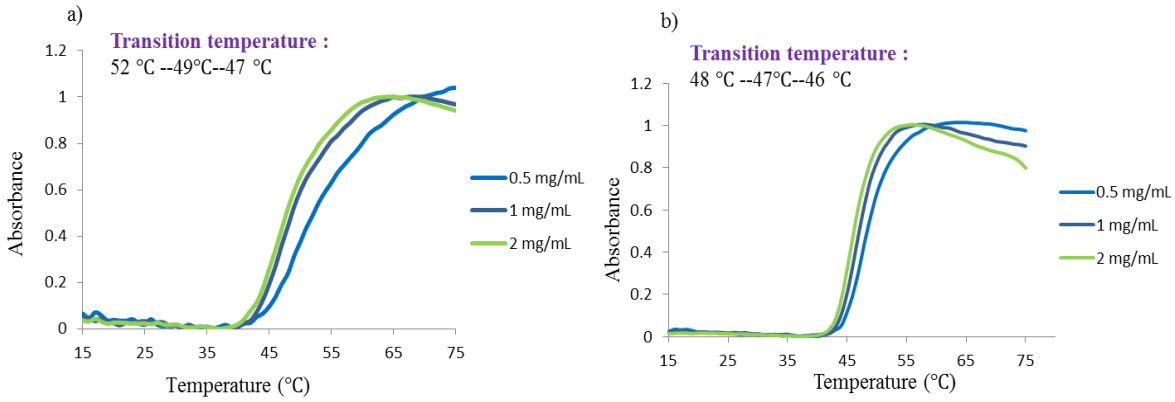

Figure 2.44: Turbidity measurements of different concentrations of polymer: (a) PF100-G(VPGVG) (**28**) and (b) PF100-GABA(VPGVG) (**29**) as observed by UV-Vis absorbance at 300 nm.

2.5.1.3 Effect of added sodium chloride on 25 and 26

The third physical parameter investigated is the concentration of NaCl in the polymer solution. It has been shown that as the concentration of NaCl is increased, the transition temperature decreases.[44]

To investigate the effect of NaCl concentration on polymer PF75-GVPGVG (**25**) and PF75-GABA(VPGVG) (**26**), four different polymer solutions which had different concentrations of NaCl were prepared and their transition temperatures measured. As shown in **Figure 2.45**, the turbidity measurements clearly confirmed that as the NaCl concentration increases, the transition temperature decreases which is the same trend that was observed for linear VPGVG. It has been suggested that anions weaken the hydrogen bonding of water to the carbonyl moiety of the amide backbone.[44] This explanation could also apply to the elastin-based side chain polymers.

For polymer PF75-GVPGVG (**25**), when the NaCl concentration increased from 0 to 0.3 M, the transition temperature decreased from 76°C to 65°C. As for polymer PF75-GABA(VPGVG) (**26**), when the NaCl concentration increased, the transition temperature decreased from 68°C to 57°C.

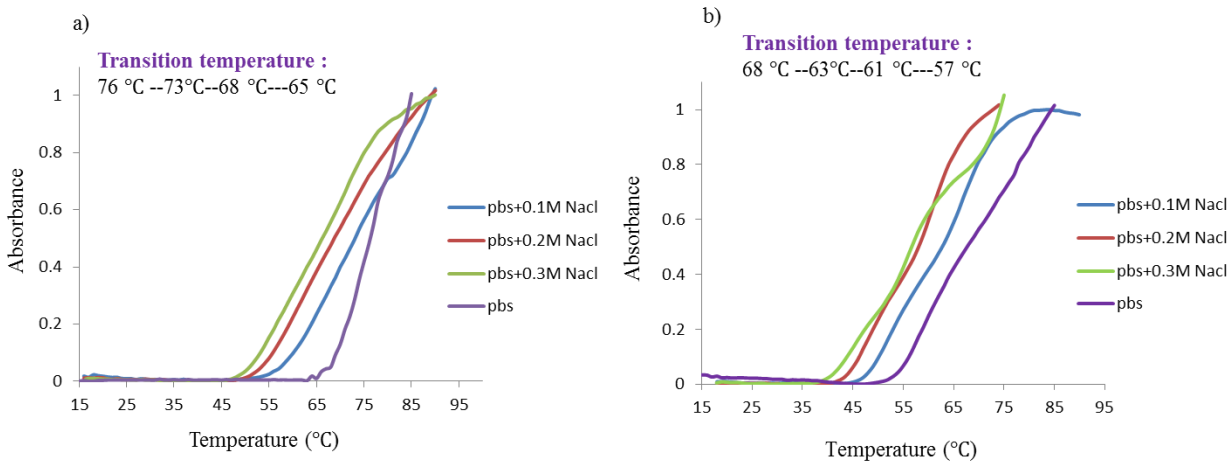

Figure 2.45: Turbidity measurements of different NaCl concentrations in PBS solutions of polymer as observed by UV-Vis absorbance at 300 nm: (a) PF75-G(VPGVG) (**25**) and (b) PF75-GABA(VPGVG) (**26**).

2.5.1.4 Summary of LCST behaviour of ESPs

In summary, we found that the transition temperature of elastin-based side chain polymers was mainly modulated by the change of chain length and molecular weight of the polymers. PF25-VPGVG (**22**) and PF50-VPGVG (**23**) showed no transition behaviour when the temperature increased in the range 20-100°C. PF75-GVPGVG (**25**) and PF75-GABA(VPGVG) (**26**) were designed and synthesised because they provided linkers between the backbone and side-chains which enable possible occurrence of polymer behaviour. The LCSTs of PF75-GVPGVG (**25**) and PF75-GABA(VPGVG) (**26**) are generally above 60°C even when the salt effect has been considered. In order to

obtain a lower transition temperature, PF100-GVPGVG (**28**) and PF100-GABA(VPGVG) (**29**) were synthesised and their transition temperatures were measured as 49°C and 47°C. The polymers were dissolved in a phosphate buffer of pH 7.4 and at a concentration of 1 mg mL^{-1}. Due to its higher molecular weight, PF100-GABA(VPGVG) (**29**) has been shown to have the lowest LCST as shown in **Figure 2.46**. The turbidity change of its solution in a small vial when the temperature increased and decreased can be seen visually. Upon heating to 40°C, the solution of PF100-GABA(VPGVG) (**29**) exhibited coacervation as the colour changed from transparent to cloudy white. This coacervation process is reversible, when the temperature is cooled down to below the T_t, it become soluble again.

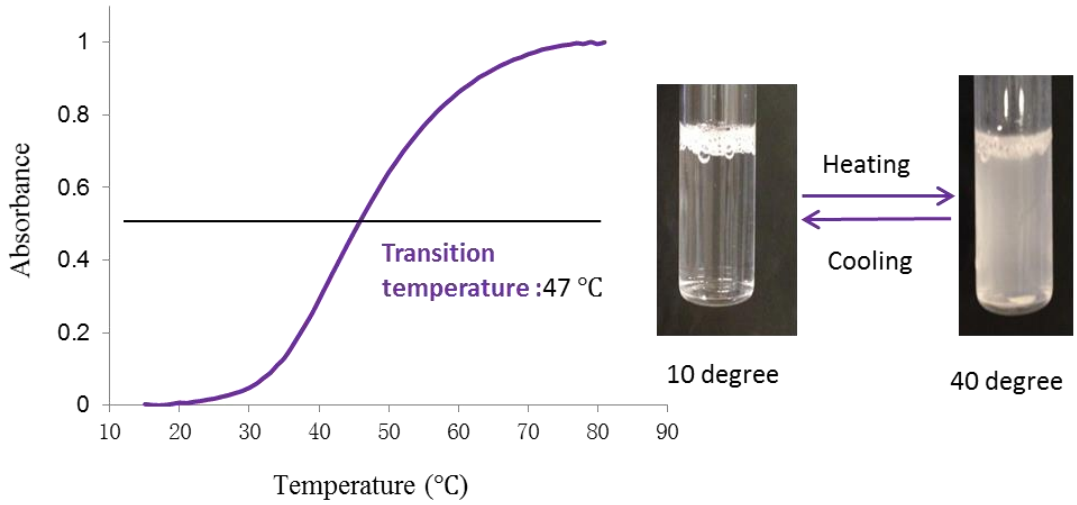

Figure 2.46: Turbidity measurements of PF100-GABA(VPGVG) (**29**) (1 mg mL^{-1}) in PBS solution at pH 7.4 as observed by UV-Vis absorbance at 300 nm. Visual turbidity change of **29** when temperature changes.

2.5.2 CD analysis of elastin-based side chain polymers

As discussed in **Section 2.5.1.4**, PF100-GABA(VPGVG) (**29**) has the lowest transition temperature (47°C) among the elastin-based side chain polymers prepared. Here, we will discuss a secondary structure study of **29**. In **Figure 2.47**, the temperature dependence CD spectra of **29** in PBS buffer with a concentration of 0.2 mg mL^{-1} were demonstrated. The spectra were obtained from 10°C to 50°C. Compared to the spectra of short elastin like peptide, the trend of MRE at 198 nm, 208 and 222 nm is almost the same.

Also at the lowest temperature (10°C), the spectra had a much smaller negative peak at 198 nm compared to peptide **10** and **11**, which means ESP **29** had a much less random coil structure at 10°C. With increasing temperature, the spectra exhibited a more obvious increase in MRE at 198 nm and 208 nm, which are signatures of β-turn formation.[45] The conformational change from random coil to β-turn occurred smoothly over a temperature range of 10°C to 50°C. Also there is a decreasing signal at 222 nm when the temperature was increased, which represents type I/III β-turn of polypeptides. The trends discussed above are indications of a structure change from a less-ordered state toward a β-turn ordered secondary structure. In **Figure 2.48**, the MRE increased slowly with increasing temperature at 198 nm. In **Figure 2.49**, the temperature of the CD spectrometer was changed from 20°C to 50°C in 3 cycles and the CD signal of **29** at 198 nm was measured. The data showed the reversibility of **29** under thermal conditions.

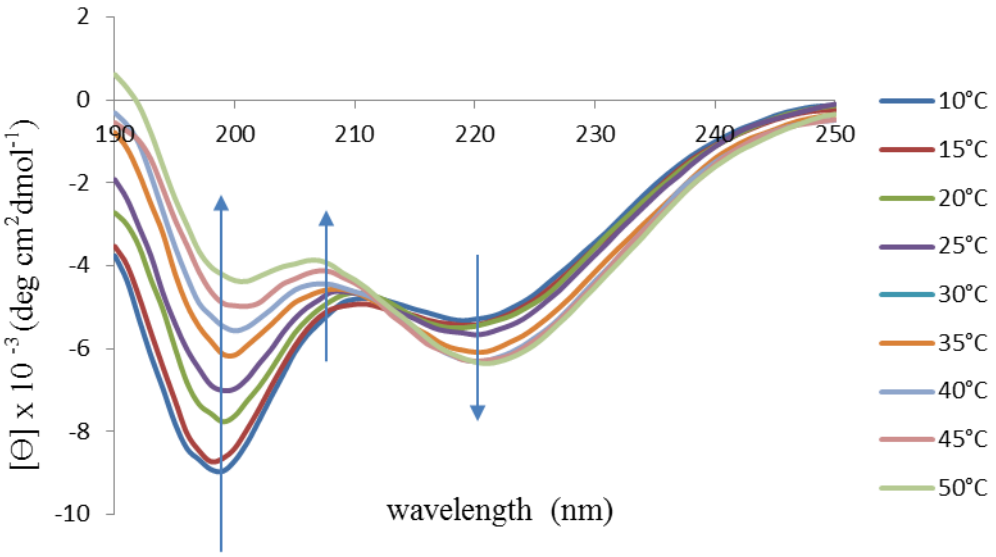

Figure 2.47: Temperature dependence CD spectra of **29** (0.2 mg mL^{-1}) in PBS buffer at pH 7.4 between 10°C and 50°C.

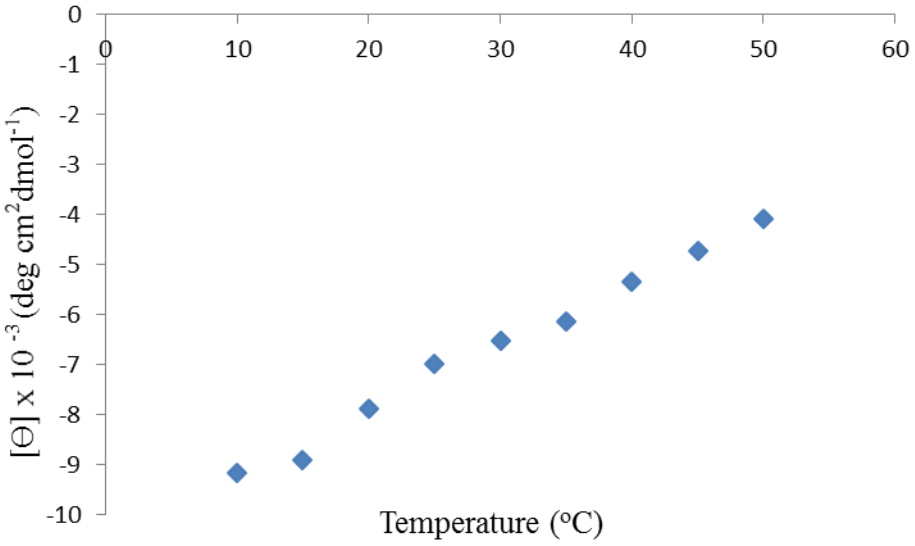

Figure 2.48: Temperature profile of $[\theta]_{198}$ values for **29** (0.2 mg mL^{-1}) in PBS buffer at pH 7.4 between 10°C and 50°C.

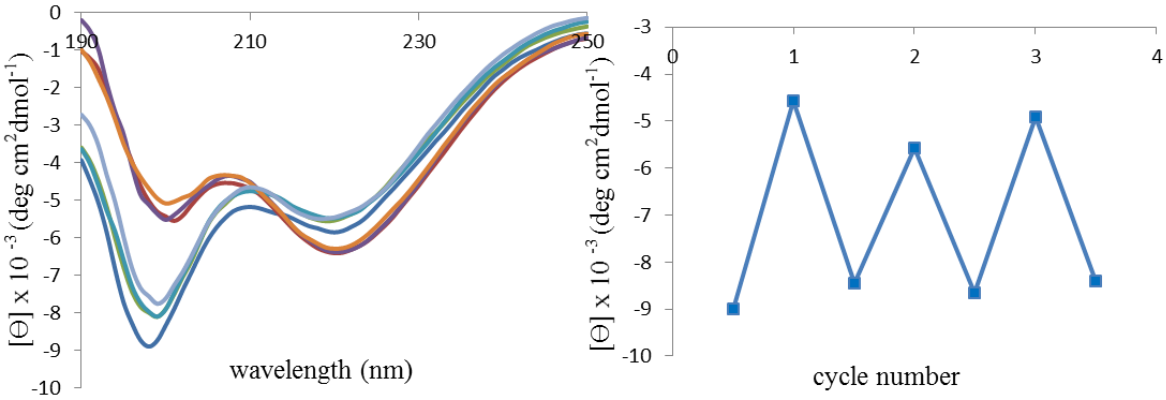

Figure 2.49: The CD spectra and the CD signal at 198 nm of **29** (0.2 mg mL^{-1}) in PBS buffer at pH 7.4 when alternating the temperatures 3 times between 20°C and 50°C.

2.6 Conclusions

We synthesised and studied short elastin-like peptides with different end groups. A solid phase peptide synthesis approach was applied and Rink Amide resin was used. Under normal physiological conditions, the short ELPs prepared are soluble in aqueous solution, but as the solution temperature is raised, they become insoluble and aggregate at a critical temperature, termed the transition temperature (T_t). The turbidimetry data of all the short elastin-like peptides showed that only peptide **10** (*N*-acetylated VPGVG) has a transition temperature (45°C) close to the ideal one (38-42°C) at pH=7.

In addition, the secondary structure of peptide **10** was found to change from random coil to a mixture of α-helix and β-turn structures when the temperature was gradually increased. The same trend was also observed with peptide **11** which has a thiol end. According to the experimental results, these stimuli-responsive short ELPs have the same properties as regular ELPs, while providing a simple and rapid synthesis method.

We used the reversible addition fragmentation chain transfer (RAFT) technique to polymerize pentafluorophenyl acrylate (PFPA) in the presence of benzyl 2-hydroxyethyl carbonotrithioate as a RAFT agent. We synthesised four polymers with different chain lengths. Different molecular weights of polyPFPA (**16**-**19**) were precipitated in methanol to be purified and then be characterized by THF GPC, NMR and FT-IR. Poly(PFPA)s were subsequently modified by attachment of short elastin-like peptides (**9**, **20**-**21**) and conversion of the terminal trithiocarbonate moiety into a thiol. We described the influence of the length of the side chain and salt concentration on LCST behaviour. Among all the elastin-based side chain polymers, ESP **29** has been proven to have the lowest transition temperature (47^{o}C) due to the highest molecular weight.

Furthermore, both short elastin-like peptide and ESPs are suitable for sequence modification and derivatisation. In the next chapter, short peptide **11** and elastin-based polymer **29** will be applied as capping ligands to make hybrid systems with metal and anti-cancer drugs which can be used in cancer therapy.

2.7 References

1. M. M. Bashir, Z. Indik, H. Yeh, N. Ornstein-Goldstein, J. C. Rosenbloom, W. Abrams, M. Fazio, J. Uitto and J. Rosenbloom, *J. Biol. Chem.*, 1989, **264**, 8887-8891.
2. W. F. Daamen, J. H. Veerkamp, J. C. M. Van Hest and T. H. Van Kuppevelt, *Biomaterials*, 2007, **28**, 4378-4398.
3. D. W. Urry, *J. Protein Chem.*, 1984, **3**, 403-436.
4. D. Meyer and A. Chilkoti, *Biomacromolecules*, 2002, **3**, 357-367.
5. D. Urry, *Angew. Chem. Int. Ed. Engl.*, 1993, **32**, 819-841.
6. D. W. Urry, *Prog. Biophys. Mol. Biol.*, 1992, **57**, 23-57.
7. D. W. Urry, R. G. Shaw and K. U. Prasad, *Biochem. Biophys. Res. Commun.*, 1985, **130**, 50-57.
8. B. Vrhovski, S. Jensen and A. S. Weiss, *Eur. J. Biochem.*, 1997, **250**, 92-98.
9. D. W. Urry, T. M. Parker, M. C. Reid and D. C. Gowda, *J. Bioact. Compat. Polym.*, 1991, **6**, 263-282.
10. D. Meyer and A. Chilkoti, *Biomacromolecules*, 2004, **5**, 846-851.

11. D. W. Urry, *J. Phys. Chem. B*, 1997, **101**, 11007-11028.
12. D. W. Urry, S. Peng and T. Parker, *J. Am. Chem. Soc.*, 1993, **115**, 7509-7510.
13. J. van Hest and D. Tirrell, *Chem. Commun.*, 2001, 1897-1904.
14. T. A. T. Lee, A. Cooper, R. P. Apkarian and V. P. Conticello, *Adv. Mater.*, 2000, **12**, 1105-1110.
15. J. Kostal, A. Mulchandani and W. Chen, *Macromolecules*, 2001, **34**, 2257-2261.
16. D. T. McPherson, C. Morrow, D. S. Minehan, J. Wu, E. Hunter and D. W. Urry, *Biotechnol. Prog.*, 1992, **8**, 347-352.
17. R. Schipperus, R. L. M. Teeuwen, M. W. T. Werten, G. Eggink and F. A. de Wolf, *Appl. Microbiol. Biotechnol.*, 2009, **85**, 293-301.
18. D. Meyer and A. Chilkoti, *Nat. Biotechnol.*, 1999, **17**, 1112-1115.
19. R. Merrifield, *J. Am. Chem. Soc.*, 1963, **85**, 2149-2154.
20. J. Neimark and J. Briand, *J. Pept. Res.*, 1993, **6**, 219.
21. W. Chan and P. White, *Fmoc Solid Phase Peptide Synthesis*, Oxford Univeristy Press, New york, 2000.
22. J. Lutz, *J. Polym. Sci. A Polym. Chem.*, 2008, **46**, 3459-3470.
23. W. Liu, M. R. Dreher, D. Y. Furgeson, K. V. Peixoto, H. Yuan, M. R. Zalutsky and A. Chilkoti, *J. Control. Release*, 2006, **116**, 170-178.
24. Y. Matsumura and H. Maeda, *Cancer Res.* 1986, **46**, 6387-6392.
25. K. Engin, D. B. Leeper, L. Tupchong and F. M. Waterman, *Clin. Cancer Res.*, 1995, **1**, 139-145.
26. K. Engin, *Control. Clin. Trials*, 1996, **17**, 316-342.
27. M. R. Dreher, A. J. Simnick, K. Fischer, R. J. Smith, A. Patel, M. Schmidt and A. Chilkoti, *J. Am. Chem. Soc.*, 2008, **130**, 687-694.
28. A. J. Simnick, C. A. Valencia, R. Liu and A. Chilkoti, *ACS Nano*, 2010, **4**, 2217-2227.
29. D. E. Meyer, B. C. Shin, G. A. Kong, M. W. Dewhirst and A. Chilkoti, *J. Control. Res.*, 2001, **74**, 213-224.
30. D. E. Meyer, G. A. Kong, M. W. Dewhirst, M. R. Zalutsky and A. Chilkoti, *Cancer Res.*, 2001, **61**, 1548-1554.
31. D. Raucher and A. Chilkoti, *Cancer Res.*, 2001, **61**, 7163-7170.
32. J. A. MacKay, M. Chen, J. R. McDaniel, W. Liu, A. J. Simnick and A. Chilkoti, *Nat. Mater.*, 2009, **8**, 993-999.
33. W. Liu, J. A. MacKay, M. R. Dreher, M. Chen, J. R. McDaniel, A. J. Simnick, D. J. Callahan, M. R. Zalutsky and A. Chilkoti, *J. Control. Release*, 2010, **144**, 2-9.
34. J. R. McDaniel, D. J. Callahan and A. Chilkoti, *Adv. Drug Deliv. Rev.*, 2010, **62**, 1456-1467.
35. V. P. Torchilin, F. Zhou and L. Huang, *J. Liposome Res.*, 1993, **3**, 201-255.
36. S. Provencher and J. Gloeckner, *Biochemistry*, 1981, **20**, 33-37.
37. J. Otvos, *Neuropeptide Protocols*, 1997, **73**, 153-161.
38. H. Reiersen, A. R. Clarke and A. R. Rees, *J. Mol. Biol.*, 1998, **283**, 255-264.
39. M. Eberhardt and P. Théato, *Macromol. Rapid Commun.*, 2005, **26**, 1488-1493.
40. C. Boyer and T. P. Davis, *Chem. Commun.*, 2009, 6029-6031.
41. C. Barner-Kowollik, *Handbook of RAFT polymerization*, John Wiley & Sons, 2008.
42. F. Fernandez-Trillo, J. C. van Hest, J. C. Thies, T. Michon, R. Weberskirch and N. R. Cameron, *Chem. Commun.*, 2008, 2230-2232.
43. L. Ayres, K. Koch and J. C. M. van Hest, *Macromolecules*, 2005, **38**, 1699-1704.

44. Y. Cho, Y. Zhang, T. Christensen, L. B. Sagle, A. Chilkoti and P. S. Cremer, *J. Phys. Chem. B*, 2008, **112**, 13765-13771.
45. Z. Ahmed, J. P. Scaffidi and S. A. Asher, *Biopolymers*, 2009, **91**, 52-60.

Chapter 3: Peptide-functionalised Gold Nanoparticles

3.1 Introduction

Colloidal gold solutions have been known and used, since ancient times, for staining glass and colouring ceramics, and in the 20th century, gold nanoparticles (GNPs) have been extensively studied due to their size dependent electronic and optical properties.[1, 2] GNPs can be easily functionalized with biomolecules which contain thiols, amines, or even phosphine moieties.[3, 4] The most common approach is to functionalize the GNPs with thiol containing molecules. Using this method it has been possible to synthesise novel hybrid materials consisting of combinations of GNPs and proteins (or peptides). The peptides and proteins utilised in these systems can fulfil different roles, acting as drug carriers, anti-cancer drugs and even cellular-targeting moieties.[5, 6]

In the last decade, a variety of peptide functionalized GNPs has been synthesised and applied in bio-detection, targeted drug delivery, cellular uptake studies, etc.[7-10] Adding peptides to citrate-capped GNPs, sometimes can produce highly stable peptide-capped nanoparticles even in an aqueous buffer, and sometimes these can result in the formation of aggregates. The ability to assemble/disassemble GNPs can be modulated by changing the peptide sequence. For example, pH-responsive peptides can change conformation in response to changes in their local environment and this can lead to aggregation of GNPs which will itself gives rise to a visual colour change. [11]

3.1.1 Gold nanoparticles (GNPs)

Colloidal gold is a suspension of nanometer-sized particles of gold in a continuous phase, usually water. The optical property of colloidal gold was not truly evaluated until Michael Faraday's work in the 1850s. In 1857 Faraday prepared the first sample of colloidal gold by using phosphorus to reduce a solution of gold chloride, which he called 'activated gold'. He investigated the relations of thin films prepared from dried colloidal solutions to light and observed reversible colour changes of the films upon pressurizing.[12] In the 20th century, various methods for the preparation of gold colloids were studied and reported.[13, 14]

GNPs are among the most stable metal nanoparticles, and they have shown fascinating properties such as size-related electronic, magnetic and optical properties. Therefore, they have been extensively investigated and applied in catalysis and biology.[15, 16]

In the early 1950s Turkevich developed an approach for the synthesis of GNPs.[17] This approach involved the reduction of hydrogen tetrachloroaurate (III) $HauCl_4$ in water by a reducing agent/stabilising ligand, such as sodium citrate.[13] Using this process, GNPs with a size ca. 20nm can be prepared. Later, in 1973 Frens improved this method and obtained GNPs with a more controlled diameter (between 16 and 147 nm).[14] In this approach the trisodium citrate to gold ratio controls the size of the GNPs. The higher the ratio, the smaller the particle size. However, the aforementioned method is not good at controlling polydispersity, which also tends to increase with particle size.

3.1.2 Preparation of peptide functionalised GNPs

Generally, a colloidal gold solution is produced by the aforementioned Turkevich-Frens approach as it is the simplest one to produce citrate capped nanoparticles.[17,14] The citrate-GNPs can be further functionalized with different peptides to improve stability. There are three main approaches to preparing peptide-functionalized GNPs: (1) ligand exchange, (2) chemical reduction, and (3) chemical conjugation.

3.1.2.1 Ligand exchange method

The ligand exchange method is the most common approach used to prepare peptide-GNPs. This method essentially involves displacement of one ligand for another[18, 19] and it was first explored by Hostetler *et al.*[18] who attempted to replace simple thiol ligands on GNPs with more complex thiols. The ligand exchange method has been successfully used to synthesise a range of GNPs capped with cysteine-terminated peptides. For example, tetra-chloroaurate ions ($AuCl_4^-$) are firstly reduced by sodium citrate and citric acid to give citrate-stabilized GNPs. In the presence of Cys-terminal peptides the citrate-stabilized GNPs undergo ligand exchange to give peptide functionalized GNPs.[20,21] This reaction proceeds due to the fact that the cysteine containing peptides have a stronger interaction with GNPs compared to the citrate ions. The sulfur-gold bond has a strength of approximately 210 kJ mol^{-1}.[22] This ligand exchange method is very useful when the desired thiol ligand is valuable or not compatible with the reductive environment. A single thiol group can be already quite

strong as a binding ligand to a gold surface, however in some complex systems, multiple thiols may be desired if higher chemical stability is required. For example, Lin *et al.*[23] reported a two-step method to attach neutral and positively charged thiols onto the gold surface. The scheme is shown in **Figure 3.1**. The first step is to reduce tetrachloroauric acid by sodium citrate and then replace the citrate and chloride by thioctic acid (TA). The second step is to replace TA by thiols containing the functional groups. Through the two-step approach, stable GNPs can be functionalized by positively charged thiols.

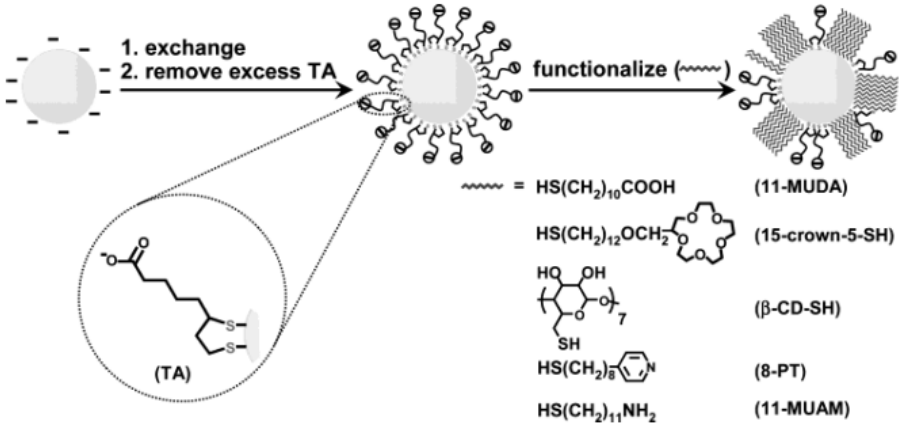

Figure 3.1: Illustration of the two-step method to attach thiols to the surface of GNPs. Reproduced from[23] with permission from American Chemical Society, copyright © 2004.

3.1.2.2 Chemical reduction

In 2005, Bhattacharjee *et al.*[24] reported an approach to prepare colloidal GNP-tripeptides through an *in situ* tyrosine reduction technique. The designed tripeptide sequence was H_2N-Leu-Aib-Tyr-Ome, and tyrosine acts as an electron-transfer agent.[25] The tyrosine at the C-terminus can reduce $AuCl_4^-$ to Au^0, and the free amine at the N-terminus of the tripeptide can attach to the gold surface resulting in a colloid suspension. The size of the tripeptide-GNPs prepared via this approach was relatively small, around 8.7 nm. However, when excess tri-peptides were added to a gold salt solution, the resultant tripeptide-GNPs aggregated due to H-bonding between the terminal NH_2 group and side chains of amino acid residues. Other tyrosine containing peptides have also been used to synthesise peptide-GNPs. For example, the peptide AG_4(NPSSLFRYLPSD) was used to reduce gold ions to GNPs and subsequently form organic-inorganic hybrid spheres.[26] The size of the particles produced was affected by temperature, and higher temperatures were found to decrease the size of the spheres.

3.1.2.3 Chemical conjugation method

Generally, GNPs are formed in aqueous solution and capped by water-soluble stabilizers, such as thiolated derivatives of PEG, glutathione or mercaptosuccinic acid. These stabilizers often have active sites that can be used to bind peptides and other biomolecules. This method of combining peptides to GNPs is known as the chemical conjugation method.

In 2009, Xie *et al.*[27] showed that nuclear localization signal (NLS) peptide functionalized-GNPs can be used as a nuclear targeting nanoprobe. As shown in **Figure 3.2**, the nanoparticles were first modified by 11-mercaptoundecanoic acid (11-MUA), the NLS peptide was then connected to the modified GNPs by carbodiimide-mediated coupling. Later in 2011, Bartczak and co-workers[28] developed a one-pot synthesis method using EDC/sulfo-NHS (*N*-hydroxy sulfosuccinimide) coupling. Using this approach the peptide KPQPRPLS was conjugated to carboxy-terminated oligoethylene glycol gold nanoparticles (OEG NPs) via EDC/sulfo-NHS coupling. The degree of peptide coupling was affected by experimental parameters, such as reaction time, concentration of reagent and the morphology of the nanocrystal.

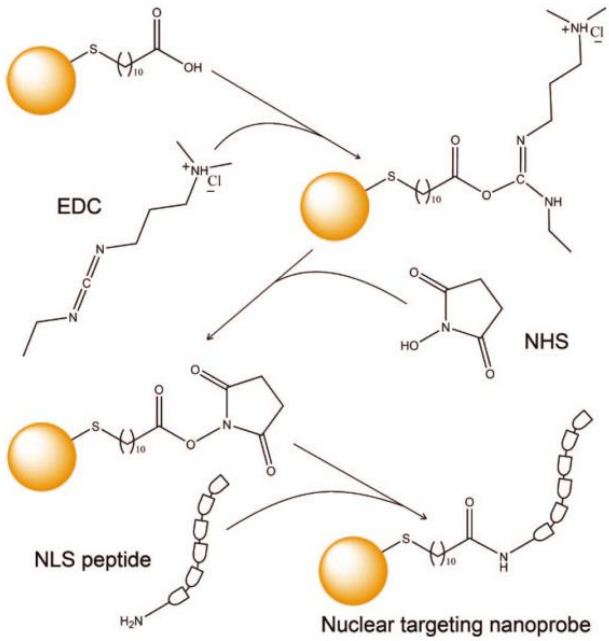

Figure 3.2: Preparation of the nuclear targeting nanoprobe. Reproduced from[27] with permission from American Chemical Society, copyright © 2009.

3.1.3 Applications of peptide functionalised GNPs

3.1.3.1 Plasmonic biosensors

As discussed peptide-functionalized GNPs have unique optical and electrical properties and their assembly can be triggered by changes in their local environment. Increasingly studies have been performed to apply these properties in the detection of metal ions, enzymes and antibodies.

For example the application of functionalised GNPs in the detection of heavy metal ions, several studies have appeared in the literature since 2007. Si *et al.*[29] developed the first peptide-functionalized GNPs to detect Hg^{2+} ions in solution. In this work the peptide-GNPs were synthesised by using the tripeptide H_2N-Leu-Aib-Tyr-Ome to reduce tetra-chloroaurate ions ($AuCl_4^-$). The UV-Vis spectrum of the peptide-GNPs solution showed an absorbance peak at 527 nm, but after adding Hg^{2+} ions, the surface plasmon resonance (SPR) showed another peak at wavelength ca. 670 nm. As shown in **Figure 3.3**, the colour of the solution also changed from red to purple. When the alkaline EDTA solution was added, the purple colour turned back to red. This method can detect Hg^{2+} ions in solution at above 4 ppm, either by the naked eye or UV-Vis spectroscopy.

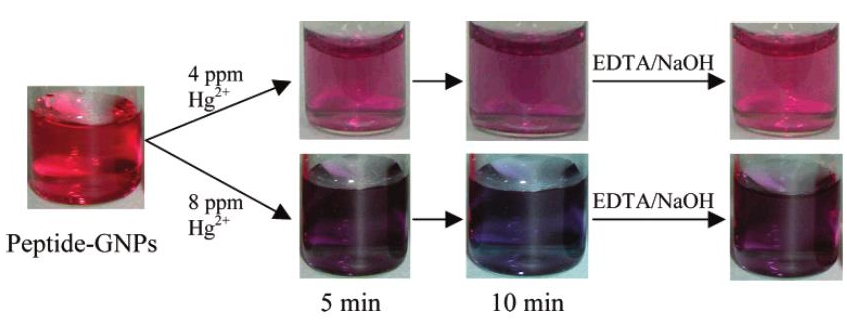

Figure 3.3: The colour change of peptide-GNPs solution in response to Hg^{2+} ions. Reprinted from [29] with permission from American Chemical Society, copyright © 2007.

In 2012, Saxena *et al.*[30] discovered a novel approach to detect bluetongue virus (BTV) specific antibodies based on multiple antigenic peptide (MAP) functionalized-GNPs. In this work, the antigenic BTV peptide was designed based on the region of VP7 protein which has specific cross reaction with BTV strains. VP7 protein of the BTV was chosen as the antigen because the protein shows high sequence homology among the serotypes.

The GNPs were decorated with antigenic BTV peptides in a format with a cystine core and four BTV arms linked through Di-Fmoc-Lys, to amplify the sensitivity. When GNPs labeled with MAP met the specific BTV antibodies, they became aggregated resulting in a colour change from pink to violet. This novel approch using MAP fuctionalized GNPs has the advantage of minimizing the risk of infectious organisms and highly specific targeting to BTV antibodies at the same time.

In 2014, Chandrawati *et al.*[31] demonstrated a label-free detection for blood coagulation factor XIII activity based on the optical and electronic properties of GNPs. Factor XIII is active in the presence of thrombin and Ca^{2+} and it catalyses the formation of a covalent amide bond between the side chains of the amino acid residues Gln and Lys. GNPs were functionalized separately with two different peptides, Cys-Ala-Leu-Asn-Asn-Gly-Gln-Gly (CALNNGQG) and Cys-Ala-Leu-Asn-Asn-Gly-Lys-Gly (CALNNGKG). If factor XIII is present the Gln-Lys bond forms an intermolecular crosslinking between the two types of GNPs and aggregation occurs. A red shift of the surface plasmon resonance (SPR) absorption band confirmed the aggregation and a solution colour change from red to blue was observed (**Figure 3.4**). The concentration of Factor XIII produced a linear relationship with the difference of the maximum absorbance peak ($\Delta\lambda_{max}$) and the concentration limit was down to 0.01U mL^{-1}.This provides a label-free and very sensitive approach to detect the activity of Factor XIII.

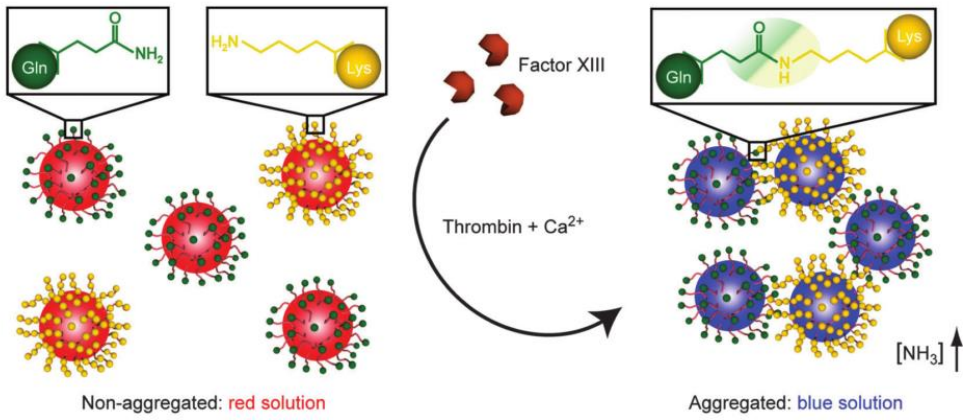

Figure 3.4: Schematic illustration of label-free detection of blood coagulation Factor XIII activity based on controlled assembly of peptide-functionalized GNPs. Reproduced from [31] with permission from Royal Society of Chemistry, copyright © 2014.

3.1.3.2 Targeted drug delivery and cellular uptake

In recent years, peptides have been used in biomedical applications, such as targeting probes, drug carriers and vaccines *etc*., because of their small size, biocompatibility, cell-penetrating ability and easy chemical synthesis and modification.[5, 6] Chan *et al.*[32] studied the uptake of GNPs in HeLa cells and found that particles with diameters between 20-60 nm have the highest cellular uptake. Also, scientists found that some peptides known as CPPs can be even specifically uptaken by certain cellular organelles. In addition, CPPs can be conjugated to an anti-cancer drug and used as a drug carrier. Functionalization of GNPs with CPPs has been developed with the aim of improving the efficiency of live cell uptake.

In 2005, Fuente and Berry[33] attached the cell pepetrating peptide Tat to GNPs in order to develop a system that was able to target the cell nucleus. The GNPs were firstly synthesised by reduction of $AuCl_4^-$ solution in the presence of tiopronin which has a thiol end group. Secondly, Au@tiopronin acid groups and Tat peptide (GRKKRRQRRR) amine groups were conjugated via EDC/NHS coupling to give Au@Tat nanoparticles (**Figuer 3.5**). This strategy has also been used to develop water-soluble and biocompatible fluorescent quantum dots which can translocate to the nucleus.[34] Human fibroblast cells (HTERT-BJ1) were used to test the biocompatibility of Au@tiopronin and Au@Tat and cell uptake was investigated by TEM. These results indicate that this Tat peptide can transfer the nanoparticles into the cell nucleus. Without peptide functionalization, Au@tiopronin nanoparticles could not penetrate the cell membrane and target the cell nucleus, proving the cell-penetrating ability of Tat peptide. This work has many potential applications in cancer therapy, however, the ratio of Tat/tiopronin on the surface is about 1:50 which is low and makes it hard to quantify Tat loading.

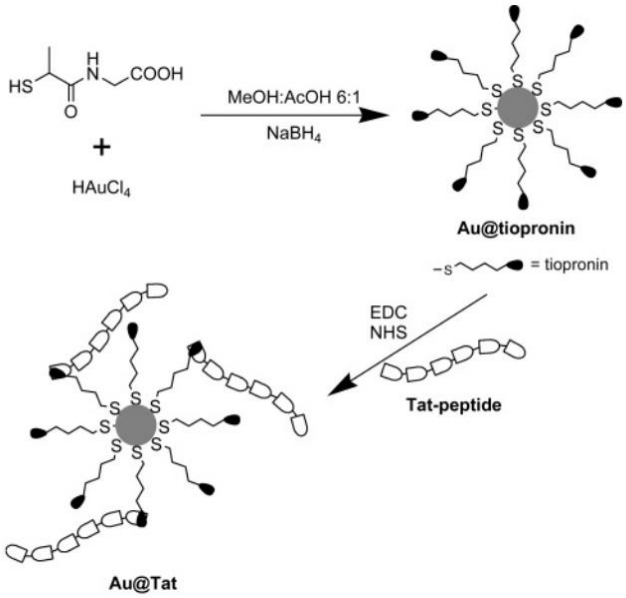

Figure 3.5: Preparation of Au@Tat nanoparticles. Reproduced from [33] with permission from American Chemical Society, copyright © 2005.

Later in 2008, Shukla *et al.*[35] reported the development of a GNP system for targeting tumour vasculature. Arg-Gly-Asp (RGD) peptide-functionalized dendrimer-entrapped GNPs which can be taken up by $\alpha_V\beta_3$ integrin-expressing cell lines were prepared. The $\alpha_V\beta_3$ integrin is an important marker of the neovasculature and is normally found during tumour angiogenesis; without it tumours cannot grow beyond 1-2 mm in size.[36] Au DENPs with a mean diameter of 3.0 nm were synthesised.[37] Human dermal microvessel endothelial cells (HDMEC) and human vascular endothelial cells (HUVEC) were used to examine the binding ability of Au DENPs and confocal microscope results confirmed the internalization of gold in the integrin-expressing cells. Given that the RGD peptide has a high affinity to $\alpha_V\beta_3$ integrin, RGD-functionalized GNPs can be used as a drug carrier system to deliver anti-cancer drugs or pro-apoptotic peptides.[38] However, the interaction between linear RGD peptides and $\alpha_V\beta_3$ integrin is often weak and the utility of individual ligands is limited for efficient tumour targeting. Arosio *et al.*[39] improved this approach by using cyclic peptide cRGD to functionalise GNPs. A short poly (ethylene glycol) (PEG) linker was used as a spacer to combine the cRGD and the GNPs, and to enhance the stability of the nanoparticle system. Experimental results with PC-3 prostate cancer cells showed that cRGD-conjugated GNPs had an enhanced affinity for $\alpha_V\beta_3$ integrin compared with the unconjugated system.

Ghosh *et al.*[40] synthesised GNPs coated with a short peptide that can promote intracellular delivery of the protein β-galactosidase (β-gal). The β-gal protein is known as a membrane impermeable protein with a high molecular weight (465 kDa). This system studied the effect of peptide structure on protein delivery. Here, the design of the peptide functionalized GNPs contained two parts: the alkyl chains and tetraethyl glycol (TEG) which can stabilize the particle and prevent interaction, the exterior peptide sequence His-Lys-Arg-Lys which can facilitate cargo translocation into membrane as shown in **Figure 3.6**. Fluorescein isothiocyanate-labelled β-galactosidase (FITC-β-gal) was used to monitor the cellular delivery of the β-gal protein. The HeLa cells were incubated with GNP-Pep/FITC-β-gal (2:1) complexes for 3 h and green fluorescence was found while when the cells were incubated with FITC-β-gal alone, no green fluorescence was found. Then confocal laser scanning microscope (CLSM) experiments confirmed that the green fluorescence was from inside the cells rather than on the surface of cells. This is a new and efficient strategy for delivering anionic proteins.

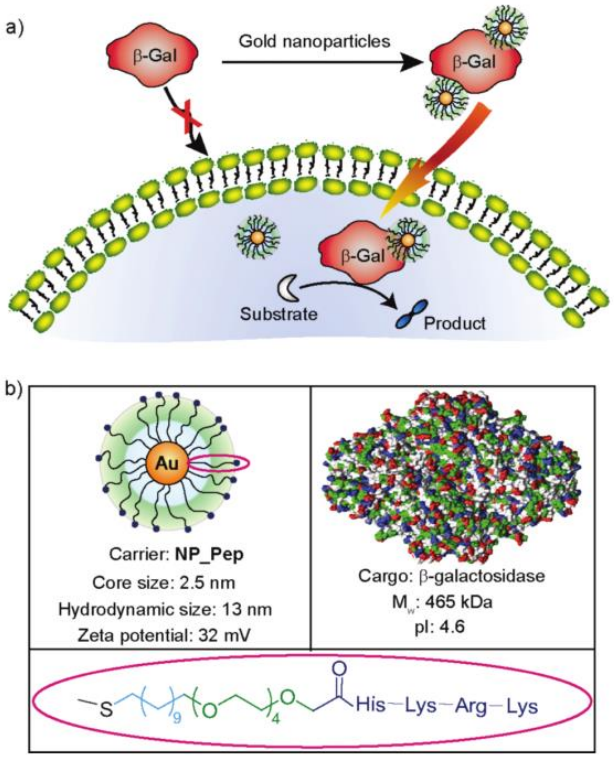

Figure 3.6: (a) Schematic representation of intracellular delivery of functional protein using gold nanoparticles; (b) Structure of the nanoparticle, the protein cargo and the ligand on the particle. Reprinted from [40] with permission from American Chemical Society, copyright © 2010.

3.1.3.3 Anti-cancer applications

A large number of antimicrobial peptides, peptide antibiotics and peptide hormones have been isolated from nature. *In vitro* experiments showed that some peptides have the ability to kill cancer cells and inhibit tumour growth. These anti-cancer peptides can be used as new cancer killing drugs and potential delivery systems have been studied. Functionalization of GNPs with a targeting peptide has been used to deliver the anti-cancer peptide into the specific tumour area.

In 2010, Chanda *et al.*[41] conjugated analogues of the peptide bombesin (BBN) to GNPs. Bombesin is a gastrin-releasing peptide (GRP) and it can specifically target cancer cell receptor sites. It is known that BBN peptides have a high affinity to GRP receptors which are overexpressed in breast, prostate and lung carcinoma. Human prostate tumour PC-3 cells were used to evaluate the GRP receptor binding affinity of BBN-functionalized GNPs. The experimental data of IC_{50} values showed that the higher the degree of BBN peptide on the GNP surface, the higher was the cell binding affinity.

A multi-functionalized GNPs system that contains both a targeting peptide and a therapeutic peptide has also been developed.[42] The RAF peptide can inhibit the protein and signalling kinase Rb-Raf-1 *in vivo* and thus it prevents cell proliferation. GNPs of 20 nm diameter were synthesised by the sodium citrate reduction method,[14] and these were then conjugated with targeting peptide (BBN) and the anti-cancer peptide RAF. The multi-functionalized GNPs were found to penetrate into HeLa cells which overexpress GPRr, while they were not taken up by SHSH-5Y cells which do not overexpress the same receptor (**Figure 3.7**). The mechanism of the selectivity and internalization into HeLa cells is still under investigated.

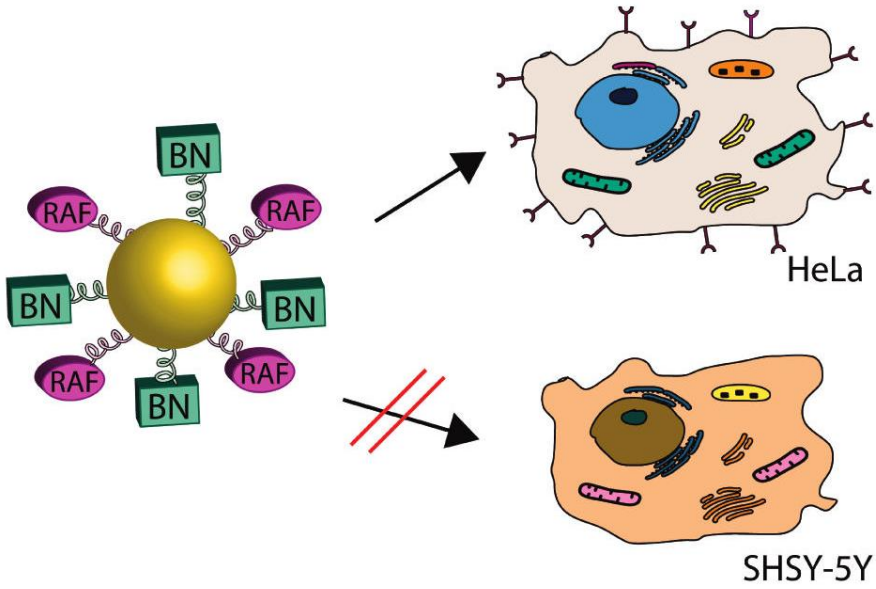

Figure 3.7: Multifunctionalization of GNPs with a targeting peptide (BBN) and an antitumoral Peptide (RAF). Reproduced from [42] with permission from American Chemical Society, copyright © 2010.

In 2012, Kumar *et al.*[43] developed novel small GNPs (2 nm) functionalized with both a therapeutic peptide (p12) and a targeting peptide (CRGDK). The targeting peptide is known to bind selectively to Nrp-1 receptors which are overexpressed in many tumour cells. Through receptor-mediated internalization, targeting peptide-functionalized GNPs can translocate into the cell and the nucleus. At the same time, the therapeutic peptide p12 binds to MDM2 and MDMX proteins leading to the expression of tumour suppressive protein p53, which limits the expression of tumour gene thus causing cell apoptosis.[44] The same GNP synthesis method as is shown in **Figure 3.8** was used, giving small Au@tiopronin to which were added peptide p12, CRGDK and both peptides together. The targeting peptide was shown to advance the cellular uptake of the GNPs with the therapeutic peptide preload, and the system could be applied in drug delivery for cancer therapy.

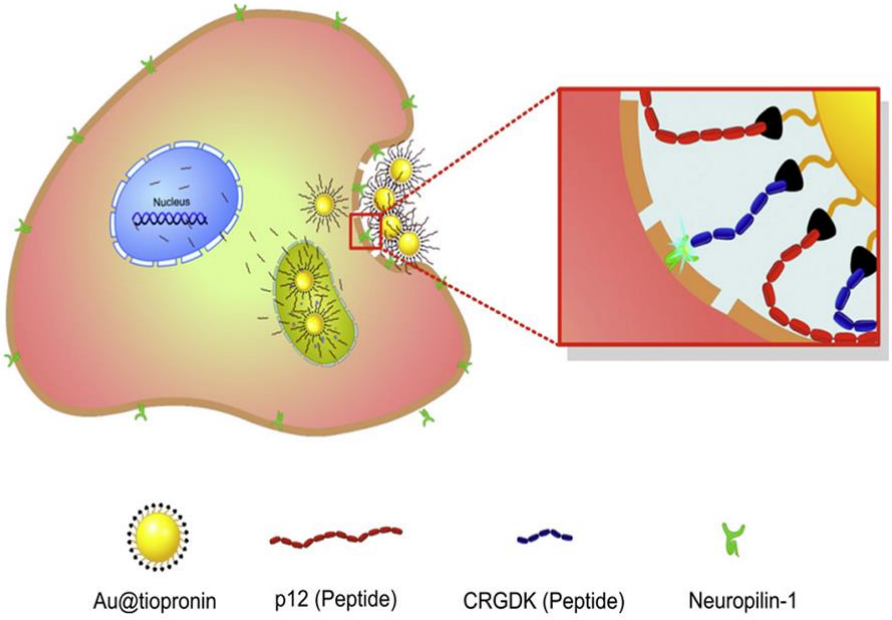

Figure 3.8: Interaction between receptor and targeting ligand enhances intracellular entry and increases response to intracellular release of the therapeutic peptide. Reproduced from[43] with permission from Elsevier, copyright © 2011.

3.1.4 Aim of this chapter

The aim of the work described in this chapter is to synthesise peptide functionalised GNPs which have potential applications in drug delivery and cancer therapy. Elastin-like polypeptides (ELPs) undergo a transition from a hydrophilic random coil to a hydrophobic β-spiral when the temperature is increased.[45] This LCST behaviour is not only displayed by poly(VPGXG), but also was found in a single ELP pentapeptide unit.[46, 47] This behaviour suggests that ELPs are suited for single-molecule and nanoscale applications.

The short pentapaptide VPGVG and elastin-based side chain polymers are both good candidates and have been used to functionalize gold surfaces which endow GNPs with stimuli sensitivities. The transition temperatures of the ELPs in aqueous buffer solution were examined using ultraviolet-visible (UV-Vis) spectroscopy. In addition, the secondary structures of the ELPs-GNPs were studied by circular dichroism (CD). In the second system, we aimed to functionalize GNPs with elastin-based side chain polymer (ESPs) through a "graft-to" strategy. Poly(PFPA) polymers were synthesised and modified by attachment of short elastin-like peptides. The ESPs were attached to the surface of GNPs through formation of gold-thiol bonds. The conformation and

aggregation properties of the ELP-functionalized GNPs in aqueous solution were tested by transmission electron microscopy (TEM), UV-Vis spectroscopy and circular dichroism (CD). In the third system, we aimed to use apoptotic peptide KLA to functionalize GNPs and study their cell toxicity and cellular uptake abilities. In the final system, the aim was to functionalize GNPs with ESPs and KLA in a 1:1 ratio. UV/visible spectroscopy, transmission electron microscopy (TEM) and dynamic light scattering (DLS) were used to observe the morphologies and size distributions of the aforementioned peptide functionalised GNPs.

3.2 Synthesis of GNPs

GNPs were synthesised using the Turkevich and Frens method.[8,9] Sodium citrate was used to reduce Au^{3+} to Au. For GNPs **A** to **E**, the same gold chloride solution was used but different amounts of sodium citrate solution were added to obtain different particle diameters. Changing the relative amounts of reactants changes the relative rates of the processes of nucleation and growth of the metal particles and the more Na_3-citrate used, the smaller the nanoparticles obtained. A standard procedure for obtaining gold colloids was used and the colour change of each solution was observed. At first, the colour of the gold chloride solution was light yellow. Then the solution started to turn dark blue when sodium citrate solution was added. After approximately 1 minute the dark blue colour suddenly changed into light red-purple which indicates the formation of gold nanoparticles (**Table 3.1**).

Table 3.1: Synthesis of GNPs.

Entry	GNPs	Solution II (1 wt% Na-citrate) (mL)	Abs Peak wavelength (nm)	Diameter based on TEM (nm)
1	**A**	2.5	520	15
2	**B**	2.0	524	19
3	**C**	1.5	526	22
4	**D**	1.0	532	28
5	**E**	0.8	538	32

* Solution I concentration: 0.01 wt% $HauCl_4$, 50 mL

As shown in **Figure 3.9** a), the diluted solution of **A** to **E** showed a gradual colour change from bright red to red-purple to purple. A UV/Vis spectrophotometer was also

employed to study the optical properties of the gold nanoparticles. The bright colour of GNPs is attributed to the surface plasmon absorption band, which is very sensitive to the size and shape of the particles. Therefore, GNPs **A** to GNPs **E** have different surface geometries which lead to different electrical densities on the particle surfaces and cause them to oscillate with different frequencies. This is due to the fact that an intrinsic function of metal nanoparticles' morphological features determines their optical properties. Based on this, the absorption spectrum of GNPs can be varied from 520 nm to 1000 nm by changing the geometry of the particle. Also, the size analysis of the GNPs could be performed by visually analysing the colour of the nanoparticle solution. The colour transition from brilliant red to deep purple indicates the formation of larger particles due to surface plasmon resonance (SPR) properties of GNPs. The UV-Vis spectrum of the colloidal solutions **A** to **E** exhibited a red shift of surface plasmon absorption peak from 520 nm to 538 nm, as shown in **Figure 3.9** b). The colour data and UV-Vis data both show that the less Na_3-citrate is used, the larger the nanoparticles.

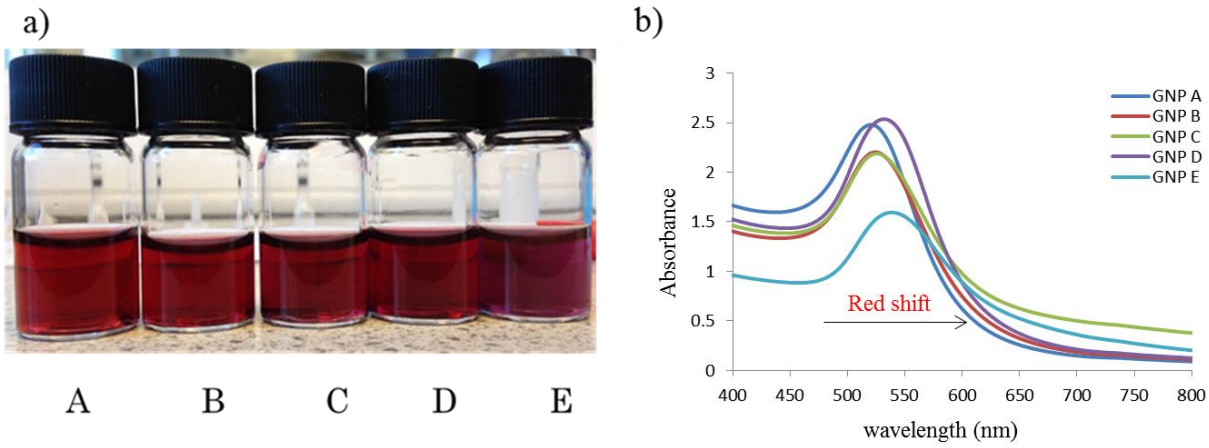

Figure 3.9: (a) The colour of solutions of GNPs **A** to **E**; (b) UV-Vis spectrum of GNPs **A** to **E**.

The sizes of the gold colloids and their morphologies were determined by transmission electron microscopy (TEM), which is the primary technique for determining the particle size, shape and the size distribution. A drop of the GNPs solution was cast on the TEM grid and blotted with tissue in air before performing the TEM measurement. In the next experiment of peptide/polymer-coated gold nanoparticles, we chose the smallest size GNPs **A**. TEM images of sample **A** obtained are shown below. In **Figure 3.10**, the diameter of GNPs in sample **A** was 14.6 ± 2.6 nm. Dynamic light scattering (DLS) was

used to observe the size distribution of GNPs **A**. The mean diameter is 20.7 nm and the polydispersity is 0.314 (**Figure 3.11**).

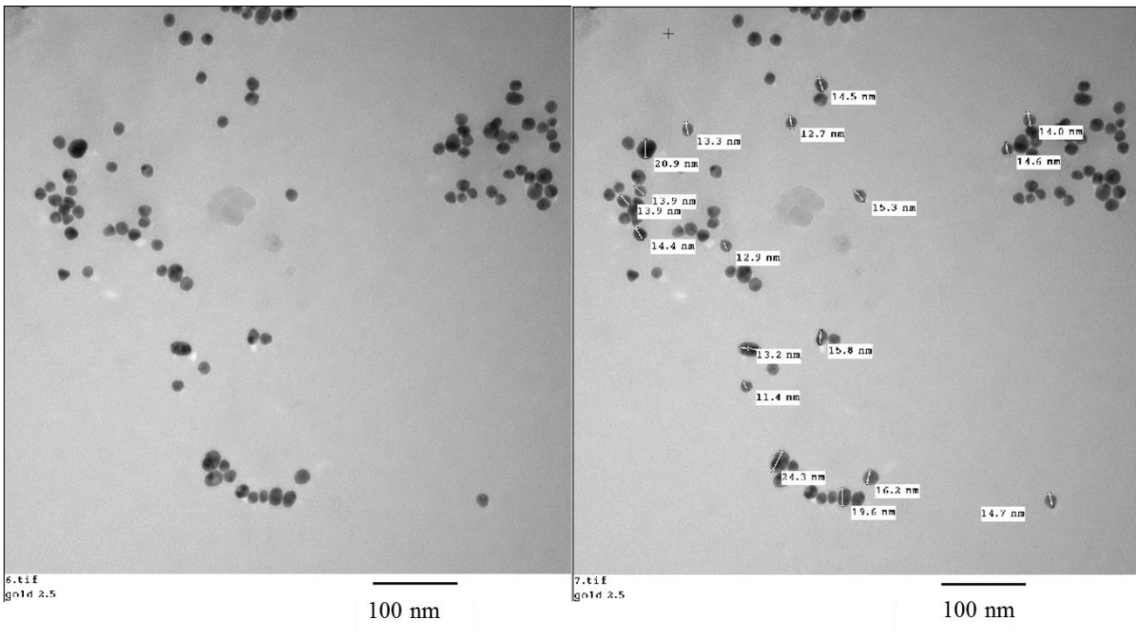

Figure 3.10: TEM images of GNPs **A**: average size is 14.6 ± 2.6 nm.

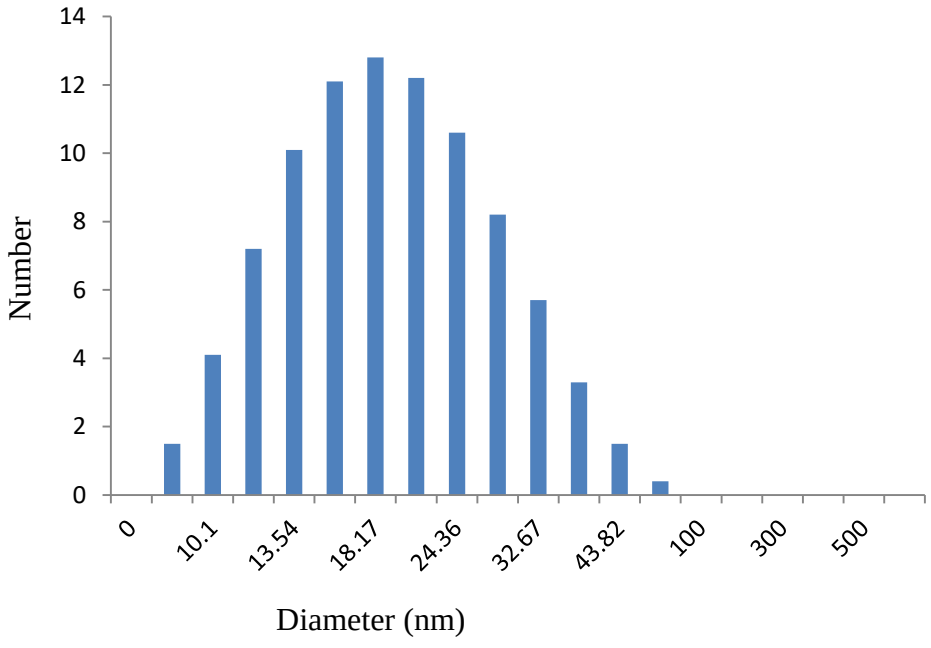

Figure 3.11: DLS traces of GNPs **A**. The average mean diameter is 20.7 nm and the polydispersity is 0.314.

3.3 Preparation and Characterization of Short ELP-GNPs

3.3.1 Synthesis of ELP-GNPs

The preparation of short elastin-like peptide-gold nanoparticle (ELP-GNPs) conjugates employed the covalent bonding interactions between the peptide thiol and the GNPs. First, the GNP solution was stirred in a small round-bottom flask under nitrogen. After one hour, the thiol-peptide (**11**) solution was added into the GNP solution to give a homogeneous mixture (**Figure 3.12**). The reaction was performed under a nitrogen atmosphere to prevent the formation of disulfide bonds.

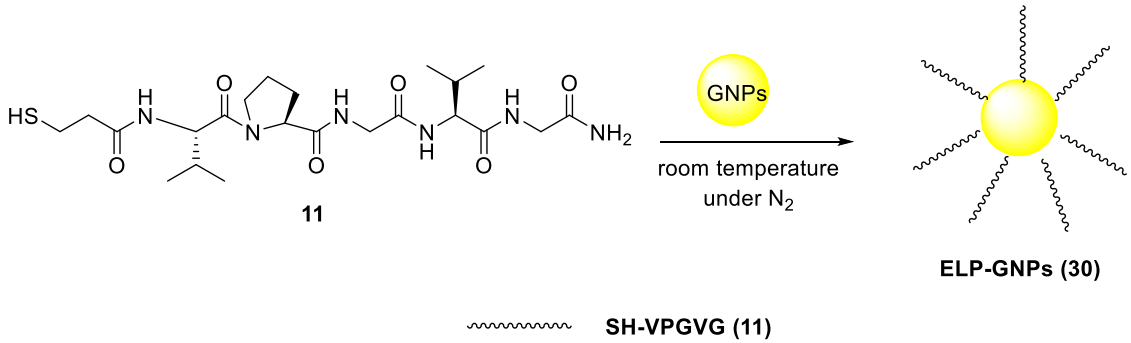

Figure 3.12: The preparation of short elastin-like peptide functionalized gold nanoparticles.

After the reaction, the solution was transferred to a dialysis bag and dialysed against deionised water for 24 hours to remove salts. If this step is omitted, the freeze-dried solution product is a greyish/white powder, which means that the extra salts have not been removed. However, the GNP-peptide obtained after dialysis and freeze drying gave a dark purple solid. This dark purple colour confirms that there are no extra salts present. This solid can be dissolved in water immediately and forms a homogeneous purple solution without precipitation.

3.3.2 Properties of ELP-GNPs

As the ELP-GNPs (**30**) have an amide group at their C-termini, the LCST behaviours were monitored at pH 7.4. Van Hest *et al.*[47] reported short elastin-based stimuli-responsive gold nanoparticles, which have a different end. In their work, Wang resin was used to synthesise the peptide giving a free carboxylic acid at the C-terminus. Only at low pH (pH< 3.6), the free carboxylic acid was protonated and the peptide showed hydrophobic character. The elastin-based gold nanoparticles showed no thermo-sensitive behaviour when the pH was above 3.6 which is the limitation of its

application. In our system, the ELP-GNPs respond to the temperature change rather than the pH change of the solution.

The phase transition behaviour of the ELP-GNPs (**30**) was studied by UV-Visible spectroscopy at a range of temperatures from 10^{o}C to 70 ^{o}C as shown in **Figure 3.13** a). At 10^{o}C, the spectrum of ELP-GNPs exhibited an absorption peak at 527 nm and this did not change significantly when the temperature was increased from 10^{o}C to 40^{o}C. Upon raising the temperature above 40^{o}C, the maximum absorption peak showed a red shift from 528 nm to 532 nm at 70^{o}C. This indicated the aggregation of the GNPs and this was supported by an accompanying colour change from red to purple as shown in **Figure 3.13** b). As a control, solutions of peptide-free GNPs were measured as well when the temperature was increased, and no changes were observed in the UV-Vis spectra. This suggested that the spectral changes of ELP-GNPs are because of the thermo-responsive property of the short elastin-like peptide layer on the surface of GNPs. Raising the temperature of the ELP-GNPs solution, the VPGVG layer underwent an intramolecular hydrophilic-hydrophobic transition which increased the aggregation of the gold colloids. The scheme of ELP-GNPs' reversible aggregation caused by the thermo-triggered phase transition of the VPGVG peptide is shown in **Figure 3.14** a).

Dynamic light scattering (DLS) also offers a good means to monitor the particle aggregation through the increase of scattered light. **Figure 3.14** b) shows the size distribution corresponding to the signal intensity at different temperatures. At 10^{o}C, the main signal of ELP-GNPs gave a diameter of ca.20 nm. When the temperature was increased to 60^{o}C, the main signal peak shifted to a diameter around 100 nm, which indicated aggregation and precipitation events.

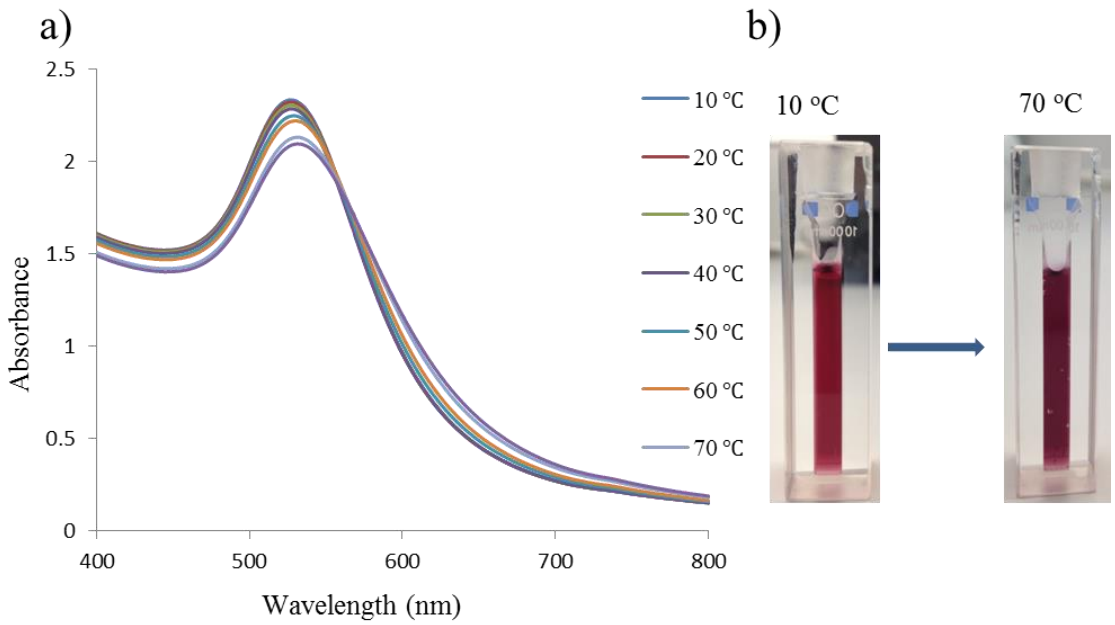

Figure 3.13: (a) Temperature-dependent absorption spectra changes for ELP-GNPs (**30**) (0.5 mg mL^{-1}) in PBS buffer at pH 7.4 from 10°C to 70°C; (b) the colour changes of ELP-GNPs (**30**) caused by the thermally-triggered phase transition of elastin-like peptide: at 10°C the colour is red which shows dispersed gold colloids, at 70°C the aggregation gives a purple colour.

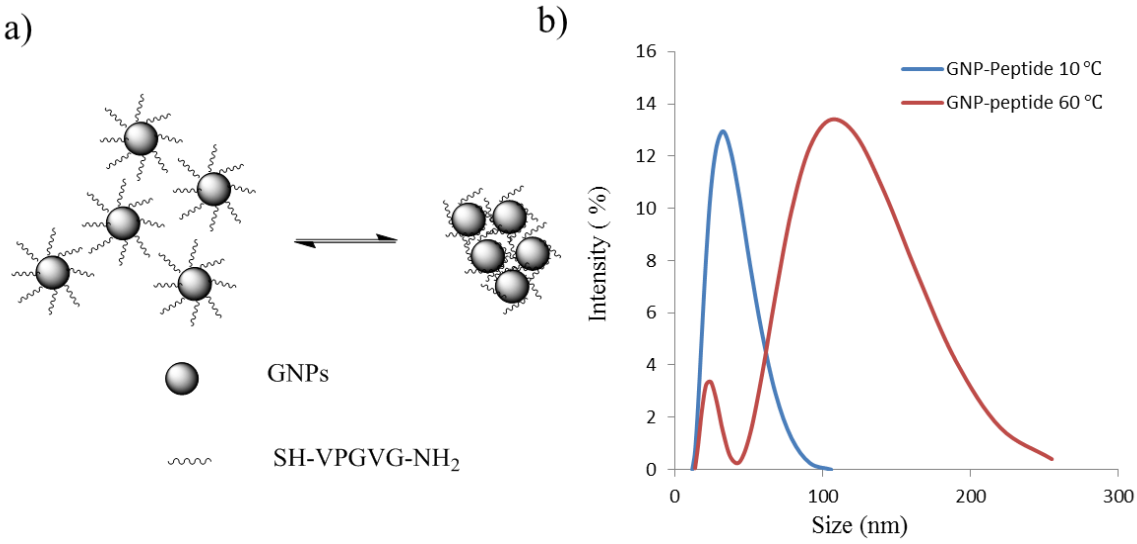

Figure 3.14: **(**a) Schematic diagram of ELP-GNPs (**30**) aggregation when temperature changes; (b) DLS results of ELP-GNPs (**30**) solutions (0.5 mg mL^{-1}, pH 7.4) showing the changes in hydrodynamic diameters of the particles/aggregates at 10°C and 60°C.

Aggregation was also observed using TEM as shown in **Figure 3.15**. The samples were prepared at 20°C and 60°C separately and then TEM images were recorded. The TEM images of GNPs below and above the phase transition temperature gave more direct evidence of ELP-GNPs (**30**) aggregation.

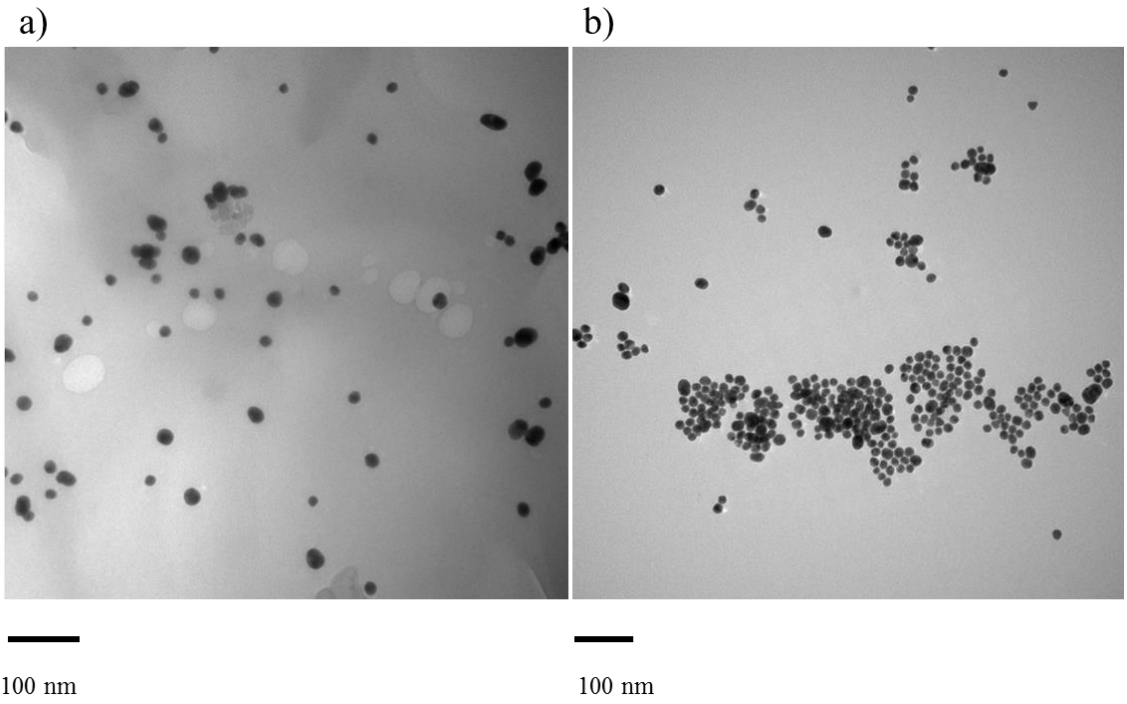

Figure 3.15: Transmission electron microscopy images of the ELP-GNPs at (a) 20^{o}C and (b) 60^{o}C.

The temperature dependencies of the secondary structure of the peptides in ELP-GNPs conjugates in dilute solution (0.2 mg mL^{-1}) were evaluated using CD spectroscopy. The spectra obtained in a PBS buffer (pH 7.4) from 10^{o}C to 70^{o}C and are shown in **Figure 3.16**. ELP-GNPs (**30**) have the same changing trend as peptide **11** shown in **Figure 2.41** (Chapter 2). This indicates that the conformation changes when the temperature increases were led by the property of the peptide conjugated to the GNPs.

At the lowest temperature (10 ^{o}C), the mean residual ellipticity (MRE) was about -7500 deg cm^{2}dmol^{-1} at 195 nm which represents a random coil. The CD peaks at 195 to 200 nm decreased with increasing temperature, with a smaller decrease in amplitude at 206 to 212 nm. With increasing temperature, the molar ellipticity [θ] value at 195 to 200 nm and 206 to 212 nm decreased which supports increasing β-turn content. When the temperature is increased, there also exists a smaller increase in CD amplitudes at 222 nm. This peak is associated with a type I/III β-turn. The data studied here exhibited an increase in MRE at 198 nm and 206 nm with increasing temperature, supporting the folding of the peptide and leading to a β-turn formation. The conformational transition from random coil to β-turn occurred gradually over a wide temperature range from 10^{o}C to 70^{o}C.

The [θ] value which changes at 198 nm was plotted with temperature in **Figure 3.17**. From 10°C to 20°C, no obvious change is observed. From 20°C to 60°C, the value increased gradually and uniformly. Then the value decreased a little when the temperature increased to 70°C. From these data we can conclude that the transition temperature is around 40°C.

In order to test the reversibility of the ELP-GNPs (**30**), a cyclic thermal response experiment was performed by changing temperature between 50°C and 10°C. **Figure 3.18** a) and b) shows the cyclic thermal response of ELP-GNPs (**30**) solutions. CD spectra were acquired at 10°C and 50°C for 5 cycles. After each temperature change, the sample was allowed to equilibrate for 5 min. These data show that the structural changes of the ELP-GNPs (**30**) are reversible and can be induced several times without apparent degradation. They also show that the temperature-induced formation of the β-turn is due to intramolecular interactions rather than intermolecular associations.

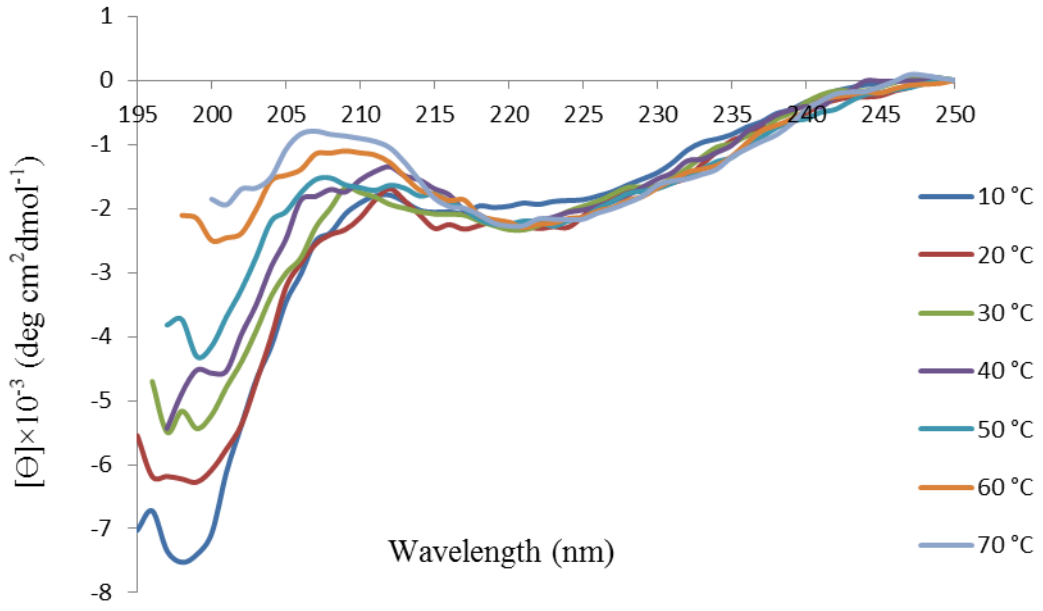

Figure 3.16: Temperature dependence circular dichroism (CD) spectra of ELP-GNPs (**30**) (0.2 mg mL^{-1}) in PBS buffer at pH 7.4 between 10°C and 70°C.

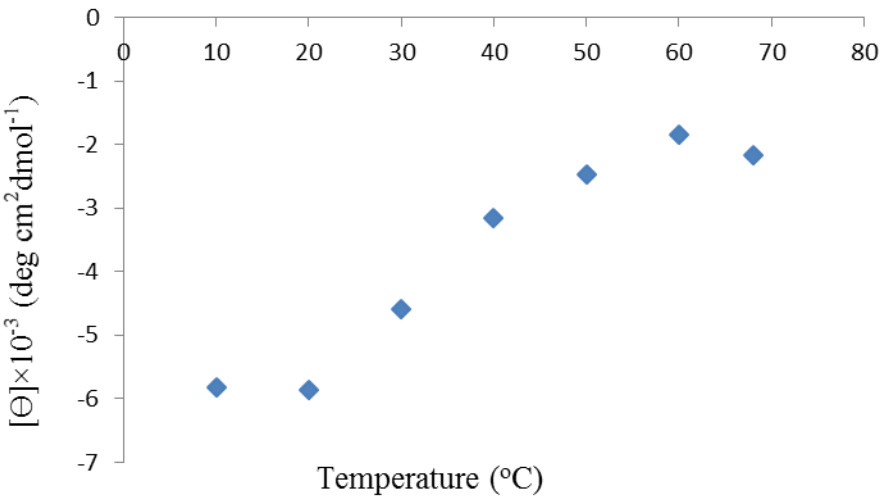

Figure 3.17: Temperature profile of $[\theta]_{198}$ values for ELP-GNPs (**30**) (0.2 mg mL^{-1}) in PBS buffer at pH 7.4 between 10°C and 70°C.

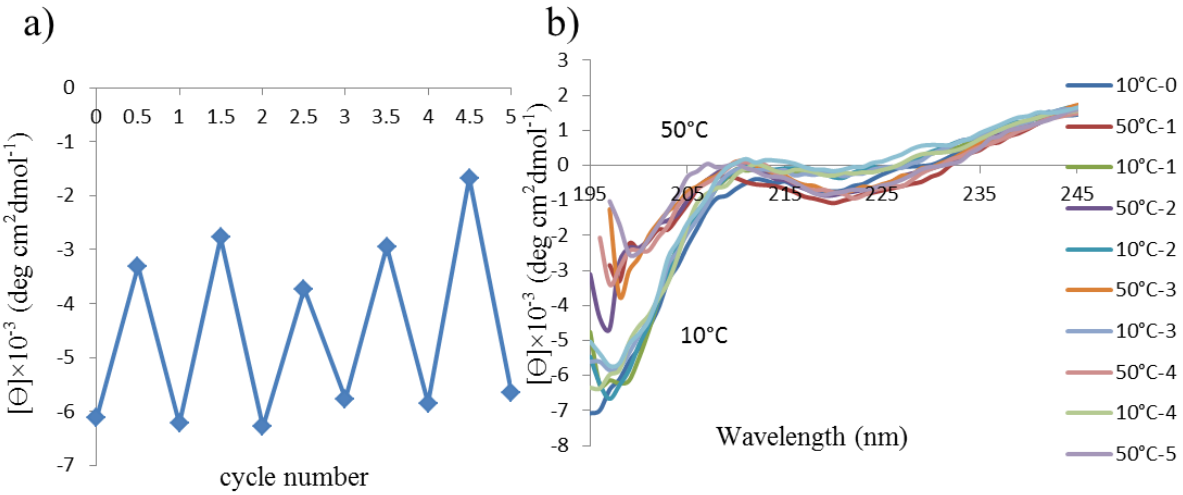

Figure 3.18: (a) The CD signal and (b) the CD spectra at 198 nm of ELP-GNPs (**30**) (0.2 mg mL^{-1}) in PBS buffer at pH 7.4 when alternating the temperature 5 times between 10°C and 50°C.

3.4 Preparation and Characterization of Elastin based side chain polymer-GNPs (ESP-GNPs)

3.4.1 Synthesis of ESP-GNPs

The preparation of elastin-like peptide functionalized polymer-coated GNPs demonstrated the reaction between macromolecular thiols and gold nanoparticles. Two elastin based polymers PF75-GABA(VPGVG) (**26)** and PF100-GABA(VPGVG) (**29)** were used to functionalise GNPs to obtain ESP_{75}-GNPs (**31**) and ESP_{100}-GNPs (**32**). Here, we describe the preparation of **32** as an example.

PF100-GABA(VPGVG) (**29**) was dissolved in 1mL deionized water and then added into 10 mL of the citrate-stablized GNPs solution and left for overnight reaction under a nitrogen atmosphere. The reaction scheme is shown in **Figure 3.19**. Then the ESP_{100}-conjugated GNPs were dialyzed (MWCO=50,000 Da) against distilled water for 3 days to remove any unreacted polymers. The ESP_{100}-GNPs (**32**) were then freeze-dried to obtain a purple fluffy powder. The freeze-dried GNPs/polymer hybrid nanoparticles were easily re-dispersed in water.

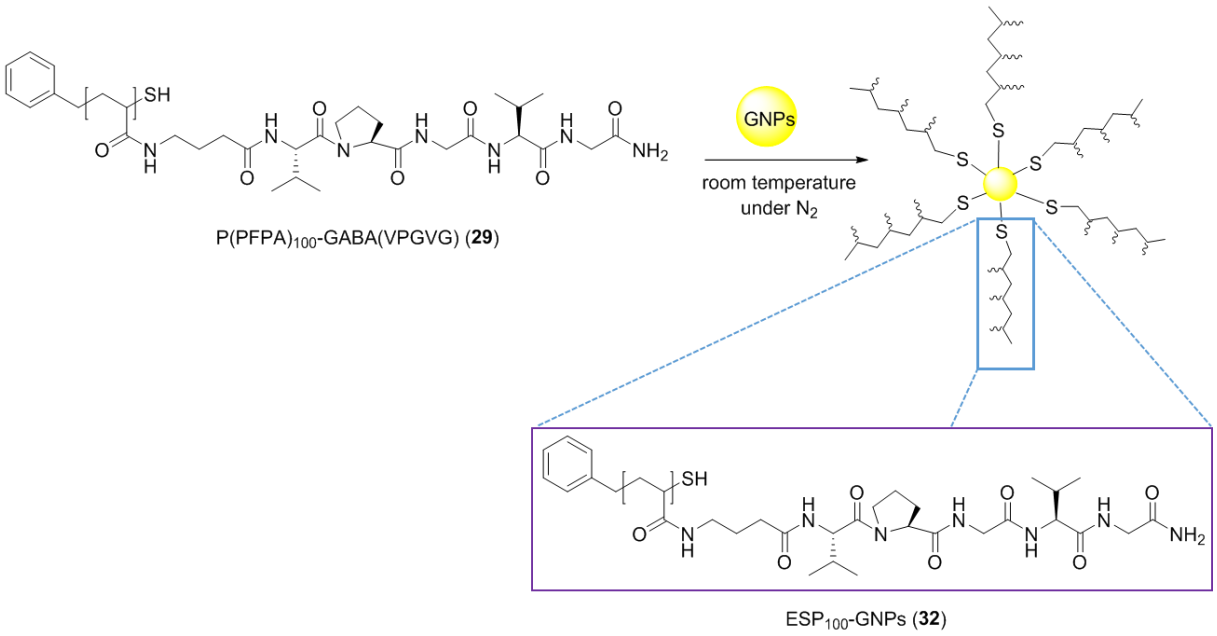

Figure 3.19: The scheme of polymer functionalized GNPs (ESP-GNPs) preparation.

TEM images of ESP_{100}-GNPs (**32**) obtained are shown below. In **Figure 3.20**, the diameter of **32** is 32.74 ± 6.7 nm on average. Dynamic light scattering (DLS) was used

to observe the size distribution of **32**, which is shown in **Figure 3.21**. The average mean diameter is 36.8 nm and the polydispersity is 0.367.

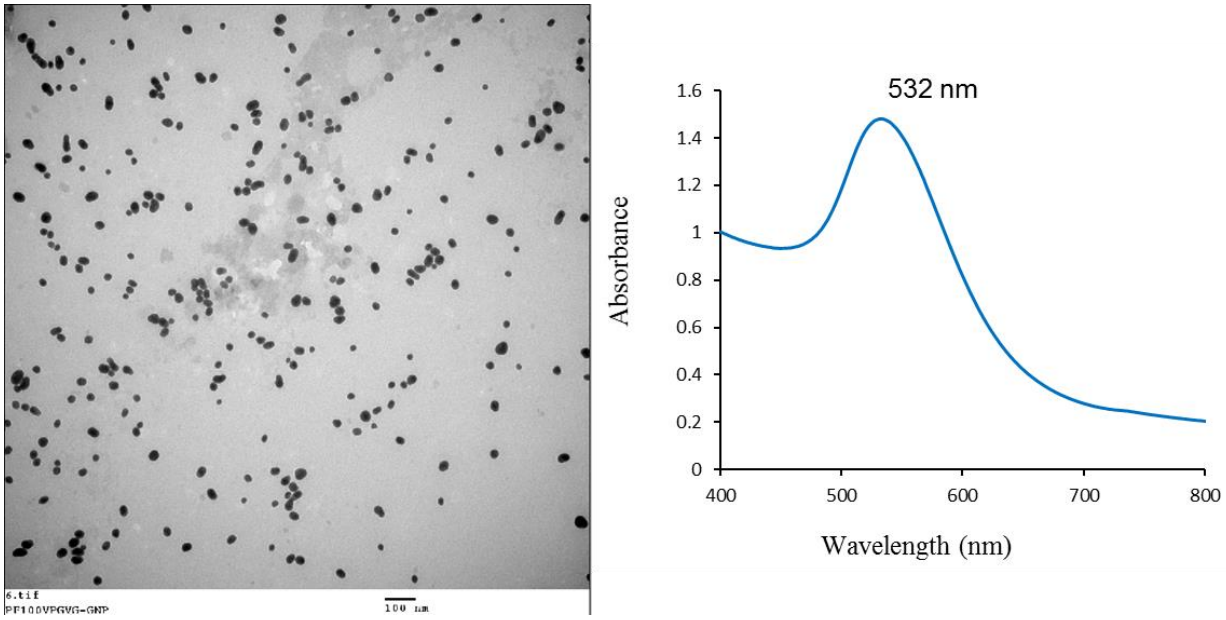

Figure 3.20: TEM image and UV-Vis data of ESP_{100}-GNPs (**32**).

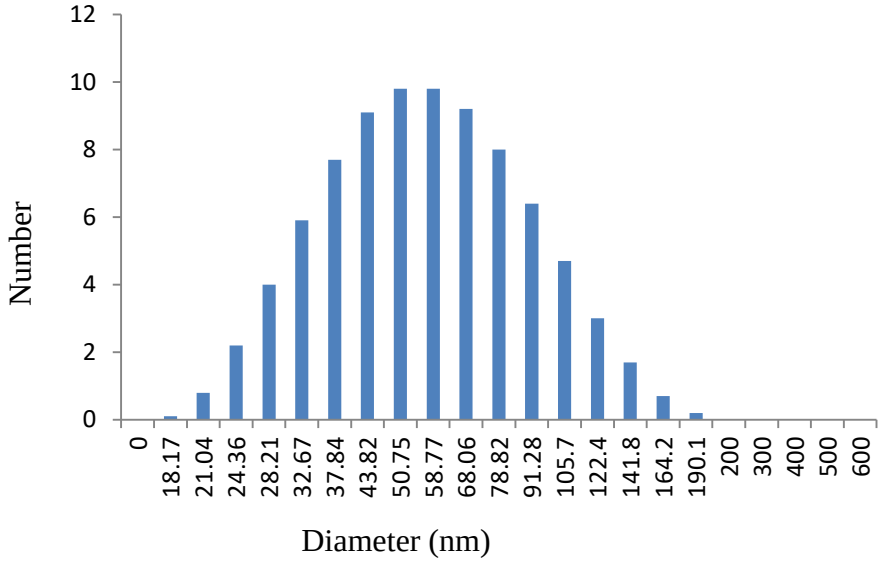

Figure 3.21: DLS traces of ESP_{100}-GNPs (**32**).

3.4.2 Properties of ESP-GNPs

We studied the thermo-responsiveness of ESP-GNPs (**31**, **32**) by turbidity measurements. The concentration of ESP_{75}-GNPs (**31**) solution was 0.5 mg mL^{-1} in PBS buffer (pH 7.4). UV-Visible spectroscopy gives good evidence of aggregation

phenomena. As shown in **Figure 3.22**, when the temperature increased the GNPs aqueous solution changed colour from red to purple accompanied by a red shift from 532 nm to 535 nm. This observation suggests that the nanoparticles aggregated and the transition temperature was around 65°C. As discussed in **Section 2.4.2.1**, the transition temperature of polymer **26** was 68°C as shown in **Table 2.6**. Here, the ESP_{75}-GNPs (**31**) showed a thermo-responsiveness very slowly from 15°C to 70°C which means that polymer **26** endowed GNPs with the same character by anchoring to the GNPs surface.

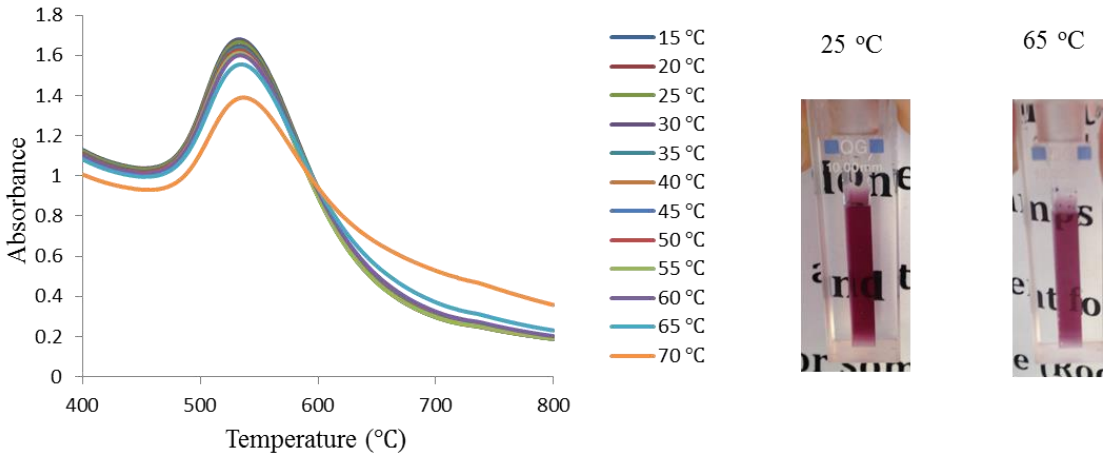

Figure 3.22: UV-Vis spectra of ESP_{75}-GNPs (**31**) versus temperature. Each spectrum was taken after an increase of 5°C (from 15°C to 70°C). Picture of ESP_{75}-GNPs (**31**) dispersed in PBS buffer at 25°C and 65°C, respectively.

The same LCST experiment was performed with ESP_{100}-GNPs (**32**) to test the sensitivity of the functionalized GNPs. Elastin-based side chain polymers in aqueous solution were mixed with the GNPs, and the strong affinity of the thiol functionality for the gold surface resulted in the assembly of polymers onto the gold surface. After polymer attachment, the solution had a slight colour change and the plasmon resonance absorption peak underwent a shift from 532 nm to 540 nm as shown in **Figure 3.23**. As ESP_{100}-GNPs (**32**) have a longer chain and a lower transition temperature than ESP_{75}-GNPs (**31**), when attached to GNPs they gave the gold solution a lower transition temperature. The colour of the solution changed from red to purple when the temperature increased from 20°C to 45°C, confirming the assembly process.

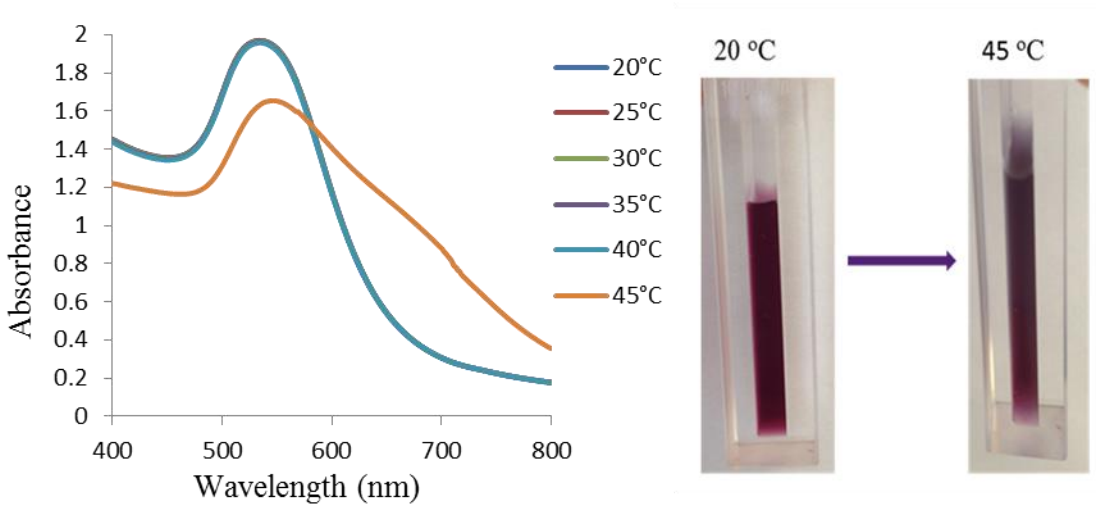

Figure 3.23: The LCST behaviour of ESP_{100}-GNPs (**32**) (0.5 mg mL^{-1}) in PBS buffer at pH 7.4 between 20°C and 45°C.

The temperature dependencies of the secondary structure of the polymer ESP_{100}-GNPs (**32**) conjugates in dilute solution (0.2 mg mL^{-1}) were evaluated using CD spectroscopy. The spectra obtained in a PBS buffer (pH 7.4) from 10°C to 65°C are shown in **Figure 3.24**. The ESP_{100}-GNPs have the same trend as polymer **29** which indicates that the polymer covered the gold nanoparticles, leading to a conformation change when the temperature increased.

At the lowest temperature (10°C), the MRE was about -12,000 deg cm^2 $dmol^{-1}$ at 195 nm which represents a random coil. The CD amplitudes at 195 to 200 nm decreased with increasing temperature, with a smaller decrease in amplitude at 206 to 212 nm. With increasing temperature, the molar ellipticity [θ] value at 195 to 200 nm and 206 to 212 nm increased, which supports increasing β-turn content. With increasing temperature, there exists a smaller increase in CD amplitudes at 222 nm. This peak is associated with a type I/III β-turn. The data studied here exhibited an increase in MRE at 198 nm and 206 nm with increasing temperature, supporting the folding of the peptide and leading to a β-turn formation. The conformational transition from random coil to β-turn occurred gradually over a wide temperature range from 10°C to 65°C.

The change in [θ] value at 198 nm was plotted against temperature in **Figure 3.25**. From 10°C to 60°C, the value increased gradually and uniformly. Then the value decreased a little when the temperature increased to 65°C. From these data we can conclude that the transition temperature is around 35°C.

In order to test the reversibility of ESP_{100}-GNPs (**32**), a cyclic thermal response experiment was performed by changing the temperature between 50°C and 20°C. **Figure 3.26** shows the cyclic thermal response of the ESP_{100}-GNPs (**32**) solution. CD spectra were acquired at 20 °C and 50 °C for 3 cycles. After each temperature change, the sample was allowed to equilibrate for 5 min. These data show that the structural changes of the ESP_{100}-GNPs are reversible and can be induced many times without apparent degradation. The CD data obtained also show that the temperature-induced formation of the β-turn structure is due to intramolecular and not intermolecular interactions.

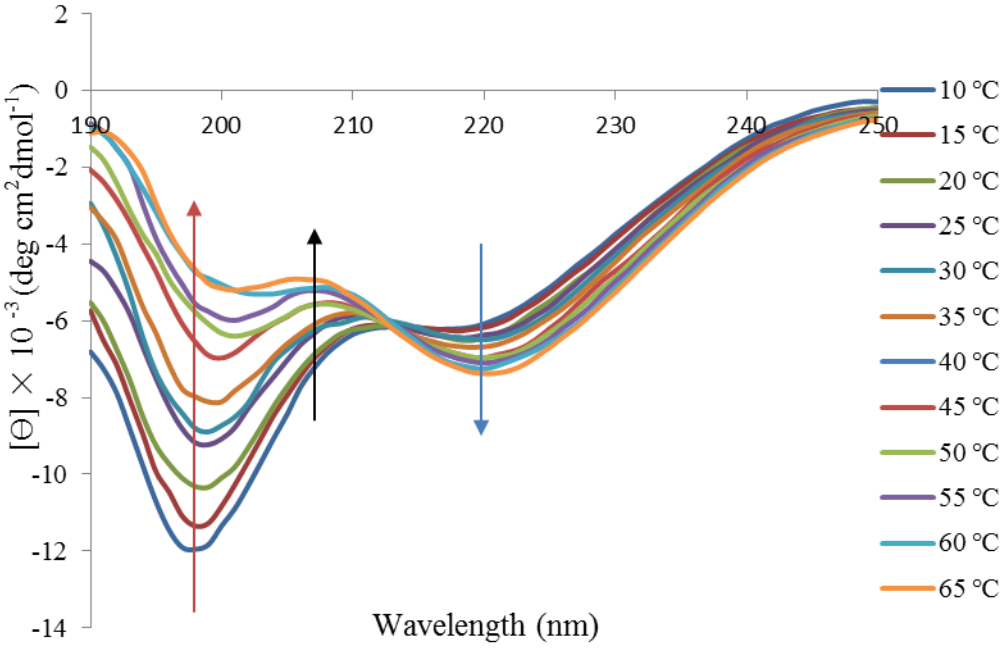

Figure 3.24: Temperature dependence CD spectra of ESP_{100}-GNPs (**32**) (0.2 mg mL^{-1}) in PBS buffer at pH 7.4 between 10°C and 65°C.

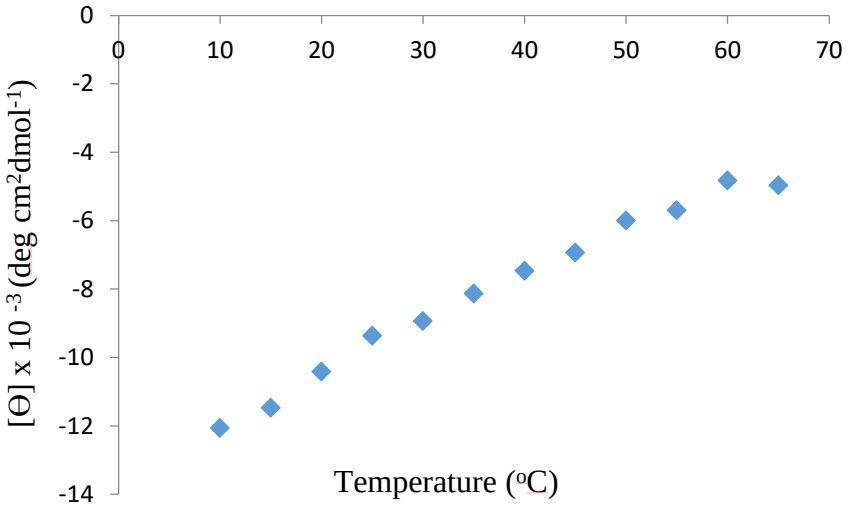

Figure 3.25: Temperature profile of $[\theta]_{198}$ values for ESP_{100}-GNPs (**32**) (0.2 mg mL^{-1}) in PBS buffer at pH 7.4 between 10°C and 65°C.

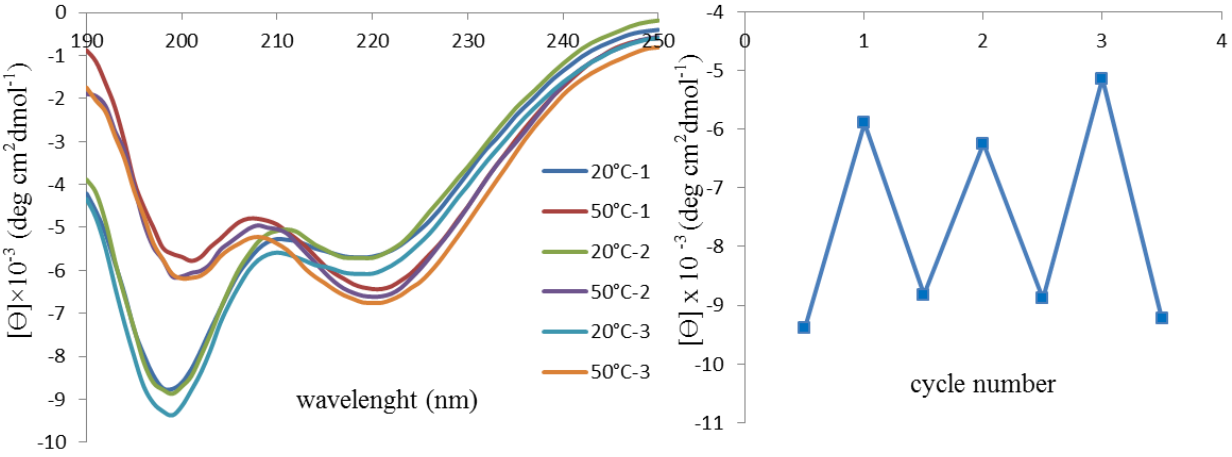

Figure 3.26: The CD spectra (left) and the CD signal at 198 nm (right) of ESP_{100}-GNPs (**32**) (0.2 mg mL^{-1}) in PBS buffer at pH 7.4 when alternating the temperature 3 times between 20°C and 50°C.

To obtain more direct proof of the aggregation of ESP_{100}-GNPs (**32**), the aggregates were observed using TEM as shown in **Figure 3.27**. The samples were prepared at 20°C and 50°C separately and TEM images were taken. The TEM images taken below and above the phase transition temperature gave more direct evidence of ESP_{100}-GNPs (**32**) aggregation. At low temperature, they are generally well dispersed, although a few aggregates may not be completely excluded. When temperature increased to 50°C,

aggregation was dominant and accompanied with the colour change of the sample solution.

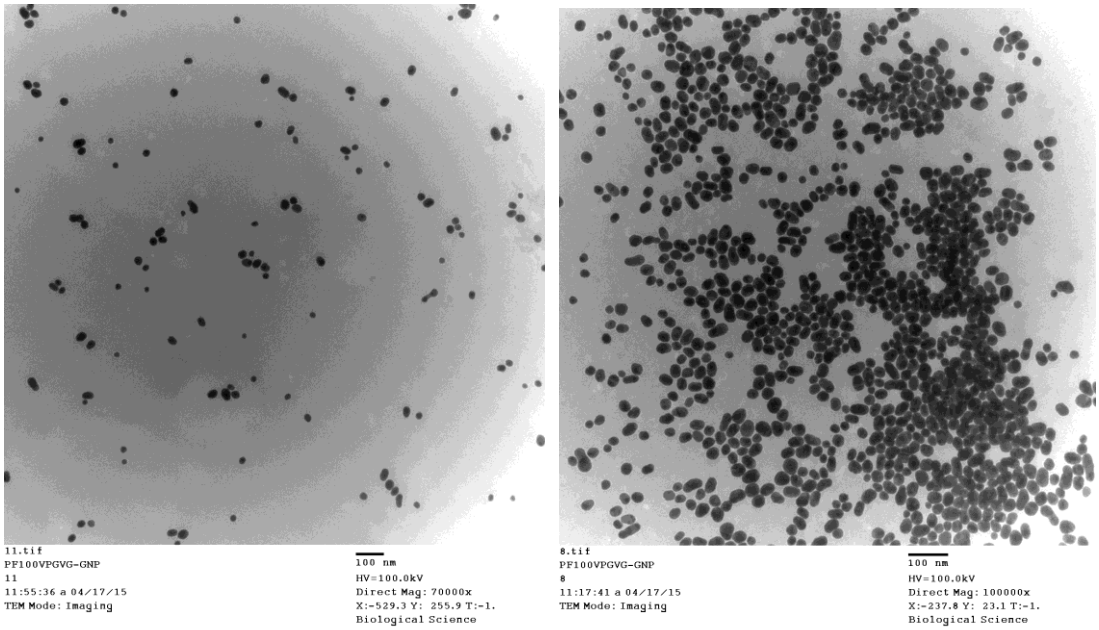

Figure 3.27: TEM data obtained of ESP_{100}-GNPs (**32**) prepared at 20°C and 50°C separately.

3.5 Preparation and Characterization of Synthesis KLA-GNPs

3.5.1 Synthesis of thiol-TTDS-KLA peptide (38)

Fmoc solid phase peptide synthesis was used to obtain the pro-apoptotic $_D$-KLA peptide (**33**), which has a sequence of $_D$-$(KLAKLAK)_2$. In order to prevent its inactivation by enzymatic hydrolysis *in vivo*, all the amino acids in its sequence were D-amino acids.

In order to conjugate $_D$-KLA (**33**) with GNPs to form KLA-GNPs hybrid nanomaterials through the thiol-Au interaction, a linker and a thiol end are needed. The linker we finally chose was Fmoc-TTDS-OH (**34**) and 3-tritylsulfanyl-propionic acid. However prior to this we tried two other linkers for comparison. As shown in **Figure 3.28**, C(Ahx)KLA (**36**) was first synthesised with Fmoc-Ahx-OH (**35**) as a spacer coupled with cysteine as the terminal amino acid which gave a free thiol end. However, the gold solution aggregated immediately when a solution of C(Ahx)KLA (**36**) was added. This may because the linker is quite short, the $_D$-KLA (**33**) is positively charged and the gold surface is negatively charged. We then lengthened spacer by using four Fmoc-Ahx-OH (**35)** and two glycine residues to obtain $C(Ahx)_4GGKLA$ (**37**). However, when this was

reacted with the gold solution, the aggregation still occurred. These results led us to finally choose a short PEG linker Fmoc-TTDS-OH (**34**). We also changed cysteine to 3-tritylsulfanyl-propionic acid as it is the same thiol end for peptide SH-VPGVG (**11**). The short PEG linker provides a more hydrophilic environment which produces a stable spacer between GNPs and $_{D}$-KLA peptide (**33**).

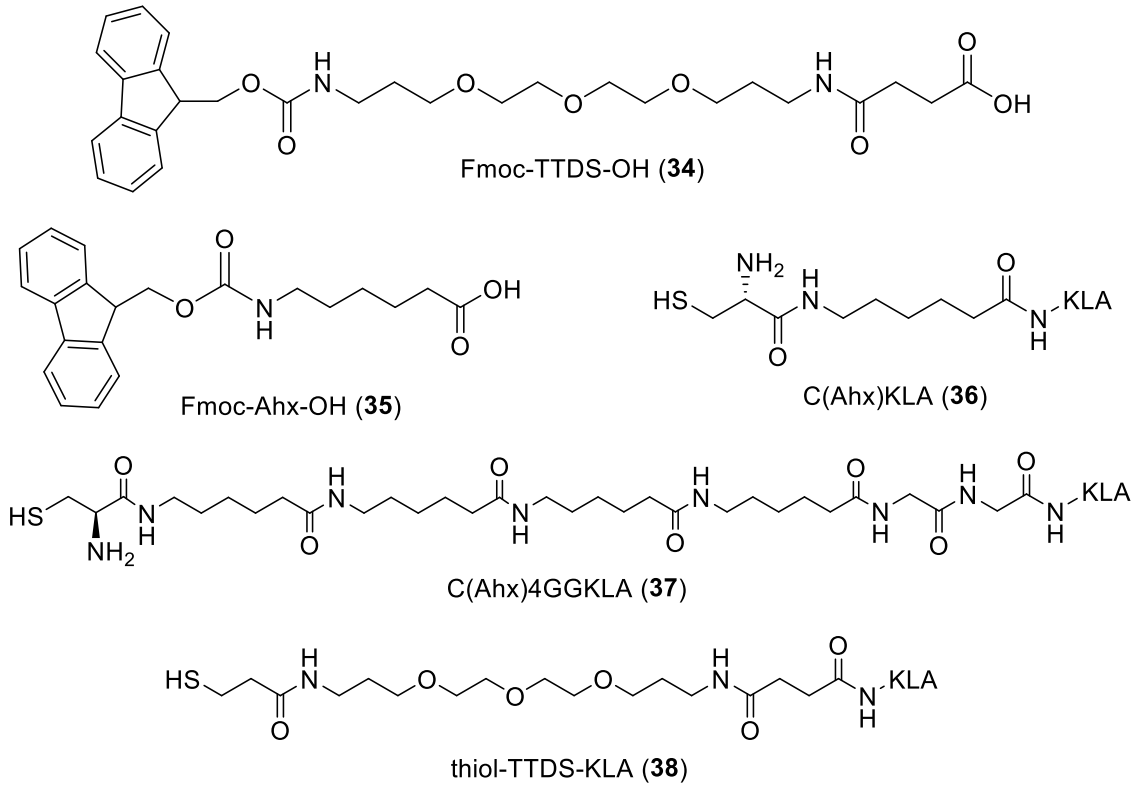

Figure 3.28: The structure of synthesised thiol-KLAs with different linkers.

The $_{D}$-(KLAKLAK)$_2$ (**33**) was synthesised manually as shown in **Figure 3.29**. Rink Amide resin was chosen to give an amide at the C-terminus meaning the overall charge of the peptide would not be affected by a pH change. Fmoc-$_{D}$-Lys(Boc)-OH, Fmoc-$_{D}$-Leu-OH and Fmoc-$_{D}$-Ala-OH were used. The coupling of each amino acid was repeated twice to make sure there were fewer deletion fragments of the final targeted peptide. In addition, a test cleavage was carried out in the middle of the sequence to check the coupling efficiency and to prove the method could be used continually. At the end of the $_{D}$-KLA peptide synthesis, the linker Fmoc-TTDS-OH (**34**) was chosen to conjugate to the peptide sequence. The coupling process is the same as coupling each amino acid. Finally, 3-tritylsulfanyl-propionic acid was added to the sequence to provide a free thiol end group. After completion of the synthesis, the resin was finally washed with DMF, DCM and diethyl ether three times separately. The cleavage of the

peptide on resin was performed by adding a cleavage cocktail, which contained TFA (95%), TIPS (2.5 %) and H_2O (2.5 %), for 3 h. TIPS acts as a scavenger preventing any side reactions. The filtrate was concentrated to a viscous solution by rotary evaporation followed by precipitation in cold ether solvent. The ether was slowly decanted and the crude thiol-TTDS-KLA (**38**) was collected. Then the crude peptide was dissolved in distilled water and freeze-dried (**Figure 3.29**).

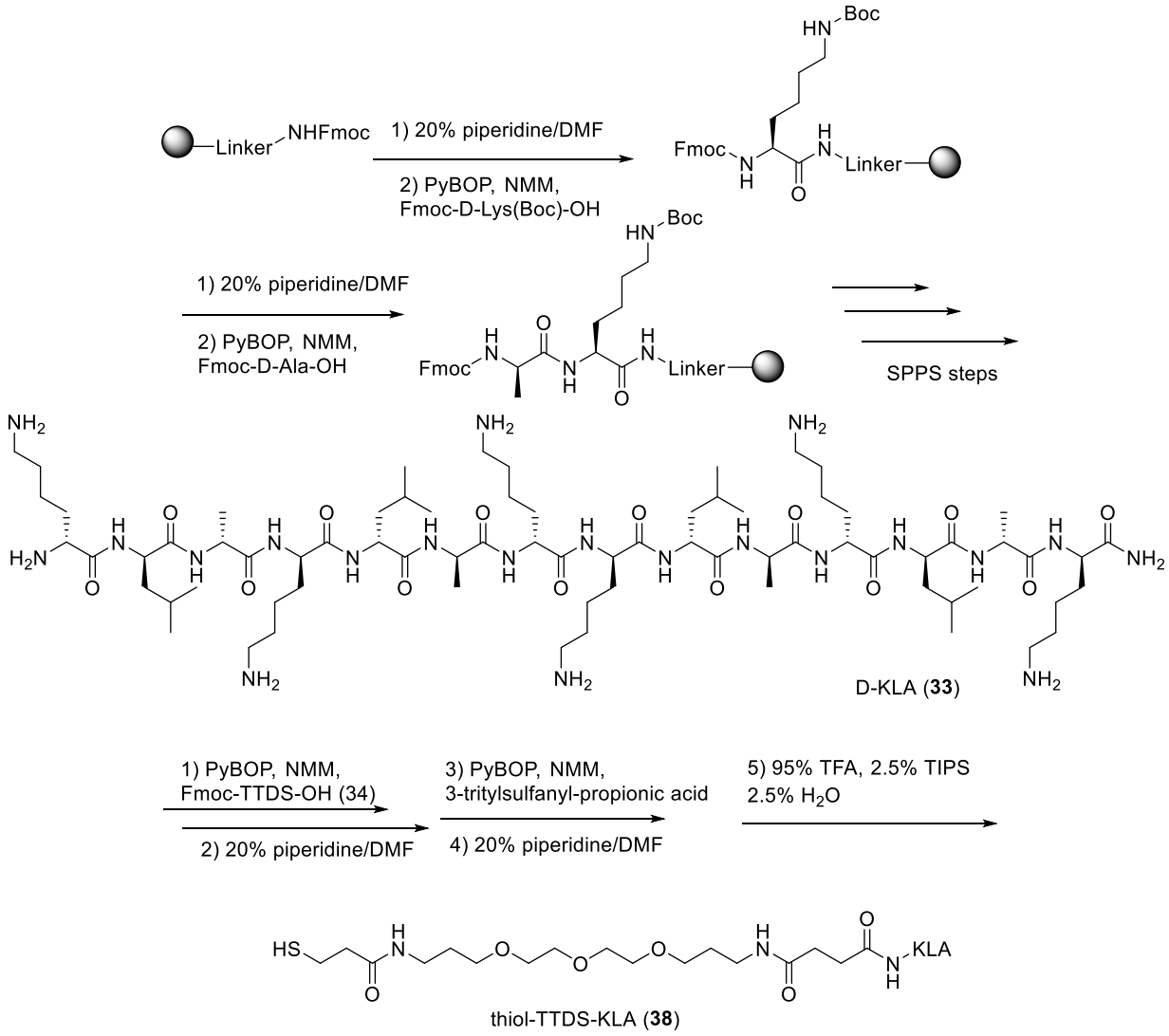

Figure 3.29: Overview showing the synthesis of $_D$-KLA (**33**) and thiol-TTDS-KLA (**38**).

Semi-preparative HPLC was used to purify the crude peptide as described in **Section 6.1.2.5**. A sample of crude peptide **38** (7~10 mg mL^{-1}) was dissolved in water and analysed using a gradient of 0-20% solvent B in 10 min, 20%-55% solvent B in 40 min and 55%-100% solvent B in 10 min. The flow rate was set to 2.0 mL/min and the

detector monitored absorbance at 220 nm. The peptide was the main peak at RT= 29.5 min, denoted by an asterisk. The chromatogram is illustrated in **Figure 3.30**. The yield of purified peptide **38** after RP-HPLC was 13%.

After purification, a small sample of the peptide was dissolved in water and analyzed by analytical HPLC, MALDI, LC-MS and accurate mass. Analytical HPLC analysis is shown as **Figure 3.31**. The retention time of the peak is 14.7 min and a tiny impurity shoulder is apparent. The molecular weight of thiol-TTDS-KLA ($C_{89}H_{169}O_{20}N_{23}S$) peptide (**38**) was examined by MALDI and found to be 1935.2 which is $[M+ Na]^+$ as shown in **Figure 3.32**. The LC-MS data was shown in **Appendix 3.3**: $[M+5H]^{5+}$ 383.0, $[M+4H]^{4+}$ 480.4, $[M+3H]^{3+}$ 639.3, $[M+2H]^{2+}$ 957.6. In **Appendix 3.4**, HRMS *m/z* (ESI) 957.6361, consistent with empirical formula $C_{89}H_{169}O_{20}N_{23}S$ with an accuracy of 5 ppm (accepted as $(M + 2H)^{2+}$).

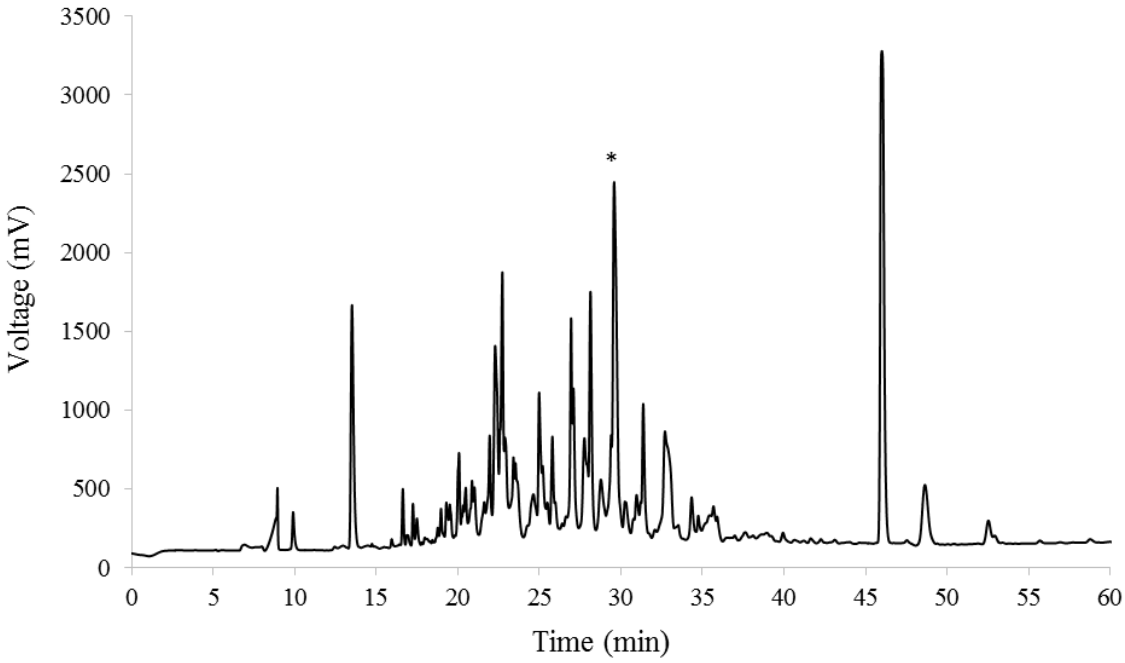

Figure 3.30: Semi-preparative HPLC chromatogram of crude peptide **38**. The peak with an asterisk on it represents the target peptide peak.

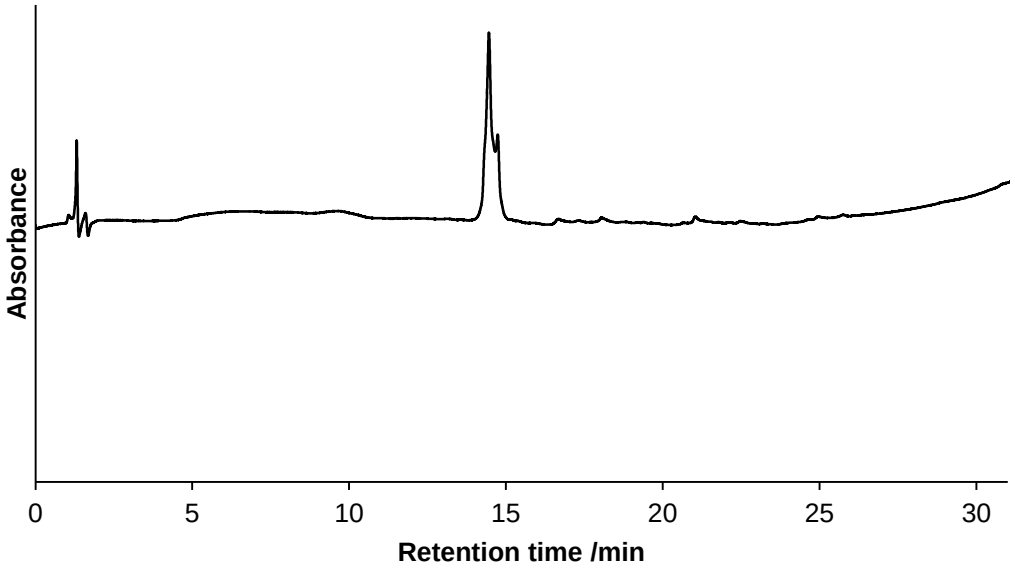

Figure 3.31: Analytical HPLC trace of purified thiol-TTDS-KLA (**38**). Retention time = 14.7 min.

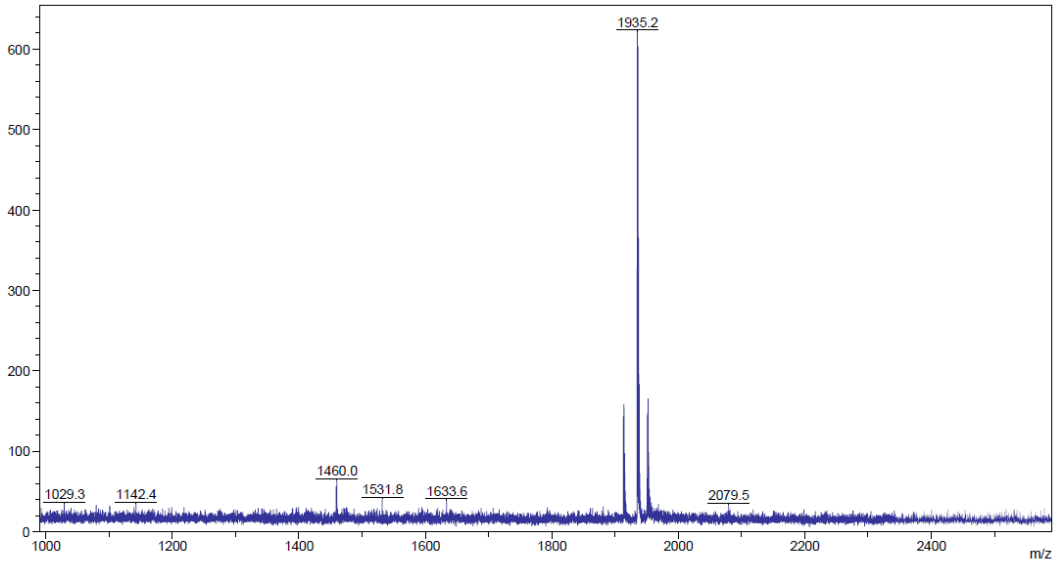

Figure 3.32: MALDI spectrum of thiol-TTDS-KLA (**38**) after RP-HPLC purification, indicationg the peaks found to confirm the presence of thiol-TTDS-KLA peptide: *m/z* 1935.2 $[M+Na]^+$.

3.5.2 Synthesis of KLA-GNPs (39)

The GNPs were synthesised via the same method as described in **Section 6.4**. However, the concentration of the mother solution of Au^{3+} was tripled to prepare more concentrated GNPs (1mM). Due to the same ratio of trisodium citrate to gold was used, the size of GNPs (1mM) is the same as GNPs A (0.3mM).

The preparation of thiol-TTDS-KLA peptide (**38**) functionalized gold nanoparticles (KLA-GNPs) was achieved through thiol-gold covalent bonding. The weight/weight ratio of peptide to gold was 2:1 to ensure an excess of peptide. A colour change from red to purple was observed when a solution of **38** was slowly added into GNPs. The mixture was stirred overnight at room temperature under a nitrogen atmosphere to prevent disulphide bond formation. Then the purple solution obtained was transferred to a dialysis bag (MWCO: 3500 Da) and dialysed against deionised water for 2 days. The KLA-GNPs (**39**) collected were then freeze-dried to obtain a dark purple solid. The structure of the KLA-GNPs (**39**) is shown in **Figure 3.33**.

TEM images of KLA-GNPs obtained are shown in **Figure 3.34**. The mean diameter of KLA-GNPs from TEM was found to be 17.7 ± 4.6 nm. Dynamic light scattering (DLS) was also used to observe the size distribution of KLA-GNPs (**Figure 3.35**). The average mean diameter is 26.5 nm and the polydispersity is 0.097. The CD spectrum of KLA-GNPs (0.2 mg mL^{-1}) obtained in a PBS buffer (pH 7.4) is shown in **Figure 3.36**. The positive bands aroud 208 nm and 225 nm were indicative of α-helical conformation of KLA-GNPs (**39**).

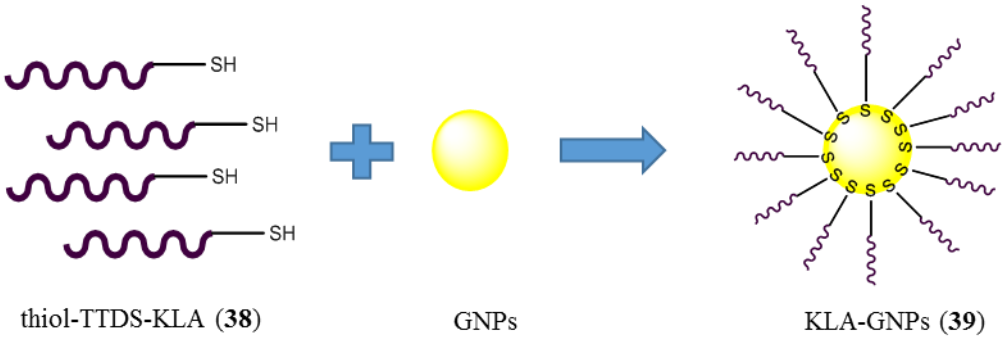

Figure 3.33: Overview of the synthesis of KLA-GNPs (**39**).

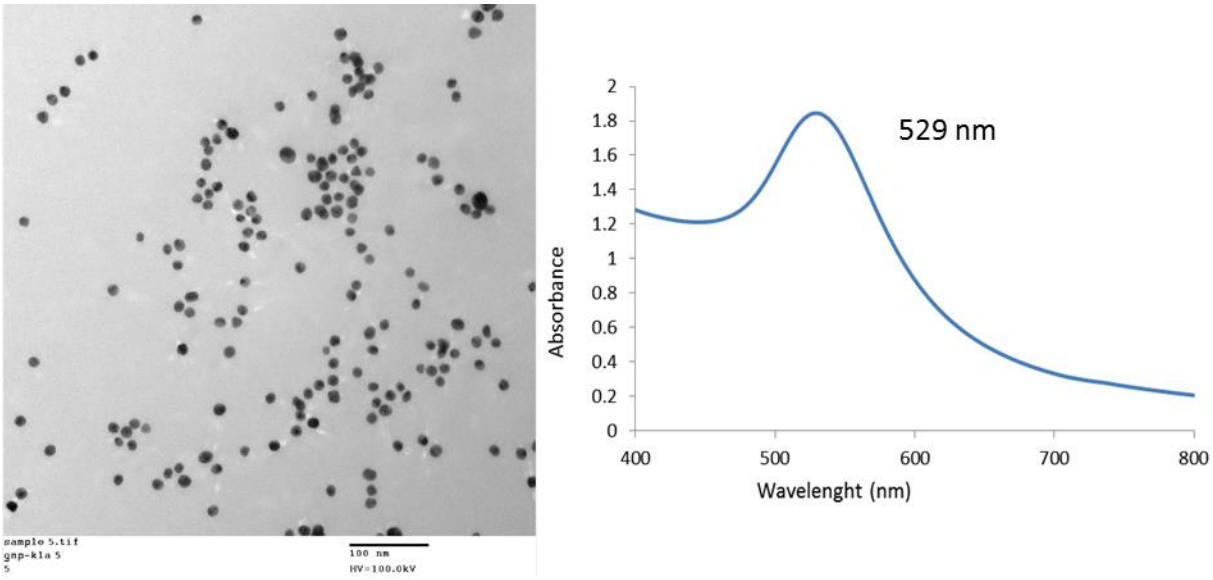

Figure 3.34: TEM image and UV-Vis analysis of KLA-GNPs (**39**).

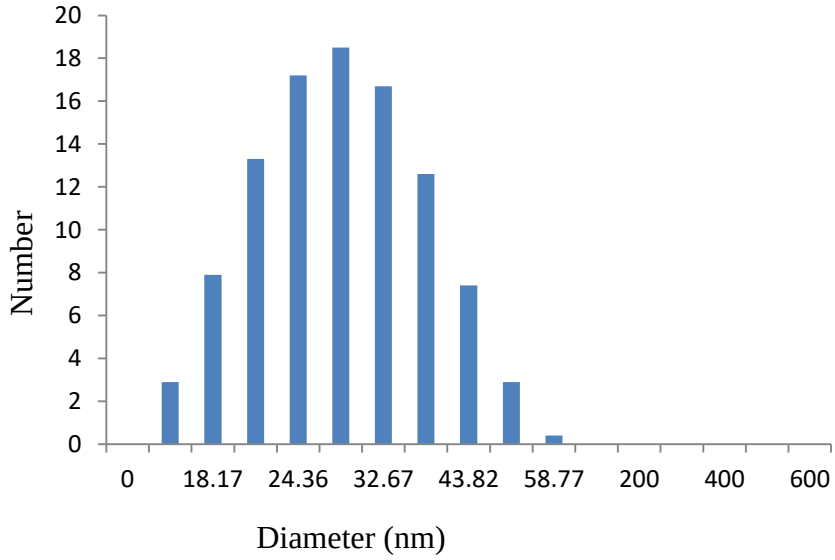

Figure 3.35: DLS traces for KLA-GNPs (**39**).

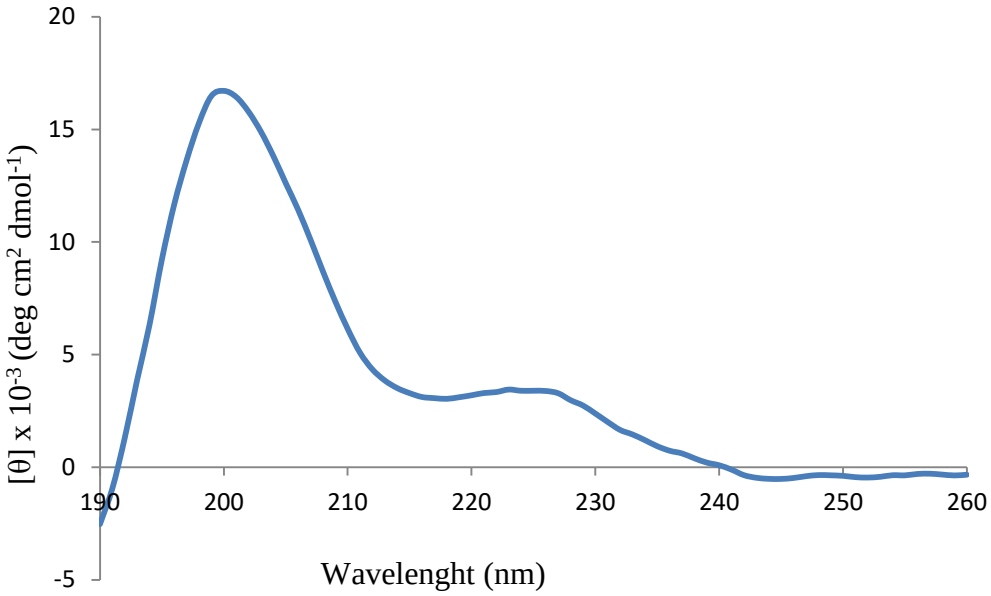

Figure 3.36: The CD spectrum of KLA-GNPs (**39**) (0.2 mg mL^{-1}) in PBS buffer at pH 7.4.

3.5.3 Cytotoxicity of KLA-GNPs (39)

(The MTT data were obtained by Lijun Jiang at Hong Kong Baptist University)

The cytotoxicity of $_{D}$-KLA peptide (**33**) and KLA-GNPs (**39**) were evaluated using HeLa cells. As **Figure 3.37** shows, a $_{D}$-KLA (**33**) exhibits lower anti-cancer activity than **39**. For **33**, the HeLa cell viability is still 56 ± 3% even at a concentration of 500 μM.

As we can see from **Figure 3.38**, KLA-GNPs (**39**) showed better anti-cancer activity than $_{D}$-KLA (**33**). At the highest concentration of **39** tested (100 μM), HeLa cell survival is only around 30 ± 3.3%. When the concentration of **39** was diluted to 50 μM, the cell viability was 73.4 ± 4.9%, which means the half maximal inhibitory concentration (IC_{50}) of KLA-GNPs (**39**) is between 50 μM and 100 μM.

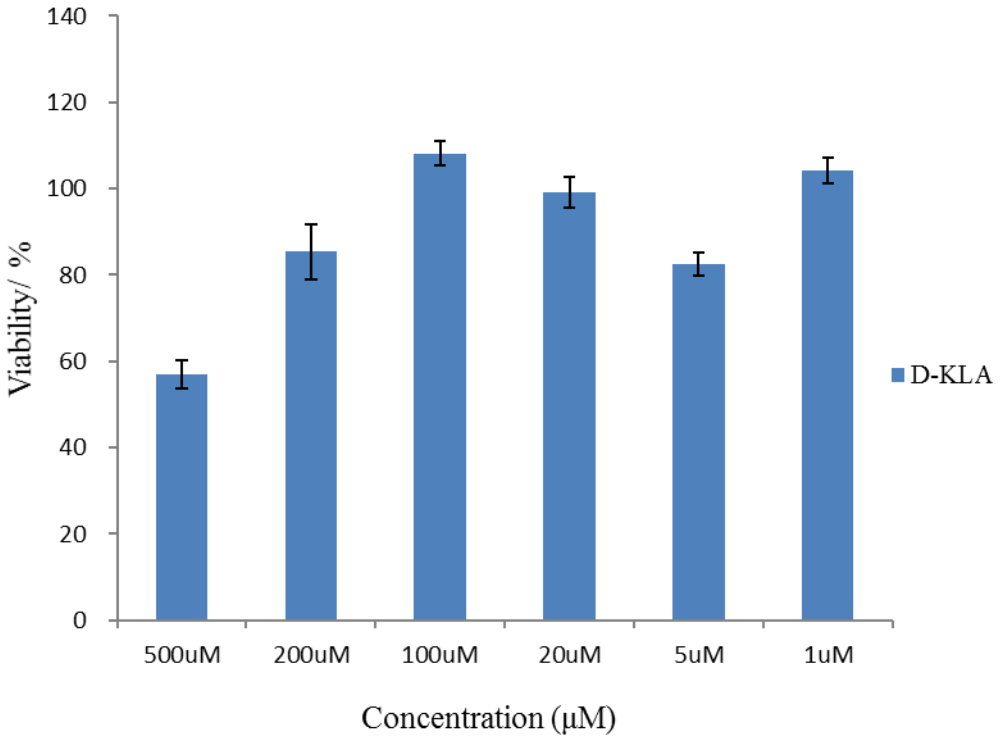

Figure 3.37: MTT assay determined cell viability of HeLa cell line after incubation with $_{D}$-KLA (**33**) for 24 h at 37°C. The data represent the mean ± standard deviation of three independent experiments.

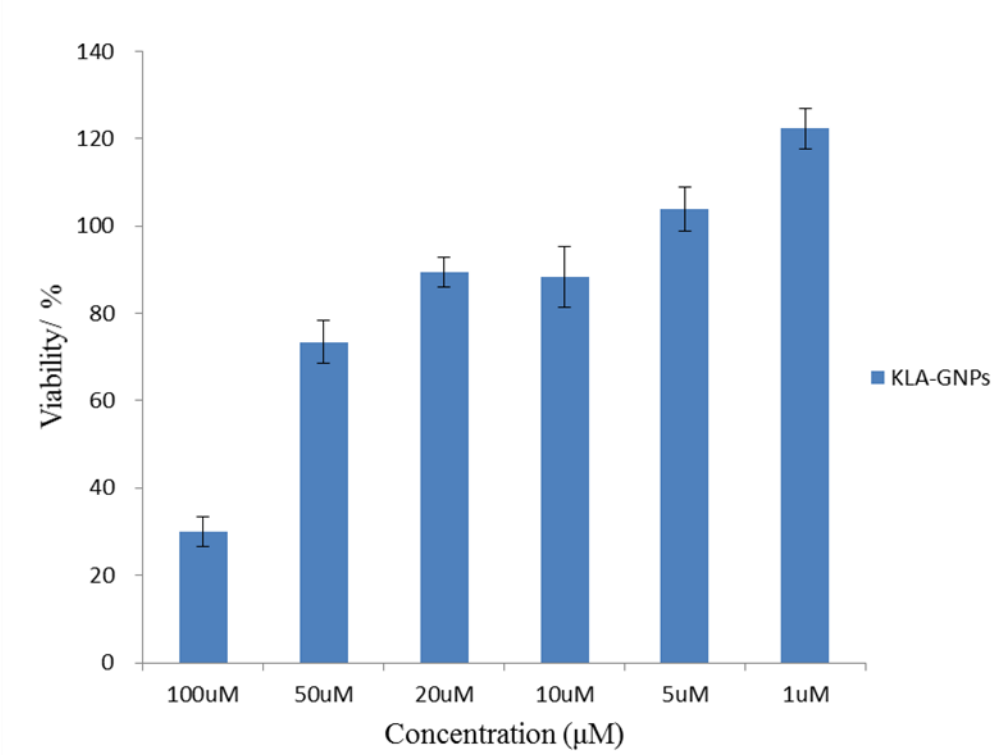

Figure 3.38: HeLa cell viability after incubation with KLA-GNPs (**39**) for 24 h at 37°C. The data represent the mean ± standard deviation of three independent experiments.

From the cytotoxicity experiment, it has been found that KLA-GNPs **39** have a lower IC_{50} value than free $_D$-KLA peptide (**33**), which suggests that **39** may have been internalized into cells. Confocal microscopy was used to confirm the cellular internalization of **39**. KLA-GNPs (**39)** incubated with HeLa cells for 24 h were examined by laser confocal microscopy. As shown in **Figure 3.39**, the localization of **39** is exactly the same as the mitochondrial tracker dye. The merged picture of **Figure 3.39** a) and b) strongly confirms that GNPs can deliver the KLA peptide (**33**) into the mitochondria of cells, leading to an improvement of anti-cancer activity.

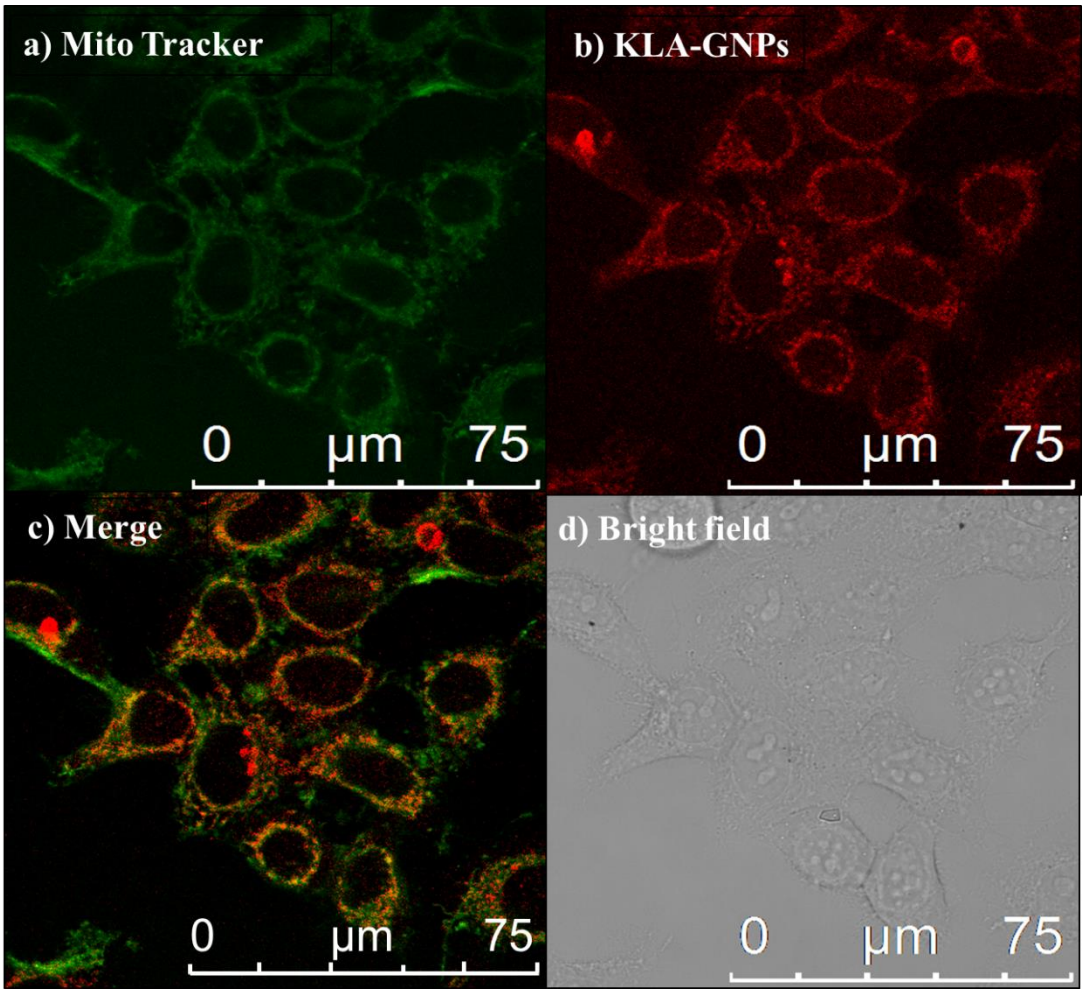

Figure 3.39: Confocal microscope images of KLA-GNPs (**39**) in HeLa cells. (Conc.: 10 µM, Incubation time: 24 h). For costaining of the mitochondria the cells were treated with Mitochondria Green™ (**a**). The images (**c**) show the merges of the respective emission channels of each line: 499–552 nm for the detection of the mitochondria (green, **a**), and 593–696 nm for the detection of the KLA-GNPs (red, **b**). Bar 15 µm.

3.6 Preparation and Characterization of KLA-ESP$_{100}$-GNPs

3.6.1 Synthesis of KLA-ESP$_{100}$-GNPs (40)

The preparations of both thiol-TTDS-KLA (**38**) and PF$_{100}$-GABA(VPGVG) (**29**) functionalized GNPs KLA-ESP$_{100}$-GNPs (**40**) were achieved using thiol-gold covalent bonding as well. The weight/weight ratio of peptide **38**, polymer **29** and GNPs was 1:1:1 to produce equal functionalization of the gold nanoparticles. In the process, thiol-KLA peptide (**38**) and polymer (**29**) were separately dissolved in deionized water. Through the use of two syringes, both peptides were simultaneously slowly added dropwise into filtered GNPs (1 mM). The mixture was stirred overnight at room temperature under a nitrogen atmosphere. The purple solution was then transferred to a dialysis bag (MWCO: 50,000 Da) and dialysed against deionised water for 24 h, after which the KLA-ESP$_{100}$-GNPs (**40**) were freeze-dried to obtain a dark purple solid. The scheme of the synthesis is shown in **Figure 3.40**.

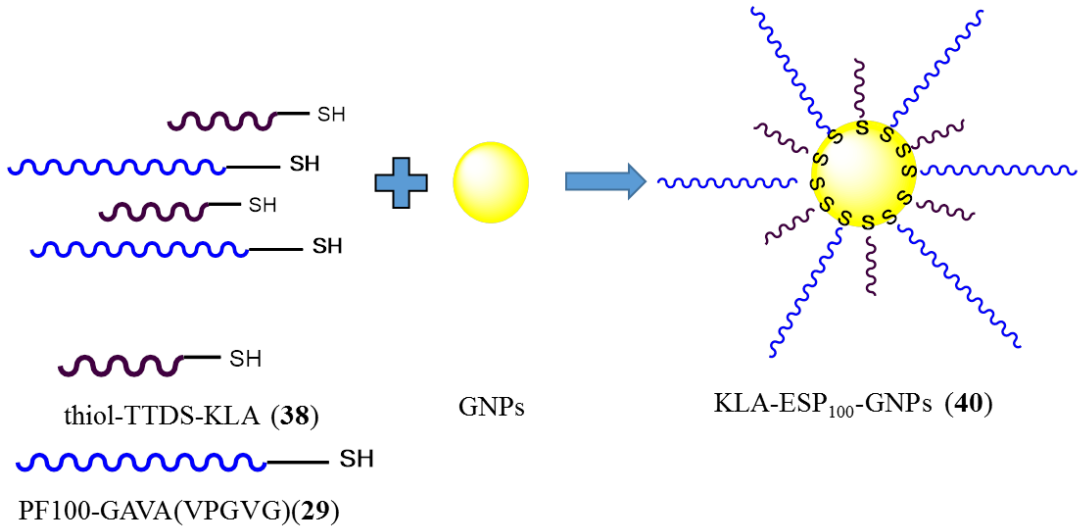

Figure 3.40: Synthesis of KLA-ESP$_{100}$-GNPs (**40**).

The TEM images of the KLA-ESP$_{100}$-GNPs (**40**) obtained are shown in **Figure 3.41**. The diameter of KLA-ESP$_{100}$-GNPs (**40**) by TEM was 22.8 ± 3.5 nm on average. The plasmon resonance band of the KLA-ESP$_{100}$-GNPs (**40**) solution was centred at 530 nm. Dynamic light scattering (DLS) was used to observe the size distribution of KLA-ESP$_{100}$-GNPs (**40**), which is shown in **Figure 3.42**. The average mean diameter was found to be 30.3 nm, and the polydispersity is 0.213.

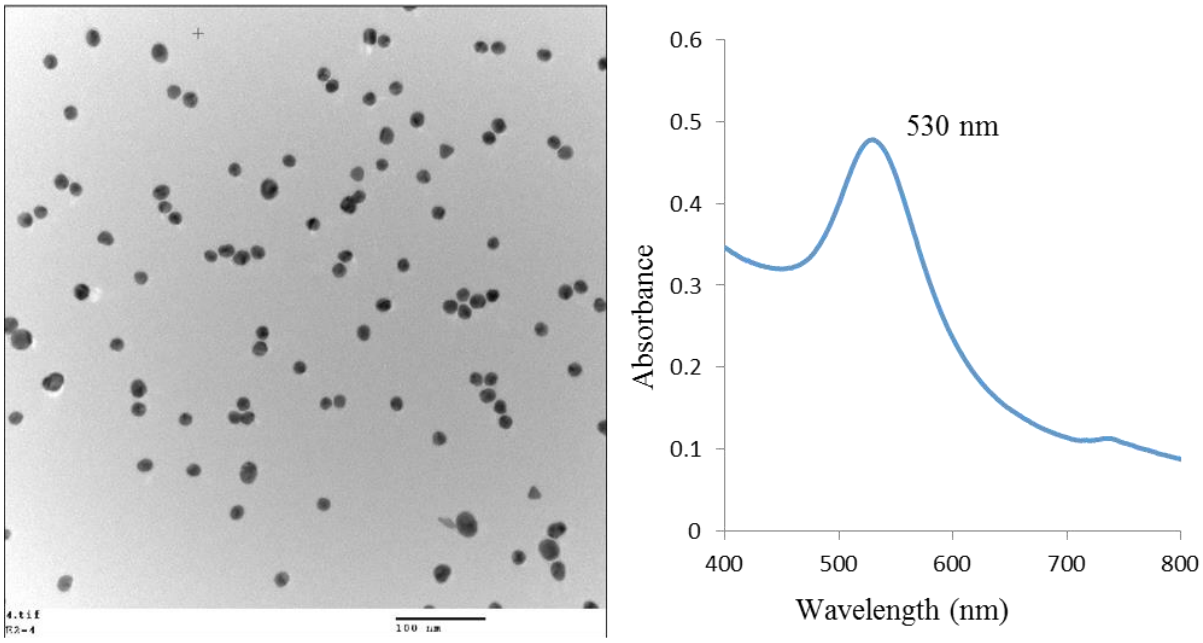

Figure 3.41: TEM image and UV-Vis data of KLA-ESP$_{100}$-GNPs (**40**).

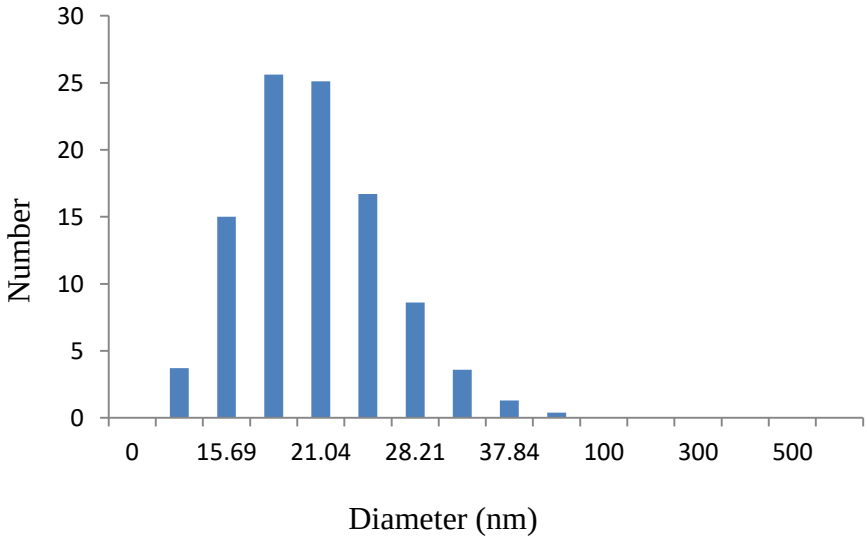

Figure 3.42: The DLS trace of KLA-ESP$_{100}$-GNPs (**40**).

3.6.2 Properties of KLA-ESP$_{100}$-GNPs (40)

The phase transition behaviour of KLA-ESP$_{100}$-GNPs (**40**) was studied by UV-Visible spectroscopy as the solution temperature was increased from 20^{o}C to 80^{o}C, as shown in **Figure 3.43**. At 20^{o}C, the spectrum of KLA-ESP$_{100}$-GNPs (**40**) exhibited an absorption peak at 530 nm and did not change significantly from 10^{o}C to 35^{o}C. Upon raising the temperature to 40^{o}C, the maximum absorption peak showed a red shift from 530 nm to 532 nm at 80^{o}C. This indicated the aggregation of nanoparticles and was accompanied

by a colour change from purple to darker purple. This suggested that the changes of KLA-ESP$_{100}$-GNPs (**40**) were because of the thermo-responsive property of the elastin-based polymer (**29)** layer on the GNPs' surface. However, the changes observed are less than for ESP-GNPs (**32**). When the temperature of the KLA-GNP-ESP$_{100}$-GNP (**40**) solution was raised from 20^{o}C to 80^{o}C, only the ESP layer underwent an intramolecular hydrophilic-hydrophobic transition, not thiol-TTDS-KLA (**38**) layer. Due to **38** having no thermo-responsive property, the UV-Vis changes are not that significant.

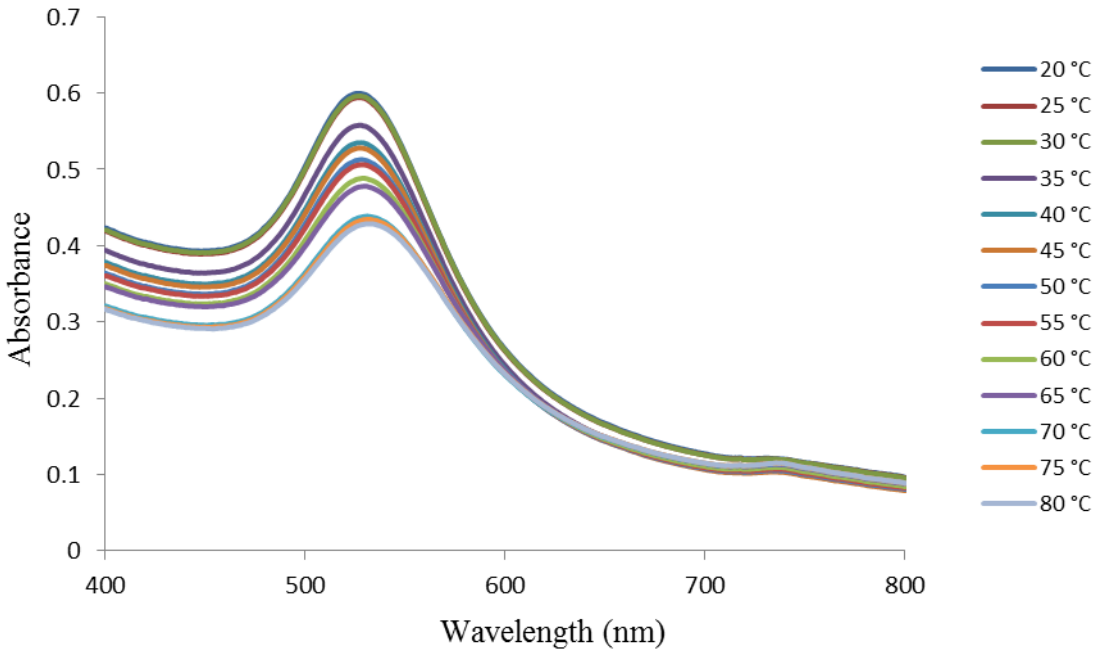

Figure 3.43: The LCST behaviour of KLA-ESP$_{100}$-GNPs (**40**) (0.2 mg mL^{-1}) in PBS buffer at pH 7.4 between 20^{o}C and 80^{o}C.

The temperature dependencies of the secondary structure of the KLA-ESP$_{100}$-GNP (**40**) conjugates in dilute solution (0.2 mg mL^{-1}) was evaluated using CD spectroscopy. The spectra obtained in PBS buffer (pH 7.4) from 20^{o}C to 90^{o}C are shown in **Figure 3.44**. The CD amplitudes at 200 to 210 nm had a positive band and the MRE at 222 nm was negative which implies a typical β-turn structure. The MRE between 190 nm and 200 nm were indistinguishable from background signals and so cannot be used to determine secondary structures. This may due to the strong β-turn structure of the KLA-ESP$_{100}$-GNPs (**40**) leading to a higher concentration of particles. The CD amplitudes at 200 to 210 nm increased with increasing temperature, with a similar scale

decrease in amplitude at 220 to 230 nm. With increasing temperature, the molar ellipticity [θ] value at 206 nm and 222 nm increased in value which supports increasing β-turn content. These peaks are known to be associated with type I/III β-turn. The conformational transition from random coil to β-turn occurred gradually over a wide temperature range from 20°C to 90°C. KLA-ESP_{100}-GNPs (**40**) still have the same trend as $P(PFPA)_{100}$-GABA(VPGVG) (**29**) and ESP_{100}-GNPs (**32**) which indicates that ESP layers were covered on the GNP surfaces which led to a conformation change when the temperature increases.

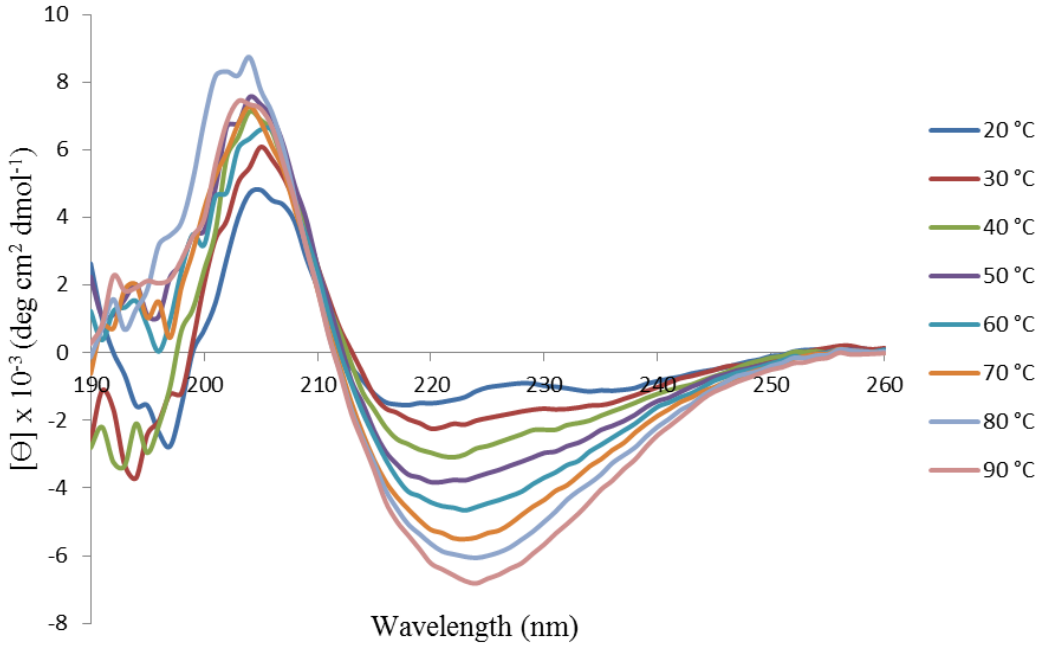

Figure 3.44: Temperature dependence circular dichroism (CD) spectra of KLA-ESP_{100}-GNPs (**40**) (0.2 mg mL^{-1}) in PBS buffer at pH 7.4 between 20°C and 90°C.

3.6.3 Evaluation of the anti-cancer properties of KLA-ESP_{100}-GNPs (40)

(The MTT data was collected by Lijun Jiang at Hong Kong Baptist University)

The anti-cancer and cytotoxic effects of KLA-ESP_{100}-GNPs (**40**) were evaluated against the HeLa cancer cell line and normal MRC-5 lung cell lines. HeLa and MRC-5 cells were treated with **40** for 1 h at 37°C or 42°C, then cell viability was determined by a MTT reduction assay.

Figure 3.45 shows the cytotoxic effect of KLA-ESP_{100}-GNPs (**40**) against HeLa cells. The concentration of **40** was started at 300 μg mL^{-1} and diluted to 1 μg mL^{-1}. At the highest concentration tested (300 μg mL^{-1}), **40** was toxic to approximately 80% of HeLa

cells at 37°C or 42°C. Within the concentration range of 300 to 100 μg mL^{-1}, the cell viability was very similar between 42°C and 37°C. These results indicate that the heat-triggered phase transition behavior of **40** had little impact on enhancing the cytotoxic effect. From concentrations 50 to 1 μg mL^{-1}, the cell viability at 42°C was a little lower than the viability at 37°C. These results may demonstrate the impact of heat-triggered phase transition on cytotoxicity. However, the difference of the two was not significant. The explanation of these results maybe that the temperature response of **40** is not sharp enough when the temperature is raised to 42°C for 1 h.

In **Figure 3.46**, the cytotoxic effect of KLA-ESP_{100}-GNPs (**40**) was evaluated in the normal lung cell line MRC-5. The data were very similar to those obtained from HeLa cells. At the highest concentration of 300 μg mL^{-1}, **40** killed approximately 80% of MRC-5 cells at 37°C or 42°C. This indicated that multi-functionalized GNPs show no selectivity between normal cells and cancer cells.

Confocal microscopy images of KLA-ESP_{100}-GNPs (**40**) incubated for 1 h at 42°C are shown in **Figure 3.47**, the GNPs have the ability to penetrate into cells this should have been seen in the images. However, there were very few red spots inside the cells. This may due to the size of KLA-ESP_{100}-GNPs (**40**) which is bigger than KLA-GNPs (**39**). From the TEM data, the size of **39** was 17.7 nm while the size of **40** was 22.7 nm. In order to further confirm this hypothesis, a confocal microscopy experiment on ESP_{100}-GNPs (**32**) will be needed. The size of ESP_{100}-GNPs (**32**) was 32.7 nm which is bigger than **40**. If **32** could not penetrate into the cells which may suggest that size is a key control point in the system. Then we can modulate the size of KLA-ESP-GNPs by changing the polymer length or the size of GNPs. In addition, the temperature responsiveness of elastin-like polymer should be more sensitive at 42°C.

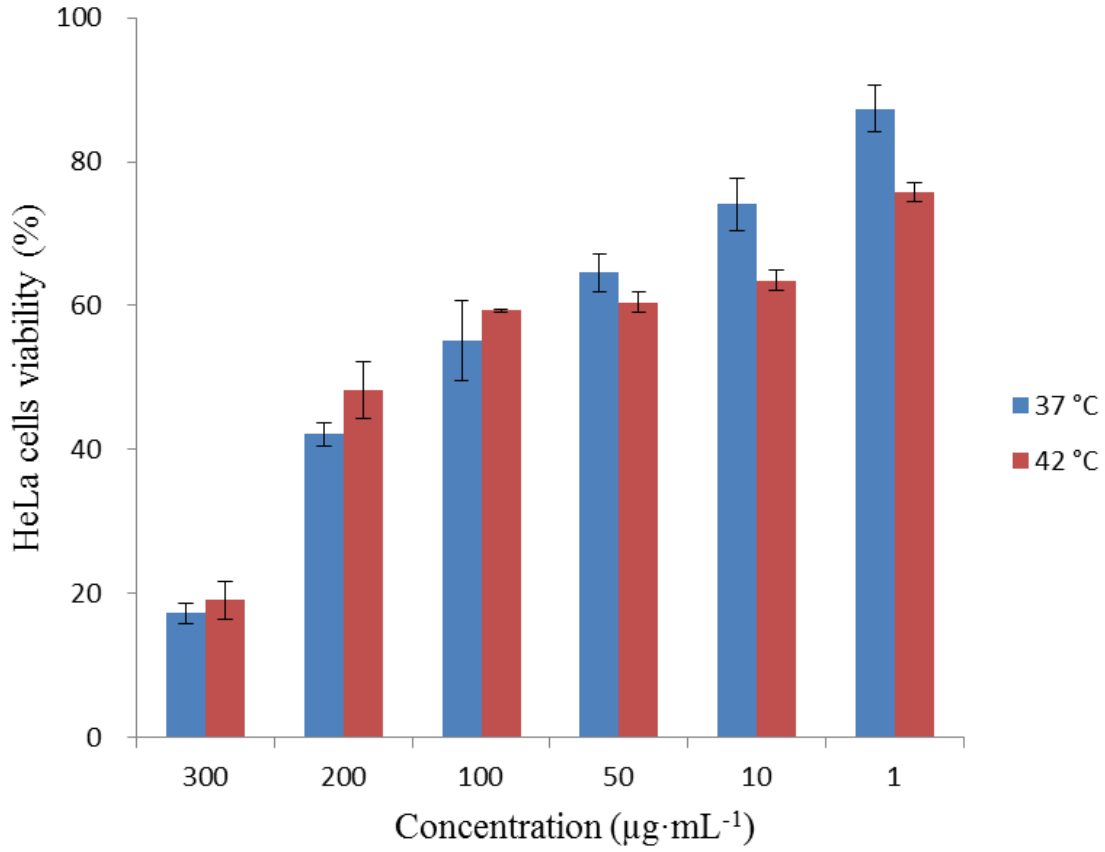

Figure 3.45: Cytotoxic effect of KLA-ESP$_{100}$-GNPs (**40**) against HeLa cancer cells.

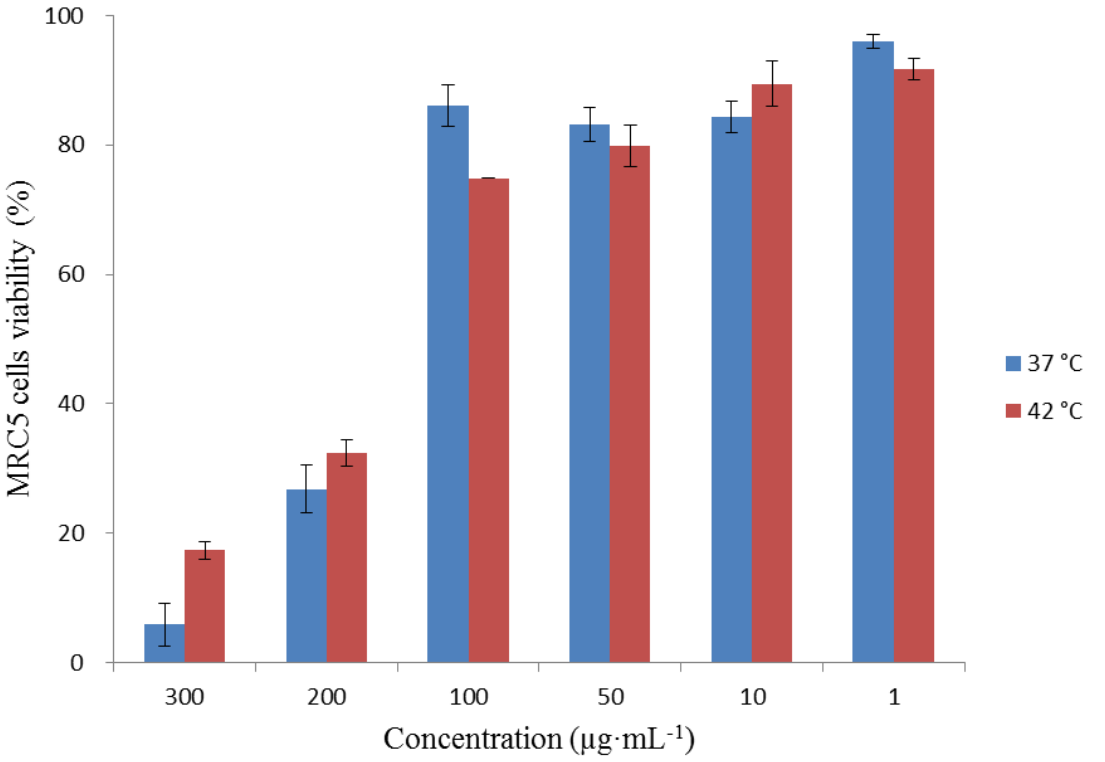

Figure 3.46: Cytotoxic effect of KLA-ESP$_{100}$-GNPs (**40**) against MRC-5 (normal lung cells).

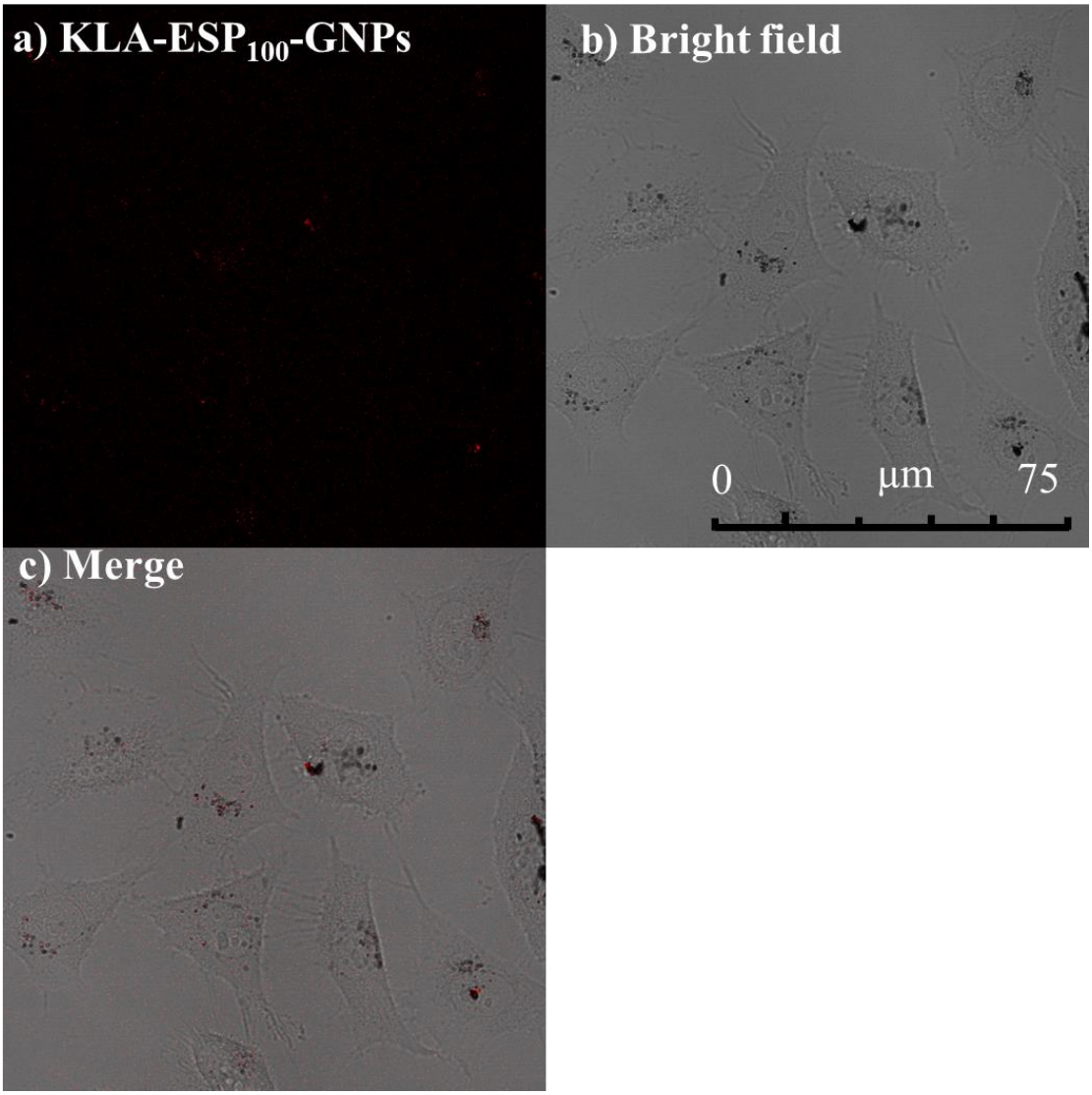

Figure 3.47: The confocal images of KLA-ESP_{100}-GNPs (**40**) in HeLa cells. (Conc.: 10 μM, Incubation time: 24 h). Bar 15 μm.

3.7 Conclusions

In this chapter, we have demonstrated the formation of several peptide functionalized GNPs. The first system was ELP-GNPs (**30**) which used short elastin-like peptides to functionalize GNPs. The conformation and aggregation properties of the ELP-GNPs (**30**) in aqueous solution were observed by transmission electron microscopy (TEM), circular dichroism (CD) and UV-Vis spectroscopy. Under normal physiological conditions, ELP-GNPs (**30**) had a red colour in aqueous solution, but as the temperature of the solution was raised to 70^{o}C, the colour changed to a red-purple colour. In addition, the secondary structure of ELP-GNPs (**30**) was found to change from random coil to a mixture of α-helix and β-turn structures when the temperature was gradually increased.

The TEM images and DLS also indicated the aggregation of ELP-GNPs (**30**) at higher temperatures.

The second system used elastin-based side chain polymers to functionalize GNPs. The thermo-responsive polymer PF_{100}-GABA(VPGVG) (**29**) was attached to GNPs through the formation of gold-thiol bonds. The conformation and aggregation properties of ESP_{100}-GNPs (**32**) in aqueous solution were investigated by UV-Vis spectroscopy. The results showed that the hybrid ESP_{100}-GNPs (**32**) have similar thermo-responsive character to the 'free' elastin-based side chain polymers. When the temperature was increased, the GNPs aqueous solution changed colour from red to purple, and this was accompanied by a red shift from 532 nm to 540 nm. CD spectra of ESP_{100}-GNPs (**32**) also supported aggregate formation when the temperature was increased from 10 to 65^{o}C. The transition temperature of ESP_{100}-GNPs was found to be around 45^{o}C.

In the third system, the anti-cancer peptide $_{D}(KLAKLAK)_2$ (**33**), was synthesised and characterized. The pro-apoptotic peptide $_{D}(KLAKLAK)_2$ was conjugated to the surface of GNPs via a gold-thiol linker. The MTT results show that KLA-GNPs (**39**) have enhanced anti-cancer properties over free KLA. It was hypothesised that the enhanced activity was due to the ability of **39** to enter cancer cells. Confocal microscopy images of KLA-GNPs (**39**) confirmed their ability to localize into cells by endocytosis, even specifically into mitochondria.

In the final system, the KLA peptide and ESP_{100} were used to functionalize GNPs in a 1:1 weight ratio. The KLA-ESP_{100}-GNPs (**40**) were characterized by UV-Vis and CD experiments. These results indicated that ESP_{100} was linked to the surface of GNPs and endowed GNPs thermo-responsibility. Cytotoxicity of KLA-ESP_{100}-GNPs was tested in HeLa cells and MRC-5 cells at 37°C or 42°C. However, the cells' viability was not much different between 42°C and 37°C and showed no selectivity between cancer cells and normal cells. In addition, confocal imaging showed no penetration inside the cells probably due to the big size of KLA-ESP_{100}-GNPs (**40**). In the future, more experiments will be designed and performed to investigate this hypothesis.

In summary, the different peptides endowed the GNPs with different properties. The elastin-like peptide, elastin-based side chain polymers and anti-cancer peptide may be

applied as capping ligands to make hybrid systems with GNPs which could be used in cancer therapy.

3.8 References

1. M.-C. Daniel and D. Astruc, *Chem. Rev.*, 2004, **104**, 293-346.
2. S. Eustis and M. A. El-Sayed, *Chem. Soc. Rev.*, 2006, **35**, 209-217.
3. F. Porta, Z. e. Krpetić, L. Prati, A. Gaiassi and G. Scarì, *Langmuir*, 2008, **24**, 7061-7064.
4. P. M. Shem, R. Sardar and J. S. Shumaker-Parry, *Langmuir*, 2009, **25**, 13279-13283.
5. J. Thundimadathil, *J. Amino Acids*, 2012, 1-13. DOI: 10.1155/2012/967347.
6. C. Borghouts, C. Kunz and B. Groner, *J. Pept. Sci.*, 2005, **11**, 713-726.
7. P. M. Tiwari, K. Vig, V. A. Dennis and S. R. Singh, *Nanomaterials*, 2011, **1**, 31-63.
8. L. A. Dykman and N. G. Khlebtsov, *Chem. Rev.*, 2013.
9. S. Rana, A. Bajaj, R. Mout and V. M. Rotello, *Adv. Drug Deliv. Rev.*, 2012, **64**, 200-216.
10. R. M. Levine, C. M. Scott and E. Kokkoli, *Soft Matter*, 2013, **9**, 985-1004.
11. S. Si and T. K. Mandal, *Langmuir*, 2007, **23**, 190-195.
12. M. Faraday, *Philos. Trans. R. Soc. Lond.*, 1857, **147**, 145-181.
13. J. Turkevich, P. Stevenson and J. Hillier, *Discuss. Faraday Soc.*, 1951, **11**, 55-75.
14. G. Frens, *Nature*, 1973, **241**, 20-22.
15. M. Haruta, *Catal.Today*, 1997, **36**, 153-166.
16. W. Cai, T. Gao, H. Hong and J. Sun, *Nanotechnol. Sci. Appl.*, 2008, **2008**.
17. J. Turkevich, P. C. Stevenson and J. Hillier, *Discuss. Faraday Soc.*, 1951, **11**, 55-75.
18. M. J. Hostetler, A. C. Templeton and R. W. Murray, *Langmuir*, 1999, **15**, 3782-3789.
19. A. C. Templeton, W. P. Wuelfing and R. W. Murray, *Acc. Chem. Res.*, 2000, **33**, 27-36.
20. R. Lévy, N. T. Thanh, R. C. Doty, I. Hussain, R. J. Nichols, D. J. Schiffrin, M. Brust and D. G. Fernig, *J. Am. Chem. Soc.*, 2004, **126**, 10076-10084.
21. Z. e. Krpetic, P. Nativo, F. Porta and M. Brust, *Bioconjugate Chem.*, 2009, **20**, 619-624.
22. C. Vericat, M. Vela, G. Benitez, P. Carro and R. Salvarezza, *Chem. Soc. Rev.*, 2010, **39**, 1805-1834.
23. S.-Y. Lin, Y.-T. Tsai, C.-C. Chen, C.-M. Lin and C.-H. Chen, *J. Phys. Chem. B*, 2004, **108**, 2134-2139.
24. R. R. Bhattacharjee, A. K. Das, D. Haldar, S. Si, A. Banerjee and T. K. Mandal, *J. Nanosci. Nanotechnol.*, 2005, **5**, 1141-1147.
25. I. Pujols-Ayala, C. A. Sacksteder and B. A. Barry, *J. Am. Chem. Soc.*, 2003, **125**, 7536-7538.
26. H.-G. Hur and J. Kim, US Patent 20,130,123,466, 2013.
27. W. Xie, L. Wang, Y. Zhang, L. Su, A. Shen, J. Tan and J. Hu, *Bioconjugate Chem.*, 2009, **20**, 768-773.
28. D. Bartczak and A. G. Kanaras, *Langmuir*, 2011, **27**, 10119-10123.
29. S. Si, A. Kotal and T. K. Mandal, *J. Phys. Chem. C*, 2007, **111**, 1248-1255.

30. V. K. Saxena, R. Deb, S. Shrivastava, C. Kantaraja, A. Kumar and S. Kumar, *Res. Vet. Sci.*, 2012, **93**, 1531-1536.
31. R. Chandrawati and M. M. Stevens, *Chem. Commun.*, 2014, **50**, 5431-5434.
32. B. D. Chithrani and W. C. Chan, *Nano Lett.*, 2007, **7**, 1542-1550.
33. J. M. de la Fuente and C. C. Berry, *Bioconjugate Chem.*, 2005, **16**, 1176-1180.
34. R. Lévy, *ChemBioChem*, 2006, **7**, 1141-1145.
35. R. Shukla, E. Hill, X. Shi, J. Kim, M. C. Muniz, K. Sun and J. R. Baker, *Soft Matter*, 2008, **4**, 2160-2163.
36. M. J. Kogan, I. Olmedo, L. Hosta, A. R Guerrero, L. J. Cruz and F. Albericio, *Nanomedicine*, 2007, **2**, 287-306.
37. Z. J. Li and C. H. Cho, *J Transl Med*, 2012, **10**, S1.
38. S. Dufort, L. Sancey, A. Hurbin, S. Foillard, D. Boturyn, P. Dumy and J.-L. Coll, *J. Drug. Target.*, 2011, **19**, 582-588.
39. D. Arosio, L. Manzoni, E. M. Araldi and C. Scolastico, *Bioconjugate Chem.*, 2011, **22**, 664-672.
40. P. Ghosh, X. Yang, R. Arvizo, Z.-J. Zhu, S. S. Agasti, Z. Mo and V. M. Rotello, *J. Am. Chem. Soc. Rev.*, 2010, **132**, 2642-2645.
41. N. Chanda, V. Kattumuri, R. Shukla, A. Zambre, K. Katti, A. Upendran, R. R. Kulkarni, P. Kan, G. M. Fent and S. W. Casteel, *Proc. Natl. Acad. Sci.*, 2010, **107**, 8760-8765.
42. L. Hosta-Rigau, I. Olmedo, J. Arbiol, L. J. Cruz, M. J. Kogan and F. Albericio, *Bioconjugate Chem.*, 2010, **21**, 1070-1078.
43. A. Kumar, H. Ma, X. Zhang, K. Huang, S. Jin, J. Liu, T. Wei, W. Cao, G. Zou and X.-J. Liang, *Biomaterials*, 2012, **33**, 1180-1189.
44. M. I. Gibson and R. K. O'Reilly, *Chem. Soc. Rev.*, 2013, **42**, 7204-7213.
45. D. W. Urry, R. G. Shaw and K. U. Prasad, *Biochem. Biophys. Res. Commun.*, 1985, **130**, 50-57.
46. H. Reiersen, A. R. Clarke and A. R. Rees, *J Mol Biol*, 1998, **283**, 255-264.
47. V. Lemieux, P. H. H. M. Adams and J. C. M. van Hest, *Chem. Commun.*, 2010, **46**, 3071-3073.

Chapter 4: Cell-penetrating peptoids as a delivery method for apoptotic peptide KLA

4.1 Introduction

4.1.1 Antimicrobial peptides as a new class of anti-cancer agents

Recently, peptides have attracted increasing attention in cancer chemotherapy due to their ease of synthesis, low immunogenicity and target specificity.[1-3] In particular research has been focused on cationic antimicrobial peptide (AMPs), also termed host defense peptides (HDPs).[4-6] AMPs have been found in almost every living organism including fungi, plants, bacteria and animals and they have been shown to have a broad spectrum of anti-infective activity against bacteria, fungi and viruses.[4] The cell selectivity of most AMPs arises due to the electrostatic interactions between the positively charged AMPs and the negatively charged membranes of bacteria.[6] As the exterior membranes of bacteria are negatively charged, the positively charged antimicrobial peptides preferentially bind to them over mammalian cells, which have neutral membranes. Research has also shown that a significant number of AMPs exhibit anti-cancer activities (**Table 4.1**).[6, 7] The molecular mechanism behind the anti-cancer properties of many AMPs is still not fully understood.

AMPs are typically short, ranging from 5 to 40 amino acids in length. They tend to contain a high number of positively charged residues (Arg or Lys) giving the peptide an overall net charge of between +2 to +9 at neutral pH.[8] AMPs can have a great degree of variation in their secondary structures. Most linear AMPs, for example the magainins, are unstructured in diluted aqueous solution, only become alpha-helical in amphipathic media, such as membranes or micelles.[9] LL37, also a linear peptide, but an exception, shows helical structure in aqueous solution. Tachyplesin 1, a cyclic peptide, forms a β-sheet due to the presence of disulphide bonds.

Table 4.1: Summary of select naturally occurring cationic antimicrobial peptides (AMPs) with anti-cancer activities.[6]

Peptide	Origin Source	Primary amino acid sequence [a]	Class	Anti-cancer Activities
BMAP-28	*Cow*	GGL**R**SLG**RK**IL**R**AW**K** **K**YGPIIVPII**R**I	α-Helix	Membranolytic
HNP-1 (β-defensin)	*Human*	AC_1YC_2**R**IPAC_3IAGE**RR** YGTC_2IYQG**R**LWAFC_3 C_1	β-sheet	Membranolytic
Lactoferricin B	*Cow*	F**K**C_1**RR**WQW**R**M**KK**L GAPSITC_1V**RR**AF	β-sheet	Membranolytic, Apoptosis inducer, Antiangiogentic
LL-37	*Human*	LLGDFF**RK**S**K**E**K**IG**K**E F**KR**IVQ**R**I**K**DFL**R**NLV P**R**TES	α-Helix	Membranolytic
Magainin 2	*Frog*	GIG**K**FLHSA**KK**FG**K**AF VGEIMNS	α-Helix	Membranolytic
Melittin	*Honeybee*	GIGAVL**K**VLTTGLPAL ISWI**KRKR**QQ	α-Helix	Membranolytic, Phospholipase A_2 activator, Phospholipase D activator
Tachyplesin 1	*Horseshoe Crab*	**K**WC_1F**R**VC_2Y**R**GIC_2Y **RR**C_1**R**	β-sheet	Binds hyaluronan and activates complement ($C1_q$) Induces cancer cell differentiation

[a] Subscripts indicate pairings of Cys residues that form disulphide bonds. Boldface indicates cationic amino acid residues.

The secondary structures of AMPs enhance their amphipathicity, which plays a very important role in their mechanism of antimicrobial action. It is known that membrane surfaces give an amphiphilic environment, the external part is hydrophilic and the internal part is hydrophobic. When AMPs bind to membranes, apart from their structural folding features (net charge, amphipathicity, hydrophobicity, secondary structure), the membrane composition also has an impact on the mechanism of how an AMP executes its function.[10] For bacterial membranes, the surface toward the exterior aqueous phase generally consists of negatively charged phospholipid head groups. For plant and animal membranes, the outer leaflet is populated by neutral lipids and cholesterol.[11]

The mechanism behind the AMP membrane-disruption process has attracted considerable attention and several models have been proposed. An appealing model which explains most AMPs' activities is the Shai-Matsuzaki-Huang (SMH) model.[11-13] The SMH model suggests that the peptide causes cell death by inserting into the bacterial membrane and creating a pore through which cellular contents leak out.[14] In this process the first step involves the peptide binding to the cell surface, and this is then followed by displacement of lipids resulting in thinning of the membrane. Finally, the increasing surface tension of the thinned lipid bilayers leads to cell lysis.

Four models are commonly used to describe the activity of AMPs and their insertion into membranes, these are the carpet model, the barrel-stave model, the toroidal-pore model and the detergent-like model.[15] As shown in **Figure 4.1**, in the carpet model, the most commonly found model, the AMP binds to the surface of membrane in a carpet-like manner. The penetration of the peptide occurs if the concentration of peptide covering the membrane is high.[12] In the barrel-stave model, specific peptide-peptide interaction between the AMPs occurs leading to the formation of a ion-channel pore.[12] In the toroidal-pore model, AMPs insert into the membrane and affect the surface bilayer in a cooperative way which increases curvature strain on the membrane surface and leads to the formation of toroid-pores.[15] These pores form at a threshold concentration of AMPs, an early step before the collapse of the membrane. In the detergent-like model, when the peptide carpet is at high concentration, the aggregation peptides behave like detergents resulting in catastrophic collapse of lipid membranes into small fragments.[16]

It has been found that certain AMPs have the ability to selectively target and kill cancer cells while sparing healthy cells. The fundamental difference in charge between the cell membranes of normal cells and malignant tumour cells is suggested as the reason behind this selective lytic activity.[17] Cancer cell membranes, typically present overall net negative charge due to a high percentage of anionic molecules such as phosphatidylserine (PS) and O-glycosylated mucines.[18, 19] In addition, the number of microvilli on cancer cells is higher than on normal healthy cells which enlarge the surface binding area for AMPs.[20]

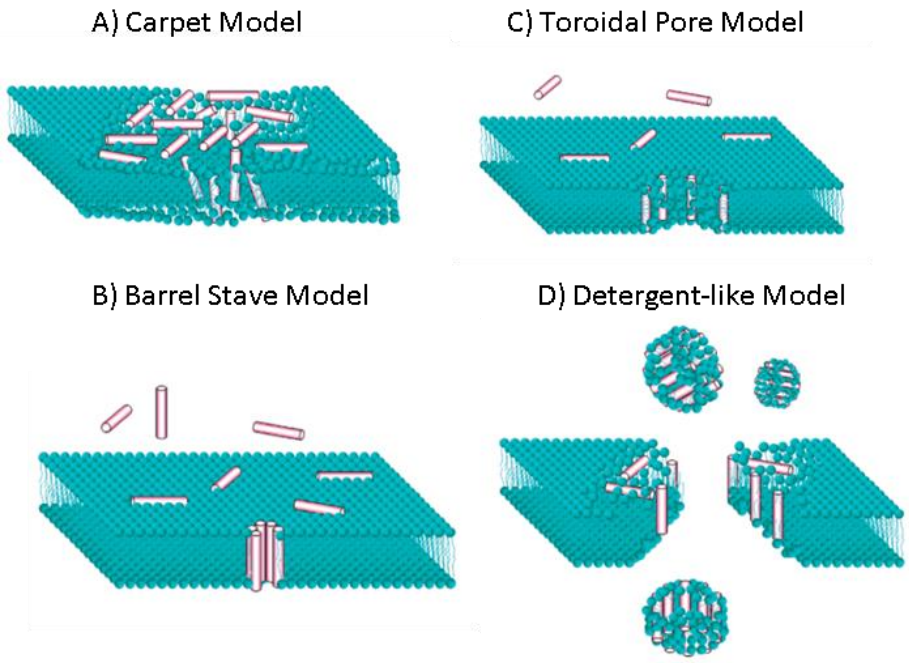

Figure 4.1: Models of AMP-induced membrane permeabilization. Reprinted from [15] with permission from American Chemical Society, copyright © 2010.

4.1.2 Anti-cancer activity of KLA peptide

It is known that the amphipathic α-helix is a common structural feature of many AMPs isolated from nature. Therefore, novel peptides with a amphipathic α-helix structure have been designed and investigated for their biological activities (antimicrobial and anti-cancer) [21, 22] Of these newly designed peptides, one of the most widely studied is $_D$-(klaklak)$_2$ (KLA peptide), which has been shown to have both significant antimicrobial and anti-cancer activities.[23, 24]

In 1996, McLaughlin *et al.*[25] designed a series of L-configured amphipathic α-helical peptides with the common sequences $[(PNN)P(PNN)]_n$ and $[(PNN)(PNN)K)]_n$ with P equal to a polar residue, N equal to Leu, Ala or Gly. The repetitive heptad approach was used to design sequences that place *i* and *i* +7 residues next to each other on helical wheels.[25, 26] Lys was chosen as the polar residue due to its high helical propensity, as were Leu and Ala. Antibacterial activities of all designed peptides against *Escherichia coli*, *Pseudomonas aeruginosa* and *Staphylococcus aureus* were tested. They found that $(KLAKLAK)_n$ (n=2 or 3) had the greatest antibacterial activities and relatively low cytotoxicities towards human erythrocytes. However, it should also be noted that $(KLAKLAK)_3$ does display strong cytotoxicity against mouse embryo fibroblast (3T3 cells) with MIC (minimum inhibitory concentration) value 9 μM.[25]

Subsequently, Ellerby and colleagues[23] demonstrated that shorter 14-mers such as $_D$-(KLAKLAK)$_2$ also have the ability to induce mitochondrial-dependent apoptosis which was proven by a swelling assay performed on rat liver mitochondria. Due to the difference of membrane potentials and charge of phospholipids, KLA peptide targeted the mitochondrial membrane (high potentials, negative charge) rather than the eukaryotic plasma membrane (low potentials, neutral charge).[23] The KLA peptide can induce mild mitochondrial swelling at 3 μM which is only 1% of the concentration required to kill eukaryotic cells. The pro-apoptotic activity of KLA comes from its cationic α-helical amphipathic structure, enabling the compound to induce permeation and swelling of mitochondria, resulting in the release of cytochrome c and cell apoptosis. [27, 28]

Despite promising apoptotic activity, KLA displays very poor permeability to the eukaryotic plasma cell membrane. Two tumour targeting peptides, cyclic peptide CNGRC and the bi-cyclic peptide ACDCRGDCFC (RGD-4C), have been conjugated to KLA to promote cellular uptake via receptor-mediated internalization.[23] A computer-generated model of CNGRC-GG-$_D$(KLAKLAK)$_2$ is shown in **Figure 4.2**.[23] Both conjugates were used to treat nude mice with human tumour xenografts. In both treatments, the volumes of the tumour were on average 10% less that of controlled groups and mice lived several months longer. This positive result indicated that the apoptotic KLA peptide has the potential to be a novel anti-cancer agent if it can be delivered across the plasma cell membrane.

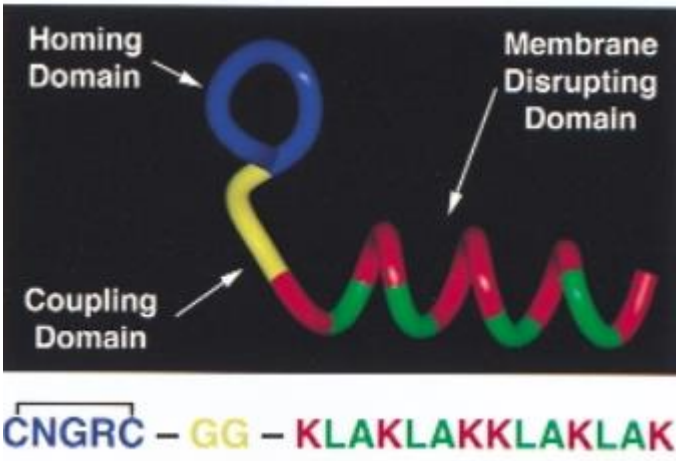

Figure 4.2: A computer generated structure of CNGRC-GG-$_D$(KLAKLAK)$_2$. Reprinted from [23] with permission from Nature Publishing Group, copyright © 1999.

Recently, an increasing area of research has been developing in relation to the design of different tumour-targeting domains combined with KLA. Fusing KLA with the cationic peptide transduction domain (PTD-5) has been tested in a variety of cell lines *in vitro*, such as MCA205 murine fibrosarcomas and human brain tumour cells (22B). The results suggest that KLA-PTD-5 conjugate was able to induce cell apoptosis.[27] Due to the poor cell penetrating ability of KLA, another approach was to fuse a cell penetrating peptide ($_D$-hepta-arginine or R_7) to KLA. The D-forms of both KLA and the cell penetrating peptide afforded better properties, such as cell permeability, resistance to protease degradation and efficient apoptosis both *in vitro* and *in vivo*.[29] This combination R_7-KLA was not designed for a specific tumour type, but had an average high cell toxicity (IC_{50} values in the range of 3-25 μM) against several different tumour cell lines (such as HeLa, fibrosarcoma and Lewis lung carcinoma). In comparison with other clinically-used anti-cancer agents, R_7-KLA showed faster kinetics of cell killing. The KLA was also conjugated to a prostate-specific membrane antigen (PSMA) peptide. This peptide conjugate (PSMA-KLA) was found to induce apoptosis in a human prostate cancer cell line with an LC_{50} 19 μM.[30] The PSMA-KLA fusion peptide selectively induced cell death in PSMA-expressing cells, thereby offering a potential therapeutic for prostate cancer.

The examples discussed above demonstrate the potential approach of combining a targeting peptide with KLA to produce a highly efficacious anti-cancer agent. Research has also been done to improve the efficacy and selectivity of KLA via conjugation to short cyclic peptides[31], nanoparticles[32-34], self-assembling peptide amphiphilic nanofibers[35] and cell penetrating peptides.[27, 29, 36-38] All these methods have improved the cellular delivery of KLA to a certain extent, however, new and efficient ways to deliver KLA into cancer cells are still needed.

4.1.3 Cell penetrating peptoids (CPPos)

Compared to antibodies, peptides, due to their smaller size, have the potential advantage of penetrating further into tissues, organs and tumours.[39, 40] During the last decade, cell penetrating peptides (CPPs) have been developed extensively and applied to CPP-based drug delivery strategies. However, despite success in the laboratory, CPPs are still generally considered to be poor candidates for the development of therapeutics due to their low stabilities in plasma, sensitivity to proteases and a short half-life.[2]

Cell penetrating peptoids (CPPos) offer a promising alternative to CPPs, as they preserve the key chemical and physical properties of CPPs. The increasing interest of newly designed peptoids is due to the most advantageous feature of a peptoids' structure, which is the stability of the repeating *N*-alkyl amide backbone unit, which renders it highly resistant towards degradation by proteases.[41]

Peptoids are comprised of repeating oligo-*N*-substituted glycine units.[42] The backbone sequence of peptoids is identical to that of peptides, with the difference in the structure arising to the position of the side chain appendage. The side chains in peptoids are attached to the nitrogen atoms of the backbone, rather than the carbon atoms (**Figure 4.3**).[43] Peptoid backbones contain no chiral centres (chiral alpha-carbon atom) and they lack a hydrogen bond donor capacity (NH group). Thus, controlling a peptoid's secondary structure e.g. helix or β-sheet is more challenging. However, chirality can be introduced into the peptoid monomer side chains, enabling a stable secondary structure to be obtained.[44-46]

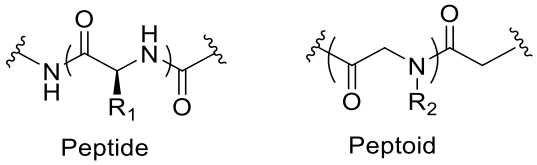

Figure 4.3: Comparison of the primary structure of peptide and peptoid oligmers.[43]

Peptoid synthesis is easy, cost-effective and efficient. The most common approach used is known as the solid phase sub-momoner strategy and this is shown in **Figure 4.4**. In the 'sub-monomer' approach, the *N*-subsitituted glycine monomer is generated from a two step process: bromacetic acid and a primary amine.

In the first step, bromoacetic acid in the presence of *N*,*N*-diisopropylcarbodiimide (DIC) is reacted with resin-bound secondary amine; this reaction is termed bromoacetylation. In the second step, an excess of primary amine replaces the resin-bound bromide via nucleopholic displacement. Bromoacetylation and amine displacement steps are repeated to obtain each monomer until the full peptoid sequence is achieved. Compared with solid-phase peptide synthesis (SPPS), the acylation of sercondary amines is more efficiently achieved by using bromoacetic acid than *N*-substituted glycine. In addition, due to the vast number of commercially availabe primary amines, this sub-monomer

appraoch has been greatly advanced to prepare novel designed peptoids. The high yields of each step allow the growth of peptoid chains, which can be up to 48 residues.[47]

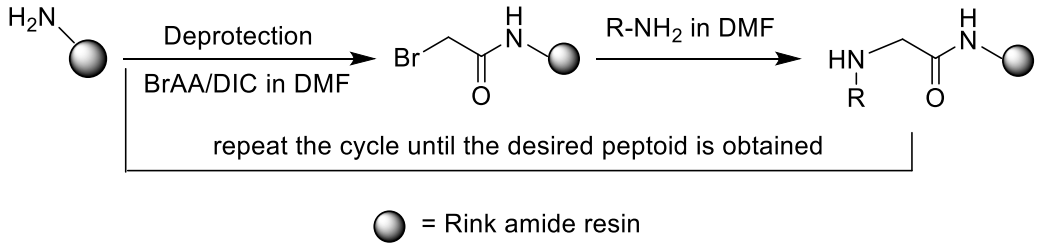

Figure 4.4: Solid-phase sub-monomer peptoid synthesis.

Generally, cell penetrating peptides (CPPs) include many polycationic amino acids in the sequence, such as Lys (lysine), Arg (arginine) and Orn (ornithine) which facilitate cell membrane uptake. By introducing cationic side chains into peptoids, similar physical and chemical properties to CPPs are retained in the corresponding CPPos. For example, a peptidomimetic form of Tat_{49-57} has been synthesised and achieves a similar function of preventing HIV replication and improving membrane translocation activity.[48, 49]

More research has been carried out to demonstrate that short peptoids have great advantages in drug delivery system.[50] Recently, Kölmel *et al.*[51] demonstrated that short CPPos can enter cells and even have organelle specificity. A range of side chains can be chosen to form novel CPPos, giving rise to different organelle targeting specificity such as the nucleus or mitochondria. As shown in **Figure 4.5**, four different sequences of rhodamine-labelled CPPos (**I**-**IV**) were listed on the left and their fluorescence confocal images of incubated HeLa cells after 24 h are shown on the right. Co-localization experiments were performed by co-staining the nuclei and mitochondria with Hoechst 33342 (blue: A, E, I, M) and Mitochondria Green™ (green: B, F, J, N) separately. Rhodamine B labelled peptoids (**I**-**IV**) were detected at 593-696 nm emission channels (red: C, G, K, O). Images D, H, L, P show the merges of these three different emission channels of each line. These four CPPos have all shown ability to be taken up by the cells and the locations of **I** to **IV** gradually change from nucleus to mitochondria.

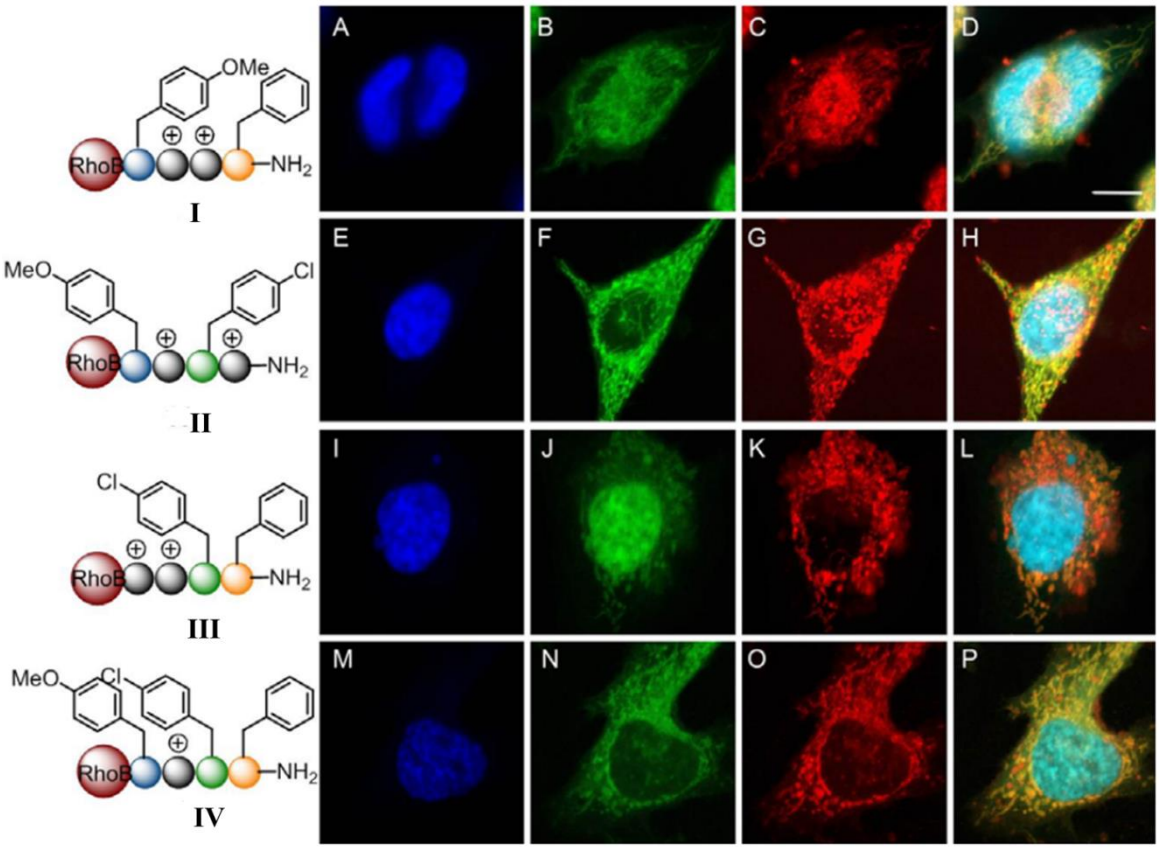

Figure 4.5: Cellular uptake of Rhodamine labelled CPPos **I-IV** in HeLa cells. 1 x 10^4 HeLa cells were treated with 1 μM of peptoid **I** (A-D), **II** (E-H), **III** (I-L), and **IV** (M-P) for 24 h at 37°C. Reproduced from [51] with permission from Pharmaceuticals.

4.1.4 Chapter aims

Our aim is to conjugate the anti-cancer peptide KLA to a series of cell penetrating peptoids (CPPos) to prepare a series of peptoid-peptide hybrids (CPPos-KLA). The investigation of anti-cancer, antimicrobial and cell penetrating properties of the hybrids will then be carried out. The anti-cancer properties of the CPPos-KLA conjugates will be analysed against HeLa cells. Differences in the side chains of CPPos makes a difference to the location of KLA peptide in cells.[51] Confocal experiments will be performed to confirm the specificity into the mitochondria area of Rhodamine B labelled KLA-CPPo6. For the antimicrobial behaviour, $_D$-/$_L$-KLA and two CPPos-KLA will be evaluated against *Staphylococcus aureus*, *Escherichia coli*, *Serratia marcescens* and *Pseudomonas aeruginosa*.

4.2 Synthesis of KLA peptide

In order to compare the effects of stereochemistry of their biological properties, both $_D$-KLA (**33**) and $_L$-KLA (**41**) were synthesised (**Figure 4.6**).

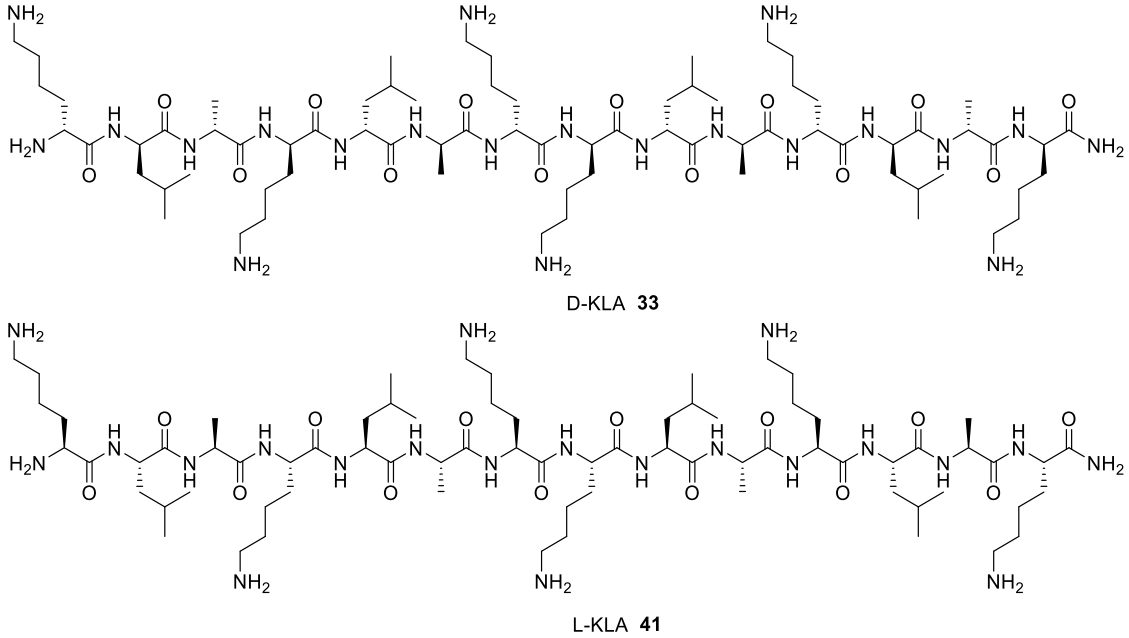

Figure 4.6: The structures of $_D$-/$_L$-KLA peptides.

The synthesis of $_D$-KLA (**33**) was achieved using Fmoc-protected D-amino acids and solid phase peptide synthesis. The coupling of each residue was undertaken twice (i.e. double coupling) in order to make sure each step had gone to completion.

Semi-preparative reverse phase HPLC was used to purify the crude peptide (as described in **Section 6.1.2.5**. A sample of crude peptide **33** (7~10 mg mL^{-1}) was dissolved in water and analysed using a gradient of 0%-55% solvent B in 40 min and 55%-100% solvent B in 10 min. The flow rate was set to 2.0 mL/min and the detector monitored absorbance at 220 nm. The peptide was the main peak at RT= 18.1 min (**Figure 4.7**). The yield of purified peptide **33** after RP-HPLC was 15%. After purification, a small sample of the peptide was dissolved in water and analyzed by analytical HPLC, MALDI, LC-MS and HRMS (accurate mass). The analytical HPLC trace is shown in **Figure 4.8**. The molecular weight of $_D$-KLA peptide was analysed by MALDI and found to be 1544.9, which is $[M+ Na]^+$ as shown in **Appendix 4.1**. The LC-MS data was $[M+3H]^{3+}$ 508.5, $[M+4H]^{4+}$ 381.7. HRMS m/z (ESI) 1523.0907, consistent with empirical formula $C_{72}H_{138}N_{21}O_{14}$ with an accuracy of 1.18 ppm (accepted as $(M + H)^+$).

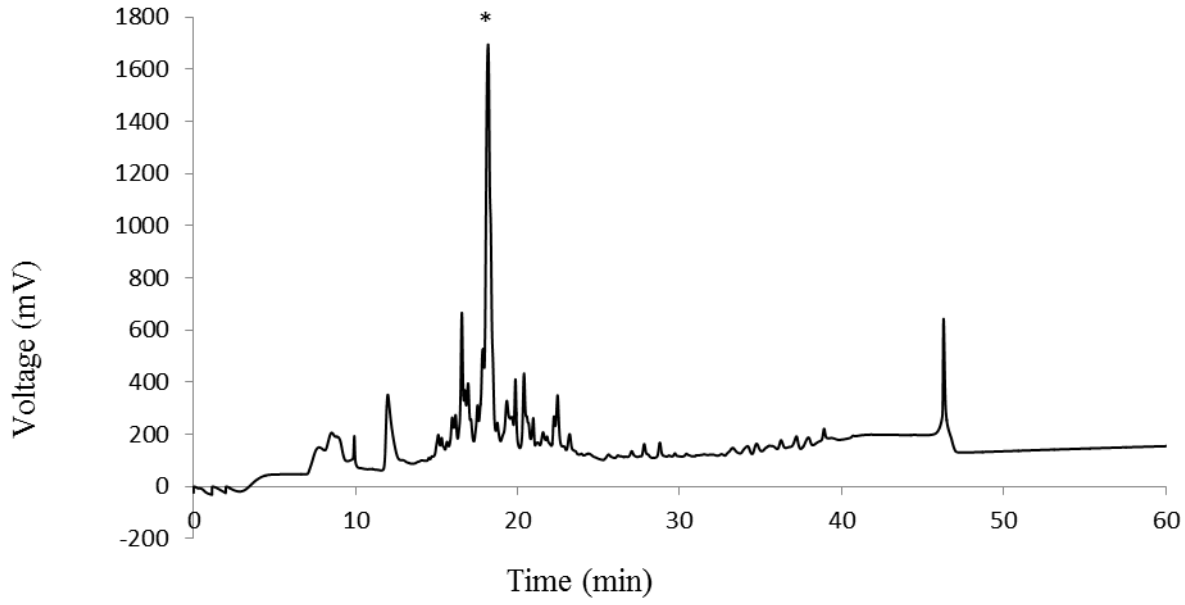

Figure 4.7: Semi-preparative HPLC chromatograph of $_{D}$-KLA peptide. HPLC purification was carried out on a semi-preparative column (C18, 250 x 10 mm, 5 µm particle size). The peptide was eluted in H_2O/MeCN +0.1% trifluoroacetic acid. Peptide **33** had a retention time = 18.1 min*.

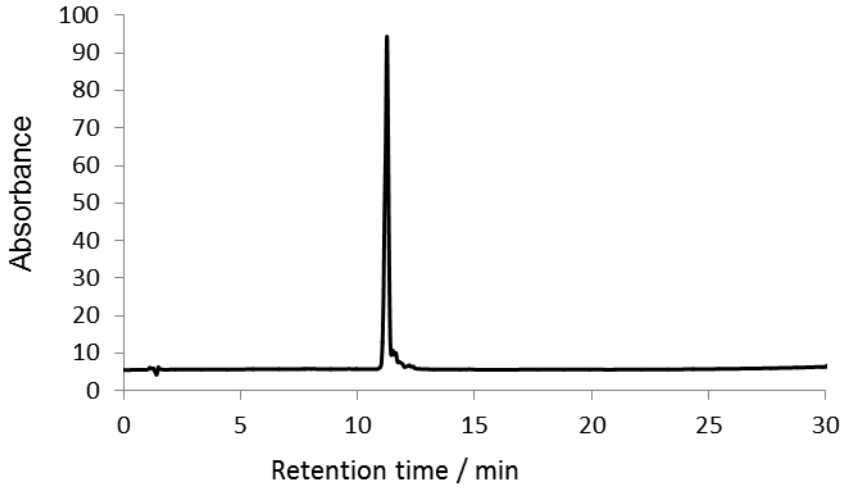

Figure 4.8: Analytical HPLC trace of purified $_{D}$-KLA peptide (**33**) using a linear gradient of 0-100% of solvent B ((*v/v*) 5% H_2O/95% CH_3CN with 0.1 TFA) over 30 min. Retention time = 11.4 min.

$_{L}$-KLA (**41**) was synthesised using the same method as $_{D}$-KLA (**33**) but with Fmoc protected L-amino acids. Semi-preparative reverse phase HPLC was used to purify crude **41** and the yield was 16%. After purification, a small sample of freeze-dried **41** (1 mg/mL) was dissolved in water and analyzed by analytical HPLC, MALDI, LC-MS and

HRMS (accurate mass). The analytical HPLC trace is shown in **Figure 4.9**. The retention time of the peak is 11.4 min and a very little impurity peak can be seen. The molecular weight of $_{L}$-KLA peptide was analysed by MALDI and found to be 1546.1 which is $[M+ Na]^{+}$. The LC-MS data was $[M+3H]^{3+}$ 508.3, $[M+4H]^{4+}$ 381.6. HRMS m/z (ESI) 1523.0878, consistent with empirical formula $C_{72}H_{138}N_{21}O_{14}$ with an accuracy of 0.72 ppm (accepted as $(M + H)^{+}$). The characterization of $_{L}$-KLA (**41**) has been attached in **Appendix 4.2**.

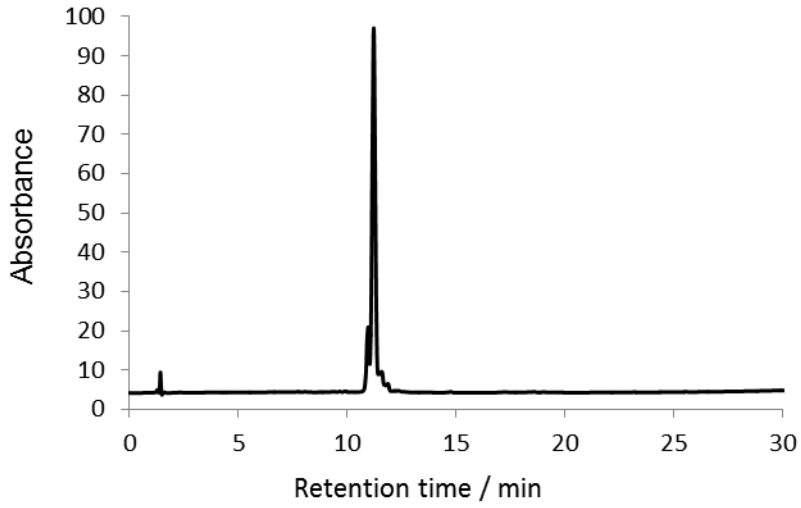

Figure 4.9: Analytical HPLC trace of $_{L}$-KLA peptide (**41**) using a linear gradient of 0-100% of solvent B ((*v/v*) 5% H_2O/95% CH_3CN with 0.1 TFA) over 30 min. Retention time = 11.4 min.

To investigate the secondary structure of $_{D}$-KLA (**33**) and $_{L}$-KLA (**41**), circular dichroism (CD) spectroscopy was used. As shown in **Figure 4.10**, as expected the peptides $_{D}$-KLA (**33**) and $_{L}$-KLA (**41**) have mirror image CD spectra. For $_{D}$-KLA (**33**), the positive bands near 208 nm and 230 nm are indicative of a random coil conformation. It is apparent that $_{L}$-KLA displays the same conformation as $_{D}$-KLA in aqueous buffer. For most linear cationic peptides, they are unstructured in diluted aqueous solution and turn to alpha-helical in membranes.

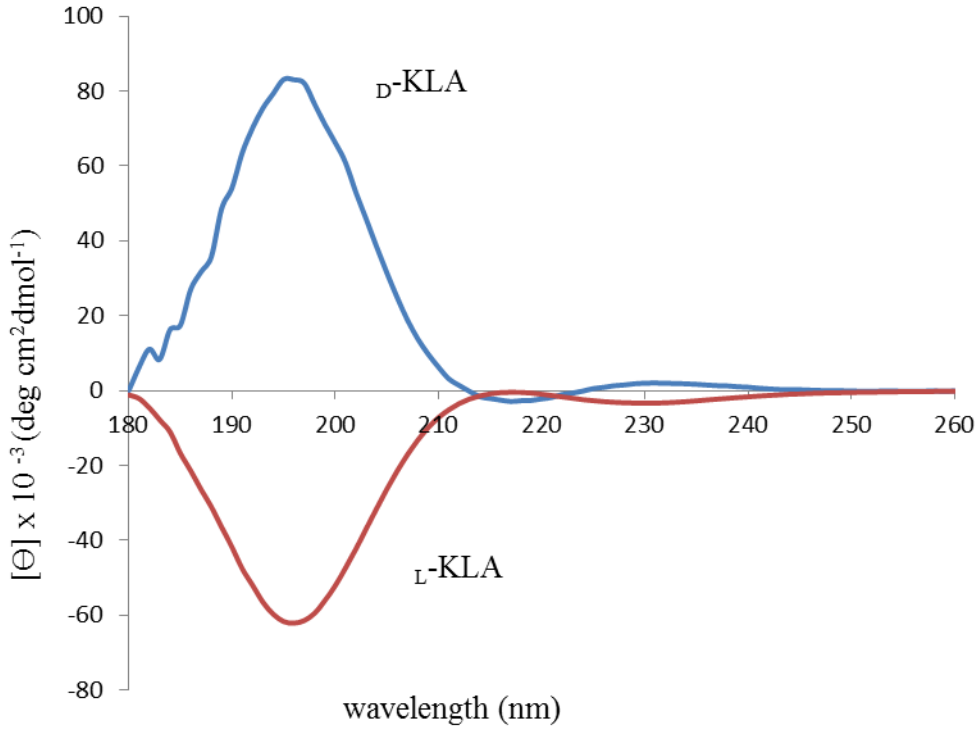

Figure 4.10: CD spectra of $_{D}$-/$_{L}$-KLA peptide in PBS buffer.

4.3 Synthesis of peptoid hybrids

4.3.1 CPPos

The peptoids were synthesised manually on resin using the sub-monomer method[22] on a shaker. The synthetic approach used to prepare all peptoids is detailed in **Figure 4.4** and discussed in **Section 4.1.3**.

The CPPos library used was designed by Kölmel *et al.*[51] have combinations of hydrophobic and hydrophilic submonomers and the total length is four. All the peptoids have at least one positive charge which gives them the ability to act as CPPos. Also, the third position of all the sequences was fixed to have a cationic and hydrophilic side chain. The other three positions were variable and modulated by replacing more hydrophobic submonomers for hydrophilic ones. Four different submonomers were used and their structures are shown in **Figure 4.11**. The peptoid syntheses were processed via applying the Boc protected diamine (**42**), benzylamine (**43**), *p*-chlorobenzylamine (**44**) and *p*-methoxybenzylamine (**45**). The Boc group of **42** was removed after the acid cleavage from the resin. In aqueous solution, the side chain of

submonomer **42** will provide a positive charge due to its protonation. The other three submonomers **43-45** can provide variable hydrophobicity into the sequence. Based on the different name of submonomers, the peptoid monomer can be name as Nlys, Nphe, Npcb and Npmb as shown in **Figure 4.11**.

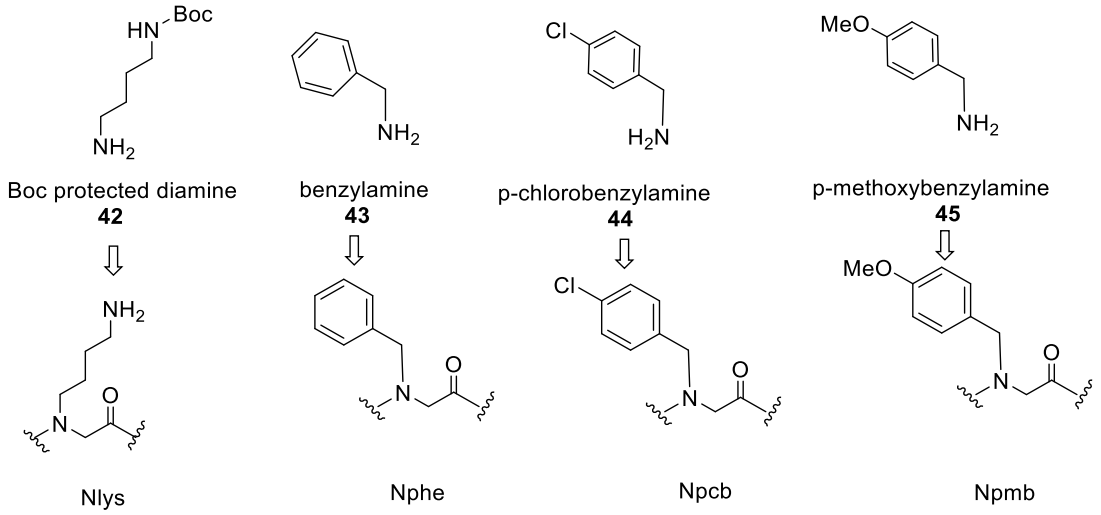

Figure 4.11: The structures of submonomers **42**-**45**, the annotation of peptoid monomers (Nlys, Nphe, Npcb, Npbm).

The original peptoid synthesis method, describing as oligomers of *N*-substituted glycine residues, was first discovered by Zuckermann *et al.* in 1992. Subsequently, increasing research has been done due to the highly efficient sub-monomer solid phase synthesis strategy. The peptoid oligomers were manually synthesised by the solid-phase sub-monomer method. Rink amide resin was swelled in DMF overnight at room temperature. The resin was treated with 20% piperidine in DMF to remove the Fmoc group. Solutions of bromoacetic acid and DIC were added into the resin. The reaction tube was placed on the shaker for 20 min at room temperature. The resin was washed with DMF before the desired amine monomer was added for 60 min on the shaker. Bromoacetylation and amine displacement (**Figure 4.4**) steps were repeated until the final monomer had been added. This procedure was repeated four times to obtain each peptoid. With the synthesis of the peptoid complete two Gly residue were coupled to the N-terminus to provide a spacer between the peptoid and peptide.

To test cleavage of the peptoid from the resin, a solution of 1 mL TFA, TIPS and H_2O (95:2.5:2.5) was added to the resin and this was left for 120 min at room temperature on the shaker. The resin was rinsed once with 0.5 mL TFA. Then the resin was removed by

filtration and the obtained peptoid was precipitated in diethyl ether. The product was then dissolved in water and freeze dried. The crude peptoids were analysed by LC-MS. The structures of all CPPos are shown in **Figure 4.12**. All the LC-MS data were shown in **Table 4.2**.

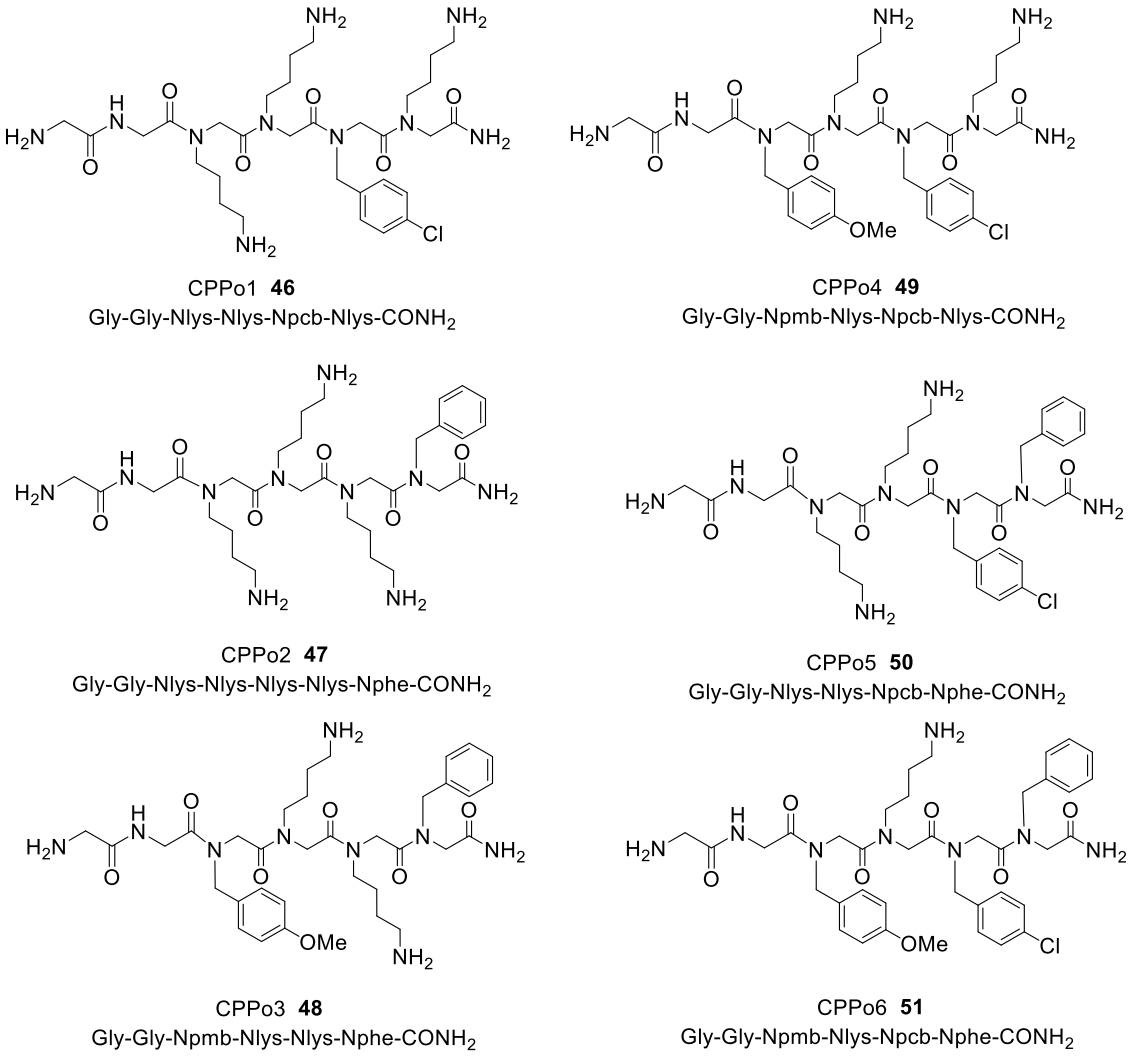

Figure 4.12: The structures of cell penetrating peptoids **46-51**.

Table 4.2: Summary of all peptoids prepared.

Name	Sequence	Molecular weight	Observed mass
Fmoc-CPPo 1 (**46**)	Fmoc-GGNlysNlysNpcbNlys	910.52	460.1 ($M+2H^+$)
Fmoc-CPPo 2 (**47**)	Fmoc-GGNlysNlysNlysNphe	885.08	443.2 ($M+2H^+$)
CPPo 3 (**48**)	GGNpmbNlysNlysNphe	711.40	356.8($M+2H^+$)
CPPo 4 (**49**)	GGNpmbNlysNpcbNlys	745.36	746.3 ($M+H^+$)
CPPo 5 (**50**)	GGNlysNlysNpcbNphe	715.35	358.7($M+2H^+$)
CPPo 6 (**51**)	GGNpmbNlysNpcbNphe	764.34	764.8($M+H^+$)

4.3.2 KLA-CPPos

The KLA peptide was added to each of the peptoids after the Gly-Gly spacer using Fmoc SPPS (**Figure 4.13**). **Table 4.3** shows all the sequences of the peptide $_D$-KLA (**33**) and peptide-peptoid hybrids **52**-**57**. The synthesis and purification process were the same as described for $_D$-KLA (**33**). Semi-preparative HPLC was used to purify as a standard method, which was described in **Section 6.1.2.5**. After purification, a small sample of each peptide-peptoid hybrid was dissolved in water and analyzed by analytical HPLC, MALDI, LC-MS and accurate mass analysis. Detailed characteristic data is given in **Appendices 4.3** to **4.8**. Here, we summarize hybrids characterization as shown in **Table 4.4** and **4.5**.

Table 4.3: Sequences of peptide-peptoid hybrids prepared

Compound	Peptide-Peptoid Hybrid Sequence
KLA-CPPo1 (**52**)	H-$(klaklak)_2$-GG-NlysNlysNpcbNlys-NH_2
KLA-CPPo2 (**53**)	H-$(klaklak)_2$-GG-NlysNlysNlysNphe-NH_2
KLA-CPPo3 (**54**)	H-$(klaklak)_2$-GG-NpmbNlysNlysNphe-NH_2
KLA-CPPo4 (**55**)	H-$(klaklak)_2$-GG-NpmbNlysNpcbNlys-NH_2
KLA-CPPo5 (**56**)	H-$(klaklak)_2$-GG-NlysNlysNpcbNphe-NH_2
KLA-CPPo6 (**57**)	H-$(klaklak)_2$-GG-NpmbNlysNpcbNphe-NH_2

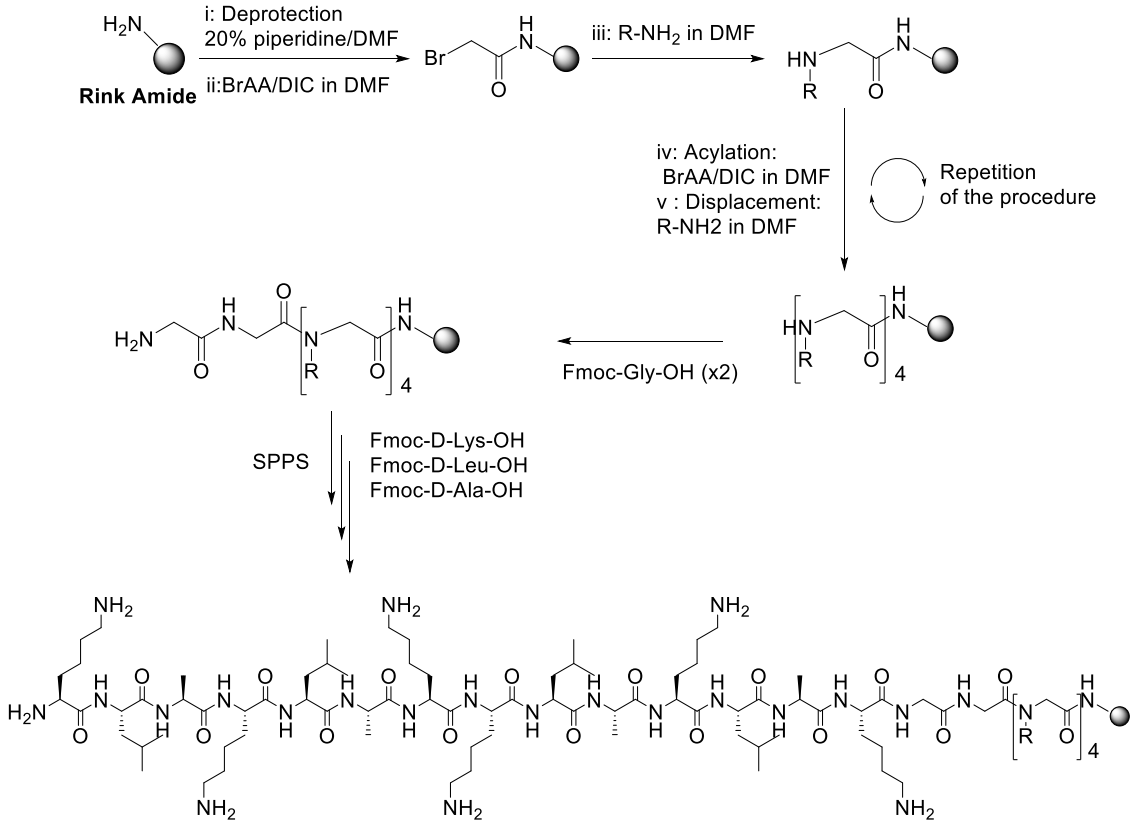

Figure 4.13: Solid phase approach to build up peptide-peptoid hybrids.

Table 4.4: Low resolution ESI-MS data for peptide-peptoid hybrids prepared.

Compounds	**Calculated Mass**	**Observed mass**[a]
KLA-CPPo1 (**52**)	2200.5	441.3 ($5H^+$)
KLA-CPPo2 (**53**)	2167.4	723.6 ($3H^+$), 434.5 ($5H^+$)
KLA-CPPo3 (**54**)	2216.4	1108.8 ($2H^+$), 555.2 ($4H^+$), 444.6 ($5H^+$)
KLA-CPPo4 (**55**)	2250.4	1126.3 ($2H^+$), 563.7 ($4H^+$), 451.3 ($5H^+$)
KLA-CPPo5 (**56**)	2220.4	1112.2 ($2H^+$), 741.4 ($3H^+$), 445.0 ($5H^+$)
KLA-CPPo6 (**57**)	2269.3	1135.6 ($2H^+$), 568.6 ($4H^+$), 455.1 ($5H^+$)

[a] Observed in ESI-MS. Parent peaks were not observed due to the mass range of the instrument (up to *m*/*z* 2000). The observed masses are doubly charged ($2H^+$) and triply charged ($3H^+$) peaks, not fragments.

Table 4.5: MALDI-ToF data for the peptide-peptoid hybrids prepared.

Compounds	Calculated mass	Observed mass[b]
KLA-CPPo1 (**52**)	2200.5	$[M+H]^+$ = 2203.5
KLA-CPPo2 (**53**)	2167.4	$[M+Na]^+$ = 2191.5
KLA-CPPo3 (**54**)	2216.4	$[M+Na]^+$ = 2240.5
KLA-CPPo4 (**55**)	2250.4	$[M+H]^+$ = 2252.9
KLA-CPPo5 (**56**)	2220.4	$[M+Na]^+$ = 2244.4
KLA-CPPo6 (**57**)	2269.3	$[M+Na]^+$ = 2293.2

[b] Observed in MALDI-ToF.

4.3.3 Rhod-KLA-CPPo6 (59)

In order to evaluate the drug delivery capability of KLA-CPPo6 within cell-based assays, KLA-CPPo6 (**57**) was fluorescently tagged with rhodamine B (**58**).

Rhodamine B has been commonly used as a dye in microscopy for biological applications as it is cheap and has a high extinction coefficient. The fluorophore Rhodamine B was coupled to the N-terminus of hybrid **57** via DIC and HOBt in DMF and incubated for 1 hour at room temperature. This process was repeated again to make sure reaction was completed. The final product was cleaved by adding trifluoroacetic acid (TFA, 95%) in DCM and shaking at room temperature for 2.5 h. The cleavage solution was filtered and the resin was thoroughly washed with MeOH until colourless. Due to the intensive colour of the Rhodamine-conjugated hybrid **57**, the process can be monitored visually. Water was added, frozen and lyophilised to give the crude product. Then, semi-preparative HPLC was used to purify **59** as a standard method. After purification, LC-MS analysis and MALDI-TOF MS of Rhod-KLA-CPPo6 (**59**) were taken. The molecular weight of **59** was analysed by MALDI and found to be 2694.6 which is $[M+ H]^+$. The LC-MS data was $[M+2H]^{2+}$ 1347.8, $[M+5H]^{5+}$ 539.7, $[M+6H]^{6+}$ 449.9. HRMS *m/z* (ESI) 540.321, consistent with empirical formula $C_{72}H_{138}N_{21}O_{14}$ with an accuracy of -3.8 ppm (accepted as $(M + 5H)^{5+}$). The characterization of Rhod-KLA-CPPo6 (**59**) is given in **Appendix 4.9**.

It is known that rhodamine B exists in 'nonfluorescent' (**58a**) and 'fluorescent' (**58b**) forms in the equilibrium shown in **Figure 4.14**. The non-fluorescent structure exists as a

closed spirolactam while the fluorescent form has an open structure. The equilibrium is controlled by the number of proton ions in the aqueous media.

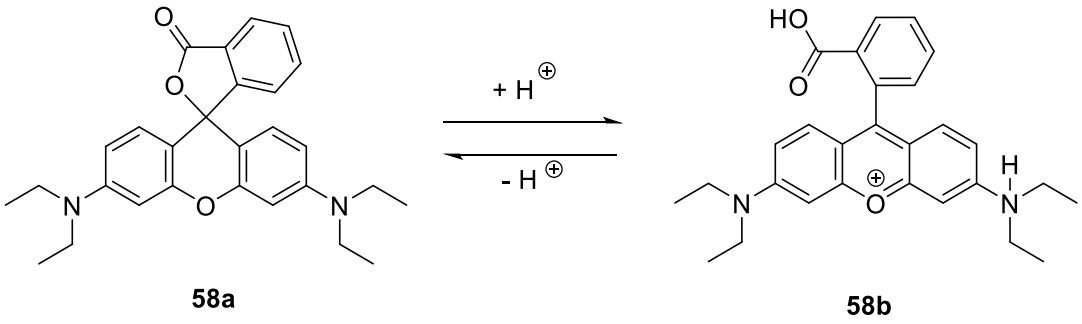

58a 58b

Figure 4.14: Structure change of rhodamine B (**58**) molecule in the presence or absence of H^+.

Analytical HPLC analysis of **59** showed two peaks with retention times at 17.6 min and 19.6 min (**Figure 4.15**). As Birtalan *et al.*[52] have discussed in a similar HPLC separation of a peptoid linked with Rhodamine, they showed that non-fluorescent has a lower retention time than fluorescent structure. Based on this, we assumed that the first peak represented the closed form of **59** and the second peak represented the fluorescent structure of **59**. We also confirmed this by adding few drops of 1% TFA into the sample tube. At the lower pH, the second peak became larger suggesting that it represents the fluorescent Rhod-KLA-CPPo6 (**59**).

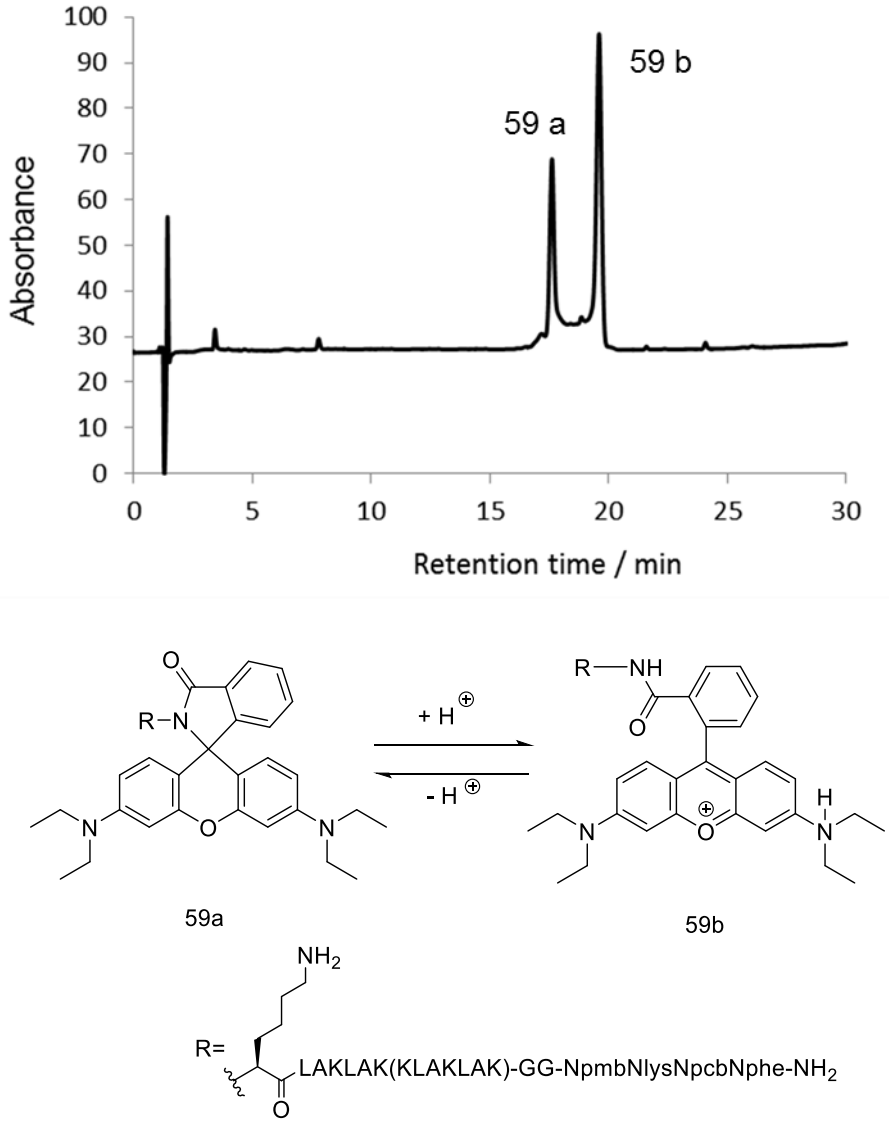

Figure 4.15: Analytical HPLC trace of purified Rhod-KLA-CPPo6 (**59**) at 220 nm and the structures that represented the two peaks.

The absorption bands of Rhod-KLA-CPPo6 (**59**) are 563 nm in PBS buffer. We measured the absorption spectra of **59** at PBS with different concentrations at pH 3, 4 and 5. At pH 3, the spectra of concentrations from 1.25 μM to 10μM are shown in **Figure 4.16**. The maximum absorbance peak was at 563 nm and the peak increased in intensity when the concentration increased. In **Figure 4.17**, the linear constant of the peak value at 563 nm of concentration 1.25 μM to 10μM was obtained and was used as the extinction coefficient of **59** at pH 3.

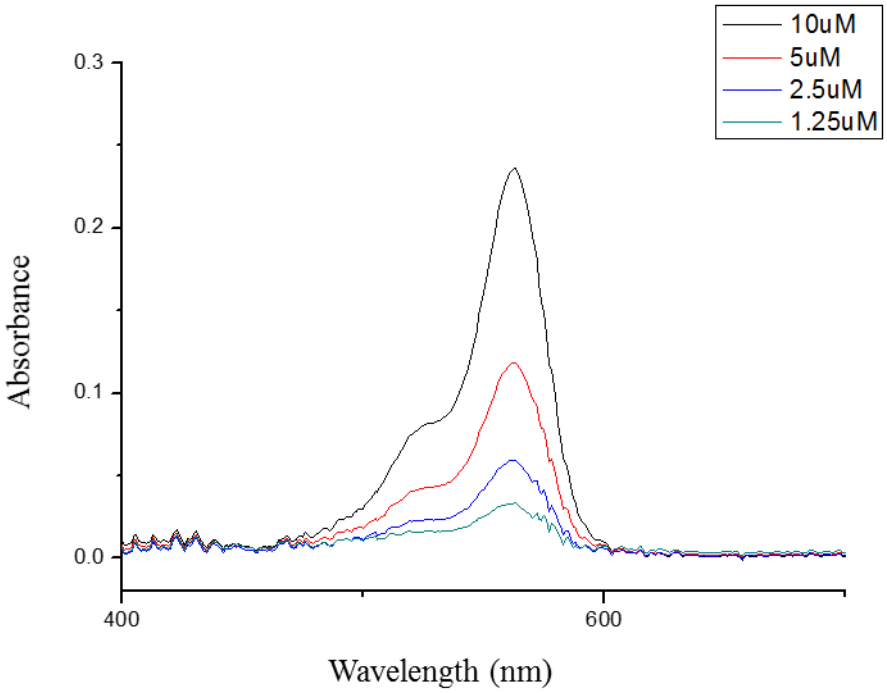

Figure 4.16: The absorbance spectra of **59** measured at PBS (pH=3) with different concentration.

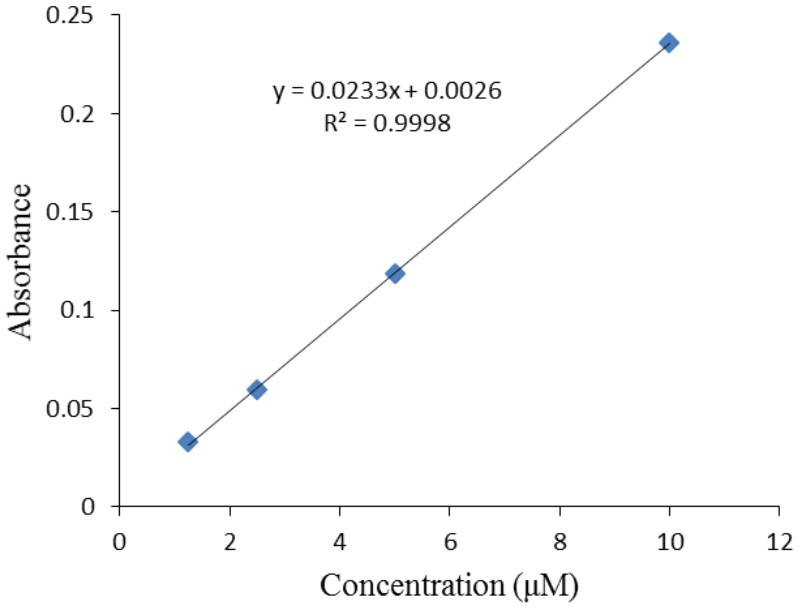

Figure 4.17: The absorbance value of **59** measured at PBS (pH=3) at 563 nm with different concentration. The extinction coefficient was calculated by the linear constant.

Table 4.6: Comparison of the absorption maxima and extinction coefficients of **59** at different pH values. (Spectra measured in PBS)

pH value	λ_{abs}(nm)	Extinction Coefficient ε [M^{-1} cm^{-1}]
3	563	23300
4	563	11400
5	563	800

4.4 Biological evaluation of peptide-peptoid hybrids

4.4.1 Cytotoxicity of KLA and KLA-CPPos

(MTT data was carried out by Lijun Jiang at Hong Kong Baptist University)

In the cytotoxicity experiment, $_D$-KLA (**33**) and the hybrids **52-57** were evaluated using HeLa cells. As we can see from **Figure 4.18**, $_D$-KLA (**33**) exhibits low anti-cancer activity, and even at a concentration of 500 μM HeLa cell viability is 56 ± 3%.

It has been reported that cell penetrating peptoids (CPPos) can be designed by varying the backbone scaffolds and side-chain appendages[51]. The combination of lipophilic and cationic residues in different peptoids have been synthesised and showed the ability to enter human cells efficiently. Here, we chose six different CPPos in the library and used them as delivery vectors to improve the cell penetrating ability and cytotoxicity of the KLA peptide.

KLA-peptoid hybrids **52-57** were incubated with HeLa cells (concentration 100 μM to 1 μM), and all showed improved anti-cancer activity compared to KLA itself (**Figure 4.19**). Hybrids **52-54** have similar properties at the highest concentration of 100 μM, with HeLa cell survive around 70%. This shows that hybrids **52-54** can deliver $_D$-KLA (**33**) into the HeLa cells but the location may not be the mitochondria. However, hybrids **55-57** have increased cytotoxicity compared to hybrids **52-54**. At the highest concentration of 100 μM, the HeLa cell viability was only 14 ± 3%, 7 ± 2%, 0.2 % for hybrid **55**, **56** and **57** respectively. At 20 μM, hybrids **55** and **56** lost activity but hybrid **57** still showed a good level of activity with HeLa cell viability 17 ± 2%.

An extra cytotoxicity experiment of peptide-peptoid **57** was under taken to more accurately define the IC_{50} value. The concentration range was controlled from 20 μM to

5 μM. At 8 μM, the viability of HeLa cells was 38 % ± 1%, which proves the IC_{50} is lower than 10 μM. While at the lowest concentration 5 μM, cell viability is over 100%. From the data as shown in **Figure 4.20**, the more accurate IC_{50} of **57** is ca. 8 μM.

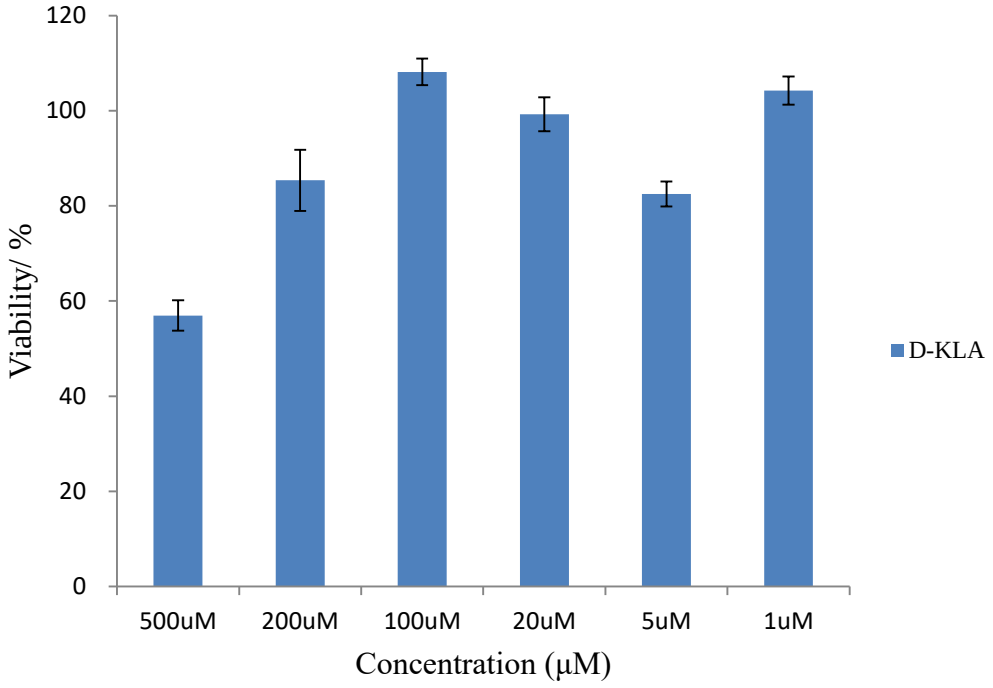

Figure 4.18: MTT assay determined cell viability of HeLa cell line after incubation with $_D$-KLA (**33**) for 24 h at 37°C. The data represent the mean ± standard deviation of three independent experiments.

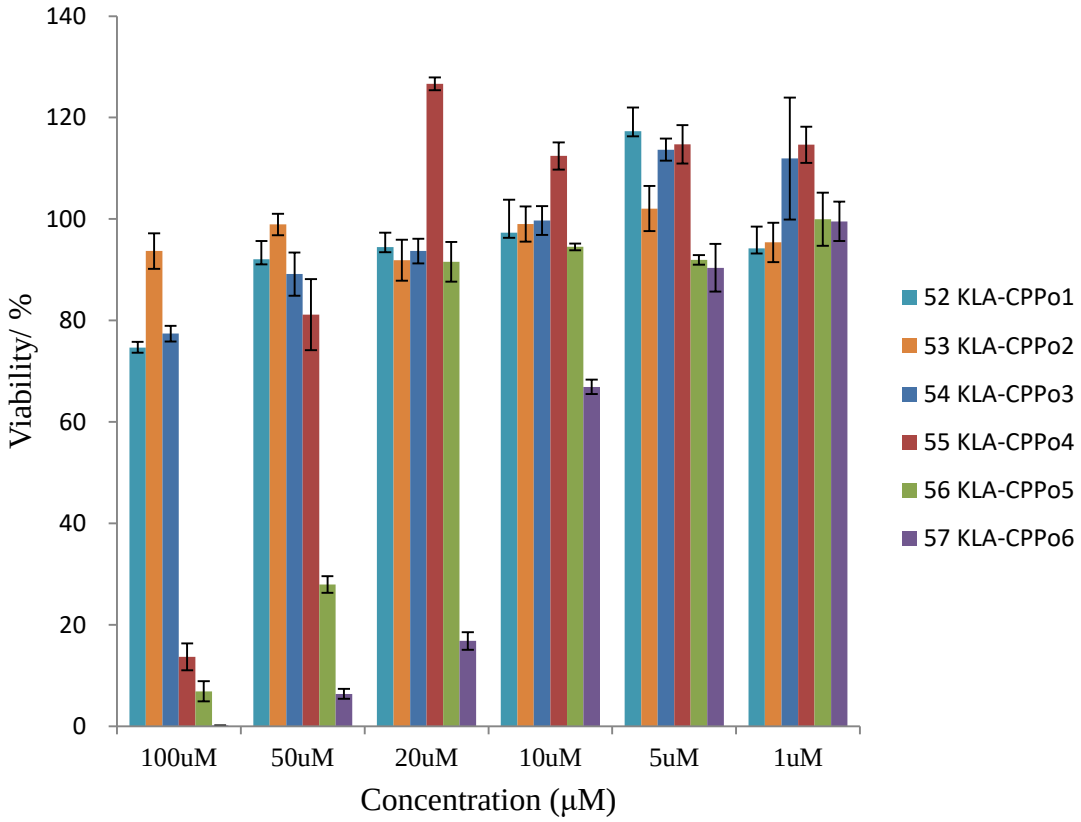

Figure 4.19: MTT assay determined cell viability of HeLa cell line after incubation with six KLA-peptoid hybrids (**52-57**) for 24 h at 37°C. The data represent the mean ± standard deviation of three independent experiments.

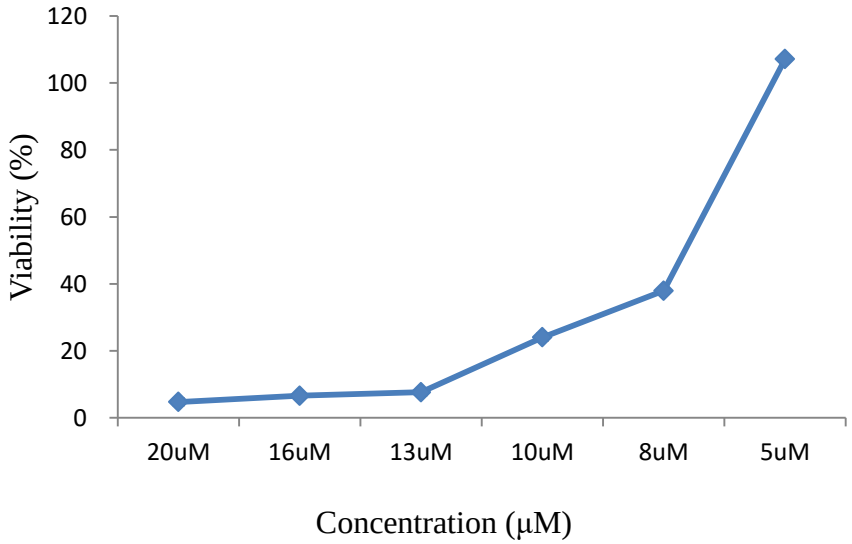

Figure 4.20: MTT assay determined cell viability of HeLa cell line after incubation with peptide-peptoid hybrid **57** for 24 h at 37°C. The data represent the mean ± standard deviation of three independent experiments.

4.4.2 Cellular uptake and *in vitro* imaging

From the cytotoxicity experiments, it was found that KLA-CPPo6 (**57**) had the best activity. We hypothesised that this was due to the fact that CPPo6 has the ability of internalizing KLA into cells and localizing it specifically in the mitochondria. In order to prove this hypothesis, a Rhodamine dye was coupled to KLA-CPPo6 (**57**) in order to produce a conjugate that could be used in fluorescence microscopy experiments. The synthesis of Rhod-KLA-CPPo6 (**59**) has been previously described.

The cellular uptake of Rhod-KLA-CPPo6 (**59**) (10 μM) into HeLa cells could be observed very clearly (**Figure 4.21**). In addition, confocal images of Rhod-KLA-CPPo6 (**59**) within the HeLa cells after incubation for 24 h were examined by laser confocal microscopy. As shown in **Figure 4.22**, Rhod-KLA-CPPo6 (**59**) co-localsises in exactly the same location as the mitochondrial tracker dye. This result confirms that CPPo6 (**51**) can deliver KLA (**33**) into mitochondria, leading to significant improvement in its anti-cancer activity.

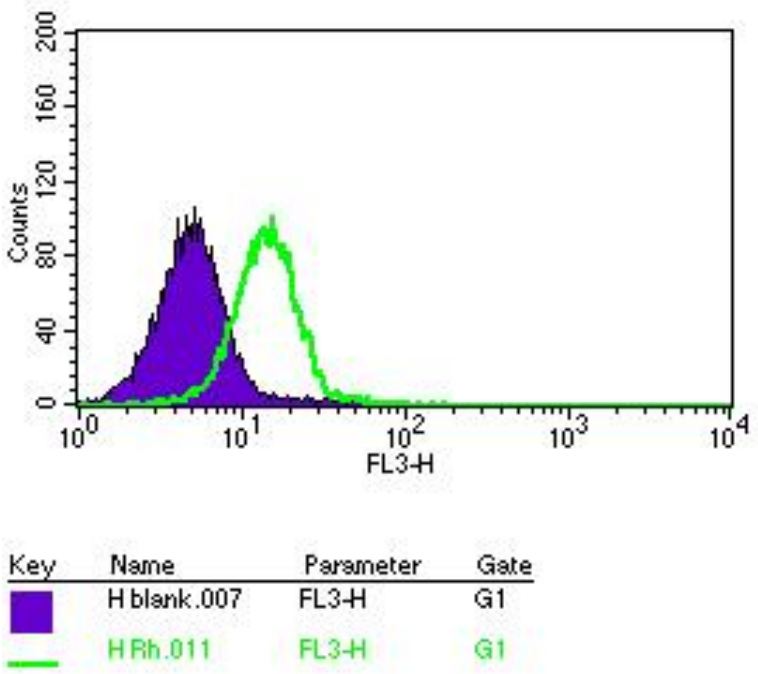

Figure 4.21: The cellular uptake of Rhod-KLA-CPPo6 (**59**) by flow cytometry in human cervical carcinoma HeLa cells.

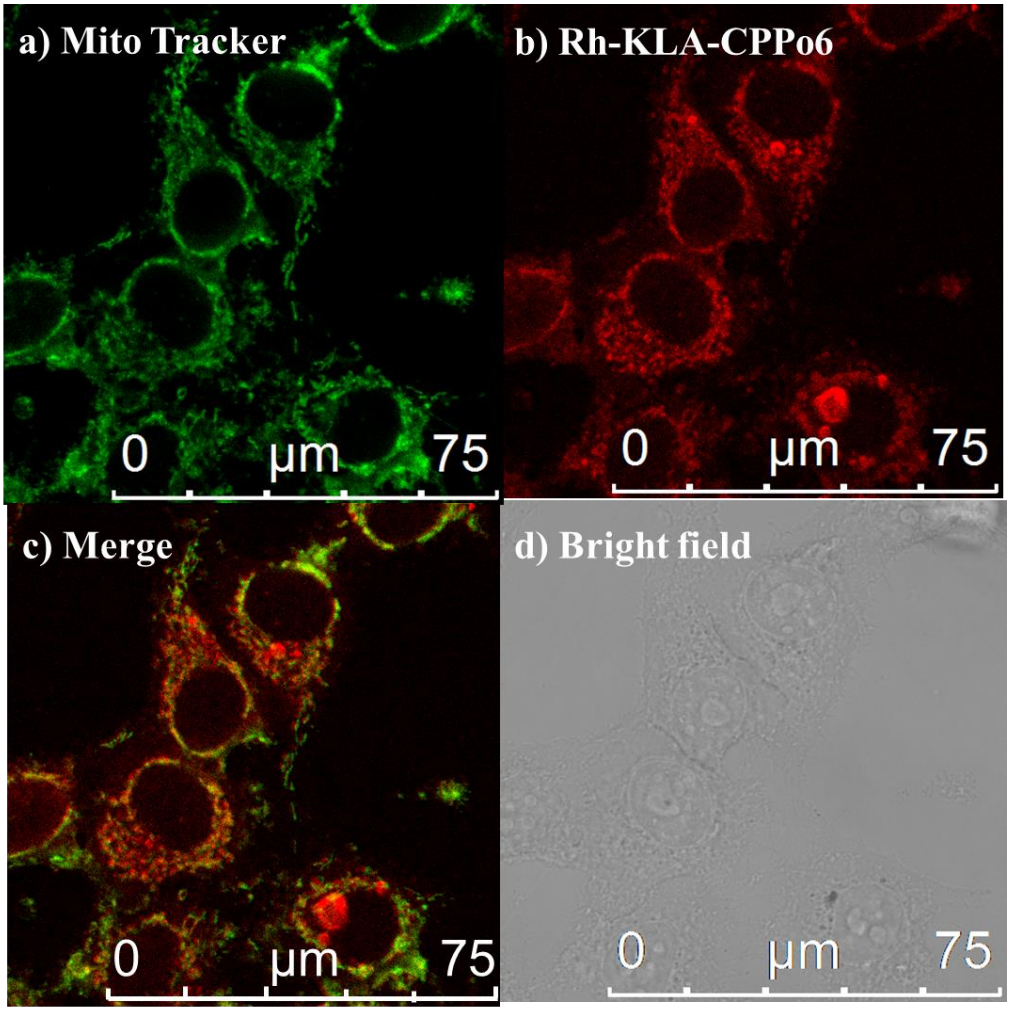

Figure 4.22: The confocal images of Rhod-KLA-CPPo6 (**59**) in HeLa cells. (Conc.: 10 µM, Incubation time: 24 h). Bar 15 µm.

4.4.3 Antibacterial screening

(Antibacterial screening data was carried out by Mark Laws at Durham University)

KLA-mediated mitochondrial membrane disruption has been demonstrated to occur in preference to disruption of the eukaryotic plasma membrane.[23] The similarity in the membrane compositions of mitochondria and gram-negative bacteria suggests that gram negative-active cationic AMPs may have potential applications in oncotherapy. This also indicates that α-helical mitochondria-targeting peptides such as KLA may possess antimicrobial activity.[53]

McGrath *et al.* have studied the antimicrobial spectrum of the KLA peptide in depth and report minor activity against *Pseudomonas aeruginosa* PAO1 and *Escherichia coli* ATCC 25922 strains (MIC of 150 µg mL^{-1} against both).[24] In an attempt to increase the stability of KLA peptide towards proteolysis, the same group also reported the

biological screening of an all-D amino acid enantiomer ($_D$-KLA). Identical MICs to those of the $_L$-KLA enantiomer were reported for all gram-negative strains tested, but $_D$-KLA was observed to have greatly enhanced stability towards proteolytic degradation (25% of $_D$-KLA vs. 100% of $_L$-KLA degraded on treatment with human liver-derived microsomes for 24 h).[24]

As discussed in **Section 4.2**, we have produced both $_L$-KLA (**41**) and $_D$-KLA (**33**) peptides; to expand upon the work of McGrath *et al.*, screening against different bacterial strains was conducted, i.e. *Staphylococcus aureus*, *Serratia marcescens* and *Pseudomonas aeruginosa*. As **Table 4.7** and **Figure 4.23** show, $_L$-KLA (**41**) was found to possess no antimicrobial activity against any of the organisms screened. However, antibacterial activity was noted for $_D$-KLA (**33**) against both gram-positive *S. aureus* (MIC 256 μg mL^{-1}; IC_{50} ~192 μg mL^{-1}) and gram-negative *E. coli* (MIC 64 μg mL^{-1}; IC_{50} ~48 μg mL^{-1}). In particular it is worth noting that the activity of $_D$-KLA (**33**) against *E. coli* is comparable to that of the antibiotic control, ampicillin (MIC 32 μg mL^{-1}; IC_{50} ~16 μg mL^{-1}).

The data recorded may be reconciled on the basis of relative biological stabilities of the two peptides. $_L$-KLA (**41**) inactivity may be due to, amongst other factors, degradation *via* proteases either secreted by the bacteria or released upon lysis of the first bacterial cells. In comparison, $_D$-KLA (**33**) will possess enhanced stability towards proteolytic degradation, potentially giving rise to the discrepancy between the antimicrobial activities of the two peptides. Alternatively, the superior antimicrobial activity of $_D$-KLA (**33**) may be due to a different, specific method of action involving binding of an unidentified membrane/intracellular component for which it possesses the requisite spatial orientation of residues to bind and elicit the antimicrobial effect. Further investigation is required to provide a definitive explanation for this observation.

When $_D$-KLA is combined with cell penetrating peptoids (CPPos), the data for **52** and **53** are similar to those of $_D$-KLA, except for the activity of the conjugates against *P. aeruginosa* which was greater, as shown in **Figure 4.24**. This may due to the peptoid section enhancing the cell penetrating ability of $_D$-KLA to interact with the cell membrane of *P. aeruginosa.* Further investigation to elucidate the mode of action of these conjugates is thus required.

When comparing the data obtained for $_D$-KLA, activities against *S. aureus* and *S. marcescens* remained the same, activities against *E. coli* have decreased (MIC 128 and 256 mgL^{-1}; IC_{50} 64 and ~96 mgL^{-1} for **52** and **53**, respectively). However, the activities against *P. aeruginosa* have increased as observed by lower MIC and IC_{50} (MIC 32 and 64 mgL^{-1}; IC_{50} ~24 and ~48 mgL^{-1} for **52** and **53**, respectively).

Table 4.7: Summary of MIC and IC_{50} values attained from biological testing (µg mL^{-1}). *IC_{50}* is the half maximal inhibitory concentration, defined as the concentration of antibiotic required for 50% inhibition of bacterial growth (achieve 50% cell viability).

Compound	**Bacteria**							
	S. aureus		*E. coli*		*S. marcescens*		*P. aeruginosa*	
	MIC	IC_{50}	MIC	IC_{50}	MIC	IC_{50}	MIC	IC_{50}
$_L$-KLA (**33**)	>256	>256	>256	256	>256	~192	>256	>256
$_D$-KLA (**41**)	256	~192	64	~48	>256	128	>256	~96
KLA-CPPo1 (**52**)	256	~192	128	64	>256	~192	32	~24
KLA-CPPo2 (**53**)	256	~192	256	~96	>256	~192	64	~48
Ampicillin	4	<2	32	~12	64	~12	256	~192

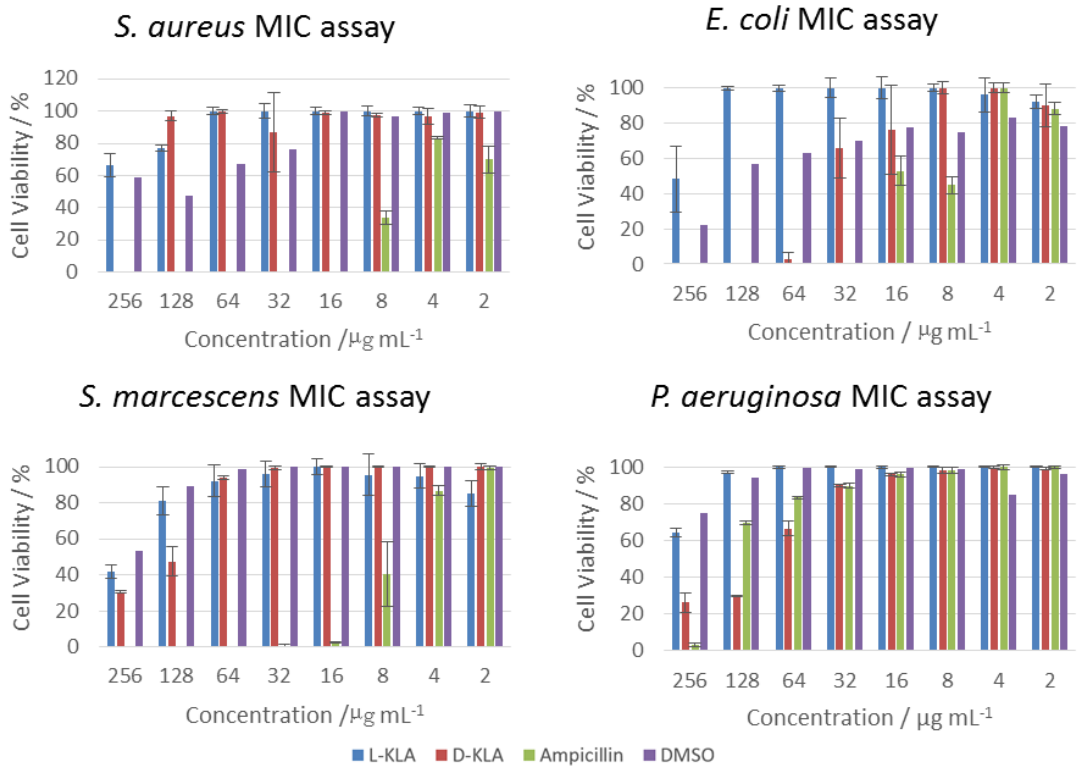

Figure 4.23: Antibacterial screening results of $_L$-KLA (**41**) and $_D$-KLA (**33**).

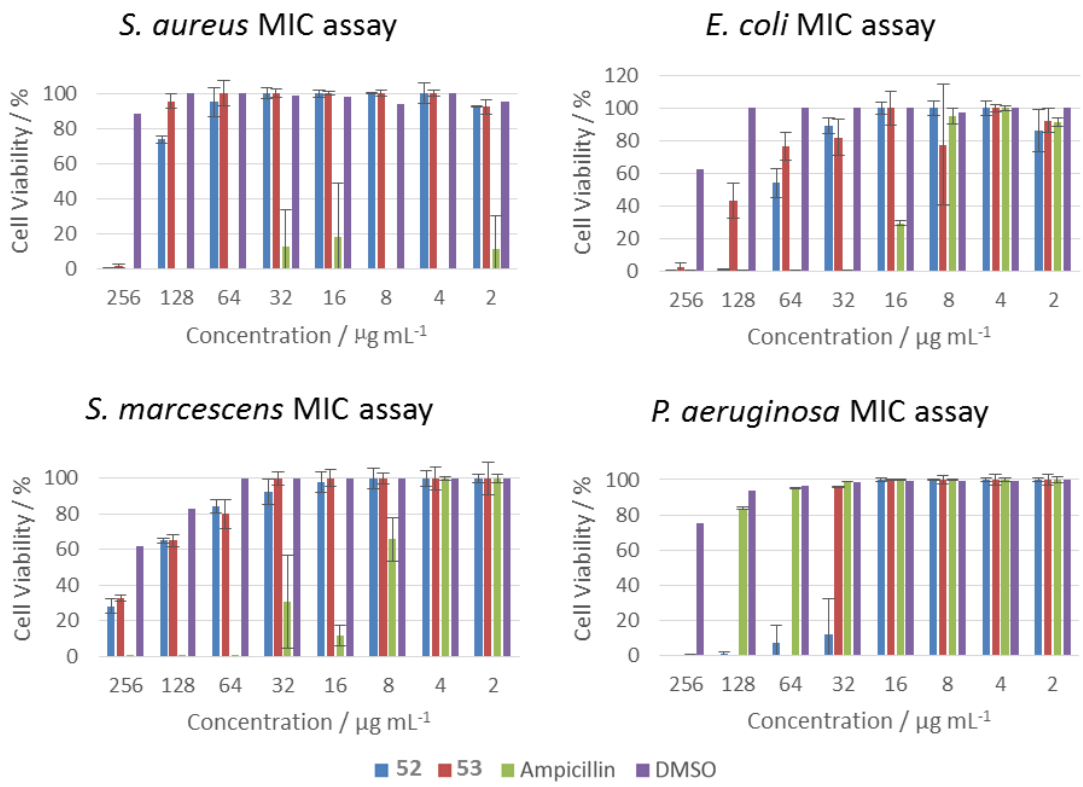

Figure 4.24: Antibacterial screening results of KLA-CPPo1 (**52**) and KLA-CPPo2 (**53**).

4.5 Conclusions

In this chapter, the known anti-cancer peptide $_{D}$-KLA was conjugated to a series of cell penetrating peptoids (CPPos) in an effort to improve its cell penetrating properties and its cytotoxicity. The advantage of using CPPos as delivery agents is that they have the same membrane-crossing ability as cell penetrating peptides, but they are stable to protease digestion. We prepared a series of CPPos-KLA hybrids (**52-57**). Each hybrid is a fusion of a short sequence peptoid and the D-form of KLA, as well as two glycine residues in the middle as a spacer. All peptide-peptoid hybrids were obtained by solid-phase synthesis. Six different cell penetrating peptoids (CPPos) were selected and conjugated with KLA and their anti-cancer properties evaluated against Hela cells. The results show that the CPPos-KLA hybrids have an increasing trend in killing ability due to the increasing of mitochondria-targeting ability. The IC_{50} of KLA-CPPo6 (**57**) (ca.8 μM) was more than 62.5 fold lower than that of $_{D}$-KLA peptide alone.

By altering the side chains of the CPPos, different organelle localization can be achieved.[51] KLA-CPPo6 labelled with Rhodamine B (**59**) was monitored by fluorescent

confocal microscopy of its cellular uptake efficiency. The Rhodamine B labelled KLA-CPPo6 (**59**) was shown to have the ability to enter cells by endocytosis and to specifically localize in the mitochondria. This system proves that CPPos have the potential to be used to deliver anti-cancer drugs with a specificity at the subcellular level.

For antibacterial experiments, both $_{L}$-KLA and $_{D}$-KLA peptides were screened against different bacterial strains. We found that $_{L}$-KLA possessed no antimicrobial activity, while $_{D}$-KLA peptide had activity against both gram-positive *S. aureus* (MIC 256 μg mL^{-1}; IC_{50} ~192 μg mL^{-1}) and gram-negative *E. coli* (MIC 64 μg mL^{-1}; IC_{50} ~48 μg mL^{-1}). The activity of $_{D}$-KLA against *E. coli* was almost as good as the antibiotic control, ampicillin (MIC 32 μg mL^{-1}; IC_{50} ~16 μg mL^{-1}).

In addition, we screened KLA-CPPo1 (**52**) and KLA-CPPo2 (**53**) against four bacterial strains as well. The data obtained were similar to $_{D}$-KLA, except for the increased activity of **52** and **53** against *P. aeruginosa*. Activities against *P. aeruginosa* have increased compared to both $_{L}$-KLA and $_{D}$-KLA, even better than Ampicillin (MIC 32 and 64 mgL^{-1}; IC_{50} ~24 and ~48 mgL^{-1} for **52** and **53**, respectively). This may be due to the novel intracellular peptoid section of the conjugates specific to *P. aeruginosa*.

4.6 References

1. P. W. Latham, *Nat. Biotechnol.*, 1999, **17**, 755-757.
2. P. Vlieghe, V. Lisowski, J. Martinez and M. Khrestchatisky, *Drug Discov Today*, 2010, **15**, 40-56.
3. S. Lien and H. B. Lowman, *Trends Biotechnol.*, 2003, **21**, 556-562.
4. M. Zasloff, *Nature*, 2002, **415**, 389-395.
5. M.-D. Seo, H.-S. Won, J.-H. Kim, T. Mishig-Ochir and B.-J. Lee, *Molecules*, 2012, **17**, 12276-12286.
6. D. W. Hoskin and A. Ramamoorthy, *Biochim. Biophys. Acta*, 2008, **1778**, 357-375.
7. R. E. W. Hancock and G. Diamond, *Trends Microbiol.*, 2000, **8**, 402-410.
8. G. Saberwal and R. Nagaraj, *Biochim. Biophys. Acta*, 1994, **1197**, 109-131.
9. E. T. Kaiser and F. J. Kezdy, *Annu. Rev. Biophys. Biophys. Chem.*, 1987, **16**, 561-581.
10. M. R. Yeaman and N. Y. Yount, *Pharmacol. Rev.*, 2003, **55**, 27-55.
11. K. Matsuzaki, *Biochim. Biophys. Acta*, 1999, **1462**, 1-10.
12. Y. Shai, *Biochim. Biophys. Acta*, 1999, **1462**, 55-70.
13. L. Yang, T. M. Weiss, R. I. Lehrer and H. W. Huang, *Biophys. J.*, 2000, **79**, 2002-2009.
14. H. V. Westerhoff, D. Juretić, R. W. Hendler and M. Zasloff, *Proc. Natl. Acad. Sci.*, 1989, **86**, 6597-6601.

15. W. C. Wimley, *ACS Chem. Biol.*, 2010, **5**, 905-917.
16. U. H. N. Dürr, U. S. Sudheendra and A. Ramamoorthy, *Biochem. Biophys. Acta*, 2006, **1758**, 1408-1425.
17. N. Papo and Y. Shai, *Cell. Mol. Life Sci.*, 2005, **62**, 784-790.
18. N. Papo and Y. Shai, *Biochemistry*, 2003, **42**, 9346-9354.
19. W.-H. Yoon, H.-D. Park, K. Lim and B.-D. Hwang, *Biochem. Biophys. Res. Commun.*, 1996, **222**, 694-699.
20. S.-C. Chan, L. Hui and H. M. Chen, *Anti-cancer Res.*, 1997, **18**, 4467-4474.
21. R. Bessalle, A. Kapitkovsky, A. Gorea, I. Shalit and M. Fridkin, *FEBS Lett.*, 1990, **274**, 151-155.
22. S. E. Blondelle and R. A. Houghten, *Biochemistry*, 1992, **31**, 12688-12694.
23. H. M. Ellerby, W. Arap, L. M. Ellerby, R. Kain, R. Andrusiak, G. Del Rio, S. Krajewski, C. R. Lombardo, R. Rao and E. Ruoslahti, *Nat. Med.*, 1999, **5**, 1032-1038.
24. D. M. McGrath, E. M. Barbu, W. H. Driessen, T. M. Lasco, J. J. Tarrand, P. C. Okhuysen, D. P. Kontoyiannis, R. L. Sidman, R. Pasqualini and W. Arap, *Proc. Natl. Acad. Sci.*, 2013, **110**, 3477-3482.
25. M. M. Javadpour, M. M. Juban, W.-C. J. Lo, S. M. Bishop, J. B. Alberty, S. M. Cowell, C. L. Becker and M. L. McLaughlin, *J. Med. Chem.*, 1996, **39**, 3107-3113.
26. K. S. Akerfeldt, J. D. Lear, Z. R. Wasserman, L. A. Chung and W. F. DeGrado, *Acc. Chem. Res.*, 1993, **26**, 191-197.
27. J. C. Mai, Z. Mi, S.-H. Kim, B. Ng and P. D. Robbins, *Cancer Res.*, 2001, **61**, 7709-7712.
28. H. Li, S. K. Kolluri, J. Gu, M. I. Dawson, X. Cao, P. D. Hobbs, B. Lin, G.-q. Chen, J.-s. Lu and F. Lin, *Science*, 2000, **289**, 1159-1164.
29. B. Law, L. Quinti, Y. Choi, R. Weissleder and C.-H. Tung, *Mol. Cancer Ther.*, 2006, **5**, 1944-1949.
30. K. Rege, S. J. Patel, Z. Megeed and M. L. Yarmush, *Cancer Res.*, 2007, **67**, 6368-6375.
31. H. M. Ellerby, D. E. Bredesen, S. Fujimura and V. John, *J. Med. Chem.*, 2008, **51**, 5887-5892.
32. W.-H. Chen, J.-X. Chen, H. Cheng, C.-S. Chen, J. Yang, X.-D. Xu, Y. Wang, R.-X. Zhuo and X.-Z. Zhang, *Chem. Commun.*, 2013, **49**, 6403-6405.
33. X. Ma, X. Wang, M. Zhou and H. Fei, *Adv. Healthc. Mater.*, 2013.
34. L. Agemy, D. Friedmann-Morvinski, V. R. Kotamraju, L. Roth, K. N. Sugahara, O. M. Girard, R. F. Mattrey, I. M. Verma and E. Ruoslahti, *Proc. Natl. Acad. Sci.*, 2011, **108**, 17450-17455.
35. S. M. Standley, D. J. Toft, H. Cheng, S. Soukasene, J. Chen, S. M. Raja, V. Band, H. Band, V. L. Cryns and S. I. Stupp, *Cancer Res.*, 2010, **70**, 3020-3026.
36. V. V. Lemeshko, *Arch. Biochem. Biophys.*, 2010, **493**, 213-220.
37. I. D. Alves, M. Carré, M.-P. Montero, S. Castano, S. Lecomte, R. Marquant, P. Lecorché, F. Burlina, C. Schatz and S. Sagan, *Biochim. Biophys. Acta*, 2014, **1838**, 2087-2098.
38. H. Y. Kim, S. Kim, H. Youn, J.-K. Chung, D. H. Shin and K. Lee, *Biomaterials*, 2011, **32**, 5262-5268.
39. R. C. Ladner, A. K. Sato, J. Gorzelany and M. de Souza, *Drug Discov. Today*, 2004, **9**, 525-529.
40. C. P. Graff and K. D. Wittrup, *Cancer Res.*, 2003, **63**, 1288-1296.

41. S. M. Miller, R. J. Simon, S. Ng, R. N. Zuckermann, J. M. Kerr and W. H. Moos, *Drug Dev. Res.*, 1995, **35**, 20-32.
42. R. J. Simon, R. S. Kania, R. N. Zuckermann, V. D. Huebner, D. A. Jewell, S. Banville, S. Ng, L. Wang, S. Rosenberg and C. K. Marlowe, *Proc. Natl. Acad. Sci.*, 1992, **89**, 9367-9371.
43. P. E. Nielsen, *Pseudo-peptides in drug discovery*, John Wiley & Sons, 2004.
44. P. Armand, K. Kirshenbaum, A. Falicov, R. L. Dunbrack, K. A. Dill, R. N. Zuckermann and F. E. Cohen, *Fold. Des.*, 1997, **2**, 369-375.
45. K. Kirshenbaum, A. E. Barron, R. A. Goldsmith, P. Armand, E. K. Bradley, K. T. V. Truong, K. A. Dill, F. E. Cohen and R. N. Zuckermann, *Proc. Natl. Acad. Sci.*, 1998, **95**, 4303-4308.
46. H.-M. Shin, C.-M. Kang, M.-H. Yoon and J. Seo, *Chem. Commun.*, 2014, **50**, 4465-4468.
47. J. E. Murphy, T. Uno, J. D. Hamer, F. E. Cohen, V. Dwarki and R. N. Zuckermann, *Proc. Natl. Acad. Sci.*, 1998, **95**, 1517-1522.
48. T. Klimkait, E. R. Felder, G. Albrecht and F. Hamy, *Biotechnol. Bioeng.*, 1999, **61**, 155-168.
49. P. A. Wender, D. J. Mitchell, K. Pattabiraman, E. T. Pelkey, L. Steinman and J. B. Rothbard, *Proc. Natl. Acad. Sci.*, 2000, **97**, 13003-13008.
50. V. Kesavan, N. Tamilarasu, H. Cao and T. M. Rana, *Bioconjugate Chem.*, 2002, **13**, 1171-1175.
51. D. K. Kölmel, D. Fürniss, S. Susanto, A. Lauer, C. Grabher, S. Bräse and U. Schepers, *Pharmaceuticals*, 2012, **5**, 1265-1281.
52. E. Birtalan, B. Rudat, D. K. Kölmel, D. Fritz, S. B. Vollrath, U. Schepers and S. Bräse, *Pept. Sci.*, 2011, **96**, 694-701.
53. S. Hyun, S. Lee, S. Kim, S. Jang, J. Yu and Y. Lee, *Biomacromolecules*, 2014, **15**, 3746-3752.

Chapter 5: Conclusions and Future Work

As outlined in the original aim of this thesis, three different delivery vehicles that have the potential to be applied in the development of new anti-cancer drug delivery systems have been studied. The research involved biomaterial design, functionalization of GNPs and the application of novel cell penetrating peptoids (CPPos).

In Chapter 2, we synthesised and studied a series of short elastin-like peptides (ELPs) with different N-terminal end groups. A solid phase peptide synthesis approach was applied and Rink Amide resin was used in all cases. Neutral solutions (pH=7) of peptide **9** (VPGVG) showed no lower critical solution temperature (LCST) behavior, but at pH 9, the free amine end was not protonated providing peptide **9** a more hydrophobic character with a transition temperature of 44^{o}C. The turbidimetry data obtained from the study of all the ELPs prepared showed that only peptide **10** (*N*-acetylated VPGVG) had a transition temperature (45^{o}C) close to the target range (38-42^{o}C) at pH 7. In order to use this short ELP in further applications (Chapter 3), an equivalent thiol-functionalized peptide **11** was synthesised. The secondary structures of peptide **10** and peptide **11** in aqueous buffer were examined using circular dichroism (CD). The results showed that they both display similar trends to previously studied long chain elastin-like peptides. The mean residue ellipticity (MRE) at 198 nm became shallower and the [θ] value at 222 nm increased when the temperature was increased, which indicated changes in structure from random coil to a more organised conformation (mixture of α-helix and β-turn structures).

As we were able to confirm that the shortest sequence studied (VPGVG) has similar LCST behaviour to that displayed by long elastin-like polypeptides, we used it to prepare elastin-based side chain polymers (ESPs). To prepare the ESPs we utilised the RAFT technique to polymerize pentafluorophenyl acrylate (PFPA). Different molecular weights of poly(PFPA) (**16-19**) were synthesised and characterized by both NMR and gel permeation chromatography (GPC). The poly(PFPA)s prepared were subsequently modified by attachment of the short ELPs in the presence of triethylamine (TEA), to

give a series of elastin-based side chain polymers (ESPs) (**22-29**). We have investigated the influence of the chain length, molecular weight and NaCl concentration on the LCST behaviour of a series of ESPs. By increasing the polymer concentration or its molecular weight, the transition temperature was lowered. These results proved that it was possible to incorporate a short ELP into a polymer to prepare a peptide-polymer grafts that displays the same properties as the free peptide. Amongst all the ESP prepared and studied, polymer **29** had the lowest transition temperature (47^{o}C at pH 7). This is because PF100-GABA(VPGVG) (**29**) had the longest polymer chain length and the longer linker between polymer backbone and side chain peptides. In future, the transition temperature of the ESP could be modulated by introducing an amphiphilic copolymers structure. The polymerized pentafluorophenyl acrylate P(PFPA) chain could be extended by adding a more hydrophobic monomer, such as butyl acrylate, via RAFT polymerization again. Then P(PFPA) part of copolymers can be subsequently modified by attachment of short ELPs which become the hydrophilic part. Through varying the chain ratio of hydrophobic and hydrophilic domains, different transition temperatures and different formulations such as micelles or vesicles can be obtained. These newly designed amphiphilic copolymers prepared via RAFT polymerization could have potential as stimuli-responsive drug delivery systems.

In Chapter 3, gold nanoparticles (GNPs) were synthesised with controlled sizes using the Frens and Turkevich method. GNPs **A** were formed and they had an average size of 15 nm as determined by transmission electron microscopy (TEM). The UV-Vis spectra of colloidal solutions of GNPs **A** exhibited a surface plasmon absorption peak at 520 nm. In the next step, GNPs **A** were functionalised with short ELP **11** to provide ELP-GNPs (**30**) hybrids. The conformation and aggregation properties of ELP-GNPs (**30**) in aqueous solution were proved by UV-Vis spectroscopy, dynamic light scattering (DLS) and transmission electron microscopy (TEM). In addition, the temperature dependencies of the secondary structure of the peptides in ELP-GNPs (**30**) hybrid were evaluated using CD spectroscopy. Compared to the trends discussed above for the free ELPs, the ELP-GNPs (**30**) were found to have the same trend as peptide **11** and peptide **10**. These data indicated that short ELPs successfully covered the GNPs and endowed the LCST behavior to the ELP-GNPs hybrids, resulting in a conformation change when the temperature was increased to around 40 ℃.

We were also able to prepare ESP hybrid GNPs; ESP_{75}-GNPs (**31**) and ESP_{100}-GNPs (**32**). ESP **26** and **29** both had thiol ends which were converted from the trithiocarbonate moiety of RAFT agent (benzyl 2-hydroxyethyl carbonotrithioate). This showed the advantageous properties of RAFT agents and the polymers made from them to be able to bond to and incorporate GNPs via thiol-gold linkages. The conformation and aggregation properties of the ESP-GNPs **31** and **32** in aqueous solution were analysed by UV-Vis spectroscopy. The results showed that both the functionalised nanoparticles **31** and **32** have similar thermo-responsive characteristics to the original ESPs. When the temperature was increased above 40^{o}C, the aqueous solution of **32** changed colour from red to purple and this was accompanied by a red shift from 532 nm to 540 nm in the UV-Vis spectra. This observation suggests that the nanoparticles were aggregated. The LCST behaviour of **32** was also confirmed by CD spectroscopy when measured across a temperature range from 10^{o}C to 65^{o}C. The ESP_{100}-GNPs **32** had the same trends as polymer **29** which indicates that the polymer was successfully conjugated to the GNPs and demonstrated a conformational change when the temperature was increased to 45^{o}C. In addition, TEM analysis of samples of **32** prepared at both 20^{o}C and 50^{o}C gave direct evidence of ESP-GNPs temperature dependant aggregation.

We also synthesised a modified version of the pro-apoptotic KLA. With a thiol end and a PEG-like linker coupled to the KLA sequence, thiol-TTDS-KLA (**38)** was prepared via SPPS and it was conjugated to GNPs via a gold-thiol bond. The KLA-GNPs (**39**) prepared were characterized by UV-Vis, DLS and TEM. In order to compare the drug delivery ability of GNPs, we evaluated the cytotoxicity of $_{D}$-KLA peptide (**33**) and KLA-GNPs (**39**) against HeLa cells. Free un-conjugated $_{D}$-KLA peptide (**33**) was found to have low cytotoxicity (IC_{50} > 500 μM) on HeLa cells. In comparison, KLA-GNPs (**39**) showed much better anti-cancer activity (100 μM > IC_{50}> 50 μM). The increased activity was believed to be due to the ability of **39** to enter into the HeLa cells and thus deliver KLA to its intracellular target, the mitochondria. Confocal imaging was used to prove the internalization of KLA-GNPs (**39**) and its specificity for the HeLa cells mitochondria. Taking all of the data together it was confirmed that GNPs can be used to deliver the apoptotic peptide KLA into mitochondrial of cancer cells, leading to improvement anti-cancer activity.

In the final system studied, we conjugated both the pro-apoptotic peptide $_{D}$-KLA peptide (**33**) and the polymer ESP_{100} (**29**) to GNPs in a weight/weight ratio of 1:1. The KLA-ESP_{100}-GNPs (**40**) prepared were fully characterized by UV-Vis, DLS and TEM. The LCST behaviour of **40** was studied using UV-Visible spectroscopy, increasing the temperature from 20^{o}C to 80^{o}C. Upon raising the temperature, the maximum absorption peak showed a red shift from 530 nm (40^{o}C) to 532 nm (80^{o}C). The results obtained suggested that there is a red shift but not as much as ESP-GNPs (**32**). The temperature dependencies of the secondary structure of the KLA-ESP_{100}-GNPs (**40**) were also evaluated via CD spectroscopy. At 20^{o}C the CD amplitudes at 200 to 210 nm had a positive band and the mean residue ellipticity (MRE) at 222 nm was negative implying a typical β-turn structure. When the temperature was increased, the MRE at 206 nm and 222 nm increased in value, which was the same trend as **29**. Compared with polymer **29**, **40** had a much more ordered β-turn structure at room temperature. The cytotoxic effects of **40** were evaluated against both HeLa and MRC-5 cell lines. The anti-cancer activity at 37°C and at 42°C was found to be relatively similar which indicated triggered phase transition behaviour of **40** showed no impact on enhancing the cytotoxicity. Confocal imaging of **40** showed very few red spots inside the cells which means **40** was not efficiently taken up by HeLa cells. This result may due to the size of KLA-ESP_{100}-GNPs (**40**) which is bigger than KLA-GNPs (**39**). In future work, this hypothesis will be tested and the size of KLA-ESP-GNPs will be modulated by changing the polymer length.

In Chapter 4, the known anti-cancer peptide $_{D}(KLAKLAK)_2$ was synthesised and characterized. $_{D}$-KLA (**33**) was then conjugated to a series of cell penetrating peptoids (CPPos) in an attempt to improve its membrane permeating ability and cytotoxicity. The advantage of using CPPos as delivery agents is that they have the same membrane-crossing ability as cell penetrating peptides, but are stable towards protease digestion. These results show that, overall, the CPPos-KLA hybrids had increased anti-cancer activities (against HeLa cells) compared to free KLA. The IC_{50} of the best hybrid, KLA-CPPo6 (**57**) (ca.8 μM) was found to be more than 62.5 fold lower than that of $_{D}$-KLA (**33**) alone. KLA-CPPo6 labelled with Rhodamine B was monitored by fluorescence confocal microscopy in order to investigate its cellular uptake efficiency. The Rhod-KLA-CPPo6 (**59**) was shown to have the ability to enter HeLa cells by endocytosis, and even specifically localize in the mitochondria. Our initial work in this

area on peptide-peptoid systems proves that CPPos have great potential to be used as vehicles to deliver anti-cancer drugs to specific subcellular locations within cancer cells. In the next step for research in this area, a targeting domain binding to specific cancer cells could be conjugated to the peptide-peptoid hybrid, which will enhance specific antitumor effects.

Chapter 6: Experimental Procedures

6.1 General experimental

6.1.1 Materials

All solvents and reagents were used as supplied unless otherwise stated. Coupling agent PyBOP (benzotriazol-1-yl-oxytripyrrolidinophosphonium hexafluorophosphate) was purchased from Novabiochem. Rink Amide resin was purchased from Bachem. 9-Fluorenylmethoxy carbamate protected valine (Fmoc Val-OH, >99%), glycine (Fmoc Gly-OH, >99%), proline (Fmoc Pro-OH, >99%), Fmoc-D-Lys(Boc)-OH, Fmoc-D-Ala-OH and Fmoc-D-Leu-OH were purchased from Bachem and were used as received.

NMM (N-Methylmorpholine), *N*,*N'*-diisopropylcarbodiimide (DIC), *N*,*N*-diisopropyl-*N*-ethylamine (DIPEA), 1-hydroxybenzotriazole (HOBt), bromoacetic acid (BrAA), piperidine, 4-methoxybenzylamine, benzylamine, 4-chlorobenzylamine and Rhodamine B were purchased from Sigma-Aldrich. *N*-(*tert*-butoxycarbonyl)-1,4-diaminobutane was purchased from TCI.

Anhydrous dimethylformamide (DMF), diethyl ether and benzene were obtained from Sigma Aldrich. The polymerization initiator 2,2'-azobisisobutyronitrile (AIBN) was supplied by Acros Organics and recrystallized from methanol before use. Pentafluorophenol and triethylamine (TEA) were purchased from Sigma Aldrich.

HPLC grade DMF was used for coupling reactions and was purchased from Sigma-Aldrich. Trifluoroacetic acid (TFA, 99%) and triisopropylsilane (TIPS, 99%) were purchased from Sigma-Aldrich and used as received. Acetic anhydride (>99%) was purchased from Sigma-Aldrich. 3-Tritylsulfanyl-propionic acid (Mpr(Trt)-OH) was purchased from Bachem and used as received. 4-Aminobutanoic acid (GABA) and 6-(Fmoc-amino) caproic acid (Fmoc-Ahx-OH) were purchased from Sigma Aldrich. N1-(9-fluorenylmethoxycarbonoyl)-1,13-diamino-4,7,10-trioxatridecan-succinamic acid

(Fmoc-TTDS-OH) was purchased from Iris Biotech GMBH. Trisodium citrate dihydrate ($C_6H_5O_7Na_3$•$2H_2O$), gold (III) chloride trihydrate ($HAuCl_4$•$3H_2O$) were both obtained from Sigma-Aldrich. All solvents and other reagents were purchased from commercial sources and used without purification.

6.1.2 Instruments

6.1.2.1 UV-Vis measurement

UV-Vis absorption spectroscopy measurements were performed using a Varian CaryBio-100 spectrophotometer equipped with a thermoelectric temperature controller. The samples were measured using a quartz cell with 1 cm path length at different temperatures and different buffer pH values. Samples of peptides were prepared in cuvettes sealed with a Teflon stopper and heated at a rate of 1 ^{o}C/min. The measurements were carried out at a fixed wavelength of 300 nm. In this study, in order to calculate the phase transition temperature, all the experimental data were normalized to 1, and lower critical solution temperature (LCST) was defined as the temperature at which 50% of the normalized turbidity was obtained.

6.1.2.2 DLS measurement

Dynamic light-scattering (DLS) measurements were conducted using a Brookhaven Instruments 90 Zeta-Plus particle size analyser. Briefly, sample solution (500μM) in phosphate buffer (10mM, pH 7.4) was prepared. Before analysis all samples were filtered through a 0.2 μm-pore-size syringe filter to minimise contamination with dust. The diameter of ELP-GNPs was measured between 10 ℃ and 60 ℃. At each temperature, the sample was incubated for 10 min.

6.1.2.3 TEM measurement

Transmission electron microscopy (TEM) was conducted on a Hitachi 7600 instrument at an acceleration voltage of 100 kV. A small drop of the colloidal gold solution was placed on a carbon-coated copper grid (200 mesh), and excess solution was removed by wicking using filter paper. The grid was dried after allowing the solvent to evaporate for several minutes and turned into a thin film of particles. TEM images were captured from different parts of the grid and with different magnifications. Approximately ten particles were measured for determining average particle diameter.

6.1.2.4 CD measurement

Circular dichroism (CD) spectra were recorded on a Jasco J-810 spectropolarimeter equipped with a Jasco PFD-425S temperature control unit. Experiments were performed in a quartz cell with a 0.1 cm path length over the range of 198-250 nm at various temperatures. The sample solution (200μM, 10mM phosphate buffer) was injected into the quartz cell. The scan speed used was 50 nm/min.

6.1.2.5 HPLC purification

Semi-preparative RP-HPLC was performed with a Perkin Elmer Series 200 LC pump fitted with a 785A UV/Vis detector using a SB-Analytical ODH-S optimal column (250 × 10 mm, 5 μm); flow rate 2 ml min^{-1}; generally linear gradient elution 0-65% of solvent B over 30 min (*A* = 0.1% TFA in 95% H_2O and 5% MeCN, *B* = 0.1% TFA in 5% H_2O and 95% MeCN). For some longer peptides, the gradient was modulated in order to detect the compound peaks in the best separation.

Purified peptides were characterised by a PerkinElmer series 200 Autosampler onto a Waters XBridge^{TM} BEH C18 column (4.6 x 100 mm, 3.5 μm particle size) which attached to a PekinElmer Series 200 LC Pump and Series 200 UV/Vis detector. The temperature of the column was 40^{o}C controlled by PerkinElmer Series 200 Peltier column oven. Peptides were eluted in H_2O/MeCN + 0.05% TFA and the gradient elution was set at 0-100% B in 30 min with flow rate 1 ml $min^{-1.}$

The LCT Premier XE mass spectrometry using a Acquity UPLC BEH analytical column (C18, 2.1 x 50 mm, 1.7 μm particle size) was carried out on a TQD mass spectrometer (Waters Ltd, UK) with a flow rate of 0.6 ml min^{-1} and a linear gradient of 5-95% of solvent B over 3.8 min (*A* = 0.1% formic acid in H_2O, *B* = 0.1% formic acid in MeCN). For accurate mass detection, QToF Premier mass spectrometry was used applied with same column and same solvent condition.

Pepetides, peptoids and peptide-peptoid hybrids identities were also confirmed by MALDI-TOF mass spectra analysis (Autoflex II ToF/ToF mass spectrometer Bruker Daltonik GmBH) operating in positive ion mode using an α-cyano-4-hydroxycinnamic acid (CHCA) matrix. The samples were prepared at concentrations of no more than 1 mg/mL.

6.1.2.6 NMR spectroscopy

^{1}H, and ^{19}F NMR spectra were recorded using Varian Mercury-400 (^{1}H, ^{13}C, ^{19}F), Bruker Avance-400 (^{1}H, ^{13}C, ^{19}F) spectrometers. $CDCl_3$, CD_2Cl_2 or DMSO-D_6 were used as solvents. All chemical shifts are quoted in parts per million relative to tetramethylsilane (δ_H = 0.00 ppm) and coupling constants are given in Hertz (Hz) to the nearest 0.5 Hz.

6.1.2.7 IR spectroscopy

Infrared spectra (IR) were recorded using a Diamond ATR (attenuated total reflection) accessory (Golden Gate).

6.1.2.8 Mass spectrometry

Electrospray mass spectra (ES) were obtained on a Micromass LCT Mass Spectrometer. High resolution mass spectra were obtained using a Thermo-Finnigan LTQFT mass spectrometer or XevoQToF mass spectrometer (Waters UK, Ltd) by Durham University Mass Spectrometry service. The samples were prepared at concentrations of no more than 1 mg/mL.

6.1.3 General experimental procedures

6.1.3.1 Manual Fmoc-SPPS

Manual SPPS was carried out at room temperature for 1.5 h with amino acid (3.0 eq.), PyBoP (3.0 eq.) and DIPEA (3.0 eq.) in a fritted polypropylene vessel. For successive couplings the vessel was drained after the each coupling cycle and the coupling cycle was repeated with fresh reagents. The Fmoc deprotection step was carried out for 15 min with a solution of 20% piperidine in DMF, followed by a further treatment for 15 min with a fresh solution of 20% piperidine in DMF. In all steps agitation was provided by shaking machine.

6.1.3.2 Peptide cleavage

Peptide-resins were washed with DCM and diethyl ether three times respectively, then left to air dry for 5 min. Subsequently the peptide-resins were treated with a (3 mL per 0.1 mmol of resin) solution of 2.5% TIPS and 2.5% H_2O in TFA for 4 h at room temperature. The cleavage cocktail was reduced to around one-fourth of its original

volume by rotary evaporator under vacuum at 40^{o}C. Then the condensed solution was added to cold diethyl ether whereas the peptide precipitated as a white powder. The supernatant was decanted off carefully and the precipitate was washed with cold diethyl ether. Then precipitate was dissolved with distilled water and freeze-dried.

6.1.3.3 Synthesis of peptoids

Fmoc-protected Rink Amide resin (normally 100-300 mg, 0.1-0.3 mmol) was swollen in DMF (minimum 1 hour, room temperature, overnight preferred) and deprotected with piperidine (20% in DMF v/v, 2 x 20 mins). After DMF washing, the resin was treated with bromoacetic acid (8 eq. wrt. resin, 2M in DMF) and DIC (8 eq. wrt. resin, 2M in DMF) for 15 min at 50 ˚C on a heated shaker with a metal block (400 rpm). The resin was washed three times with DMF, before the desired amine submonomer was added (4 eq. wrt. resin, 1M in DMF) and allowed to react for 15 min at 50 ˚C. The resin was washed three times with DMF again. The bromoacetylation and amine displacement steps were repeated until the final submonomer had been added and the desired peptoid sequence had been obtained. Cleavage was performed with TFA (95%), TIPS (2.5%) and H_2O (2.5%) for 90 min at room temperature. The cleavage cocktail was collected in a 50 ml falcon tube and precipitated with 50 mL diethyl ether. The solution was centrifuged for 15 min at 5,000 rpm. Afterwards, the ether phase was decanted. The crude was dissolved in acidified H_2O (with 0.1% TFA) or a mixture of acidified H_2O and MeCN, and lyophilized. The crude products were redissolved in acidified H_2O (with 0.1% TFA) or a mixture of acidified H_2O and MeCN, and purified by RP-HPLC. A typical method used for the purification was 0–50% B over 60 min then 50-100% B over 15 min (A = 0.1% TFA in 95% H_2O and 5% MeCN, B = 0.1% TFA in 5% H_2O and 95% MeCN) at 250 nm wavelength. Relevant fractions were collected, lyophilised and analysed by LC-MS and MALDI-TOF.

6.1.4 Anti-cancer screening and anti-bacterial screening by collaborators

(The cell culture, MTT, celluar uptake and confocal experiments were carried out by Lijun Jiang at Hong Kong Baptist University)

6.1.4.1 Cell culture

Human cervical carcinoma HeLa cells were purchased from the American type Culture Collection (ATCC) (#CCL-185, ATCC, Manassas, VA, USA). The HeLa cells were

grown in Dulbecco's Modified Eagle Medium (DMEM) supplemented with 10% fetal bovine serum (FBS), 1% penicillin and streptomycin at 37°C and 5% CO_2.

6.1.4.2 MTT assay

Cells (10^5 per sample) were incubated in a 96 well-plate overnight. Afterwards, HeLa or MRC-5 cells treated with the peptide or peptoid for 24 h were further incubated in dark for 24h. Cell viability was determined by the 3-(4,5-Dimethyl-2-thiazolyl)-2,5-diphenyl-2-H-tetrazolium bromide (MTT) reduction assay. The cell monolayers were rinsed with PBS and then incubated with 0.5 mg/ml MTT solution for 3 h (5% CO_2, 37°C). The formazan crystal formed was dissolved in DMSO and the absorbance of dissolved formazan crystal at 540 and 690 nm was measured using a 96-well plate reader (ELx800 Absorbance Microplate Reader).

6.1.4.3 Flow cytometry analysis on cellular uptake

Cells (10^5 per sample) were seeded to 35 mm Petri dish for overnight and then the cells were incubated with Rhod-KLA-CPPo6. Afterwards cells were trypsinized and washed twice with phosphate-buffered saline (PBS). The Rhod-KLA-CPP06's uptake by cells was analysed by flow cytometry. The cells were excited with 488 nm argon laser and emission was collected with FL-3 (equipped with 650 nm long pass filter) and 10000 events were analysed.

6.1.4.4 Confocal microscopic imaging

Cells were seeded onto coverslip in 35 mm culture dishes overnight. The cells were initially incubated with Rhod-KLA-CPPo6 for 30 min in the dark. The emitted fluorescent signals were examined using a Leica SP5 (upright configuration) confocal microscope equipped with argon laser, HeCd laser and a femtosecond-pulsed Ti: Sapphire laser (Libra II, Coherent) inside the tissue culture chamber (5% CO_2, 37°C). A 40*oil immersion objective and a pinhole size of 110 μm was used for image capture.

6.1.4.5 Bacterial MIC determination

(The anti-bacterial screening experiments were carried out by Mark Laws at Durham University)

Species used in MIC assays included gram-negative *Escherichia coli* K12 W3110, *Pseudomonas aeruginosa* laboratory strain PAO2 and *Serratia marcescens* laboratory

strain and gram-positive *Staphylococcus aureus* NCTC 6571 and *Micrococcus luteus* laboratory strain.

Bacterial cultures were prepared by streaking the bacterial strains on to agar plates with an inoculation loop and incubating overnight at 37 ℃. A single colony was then selected and placed in 5 mL of Iso-Sensitest broth using an inoculation loop and incubated at 37 ℃ with shaking overnight.

MIC values were attained according to the protocol described by J. M. Andrews *et al.*[1] and were conducted in 96-well microtitre plates in triplicate. 10-50 µL of each overnight culture was inoculated into 1.2 mL of Iso-Sensitest broth and grown at 37 ℃ with shaking. An inoculum density of ~10^4 cfu/spot was determined by comparison with 0.5 MacFarland standard (240 µM $BaCl_2$ in 0.18 M $H_2SO_{4\ aq.}$) and was found to relate to an A_{650nm} of 0.07 after calibration with regular Iso-Sensitest broth. The inoculum was diluted ten-fold with Iso-Sensitest broth before use (to ~10^3 cfu/spot). Peptide solutions were initially dissolved in DMSO (5 mg mL^{-1}) and then diluted further with Iso-Sensitest broth to achieve a concentration range of 4 mgL^{-1} to 512 mgL^{-1} using 2-fold serial dilutions. Samples were vortexed between dilutions where necessary to aid dissolution. 50 µL of inoculum and 50 µL of peptide solution were added to each test well to achieve a final concentration range of 2 mgL^{-1} to 256 mgL^{-1}. Separate dilutions of ampicillin and DMSO were made up in a similar manner to act as a positive antibacterial control and a +DMSO control, respectively. 50 µL of inoculum and 50 µL of Iso-Sensitest broth were used as a positive control and 100 µL of inoculum was used as a negative control. Positive and negatives controls were conducted multiple times in parallel per plate. MIC was defined as the lowest concentration which completely inhibited bacterial growth after incubation at 37 ℃ for 16 h with shaking. IC_{50} was defined as the concentration of antibiotic which achieved a 50% inhibition of bacterial growth after incubation at 37 ℃ for 16 h with shaking. Quantitative data were attained as A_{650nm} values using a BioTek® Synergy™ H4 Hybrid Multi-Mode Microplate Reader.

6.2 Synthesis of short Elastin-like peptides

6.2.1 Synthesis of peptide H-VPGVG-NH_2 (9)

Solid-phase peptide synthesis with an Fmoc-protecting group strategy and Rink Amide resin was employed to synthesise the peptide H-VPGVG-NH_2 (**9**). A suspension of Rink Amide resin (0.25 g, 0.19 mmol, 1 eq) was pre-swollen in DCM for 30 min and washed by DMF three times. Then, 20% (*v/v*) piperidine in DMF was added for 5 min to remove the Fmoc group and this was repeated three times. After each time the resin was washed with DMF (3 × 5 mL). Fmoc-Gly-OH (0.11 g, 0.37 mmol, 2 eq) was pre-activated with PyBOP (0.19 g, 0.36 mmol, 2 eq) and NMM (40μL, 0.37 mmol, 2 eq) in DMF for 10 min and then was added into the pre-swollen resin, the reaction mixture was constantly agitated for 2 h. This procedure was then repeated with the following four amino acids: Fmoc-Val-OH (0.13g, 0.37 mmol, 2 eq), Fmoc-Gly-OH (0.11 g, 0.37 mmol, 2 eq), Fmoc-Pro-OH (0.13 g, 0.37 mmol, 2 eq), and Fmoc-Val-OH (0.13 g, 0.37 mmol, 2 eq). Piperidine (20% *v/v*) in DMF was added to the resin to remove the Fmoc group. The resin was washed repeatedly with DMF, DCM and diethyl ether. Peptide **9** was then cleaved from the resin using 3 mL of 95% TFA containing 2.5% of water and 2.5% of TIPS. After cleavage for 3 h, the resin was removed by filtration and the obtained peptide was precipitated in diethyl ether. The product was then dissolved in water and freeze dried. 45 mg of peptide **9** was obtained, yield was 56%.
LC-MS for peptide **9** (VPGVG-NH_2): 427.2 ($M+H^+$), MW: 426 Da.

HRMS *m/z* (ESI) 427.2663, consistent with empirical formula $C_{19}H_{35}N_6O_5$ with an accuracy of 1.4 ppm (accepted as $(M + H)^+$).

Analytical RP-HPLC using a linear gradient of 0-100% of solvent B – this being (*v/v*) 5% H2O/95% CH_3CN with 0.1% TFA as explained in **Section 6.1.2.5** – over 30 min showed a retention time of **9** at 7.8 min.

6.2.2 Synthesis of acetylated peptide Ac-VPGVG-NH_2 (10)

Acetylated peptides were synthesised using 20% *v/v* acetic anhydride in DMF to cap the end groups of the peptides and the same coupling procedure for peptide **9** was applied. The resin (0.1 g, 0.74 mmol g^{-1}) was swelled and washed three times in 9 mL of DCM for 15 min. Then 10 mL DMF containing 20% *v/v* piperidine was added to remove the Fmoc group. After that 10 mL DMF solution containing 20% v/v acetic anhydride was

added and reacted for 30 min, twice. When the reaction had finished, the resin was first rinsed with DMF and Et_2O twice each, and then the peptide was cleaved from the resin using 95% TFA, 2.5% water and 2.5% TIPS for 3 h to remove any reactive side chain of the amino acids. The peptide was precipitated in cold Et_2O in a round-bottom flask for 5 min and then the solution was evaporated. The peptide was dissolved in water and freeze dried to obtain the product. 17 mg of peptide **10** was obtained, yield was 50%.
LC-MS for peptide **10**: 469.2 ($M+H^+$), 938.1 ($2M+H^+$), MW: 468 Da.

HRMS *m/z* (ESI) 469.2769, consistent with empirical formula $C_{21}H_{37}N_6O_6$ with an accuracy of 1.3 ppm (accepted as $(M + H)^+$).

Analytical RP-HPLC using a linear gradient of 0-100% of solvent B – this being (*v/v*) 5% H2O/95% CH_3CN with 0.1% TFA as explained in **Section 6.1.2.5** – over 30 min showed a retention time of **10** at 10.3 min.

6.2.3 Synthesis of thiol-functionalised peptide SH-VPGVG-NH_2 (11)

3-Tritylsulfanyl-propionic acid was used to synthesise the thiol-functionalized peptide SH-VPGVG. First, 0.1 g Rink Amide resin (0.77 mmol g^{-1}) loaded with Fmoc-peptide VPGVG (0.077 mmol, 1 eq) was pre-swollen in DCM for 30 min and washed with DMF three times. Then, 20% *v/v* piperidine in DMF was added for 5 min to remove the Fmoc group and the procedure was repeated three times. After each time the resin was washed with 9 mL DMF three times. The exposed amino acid was coupled by adding a mixture of 3-tritylsulfanyl-propionic acid (0.134 g, 0.385 mmol, 5 eq) with PyBOP (0.197 g, 0.385 mmol, 5 eq) and NMM (50 μL, 0.385 mmol, 5 eq) in 10 mL DMF. The mixture was shaken for 2 h, after which the resin was washed thoroughly with DMF. When the reaction was complete, the resin was rinsed repeatedly with DCM and diethyl ether three times each. The thiol-functionalized peptide was cleaved from the resin using 3 mL of 95% TFA containing 2.5% water and 2.5% TIPS to remove any reactive side chain of the amino acids. After 3 h, the resin was removed by filtration and the obtained peptide was precipitated in cold diethyl ether. The product was then dissolved in water and then freeze dried. From 0.1 g of rink amide resin, 10 mg of thiol-peptide (**11**) was obtained and yield was 25 %.
LC-MS for peptide **11**: 515.1 ($M+H^+$), MW: 514 Da.
HRMS *m/z* (ESI) 515.2652, consistent with empirical formula $C_{22}H_{39}N_6O_6S$ with an accuracy of 0.4 ppm (accepted as $(M + H)^+$).

Analytical RP-HPLC using a linear gradient of 0-100% of solvent B (solvent A = 0.1% TFA in 95% H_2O and 5% MeCN, solvent B = 0.1% TFA in 5% H_2O and 95% MeCN), over 30 min showed a retention time of **11** at 11.7 min.

6.3 Synthesis of Elastin-based side chain polymers

6.3.1 Synthesis of pentafluorophenyl acrylate (14)

Pentafluorophenyl acrylate (PFPA) was synthesised as described in the literature.[2] In a two neck round bottomed flask connected to a N_2 supply, pentafluorophenol (PFP) (10g, 54.3 mmol, 1 eq) and triethylamine (TEA) (6.6g, 65.2 mmol, 1.2 eq) were dissolved in 100 mL of dry diethyl ether and the mixture was cooled in an ice bath. Acryloyl chloride (6.0 g, 66.3 mmol, 1.2 eq) was added drop-wise through a needle under cooling with an ice bath. The clear solution of PFP and TEA turned into a white suspension immediately. Then remove the ice bath and the suspension was stirred overnight at ambient temperature with N_2 protection.[3]

The precipitated triethylamine hydrochloride salt was removed by filtration, and the solid was washed with diethyl ether. After evaporation of the solvent, the residue was filtered again to obtain a clear yellow liquid. The reaction mixture containing the unreacted PFP (**12**), acryloyl chloride (**13**) and crude product (**14**) were analysed by TLC (petroleum ether 40-60^oC as eluent). The TLC showed two spots with R_f values of 0.48 and 0.68 which are due to PFP and crude product respectively. The yellow crude product was purified by using an auto column chromatography. The column material was silica gel and the solvent we used was petroleum ether (40-60^oC). The collected fraction was putted on the rotary evaporator to remove the petroleum ether. After evaporation, the final product was obtained (6.7 g, 27.5 mmol) and the yield was 52%. Pure PFPA was stored in the refrigerator.

^{1}H-NMR (400 MHz, 298K, $CDCl_3$) δ_H / ppm: 6.65 (1H, dd, Hc), 6.28 (1H, dd, Ha), 6.13 (1H, dd, Hb). ^{13}C-NMR (400 MHz, 298K, $CDCl_3$) δ_C / ppm: 161.7 (1C, s, CO), 141.2 (2C, m, C2), 139.5 (1C, m, C4), 137.9 (2C, m, C3), 135.4 (1C, s, CH_2), 125.3 (1C, s, CH), 125.0 (1C, m, C1).

6.3.2 Synthesis of RAFT agent (15)

(The synthesis was carried out by Ali Abdulkarim at Durham University)

In a one neck round bottom flask, potassium phosphate (27.2g, 128 mmol) was stirring in 350 mL of acetone. After 10 min, mercaptoethanol (10g, 128 mmol, 1 eq) was added into the suspension. The solution was stirred for 10 min and followed by the dropwise addition of carbon disulfide (21.9 g, 128 mmol, 1 eq) in ice bath and the solution was turned to yellow. After another 10 min, benzyl bromide (29.2g, 384.5mmol, 3eq) was added slowly through a funnel and the reaction was continuously stirred at ambient temperature for 30 min. The reaction scheme is described as in **Figure 6.1**.

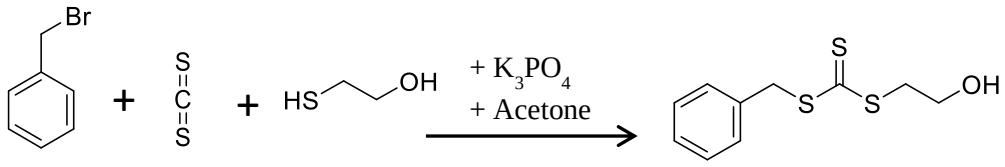

Figure 6.1: Synthesis of RAFT agent benzyl 2-hydroxyethyl carbonotrithioate (**15**).

After reaction, the precipitated potassium bromide salt was removed by filtration, and the solid was washed with acetone. After evaporation of the solvent, the residue was filtered again to obtain a clear liquid. The yellow crude product was purified by using an auto column chromatography. The eluent ratio was 3:1 of petroleum ether (40-60 ^{o}C) and ethyl acetate. The final product was putted under high vacuum to remove all solvents. The product was obtained as light yellow oil in a yield of 72% (22.3g). The synthesised RAFT agent was characterised by ^{1}H NMR spectroscopy (**Appendix 6.1**) in solvent $CDCl_3$. Pure benzyl 2-hydroxyethyl carbonotrithioate was stored in the freezer.

The product was characterized by ^{1}H-NMR ($CDCl_3$): 7.31-7.11 (5H, m, Ph), 4.52 (2H, s, benzyl-CH_2), 3.74 (2H, q, -CH_2-OH), 3.48 (2H, t, -S-CH_2).

6.3.3 Synthesis of poly(pentafluorophenyl acrylate) polymers

Here we give one example of polymerisation of poly (pentafluorophenyl acrylate) poly(PFPA)-100 (**19**). Pentafluorophenyl acrylate (PFPA) (0.5g, 2.1 mmol, 100 eq), benzyl 2-hydroxyethyl trithiocarbonate (5.1mg, $2.1x10^{-5}$ mol, 1 eq), AIBN solution (2.0 mg, $1.05x10^{-5}$ mol, 0.5 eq) and benzene (5.0 mL) were added to a schlenk tube with stirring. The solution was cooled down in an ice bath and purged with nitrogen for 30 min. After that, the ice bath was removed and the solution was heated to 70^{o}C for 6 h. Conversion was determined by ^{1}H NMR.

After 6 h, the schlenk tube was cooled at ambient temperature with N_2 protection. Then the reaction was quenched by putting the whole tube into a box of dry ice for 10 min. Afterwards the product could be left under atmospheric oxygen. Then solution was partially removed under vacuum and the rest was precipitated in methanol which was cooled to 0^{o}C beforehand. After centrifuging and decanting the methanol, the polymer was dissolved in THF and re-precipitated again. The operation was repeated three times to remove any unreacted RAFT agent and any trace monomers. The polymer was dried under vacuum oven over night to yield a yellow powder. The sample was characterized by THF GPC, ^{1}H-NMR and ^{19}F NMR (CD_2Cl_2) and FT-IR spectroscopy. The experiments of all the polymers (**16**-**19**) synthesised are summarized in **Table 2.2**.

Taking P(PFPA)-100 (**19**) as an example. The coversion rate is calculated based on the equation shown as below.

The equation is given below (eq.1).

$$\text{Conversion} = \left[\frac{\text{Ipolymer}}{\text{Imonomer} + \text{Ipolymer}} \right] \text{x } 100\% \qquad (1)$$

So for **19**, the integral of polymer peak (c) is 4.69, while the monomer peak is 1.00. (**Figure 2.33**)

$$\text{Conversion} = \left[\frac{4.69}{4.69 + 1.00} \right] \text{x } 100\% = 83\% \qquad (2)$$

Theoretical M_n was calculated using the following equation:

$$M_{n,theor} = [M]/[RAFT] \text{ x } MW_{monomer} + MW_{RAFT\ agent}$$

[M]/[RAFT] represents the ratio of monomer and RAFT agent concentration, $MW_{monomer}$ is the molar mass of PFPA (**14**) (238 g.mol^{-1}) and $MW_{RAFT\ agent}$ is the molar mass of RAFT agent **15** (244 g.mol^{-1}).

Experimental M_n was measured by ^{1}H NMR spectroscopy and calculated by the following equation:

$$M_{n,NMR} = [\, I^{\text{CH at 3.0 ppm}} / (I^{\text{phenyl group at 7.2 ppm}} /5)] \text{x } MW_{monomer} + MW_{RAFT\ agent}$$

$I^{\text{CH at 3.0 ppm}}$ and $I^{\text{phenyl group at 7.2 ppm}}$ are corresponding to the intensity of signals at 3.0 ppm and 7.2 ppm respectively.

^{1}H-NMR and ^{19}F NMR spectra of P(PFPA)-25,50,75 (**16-18**) can be found in **Appendices 2.1-2.3**. ^{1}H-NMR and ^{19}F NMR spectra of P(PFPA)-100 (**19**) are shown in **Figure 2.34**.

6.3.4 Synthesis of short elastin-like peptides for coupling to P(PFPA)

Solid-phase peptide synthesis with an Fmoc-protecting group strategy and rink amide resin was employed to synthesise the peptide **9**, **20** and **21** as described in **Table 2.3**. The synthesis approach was the same as peptide **9** discussed in **Section 6.2.1**.

Rink Amide resin (0.25 g, 0.19 mmol, 1 eq) was pre-swollen in DCM for 30 min and washed by DMF three times. Then, 20% v/v piperidine in DMF was added for 5 min to remove the Fmoc group and this was repeated three times. After each time the resin was washed with DMF (3 × 5 mL). Fmoc-Gly-OH (0.11 g, 0.37 mmol, 2eq) was pre-activated with PyBOP (0.19 g, 0.36 mmol, 2 eq) and NMM (40 μL, 0.37 mmol, 2eq) in DMF for 10 min. Finally, the pre-activated solution was added to the pre-swollen resin, and the reaction mixture was constantly agitated for 2 h. After this, the resin was washed with DMF (3 × 5 mL). The reaction sequence was repeated to ensure complete functionalization. At the last coupling process, amino acids Fmoc-Gly-OH (0.11 g, 0.37 mmol, 2 eq) and 4-(Fmoc-amino) butyric acid (Fmoc-GABA-OH) (0.12 g, 0.37 mmol, 2 eq) was added respectively for **20** and **21**. The peptide was then cleaved from the resin using 3 mL of 95% TFA containing 2.5% of water and 2.5% TIPS. After cleavage for 3 h, the resin was removed by filtration and the obtained peptide was precipitated in diethyl ether.

From 0.25 g of Rink Amide resin, 45 mg of purified peptide **9** was obtained (yield: 56%); 48 mg of purified peptide **20** was obtained (yield: 53%); 53 mg of purified peptide **21** was obtained (yield: 55%).

LC-MS for **9** (VPGVG-NH_2): 427.2 ($M+H^+$), MW: 426 Da. Analytical retention time was 7.8 min. LC-MS for **20** (GVPGVG-NH_2): 484.0 ($M+H^+$), MW: 483 Da. Analytical retention time was 8.3 min. LC-MS for **21** (GABA-VPGVG-NH_2): 511.9 ($M+H^+$), MW: 511 Da. Analytical retention time was 9.1 min.

All the retention time was measured by analytical RP-HPLC using a linear gradient of 0-100% of solvent B (solvent A = 0.1% TFA in 95% H_2O and 5% MeCN, solvent B = 0.1% TFA in 5% H_2O and 95% MeCN) over 30 min.

6.3.5 Synthesis of elastin-based side chain polymers (22-29)

An example is given for the peptide modification of Poly(PFPA) as follows: Poly(PFPA) (20 mg, 8.2×10^{-5} mol of pentafluorophenyl groups) was dissolved in 2.5 mL of DMF in a glass vial. The solution was purged with nitrogen. Peptide solution was prepared by dissolution of peptide **9** (50 mg, 1.2×10^{-4} mol) in dimethyl sulfoxide (DMSO) (0.7 mL). Triethylamine (18 µL, 1.3×10^{-4} mol) was then added to the peptide solution. The peptide solution was subsequently added slowly to the poly(PFPA) solution by using a syringe. The solution was stirred for 5 h or overnight at 30°C and the colour of the solution changed from orange to very light yellow.

After reaction, the polymer was dialyzed (MWCO=3500 Da) against water for 3 d to remove any unreacted peptide. The elastin-based side chain polymer was freeze dried and analysed by ^{1}H NMR, ^{19}F NMR in d_6-DMSO, GPC and FT-IR spectroscopies (**Appendices 2.6-2.13**).

6.4 Synthesis of Gold nanoparticles (GNPs)

Gold nanoparticles (GNPs) were synthesised by using Frens and Turkevich method.[4] All glassware used for synthesis of colloidal gold was cleaned using aqua regia (3:1 HCl: HNO_3), rinsed extensively with water, and dried in the oven at 60 ℃. A $HAuCl_4 \bullet 3H_2O$ solution (0.01 wt %, 0.3 mM, 50 mL) was brought to boiling with rapid stirring in a 100 mL round-bottom flask fitted with a reflux condenser. Once the solution resumed boiling, trisodium citrate (1 wt%, 1.5 mL) solution in water was added quickly with continued stirring, after that the solution started to turn to dark blue and finally red. The reaction was refluxed for 5 min and stirring continued for another 30 min. The colloidal gold suspension was cooled to room temperature and filtered through a 0.2 µm filter. The diameter of the colloids was determined by transmission electron microscopy (TEM) and dynamic light scattering (DLS).

6.5 Synthesis of short elastin-like peptide functionalised GNPs (ELP-GNPs)

The synthesis of short elastin-like peptide functionalized gold nanoparticles (ELP-GNPs) used the reaction between thiol and gold nanoparticles. Thiol-peptide (7 mg, 0.01 mmol) was dissolved in 1mL deionized water and then added into a 20 mL filtered GNP solution (0.3 mM, 0.006 mmol of Au). The mixture of the thiol-peptide and GNPs was stirred overnight at room temperature in a small round-bottom flask under nitrogen. After that the solution was transferred to a dialysis bag (MWCO: 3500 Da) and dialysed against deionised water for 24 h. The ELP-GNPs (**30**) were then freeze-dried to obtain a dark purple solid.

6.6 Synthesis of polymer functionalised GNPs (ESP-GNPs)

The fabrication of elastin-like peptide functionalized polymer coated gold nanoparticles used the reaction between thiol and gold nanoparticles. $P(PFPA)_{100}$-GABA(VPGVG) (10mg, 0.0007 mmol) was dissolved in 1mL deionized water and then added into a 10 mL of the citrate-stablized gold nanoparticle solution (0.3 mM, 0.003 mmol of Au). The reaction was taken overnight and under N_2 protection. Then the polymer coated GNPs were dialyzed (MWCO=50,000 Da) against water for 3 d to remove any unreacted polymers. The GNP-polymer was then freeze-dried to obtain a purple fluffy powder.

6.7 Synthesis of KLA peptide functionalized GNPs (KLA-GNPs)

6.7.1 Synthesis of GNPs

The gold nanoparticles were synthesised via the same method as described in **Section 6.4**. However, the concentration of the mother solution of Au^{3+} is tripled. Briefly, 50 mL of 1 mM the $HAuCl_4 \bullet 3H_2O$ was dissolved in a 150 mL round bottomed flask and refluxed for 5 mins. Then, 8.5 mL of trisodium citrate solution (1 wt%, 38.8 mM) was added quickly into the boiling solution and a colour change from light yellow to dark blue was observed immediately. And 1 min later, the colour changed again from dark blue to red and the solution was refluxed for another 10 mins. Cool the solution to room temperature naturally and subsequently filtered through 0.45 μm aqueous phase membrane filter and the gold nanoparticle were used for the next functionalization.

6.7.2 Synthesis of thiol-TTDS-KLA (38)

The $_{D\text{-}(}$KLAKLAK)$_2$ peptide was synthesised manually using a standard Fmoc chemistry through the solid phase peptide synthesis. Briefly, Rink Amide resin (0.77 mmol g^{-1} loading, 0.13 g, 0.1 mmol) was weighed out and swollen in a fritted PTFE reaction vessel for 1 hour in DMF. Then using 20% piperidine in DMF for 5 min and 10 min to deprotect the resin and washed by DMF three times after the deprotection. The coupling of the first residue used 3 equiv (relative to the substitution degree of resin) Fmoc-protected amino acid, PyBOP (0.3 mmol, 158 mg) and DIPEA (0.6 mmol, 115 μL) in a DMF solution for 1 hour at room temperature. The reacton vessel was placed on a shaker for the duration of the coupling steps and each residue was coupled twice. During the synthesis, Fmoc protection groups were removed by 20% piperidine/DMF. At the end of the KLA synthesis, the linker of Fmoc-TTDS-OH (0.3 mmol, 162 mg) was conjugated to the peptide sequence. The coupling process is the same as coupling each amino acid. Finally, 3-tritylsulfanyl-propionic acid (0.3 mmol, 104 mg) was added to the sequence to provide a free thiol end.

After the completion of the synthesis, the resin was finally washed with DMF, DCM and diethyl ether three times separately. The cleavage of the peptide on resin was performed by adding a cleavage cocktail in to the vessel, which containing TFA (95%), TIPS (2.5 %) and H_2O (2.5 %) for 3 h. The filtration was concentrated to a viscous solution by rotary evaporation and followed by precipitation in cold ether solvent. Decant the ether slowly and the crude product was collected. Then the crude peptide was dissolved in distilled water and freeze dried.

The molecular weight of thiol-TTDS-KLA ($C_{89}H_{169}O_{20}N_{23}S$) peptide was analysed by MALDI and found in 1935.2 which is $[M+ Na]^+$. HRMS *m/z* (ESI) 957.6361, consistent with empirical formula $C_{89}H_{169}O_{20}N_{23}S$ with an accuracy of 5 ppm (accepted as $(M + 2H)^{2+}$).

Analytical RP-HPLC using a linear gradient of 0-100% of solvent B – this being solvent A = 0.1% TFA in 95% H_2O and 5% MeCN, solvent B = 0.1% TFA in 5% H_2O and 95% MeCN – over 30 min showed a retention time of **38** at 14.7 min.

6.7.3 Synthesis of KLA-GNPs (39)

The synthesis of SH-TTDS-KLA peptide functionalized gold nanoparticles (KLA-GNPs) was achieved through thiol-gold covalent bonding. The weight ratio of peptide to gold is 2:1 to make the peptide excess to gold nanoparticles. In the process, 3.5 mg of peptide was dissolved in 1 mL deionized water and slowly dropped into 10 mL (0.01 mmol, 1.9 mg) of filtered gold nanoparticles (1 mM) and the colour changed from red to purple. The mixture was stirred overnight at room temperature with nitrogen protection. Then the purple solution was transferred to a dialysis bag (MWCO: 3500 Da) and dialysed against deionised water for 2 d. The KLA-GNPs were then freeze-dried to obtain 4 mg of dark purple solid.

6.8 Synthesis of KLA-ESP$_{100}$-GNPs (40)

The preparation of thiol-TTDS-KLA and PF100-GABA(VPGVG) peptides functionalized gold nanoparticles (KLA-ELP$_{100}$-GNPs) was achieved via thiol-gold covalent bonding. The weight ratio of peptides used was 1:1. In the process, 2 mg of thiol-TTDS-KLA (**38**) and 2 mg of PF100-GABA(VPGVG) (**29**) were dissolved in 0.5 mL deionization water separately. Through two separate syringes, both peptides were dropped slowly into 10 mL of filtered GNPs (0.01 mmol, 1.96 mg) and the colour changed from red to purple. The mixture was stirred overnight at room temperature under nitrogen. Then the purple solution was transferred to a dialysis bag (MWCO: 50,000 Da) and dialysed against deionised water for 24 h. The KLA-ELP$_{100}$-GNPs were then freeze-dried to obtain 5 mg of dark purple solid.

6.9 Synthesis of $_{D-/L-}$KLA peptides

The $_{D-(}$KLAKLAK)$_2$ peptide (**33**) was synthesised manually using a standard Fmoc chemistry through solid phase peptide synthesis. Briefly, the Rink Amide resin (0.77 mol/g loading, 0.1 mmol) was weighed out and swollen in a fritted PTFE reaction vessel for 1 hour in DMF. Then using 20% piperidine in DMF for 5 mins and 10 mins to deprotect the resin and washed by DMF three times after the deprotection. The coupling of the first residue used 3 equiv (relative to the substitution degree of resin) Fmoc-protected amino acid, 3 equiv of PyBOP and 6 equiv of DIPEA in a DMF solution for 1 hour at room temperature. The reacton vessel was placed on a shaker for the duration of the coupling steps and each residue was coupled twice. During the

synthesis, Fmoc protected groups was deprotected with 20% piperidine/DMF. The coupling steps were repeated for the rest amino acids. A test cleavage was carried out at 7th amino acid using 1 mL cleavage cocktail (95% TFA, 5% TIPS and 5% water) with shaking at room temperature for 2 h. Final cleavage from resin was taken by 3 mL of same cleavage cocktail for 3 h. The filtrate was concentrated to a viscous solution by rotary evaporation and followed by precipitation in cold ether solvent. Decant the ether slowly and the crude product was collected. Then the crude peptide was dissolved in distilled water and freeze dried. Semi-preparative HPLC was used to purify **33** as described in **Section 6.1.2.5**. After HPLC purification, 23 mg $_{D}$-KLA was obtained and the yield was 15%. For $_{L}$-KLA, 25 mg was obtained with a yield 16%.

The molecular weight of $_{D}$-KLA (**33**) was analysed by MALDI and found in 1544.9 which is [M+ Na]$^{+}$. LC-MS for $_{D}$-KLA: 508.5 (3H^{+}), 381.7 (4H^{+}), MW: 1523.1 Da. (**Appendix 4.1**)

The molecular weight of $_{L}$-KLA (**41**) was analysed by MALDI and found in 1946.1 which is [M+ Na]$^{+}$. LC-MS for $_{L}$-KLA: 508.3 (3H^{+}), 381.6 (4H^{+}), MW: 1523.1 Da. (**Appendix 4.2**)

Analytical RP-HPLC using a linear gradient of 0-100% of solvent B – this being solvent A = 0.1% TFA in 95% H_2O and 5% MeCN, solvent B = 0.1% TFA in 5% H_2O and 95% MeCN – over 30 min showed a retention time of **33** and **41** both at 11.4 min.

6.10 Synthesis of peptoid hybrids

6.10.1 Synthesis of peptoids

The peptoid oligomers were synthesised using the solid-phase sub-monomer method [5, 6]. The Rink Amide resin (135 mg, 100 μmol, 1.00 equiv) was covered with 5 mL DMF and swollen overnight at room temperature. The solvent was filtered and the resin was thoroughly washed with DMF. The resin was treated with 20% piperidine in DMF (5 min and 15 min with 3 mL each), and thoroughly washed with DMF. A solution of bromoacetic acid (1 mL, 0.6M in dry DMF, 3.00 equiv) and DIC (0.2 mL, 50% v/v in DMF, 3.00 equiv) was added to the resin. The reaction tube was placed on the shaker for 20 min at room temperature. The resin was washed with DMF (3 × 2 mL) before the required amine sub-monomer (1mL, 1.0 M in DMF, 3.00 equiv) was added for 60 min

on the shaker. Bromoacetylation and amine displacement steps were repeated until the final submonomer had been added. This procedure was repeated four times to obtain each peptoid. The resin was washed with DMF (3 × 2 mL each). To a solution of Fmoc-Gly-OH (78 mg, 3.00 equiv) in DMF (2 mL) were added PyBOP (156 mg, 3.00 equiv) and DIPEA (115 μL, 6.00 equiv) before adding to the resin. The reaction was taken 60 min on the shaker at room temperature. The reaction conditions were used a second time as described above (double coupling). The resin was washed with DMF (3 × 5 mL each). The resin was treated with 20% piperidine in DMF (3 × 5 min with 3 mL each), and thoroughly washed with DMF. The solution of Fmoc-Gly-OH (78 mg, 3.00 equiv), PyBOP (156 mg, 3.00 equiv) and DIPEA (115 μL, 6.00 equiv) in DMF (2 mL) were added again to the resin. Each amino acid coupling was carried out twice on the shaker. The reaction time was 60 min for each coupling. Two glycines were coupled to the peptoid at the N-terminus.

To test cleave the peptoid from the resin, a solution of 1 mL TFA, TIPS and H_2O (95:2.5:2.5) was added to a small amount of the resin and allowed to incubate for 120 min at room temperature on the shaker. The resin was rinsed once with 0.5 mL TFA. Then the resin was removed by filtration and the obtained peptoid was precipitated in diethyl ether. The product was then dissolved in water and freeze dried. The crude peptoids were analysed by LC-MS. Summary of the data is shown in **Table 4.2** (Chapter 4).

6.10.2 Synthesis of KLA-CPPos

Peptide-peptoid hybrids were synthesised according to the above peptoid synthesis protocol, followed by standard peptide Fmoc/tBu-methodology and PyBOP/DIPEA coupling. Here we give one example of KLA-CPPo1 (**52**) coupling procedure. The Rink Amide resin (135 mg, 100 μmol, 1.00 equiv) containing the CPPos was covered in 5 mL DMF for at least 30 min to be pre-swollen. The resin was treated with 20% piperidine in DMF (3 × 5 min with 3 mL each), and thoroughly washed with DMF. The solution of Fmoc-$_D$-Lys(Boc)-OH (154mg, 3.00 equiv), PyBOP (156mg, 3.00 equiv) and DIPEA (115 μL, 6.00 equiv) in DMF (2 mL) were added to the resin. The reaction was shaken at room temperature for 60 min. The reaction conditions were repeated a second time as described above (double coupling). The same method was applied when adding Fmoc-$_D$-Leu-OH and Fmoc-$_D$-Ala-OH to the resin. The cleavage of the

peptide-peptoid hybrid was using a solution of 1 mL TFA, TIPS and H_2O (95:2.5:2.5), and the resin was shaking for 4 h at room temperature. After HPLC-purification 24 mg of CPPo1 (**52**) was obtained with a yield of 11%. Analytical HPLC, accurate mass and MALDO-ToF data of all the peptide-peptoid hybrids (**52**-**57**) are shown in **Appendix 4.3**-**4.8**.

6.10.3 Rhodamine-KLA-CPPo6 (59)

The Rink Amide resin (34 mg, 25 μmol, 1.00 equiv) was covered in 5 mL DMF for at least 30 min to be pre-swollen. Afterwards the resin was washed with 3 × DMF (3 mL). The Fmoc deprotection was treated with 20% piperidine in DMF (5 min and 15 min with 3 mL each), and thoroughly washed with DMF. Rhodamine B (59.6 mg, 0.125 mmol, 5.0 equiv) was coupled using DIC (31.9μL, 0.125 mmol, 5.0 equiv) and HOBt (16.9 mg, 0.125 mmol, 5.0 equiv) in DMF for 1 hour at room temperature. This process was repeated again to make sure the full completion of the reaction. Finally, the crude product was cleaved by adding trifluoroacetic acid (95% in CH_2Cl_2) and shaking at room temperature for 2.5 h. The cleavage solution was filtered and the resin was thoroughly washed with MeOH. This procedure of adding cleavage solution and rinsing with methanol was repeated until the cleavage solution was colourless. Water was added, frozen and lyophilised to give crude product. After purification by semi-preparative HPLC, 5 mg pure product was obtained with a yield of 15%. The LC-MS analysis and MALDI-TOF MS of Rhod-KLA-CPPo6 were shown in following data (**Appendix 4.9**):

LC-MS of Rhod-KLA-CPPo6: 1347.8 ($2H^+$), 539.7 ($5H^+$), 449.9 ($6H^+$). MALDI of Rhod-KLA-CPPo6: $[M+H]^+$=2696.4. HRMS *m/z* (ESI) 540.321, consistent with empirical formula $C_{72}H_{138}N_{21}O_{14}$ with an accuracy of -3.8 ppm (accepted as $(M + 5H)^{5+}$). Analytical RP-HPLC using a linear gradient of 0-100% of solvent B – this being (*v/v*) 5% H2O/95% CH_3CN with 0.1% TFA as explained in **Section 6.1.2.5** – over 30 min showed a retention time of **59** at 19.6 min.

6.11 References

1. J. M. Andrews, *J. Antimicrob. Chemother.*, 2001, **48**, 5-16.
2. F. D. Jochum and P. Theato, *Macromolecules*, 2009, **42**, 5941-5945.
3. C. Boyer and T. P. Davis, *Chem. Commun.*, 2009, 6029-6031.

4. G. Frens, *Nature*, 1973, **241**, 20-22.
5. R. N. Zuckermann, J. M. Kerr, S. B. Kent and W. H. Moos, *J. Am. Chem. Soc.*, 1992, **114**, 10646-10647.
6. T. S. Burkoth, A. T. Fafarman, D. H. Charych, M. D. Connolly and R. N. Zuckermann, *J. Am. Chem. Soc.*, 2003, **125**, 8841-8845.

Appendices

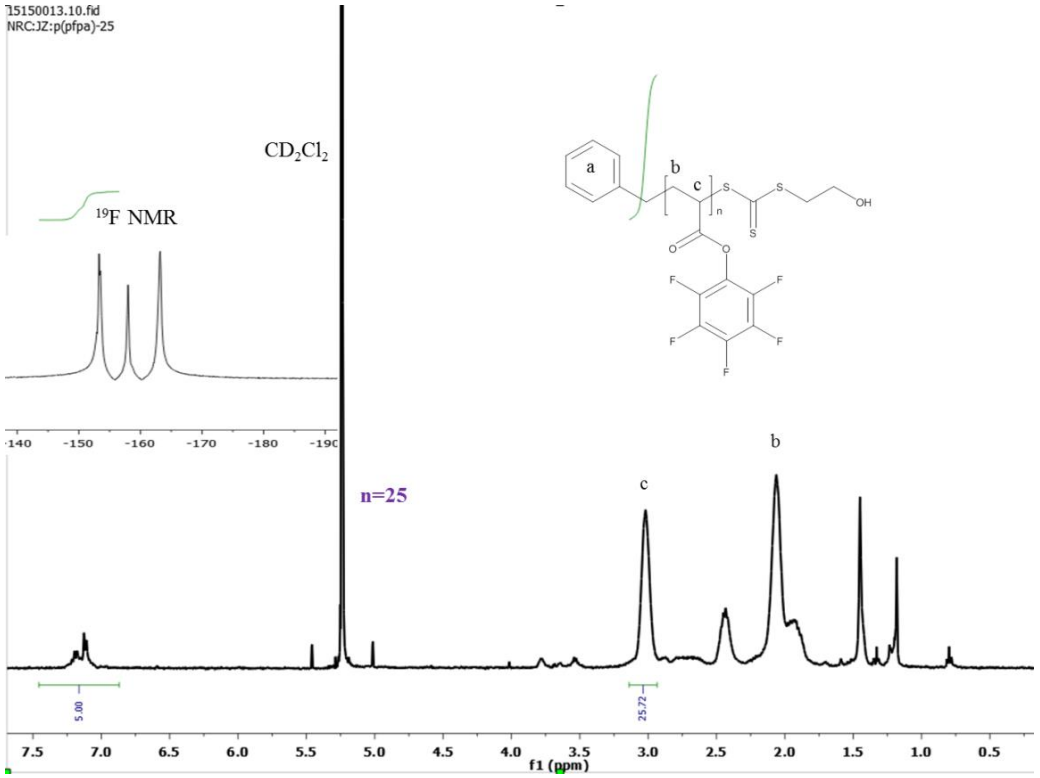

Appendix 2.1: ^{1}H NMR and ^{19}F NMR spectra of P(PFPA)-25 (**16**) in solvent CD_2Cl_2.

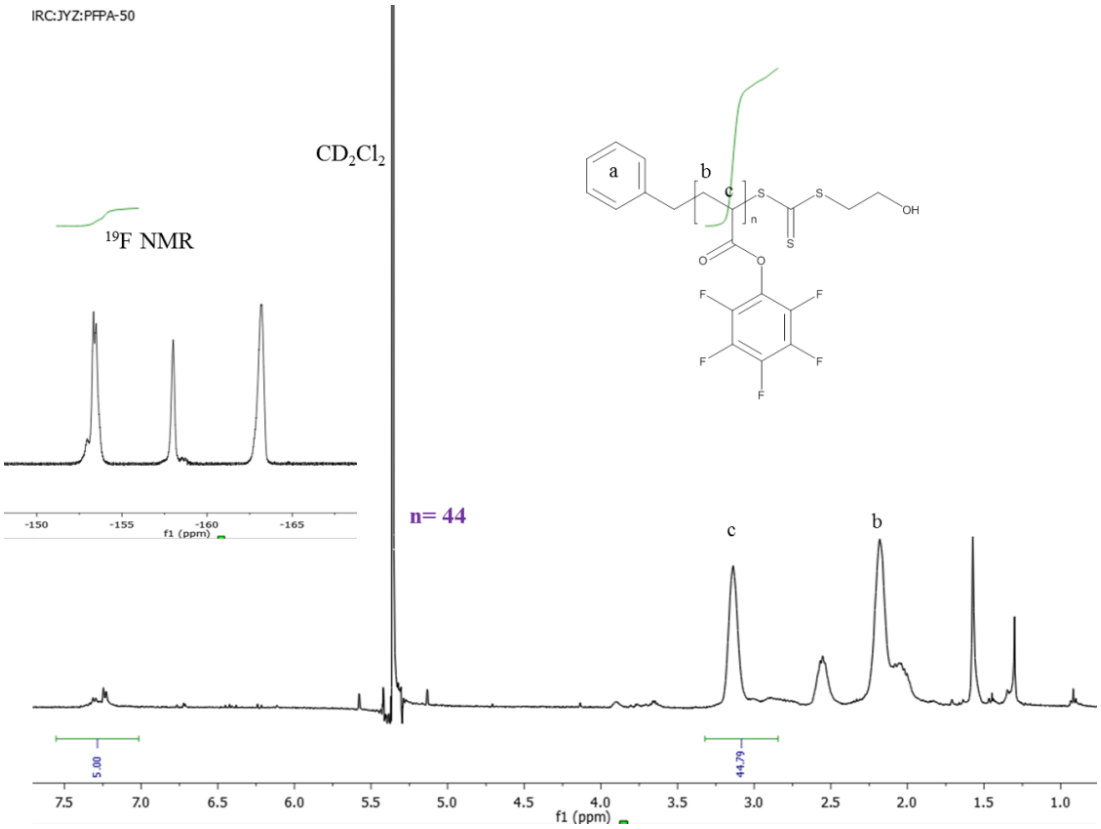

Appendix 2.2: ^{1}H NMR and ^{19}F NMR spectra of P(PFPA)-50 (**17**) in solvent CD_2Cl_2.

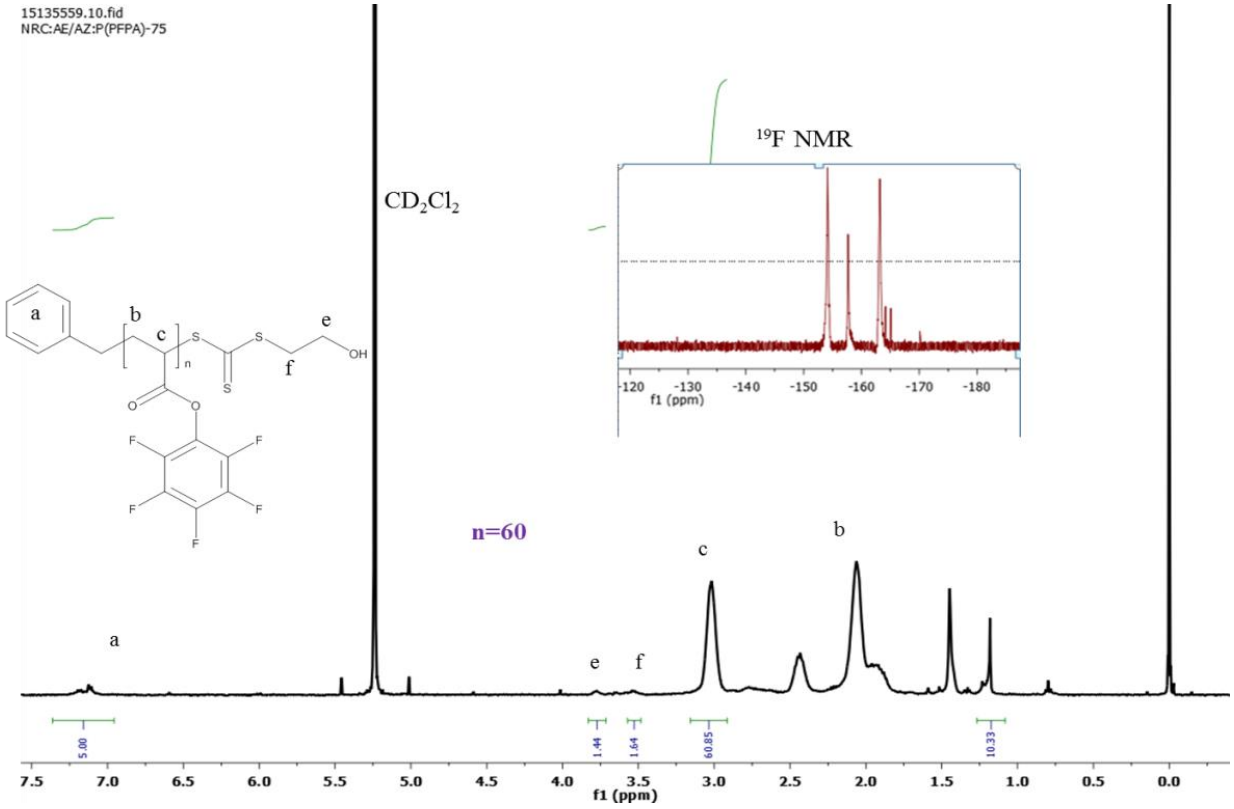

Appendix 2.3: ^{1}H NMR and ^{19}F NMR spectra of P(PFPA)-75 (**18**) in solvent CD_2Cl_2.

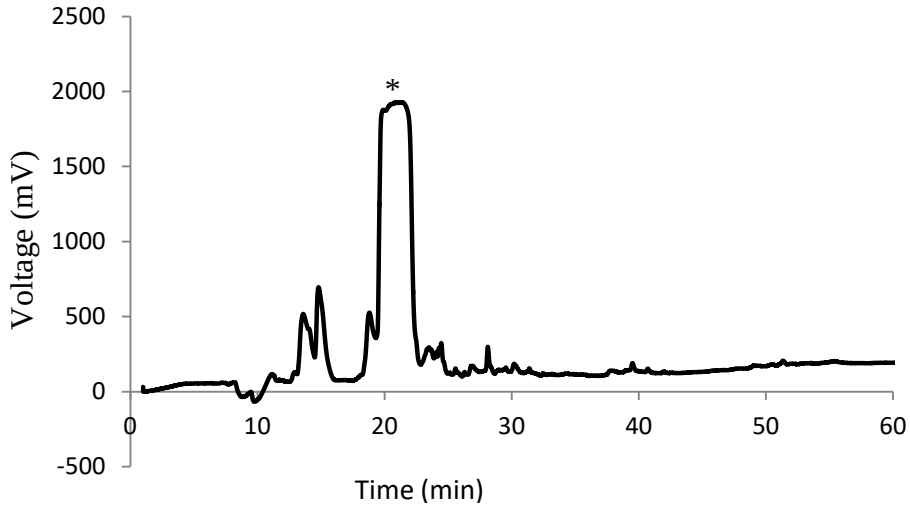

Appendix 2.4: Semi-preparative HPLC chromatogram of crude peptide **20** (GVPGVG). The peak with an asterisk on it represents the target peptide peak. 0-100% solvent B in 45 min. Retention time = 18.0-22.5 min.

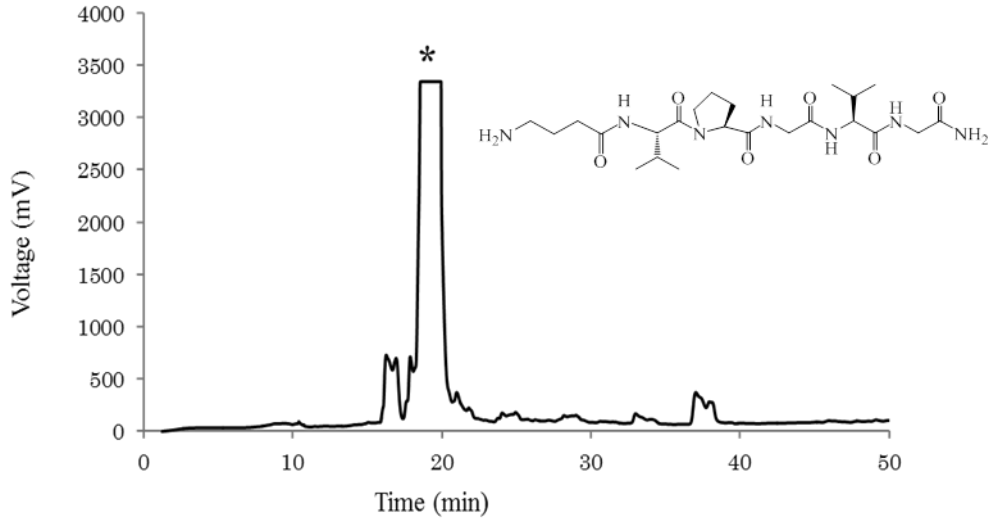

Appendix 2.5: Semi-preparative HPLC chromatogram of crude peptide **21** (GABAVPGVG). The peak with an asterisk on it represents the target peptide peak. Retention time = 18.6-20.5 min.

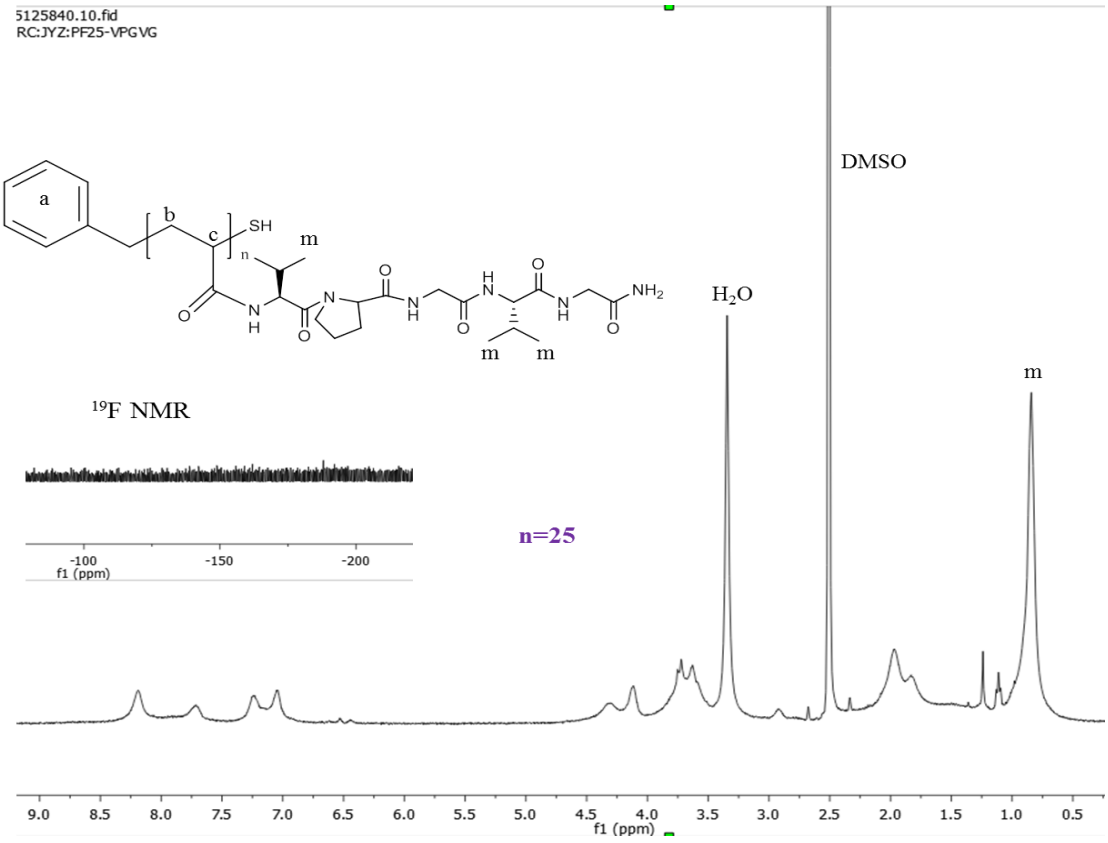

Appendix 2.6: ^{1}H NMR and ^{19}F NMR spectra of PF25-VPGVG (**22**) in d_6-DMSO.

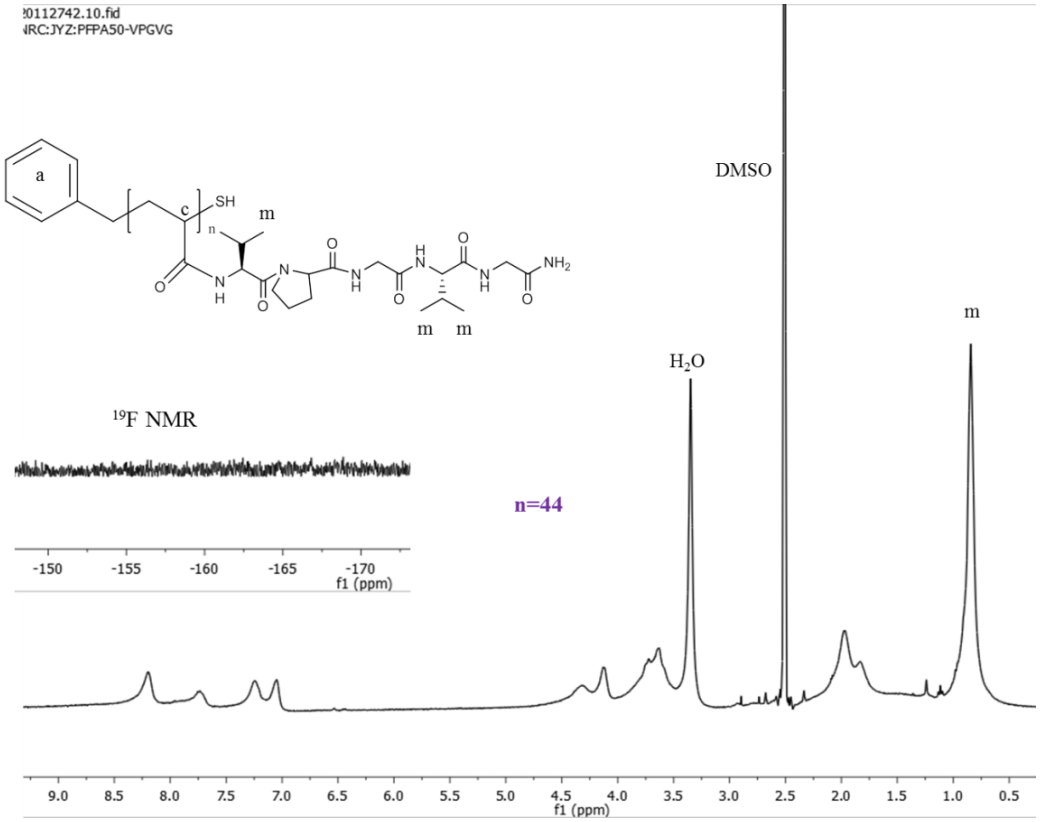

Appendix 2.7: ^{1}H NMR and ^{19}F NMR spectra of PF50-VPGVG (**23**) in d_6-DMSO.

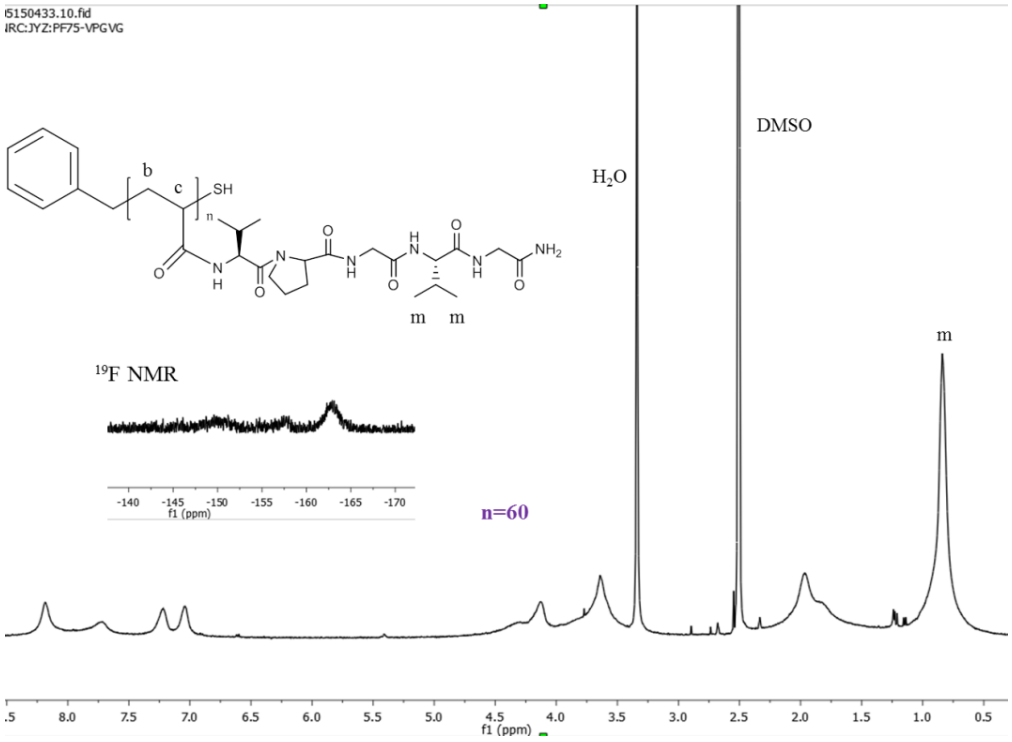

Appendix 2.8: ^{1}H NMR and ^{19}F NMR spectra of PF75-VPGVG (**24**) in d_6-DMSO.

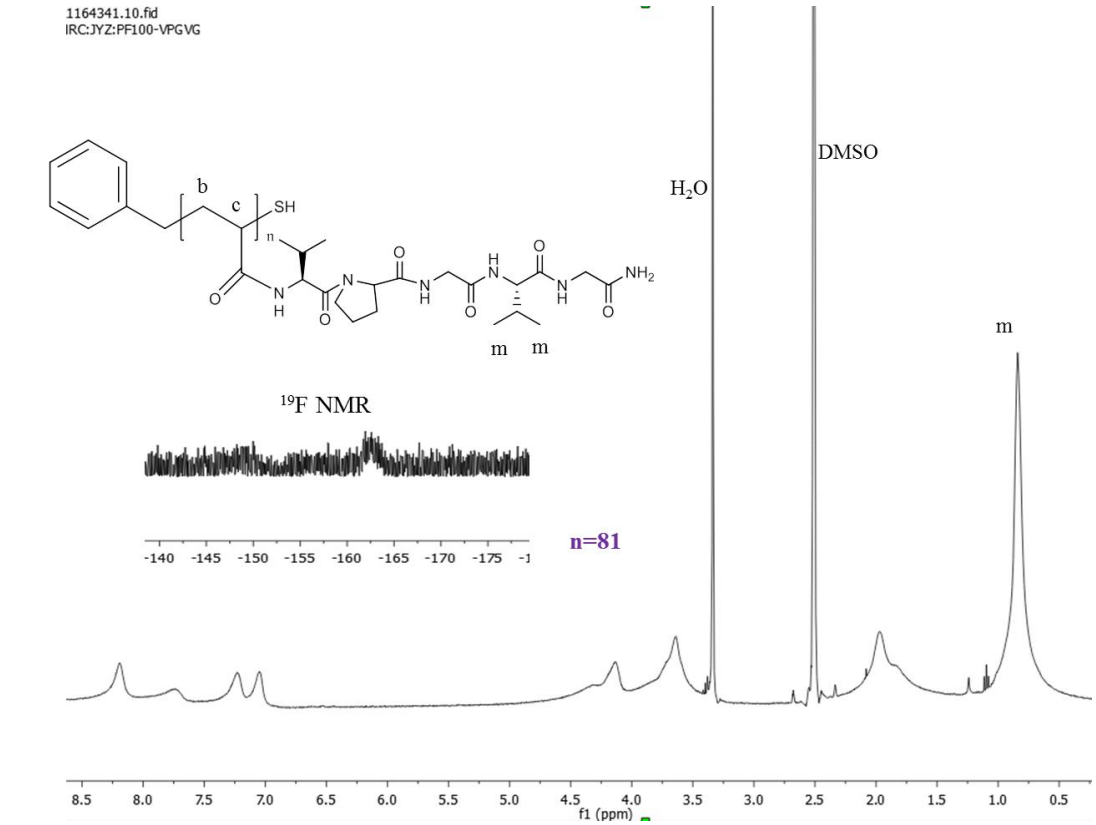

Appendix 2.9: ^{1}H NMR and ^{19}F NMR spectra of PF100-VPGVG (**27**) in d_6-DMSO.

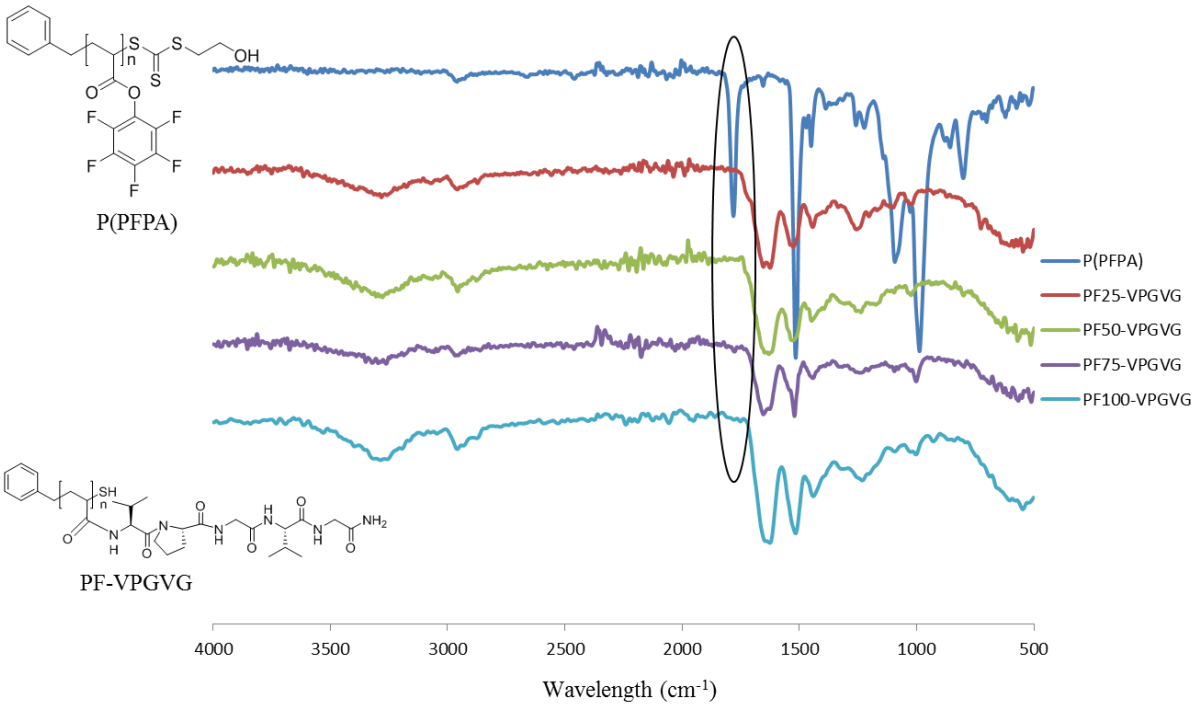

Appendix 2.10: ATR-FTIR spectra of P(PFPA) and PF(25,50,75,100)-VPGVG.

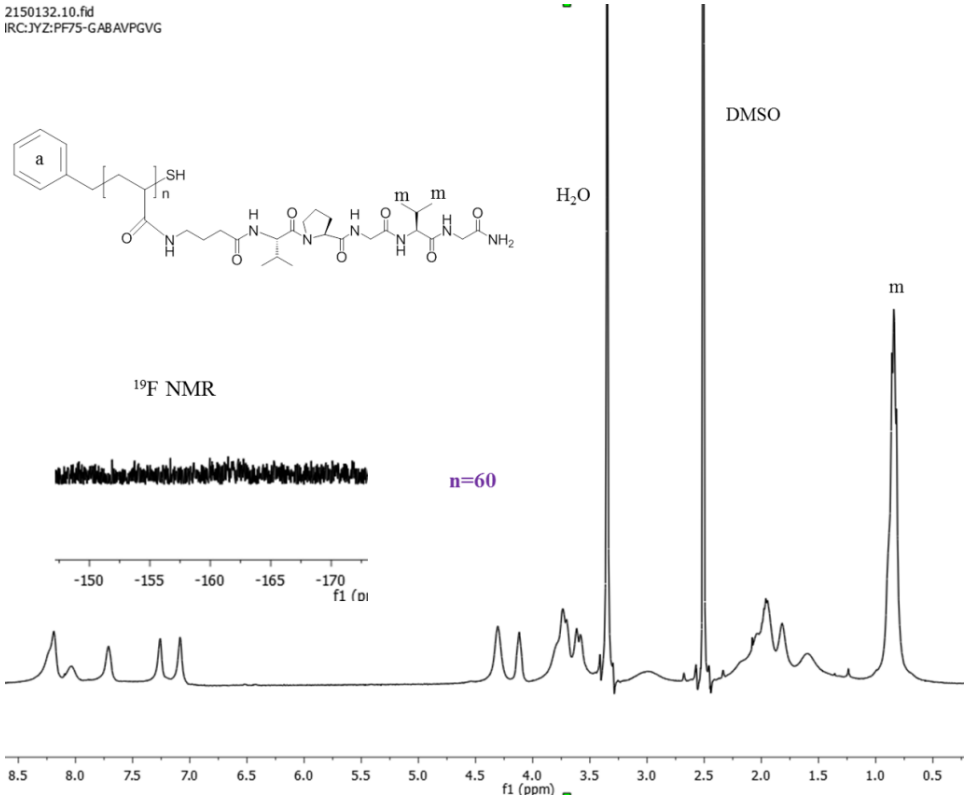

Appendix 2.11: ^{1}H NMR and ^{19}F NMR spectra of PF75-GABAVPGVG (**26**) in d_6-DMSO.

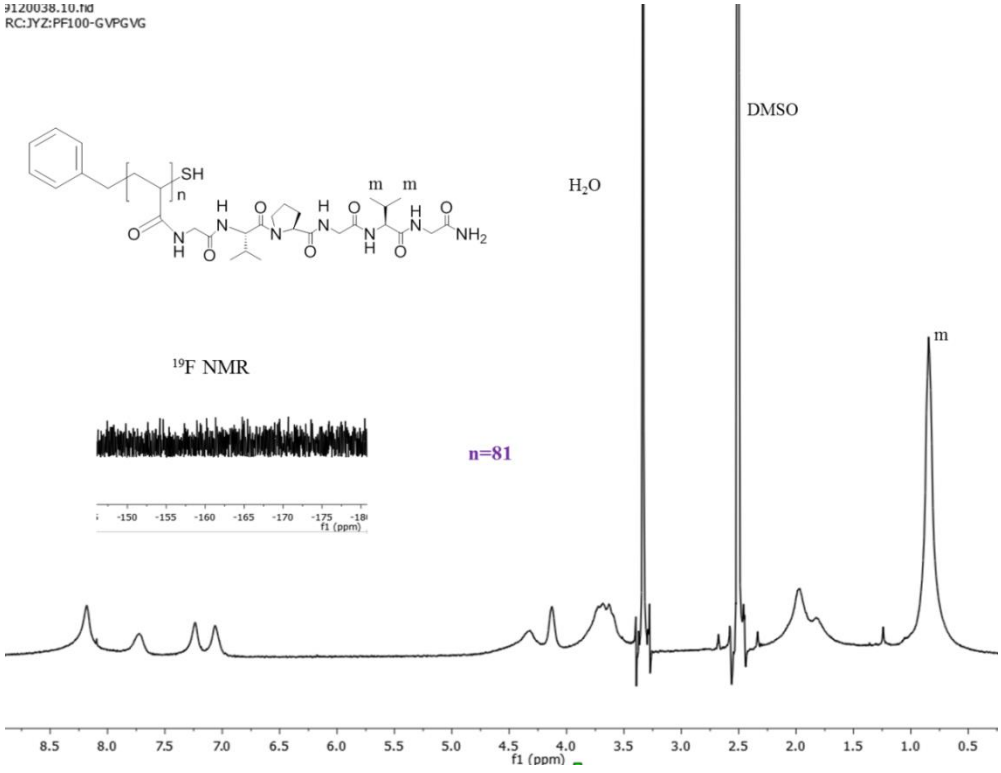

Appendix 2.12: ^{1}H NMR and ^{19}F NMR spectra of PF100-GVPGVG (**28**) in d_6-DMSO.

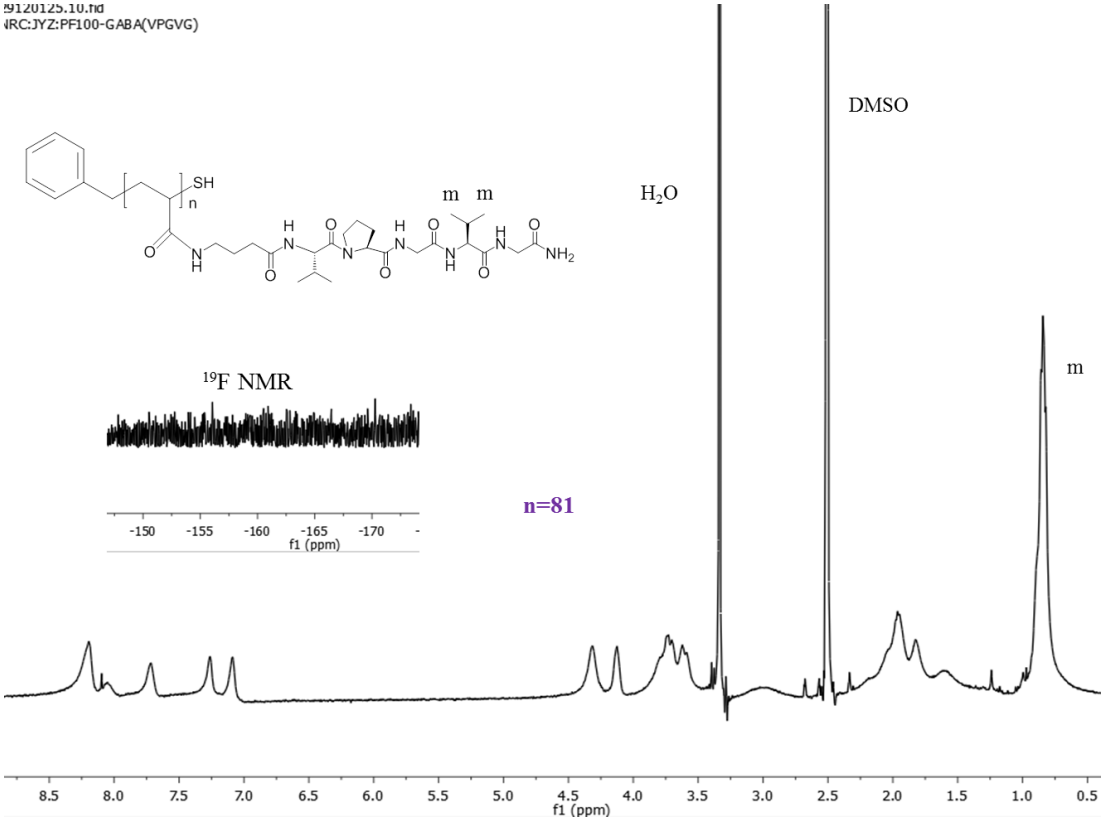

Appendix 2.13: ^{1}H NMR and ^{19}F NMR spectra of PF100-GABAVPGVG (**29**) in d_6-DMSO.

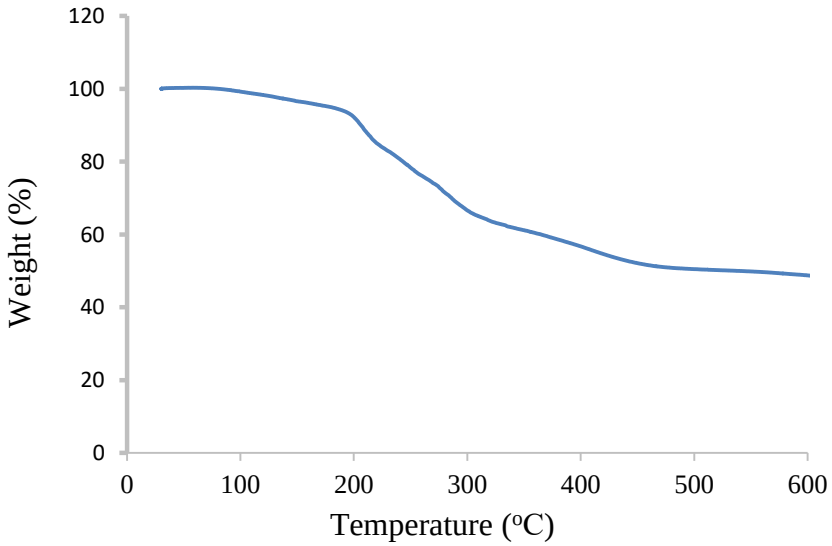

Appendix 3.1: TGA for ELP-GNPs (**30**) nanoparticles revealed 42% mass decrease between 200°C and 500°C.

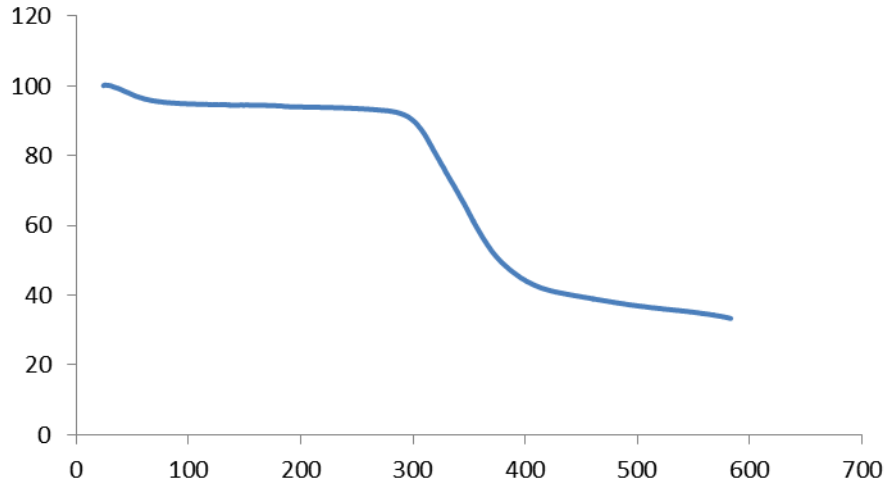

Appendix 3.2: TGA for ESP_{100}-GNPs (**32**) nanoparticles revealed 56% mass decrease between 200°C and 500°C.

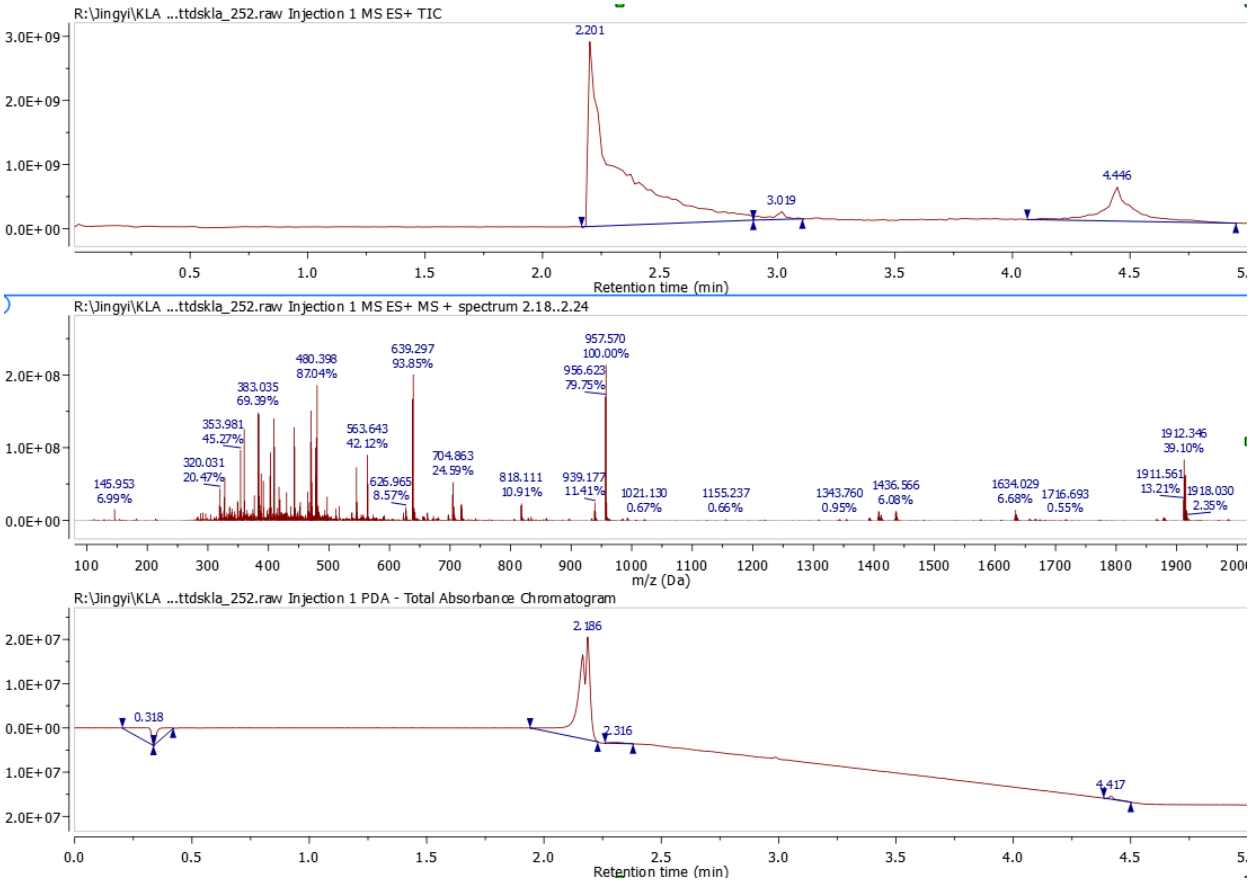

Appendix 3.3: LC-MS spectrum of thiol-TTDS-KLA (**38**).

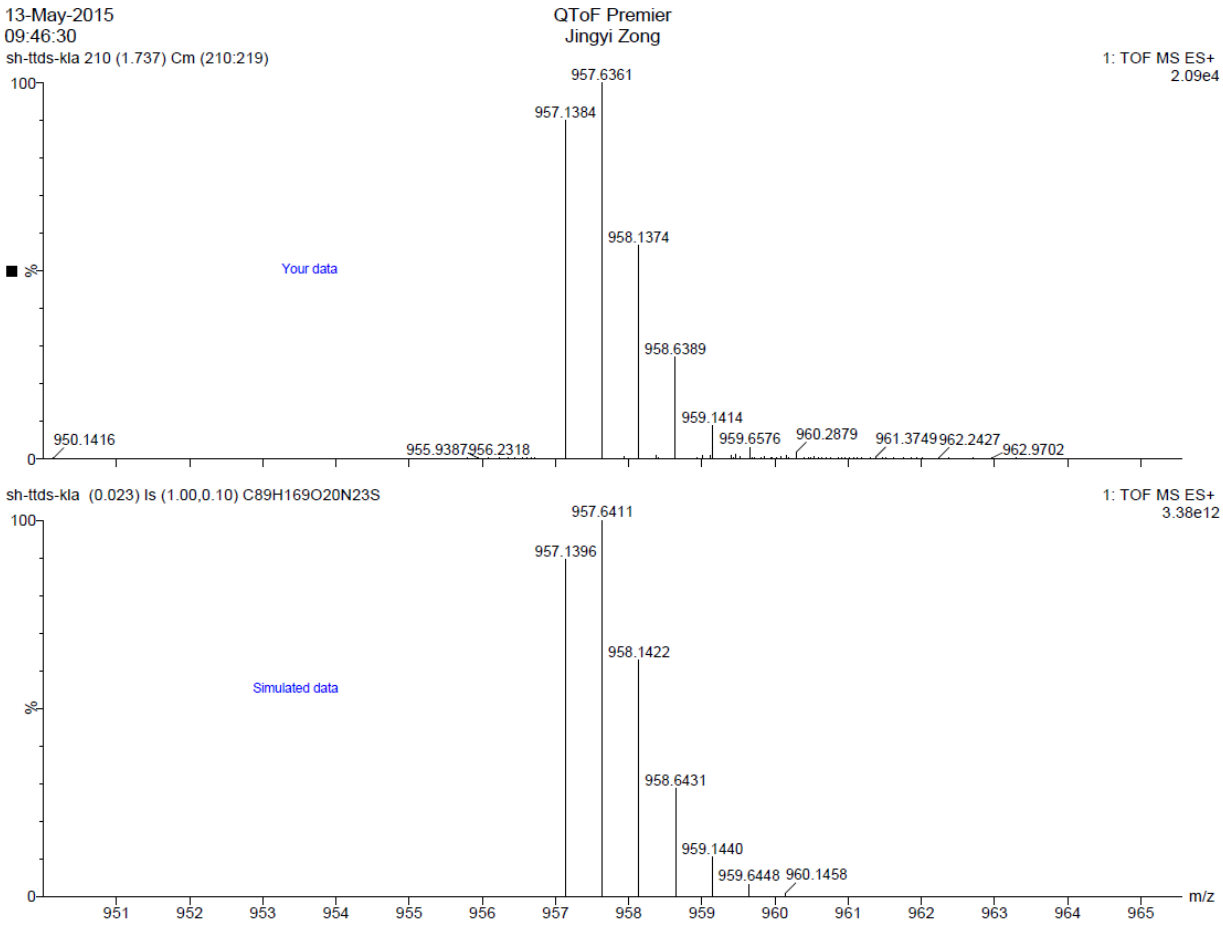

Appendix 3.4: HRMS *m/z* (ESI) 957.6361, consistent with empirical formula $C_{89}H_{169}O_{20}N_{23}S$ with an accuracy of 5 ppm (accepted as $(M + 2H)^{2+}$).

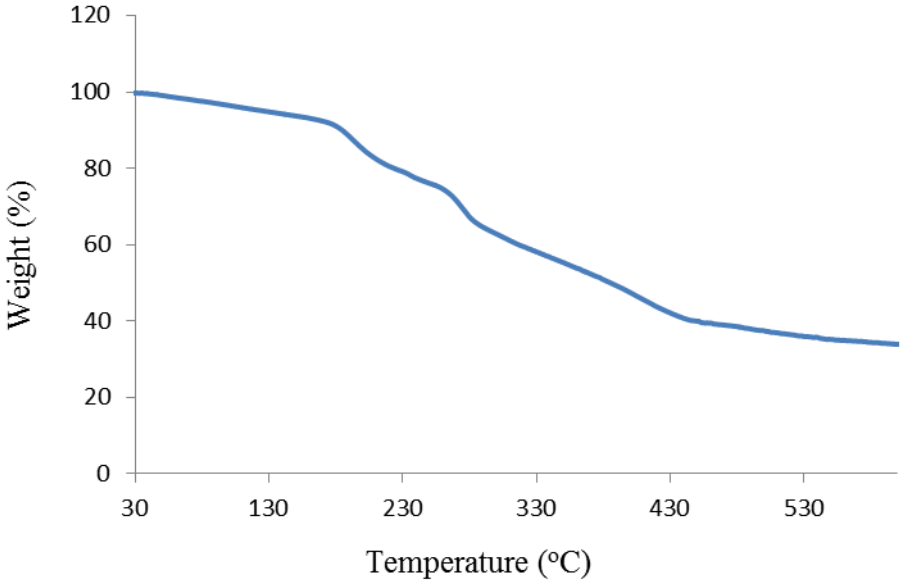

Appendix 3.5: TGA for KLA-GNPs (**39**) nanoparticles revealed 47% mass decrease between 200°C and 500°C.

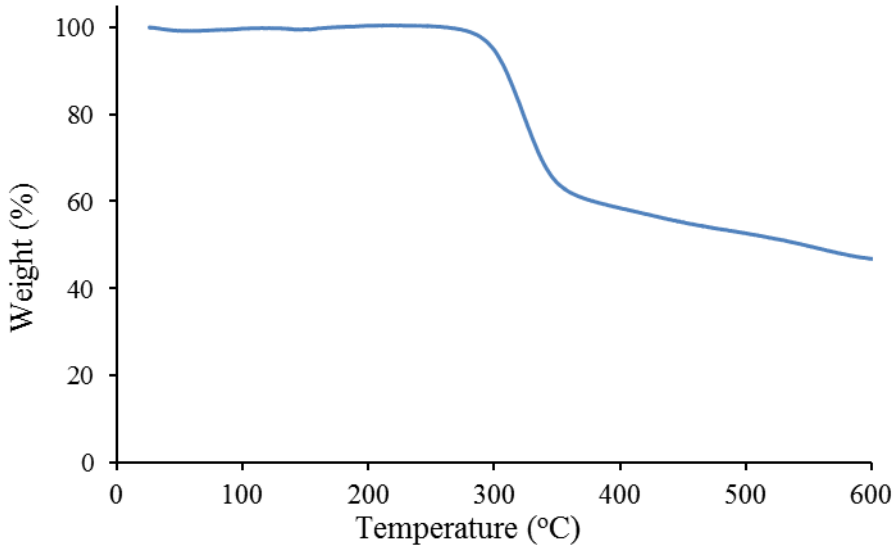

Appendix 3.6: TGA for KLA-ESP_{100}-GNPs (**40**) nanoparticles revealed 48% mass decrease between 200°C and 500°C

Appendix 4.1: Structure, analytical HPLC, MALDI-ToF, and accurate mass data for $_{D}$-KLA (**33**).

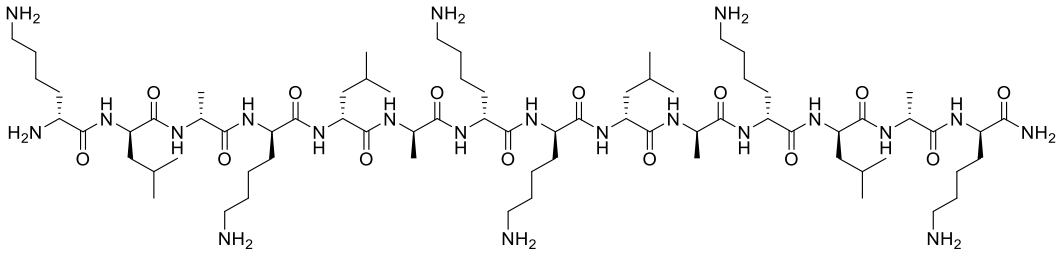

a

D-KLA; H-klaklakklaklak-NH$_2$

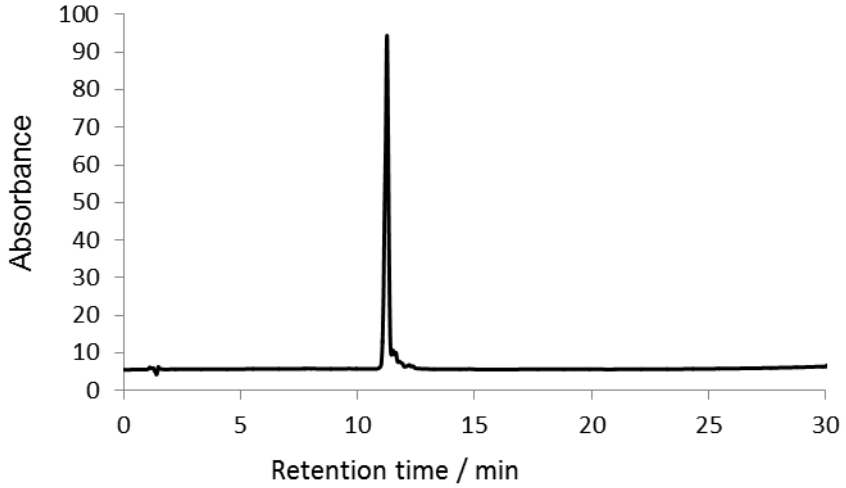

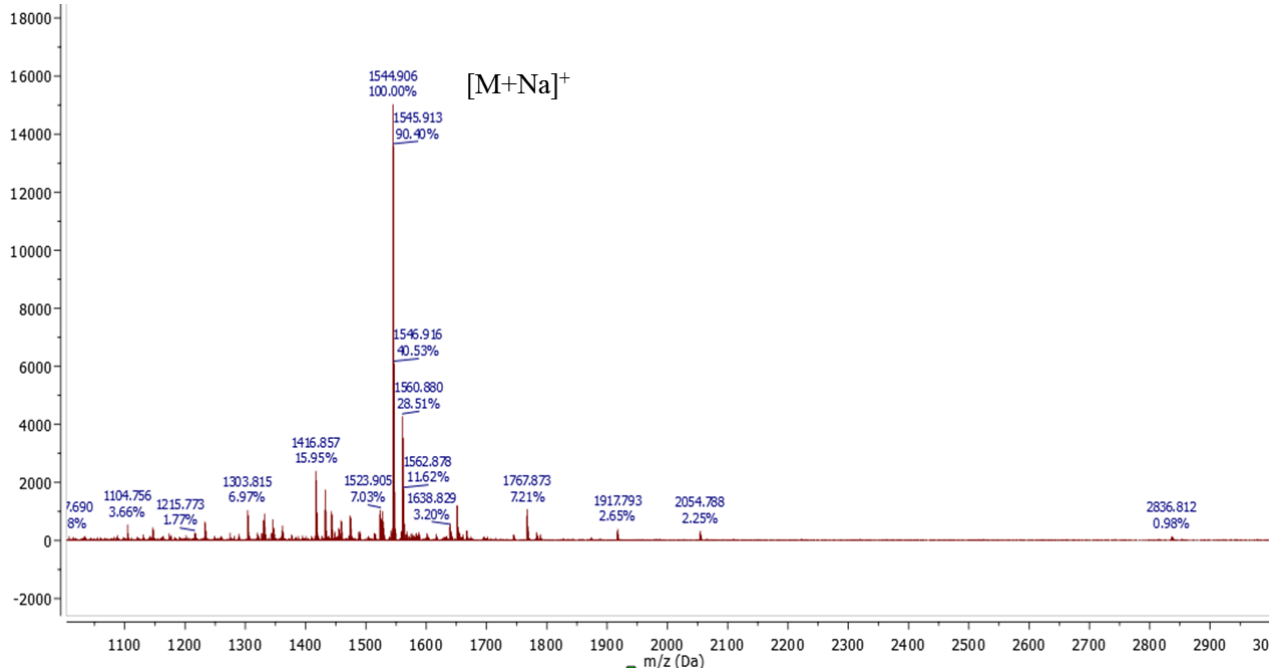

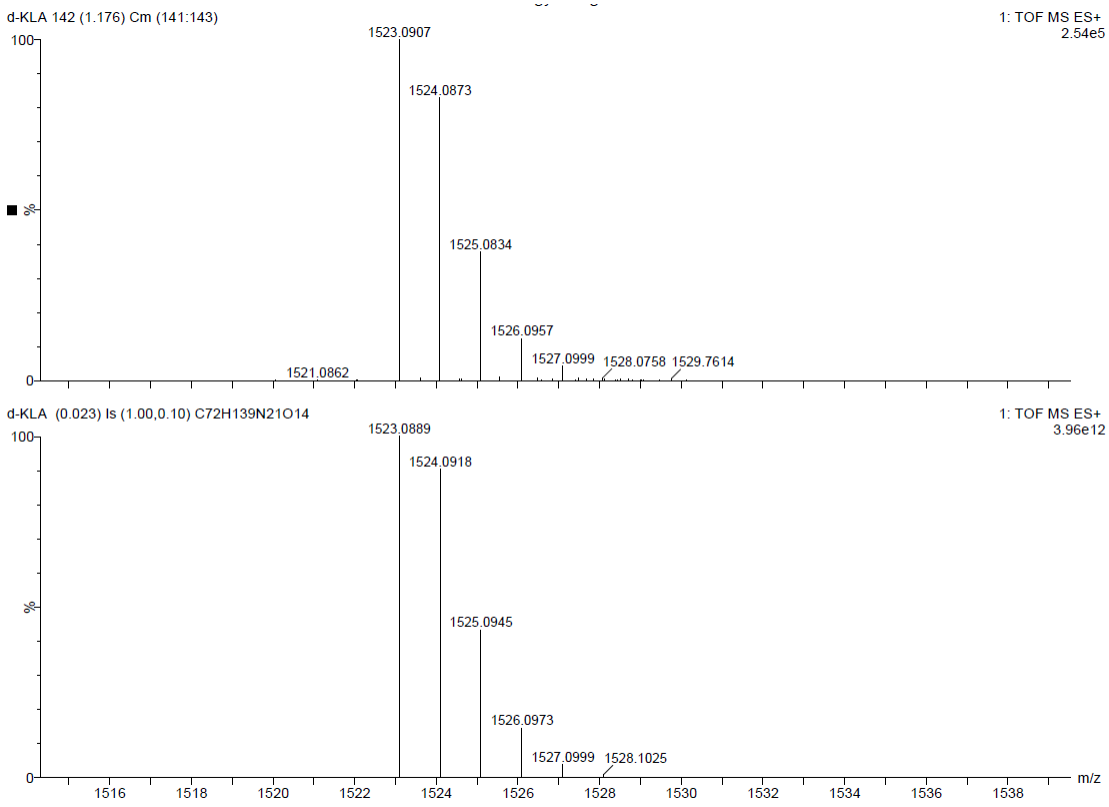

HRMS *m/z* (ESI) 1523.0907, consistent with empirical formula $C_{72}H_{138}N_{21}O_{14}$ with an accuracy of 1.18 ppm (accepted as $(M + H)^+$).

Appendix 4.2: Structure, analytical HPLC, MALDI-ToF, and accurate mass data for L-KLA (**41**).

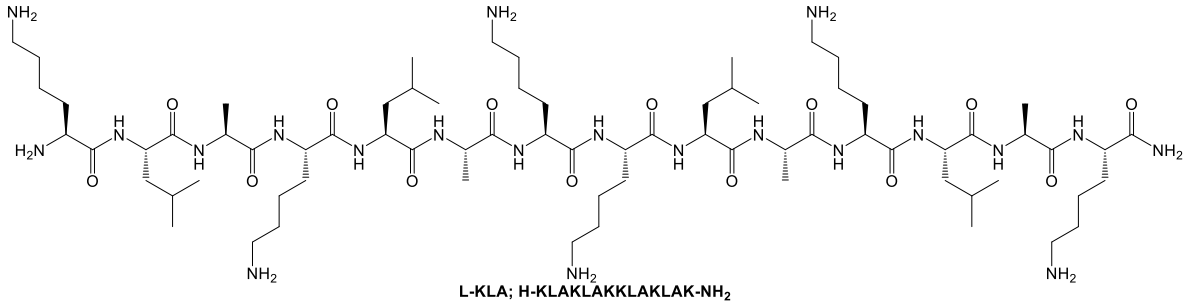

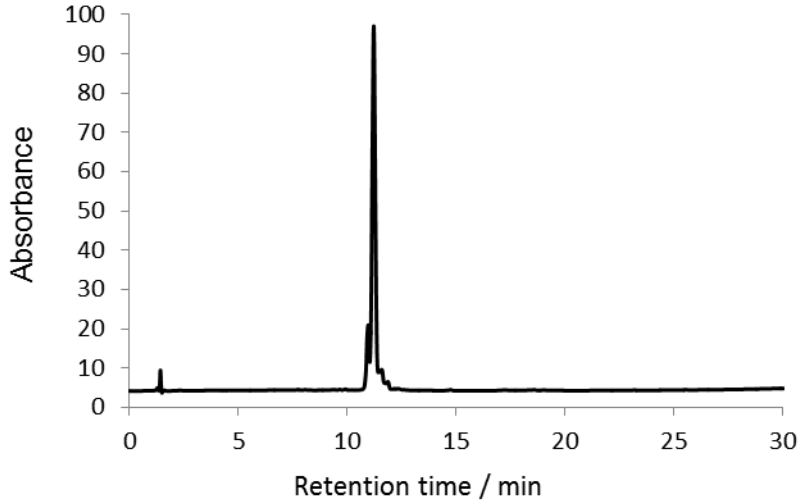

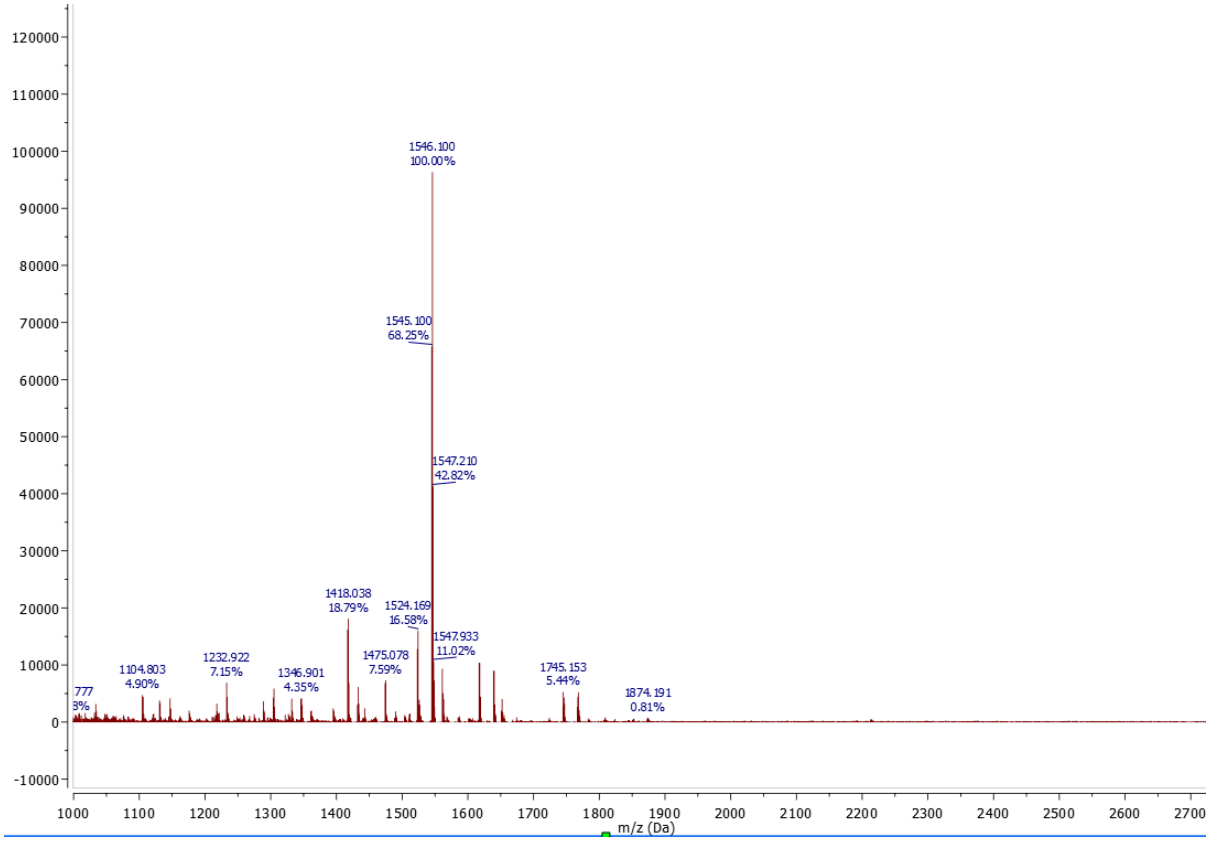

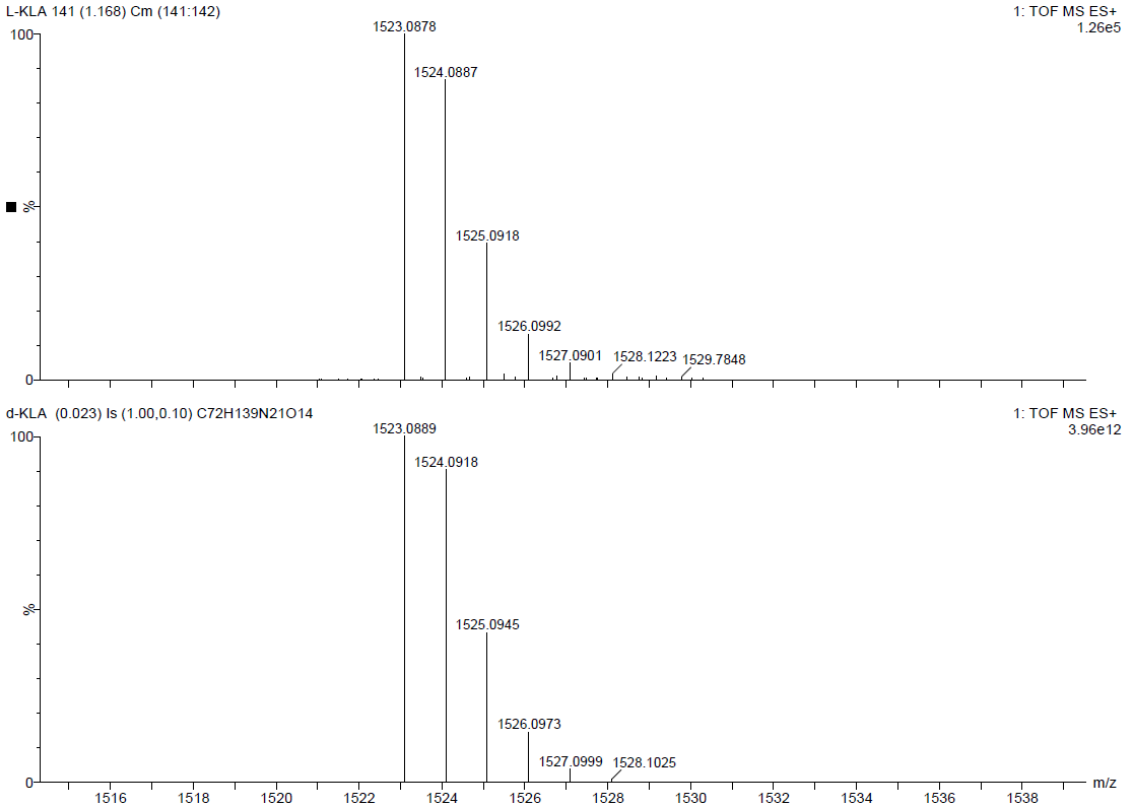

HRMS *m/z* (ESI) 1523.0878, consistent with empirical formula $C_{72}H_{138}N_{21}O_{14}$ with an accuracy of 0.72 ppm (accepted as $(M + H)^+$).

Appendix 4.3: Structure, analytical HPLC, MALDI-ToF, and accurate mass data for KLA-CPPo1 (**52**).

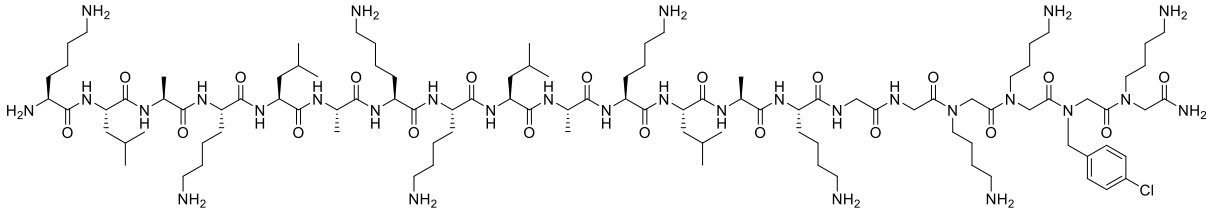

52

H-klaklakklaklak-GG-*N*lys*N*lys*N*pcb*N*lys-NH_2

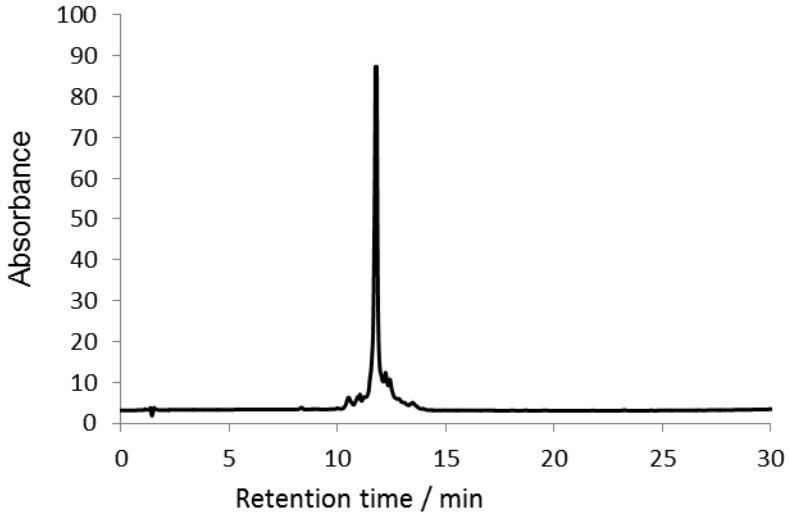

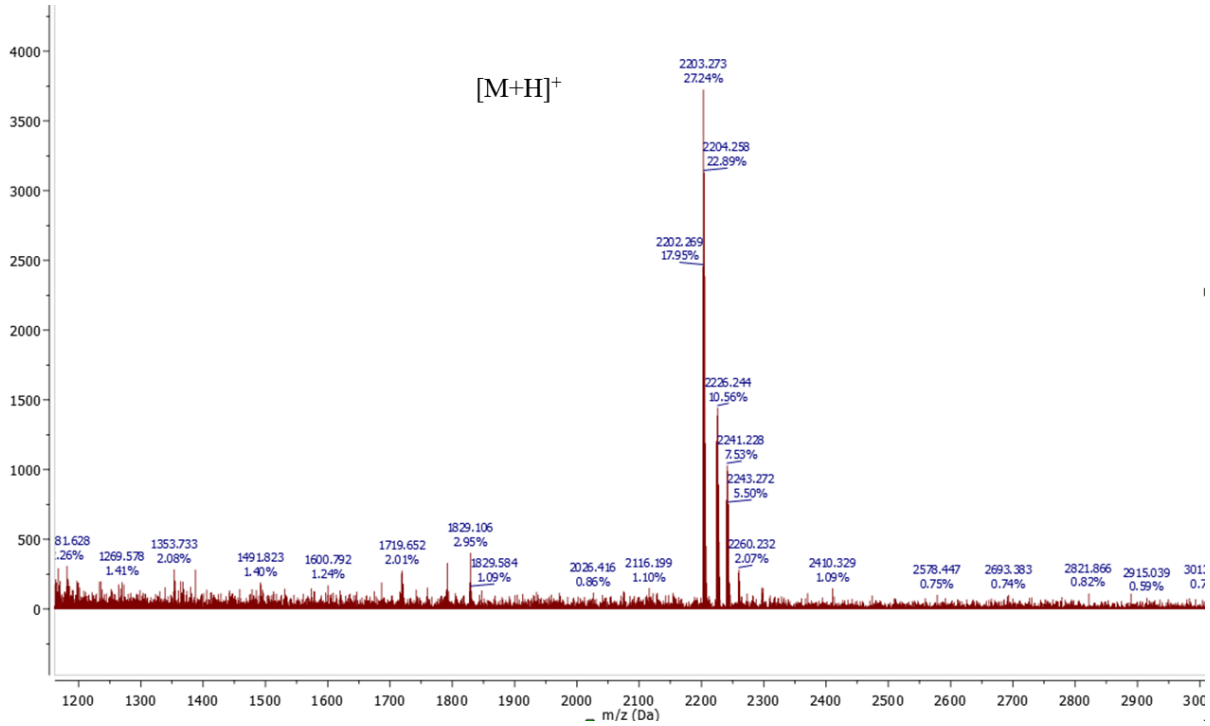

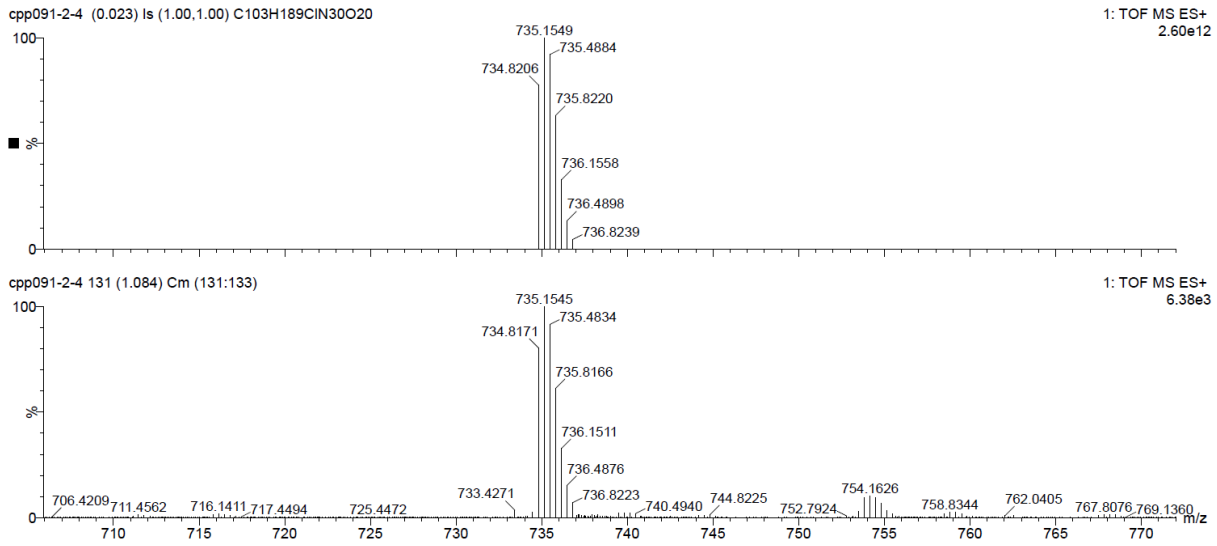

HRMS *m/z* (ESI) 735.1545, consistent with empirical formula $C_{103}H_{189}ClN_{30}O_{20}$ with an accuracy of -0.54 ppm (accepted as $(M + 3H)^{3+}$).

Appendix 4.4: Structure, analytical HPLC, MALDI-ToF, and accurate mass data for KLA-CPPo2 (**53**).

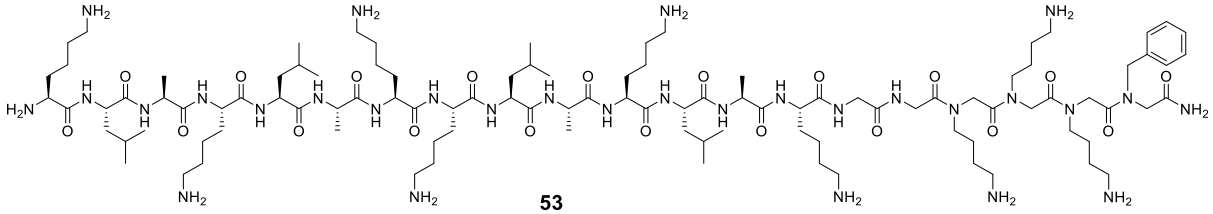

53

H-klaklakklaklak-GG-*N*lys*N*lys*N*lys*N*phe-NH_2

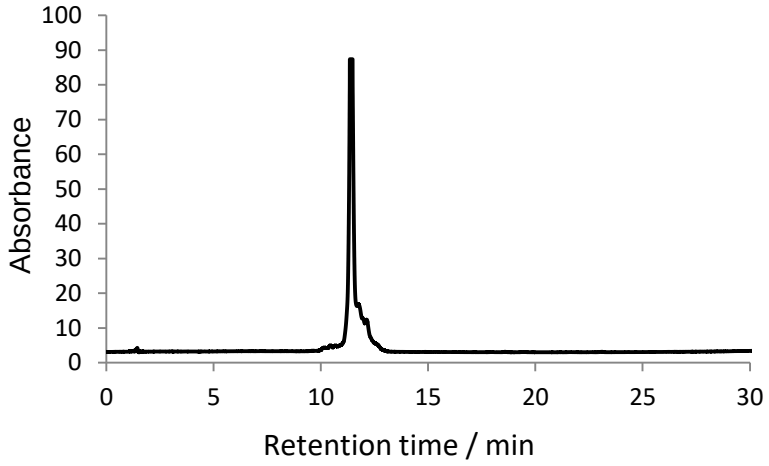

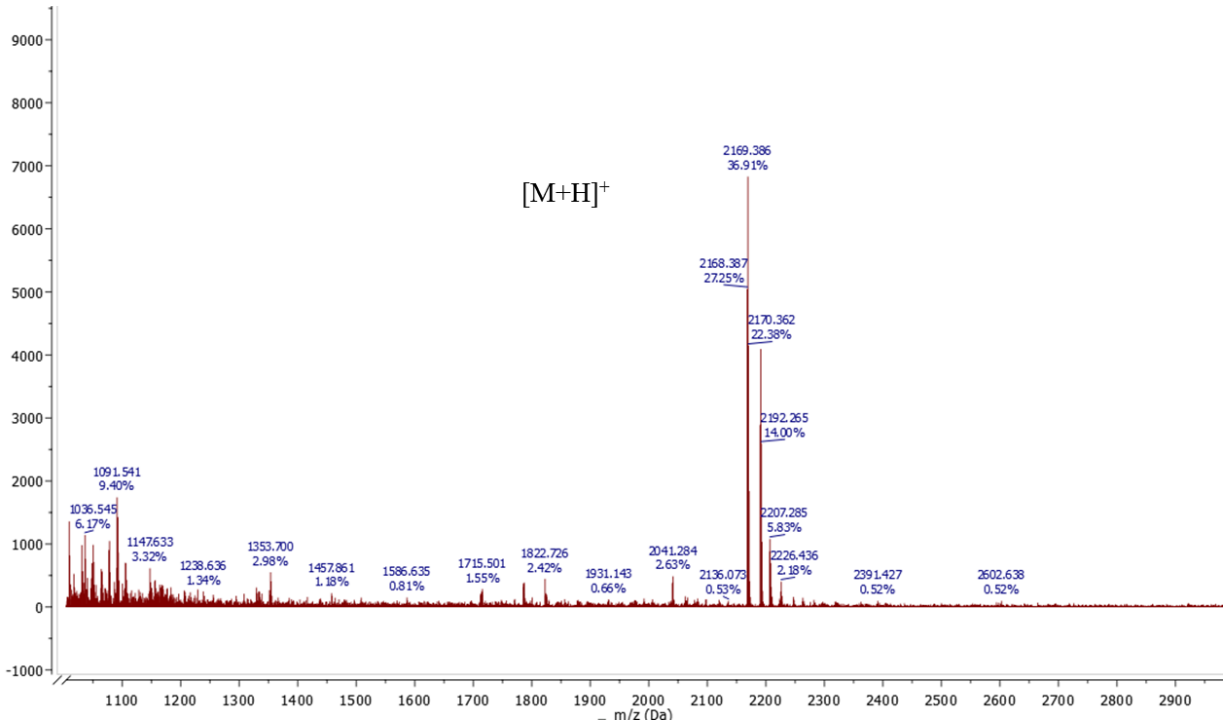

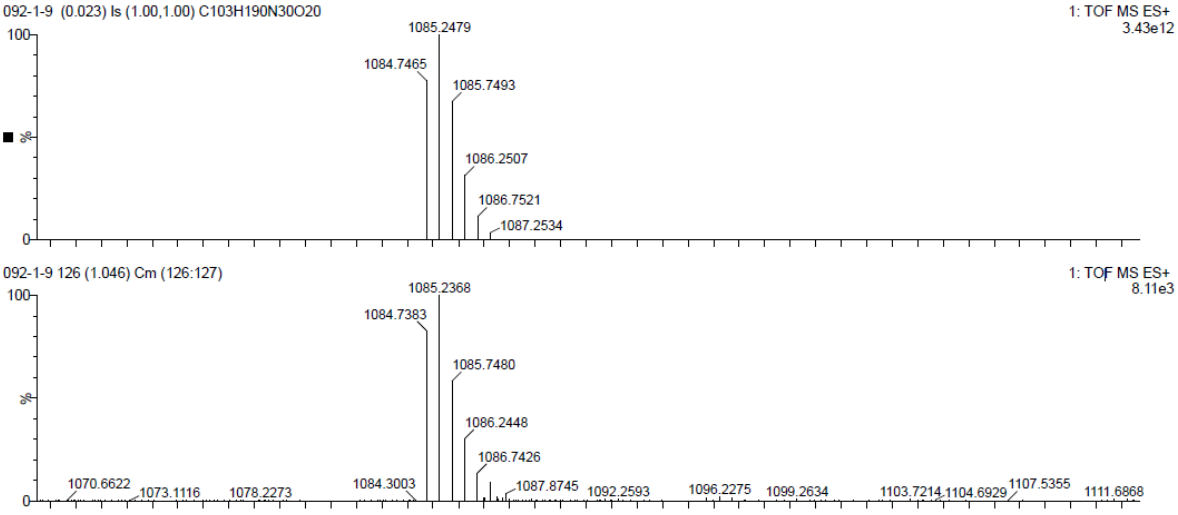

HRMS *m/z* (ESI) 1085.2368, consistent with empirical formula $C_{103}H_{190}N_{30}O_{20}$ with an accuracy of -10.2 ppm (accepted as $(M + 2H)^{2+}$).

Appendix 4.5: Structure, analytical HPLC, MALDI-ToF, and accurate mass data for KLA-CPPo3 (**54**).

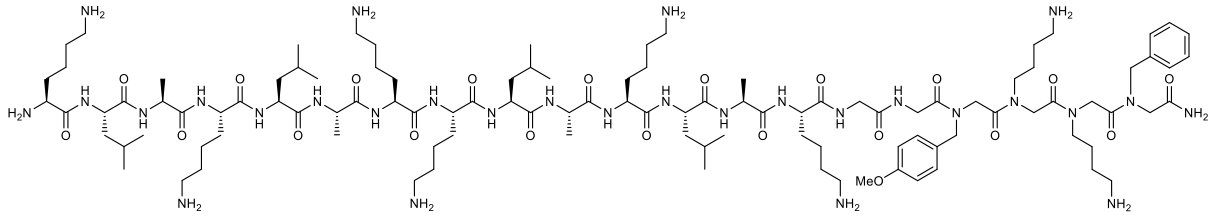

54

H-klaklakklaklak-GG-*N*pmb*N*lys*N*lys*N*phe-NH_2

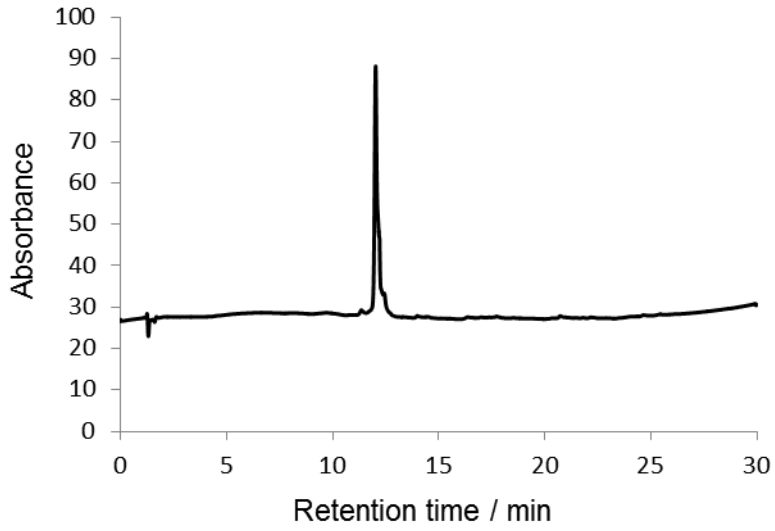

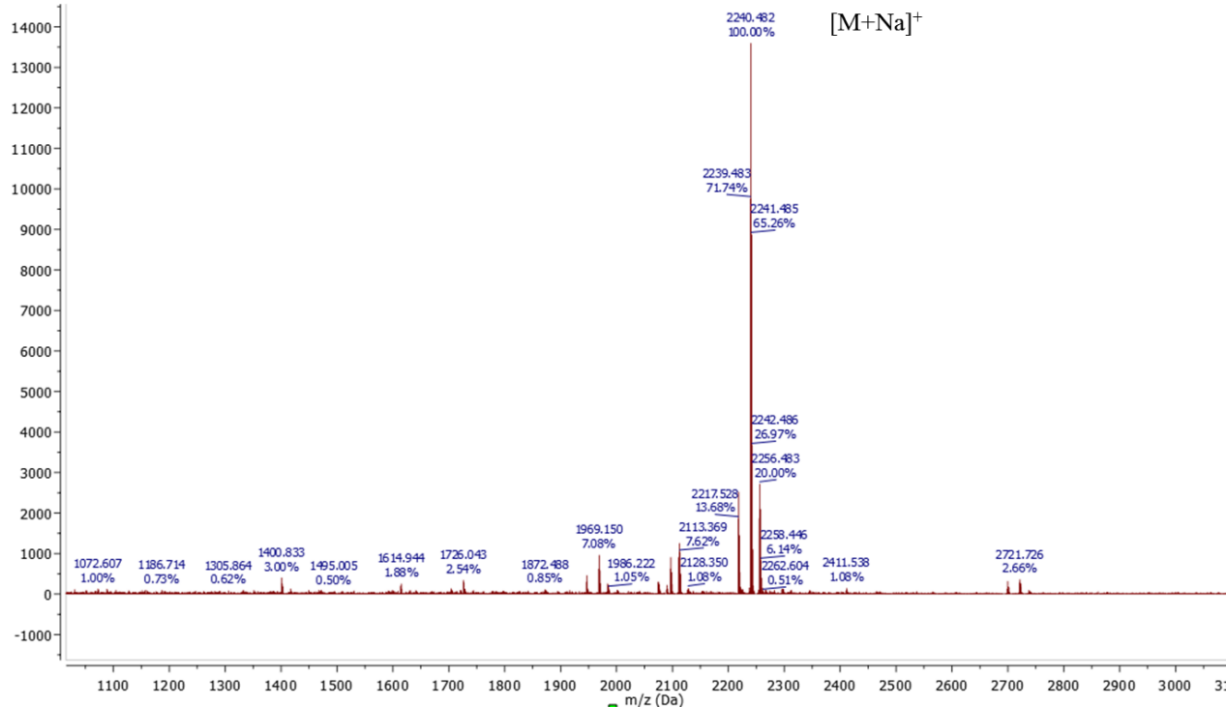

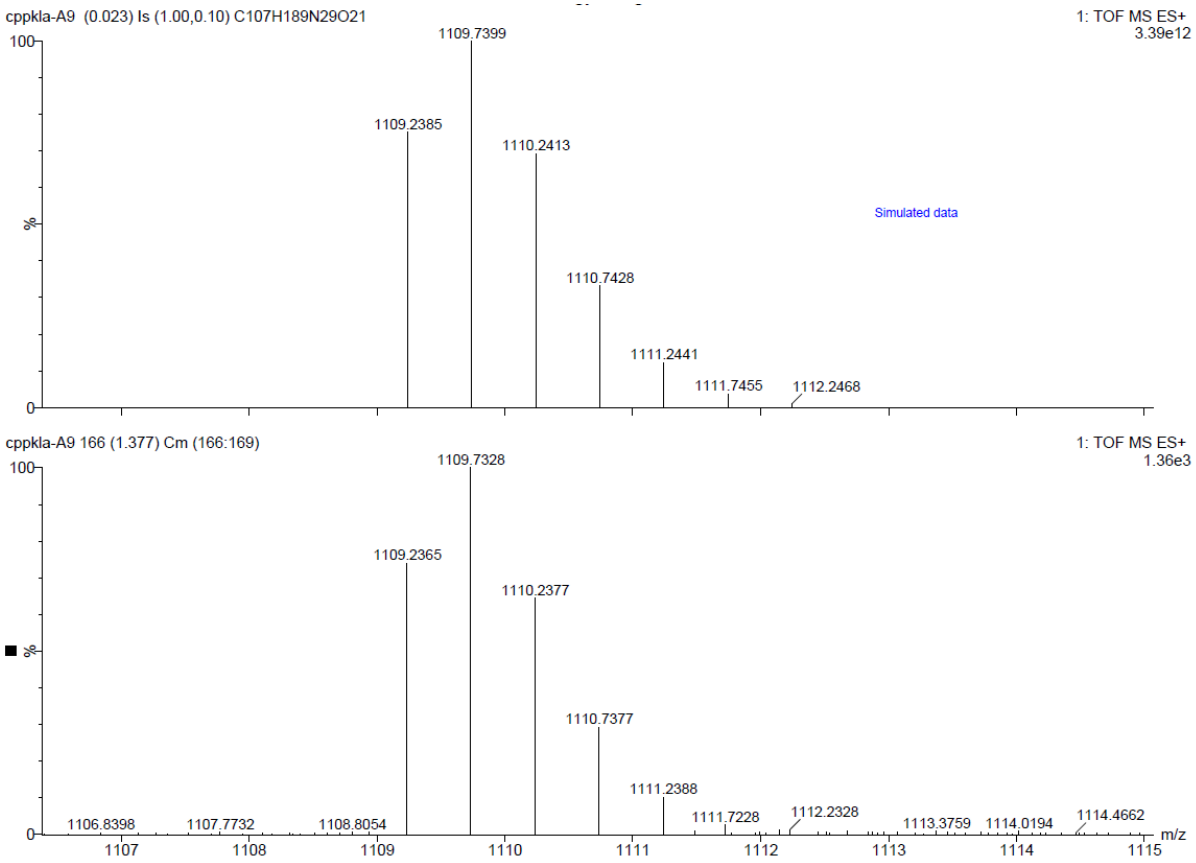

HRMS *m/z* (ESI) 1109.7328, consistent with empirical formula $C_{107}H_{189}N_{29}O_{21}$ with an accuracy of 6.4 ppm (accepted as $(M + 2H)^{2+}$).

Appendix 4.6: Structure, analytical HPLC, MALDI-ToF, and accurate mass data for KLA-CPPo4 (**55**).

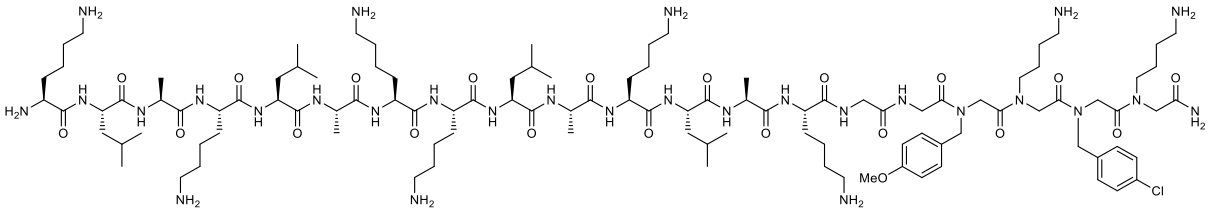

55

H-klaklakklaklak-GG-*N*pmb*N*lys*N*pcb*N*lys-NH_2

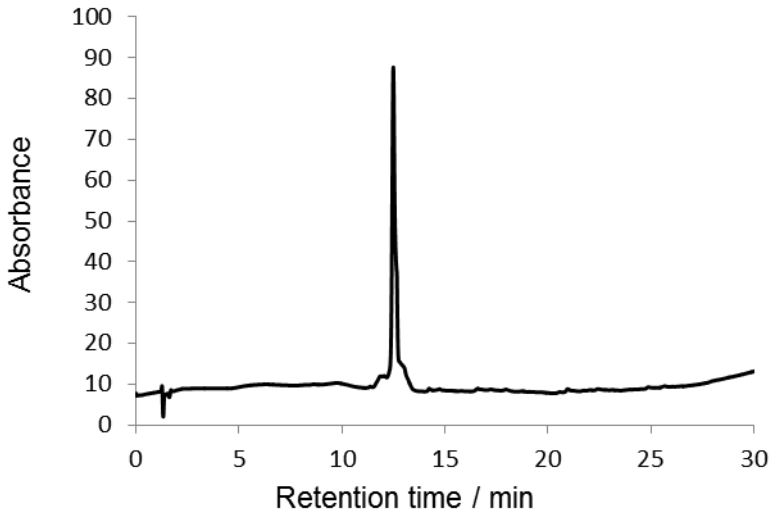

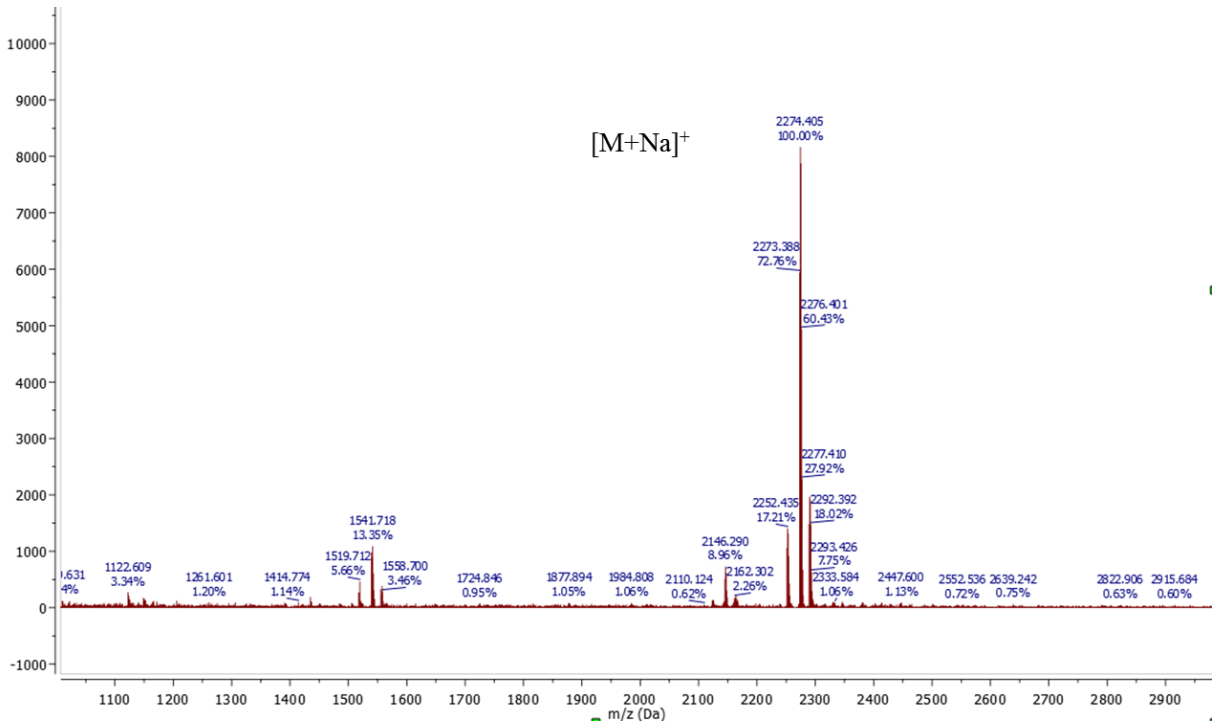

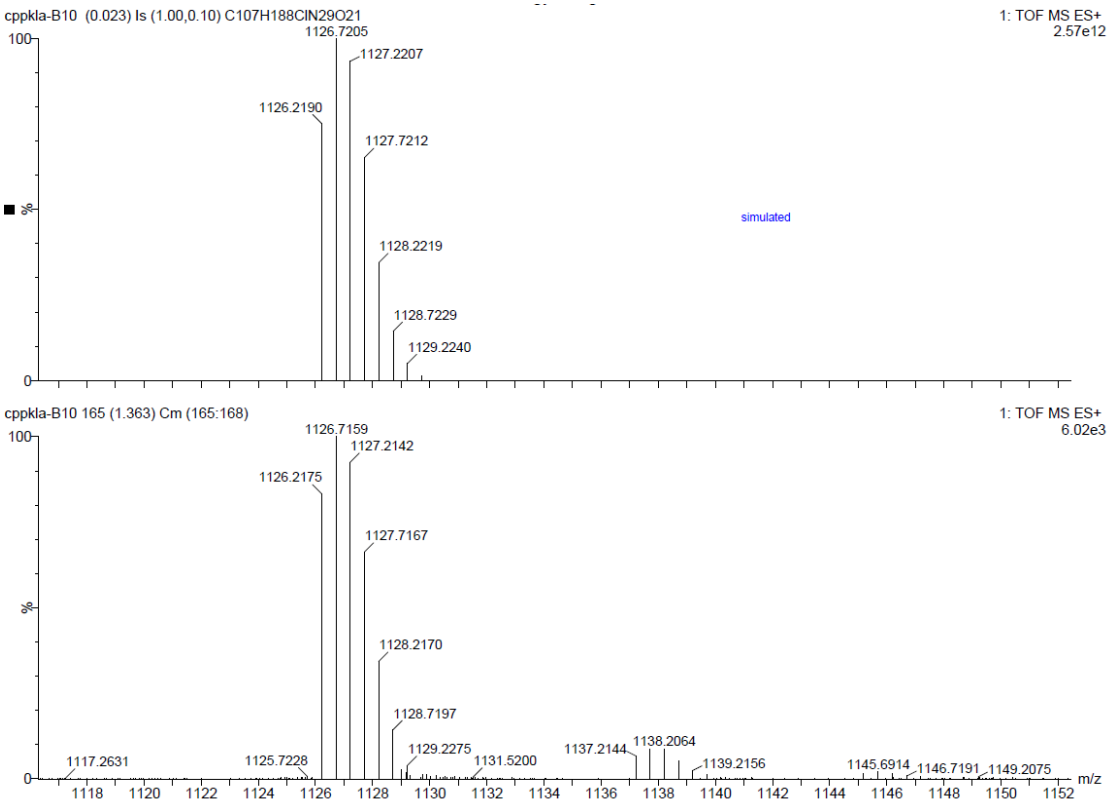

HRMS *m/z* (ESI) 1126.7159, consistent with empirical formula $C_{107}H_{188}N_{29}O_{21}Cl$ with an accuracy of 4.0 ppm (accepted as $(M + 2H)^{2+}$).

Appendix 4.7: Structure, analytical HPLC, MALDI-ToF, and accurate mass data for KLA-CPPo5 (**56**).

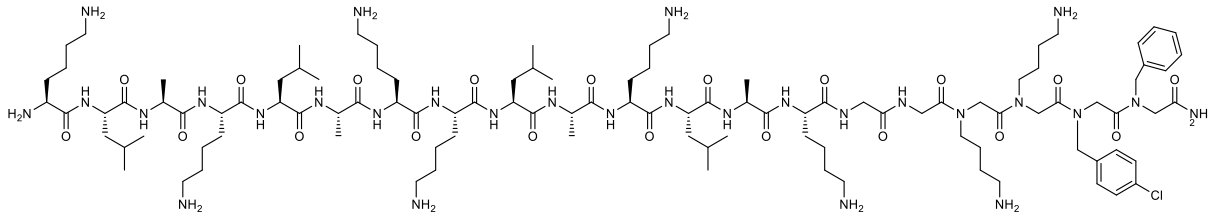

56

H-klaklakklaklak-GG-*N*lys*N*lys*N*pcb*N*phe-NH_2

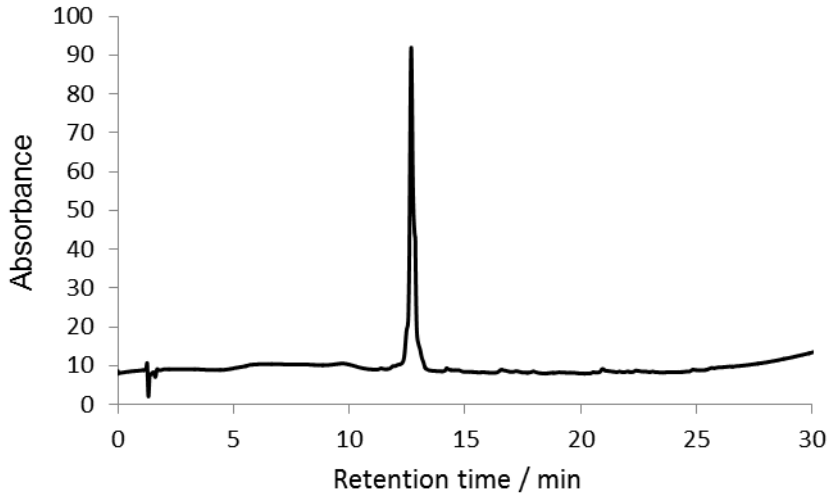

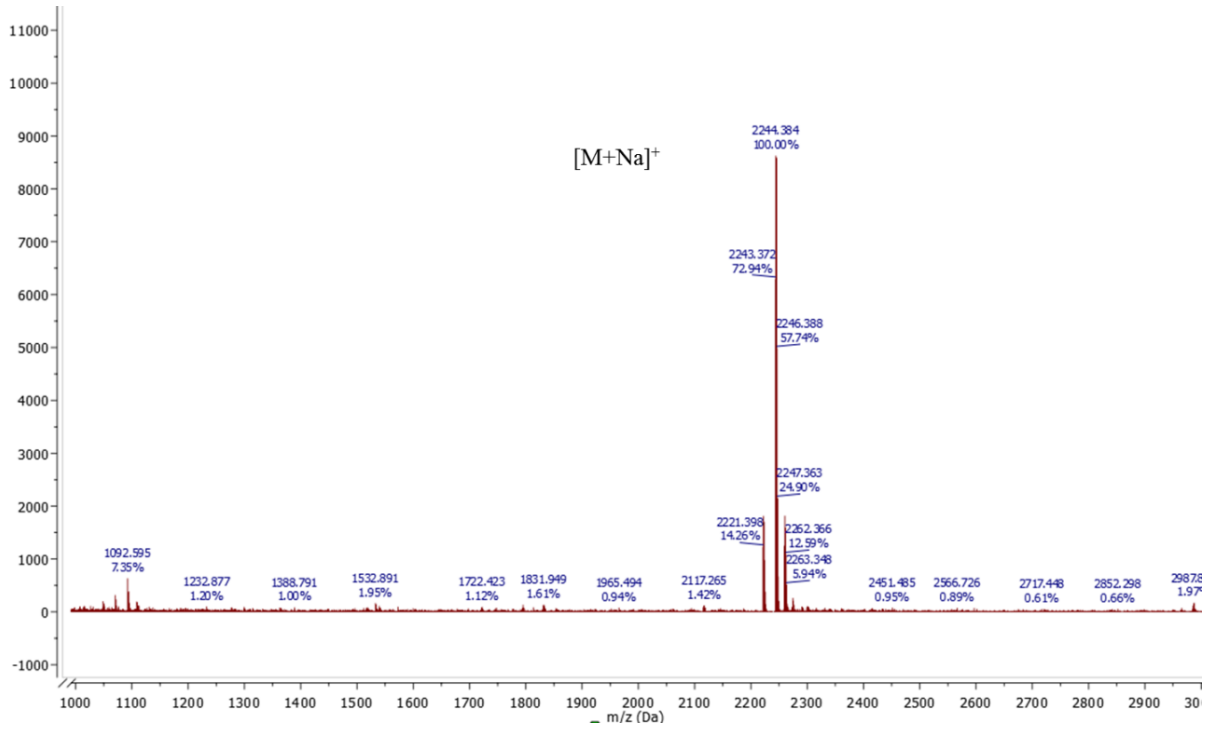

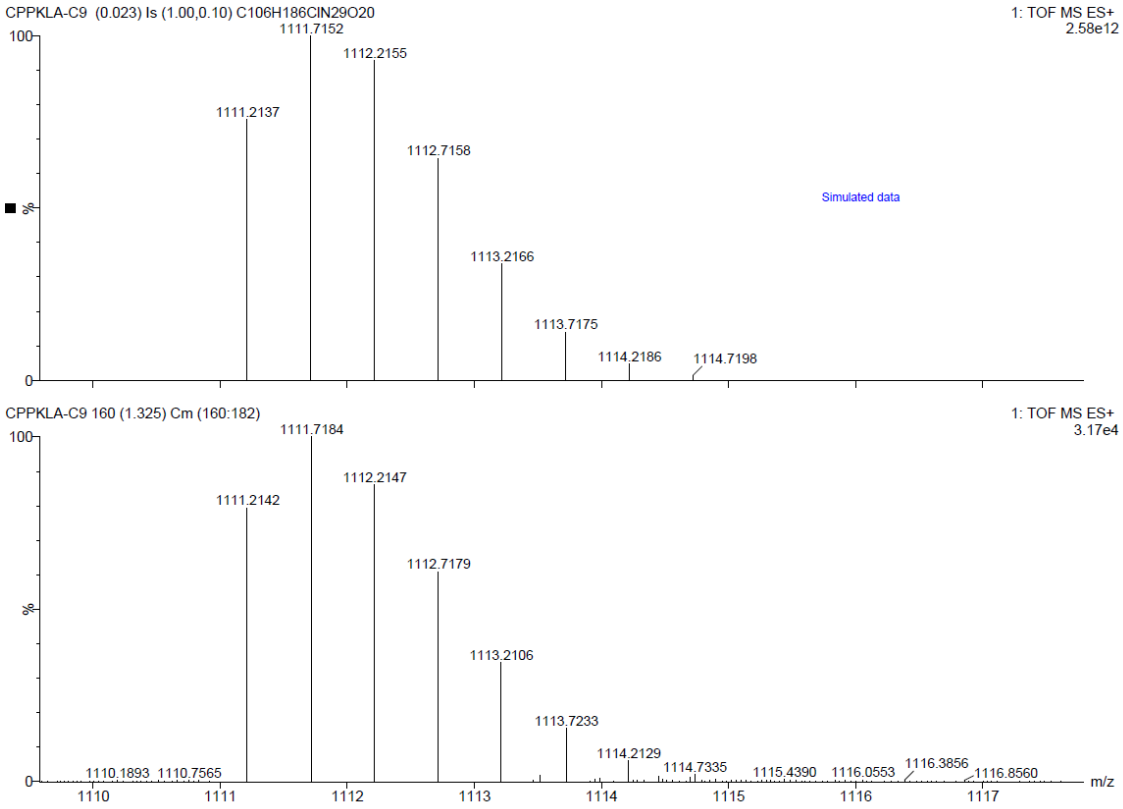

HRMS *m/z* (ESI) 1111.7184, consistent with empirical formula $C_{106}H_{186}N_{29}O_{20}Cl$ with an accuracy of 2.8 ppm (accepted as $(M + 2H)^{2+}$).

Appendix 4.8: Structure, analytical HPLC, MALDI-ToF, and accurate mass data for KLA-CPPo6 (**57**).

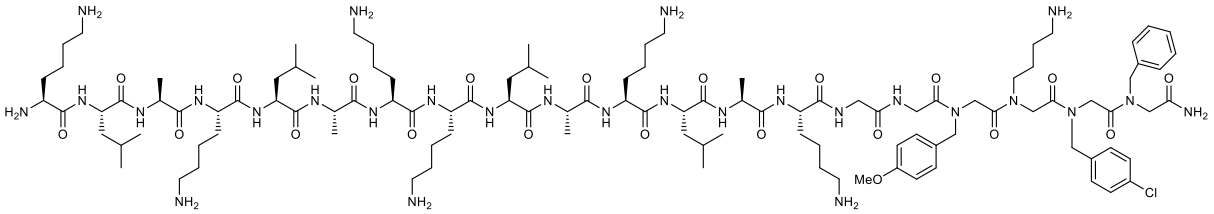

57

H-klaklakklaklak-GG-*N*pmb*N*lys*N*pcb*N*phe-NH_2

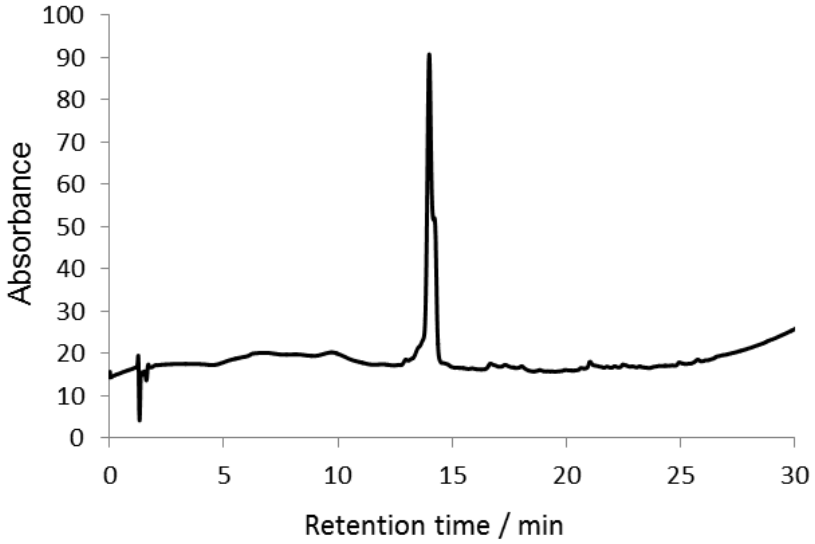

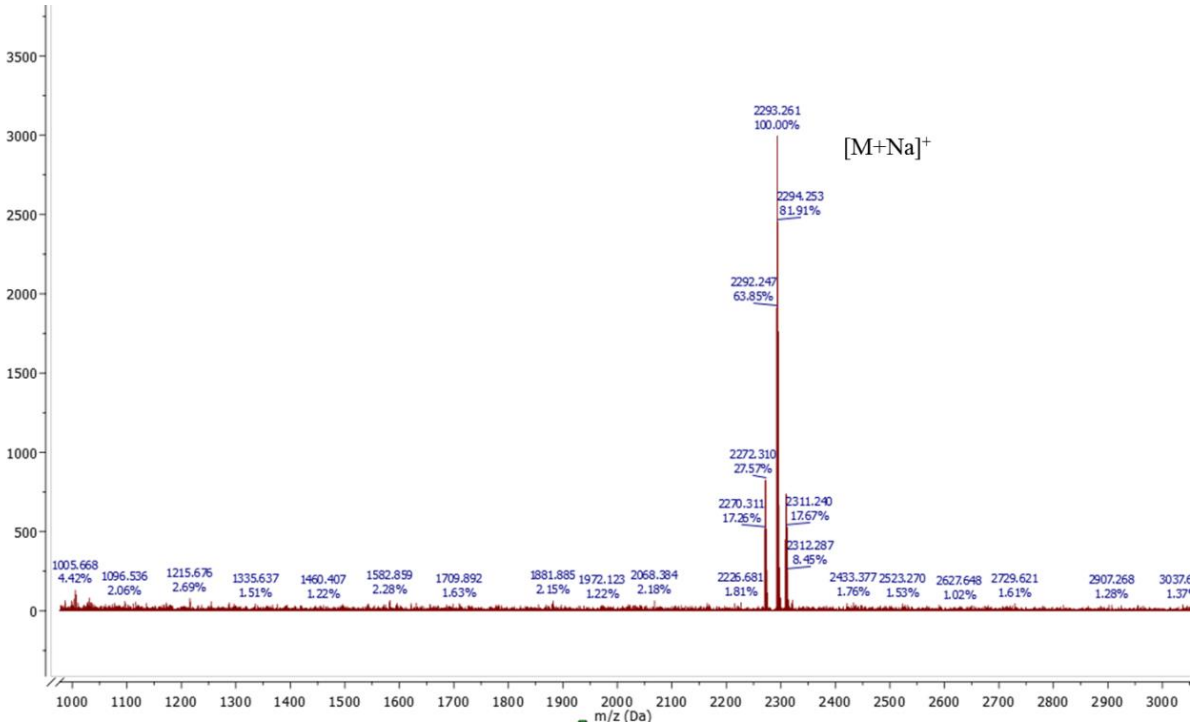

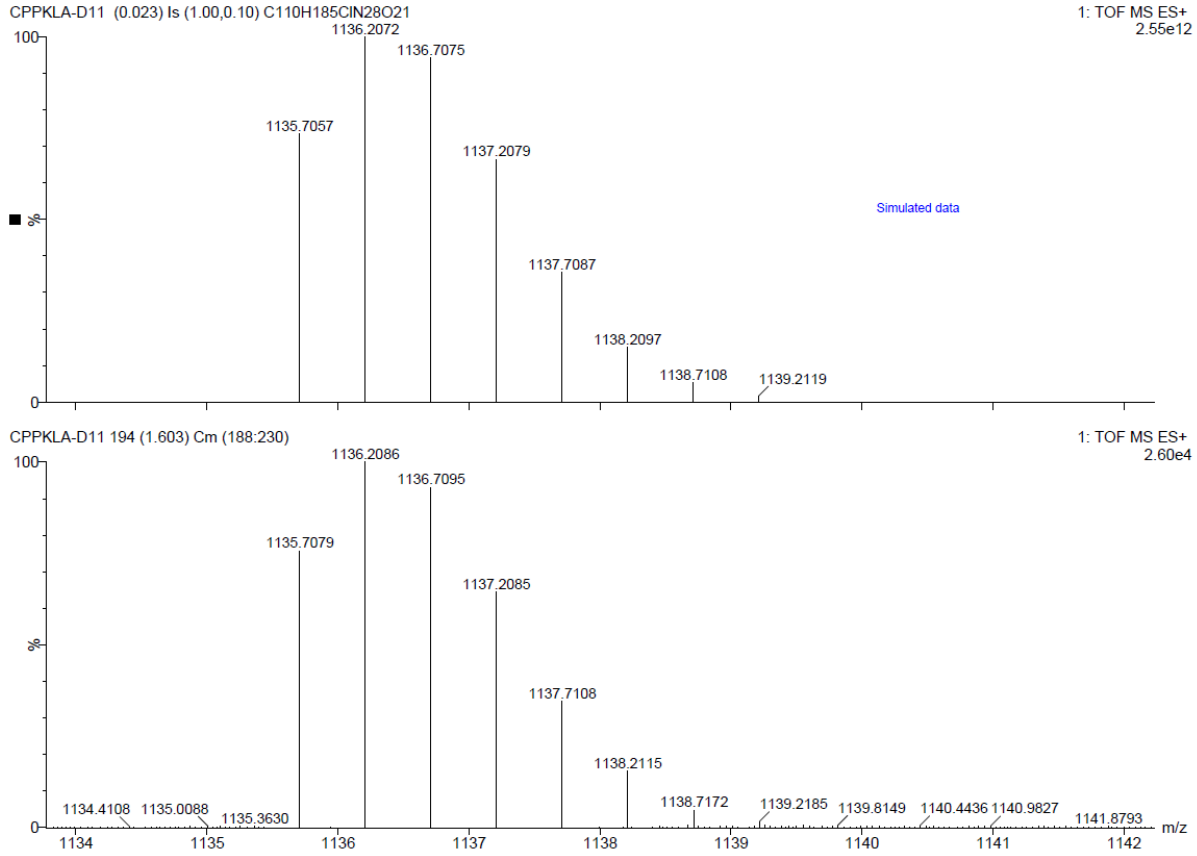

HRMS *m/z* (ESI) 1136.2086, consistent with empirical formula $C_{110}H_{185}N_{28}O_{21}Cl$ with an accuracy of 1.2 ppm (accepted as $(M + 2H)^{2+}$).

Appendix 4.9: Structure, analytical HPLC, MALDI-ToF, and accurate mass data for Rhod-KLA-CPPo6 (**59**).

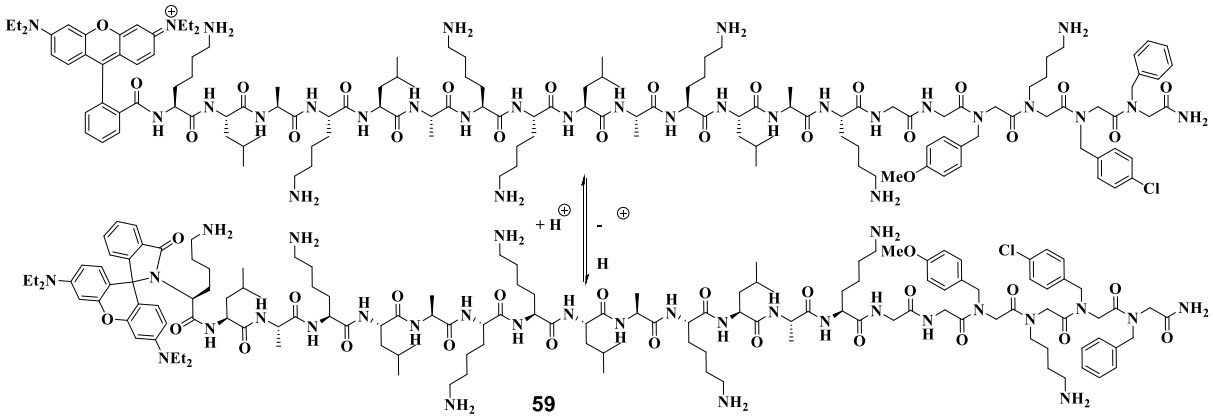

59

RhoB-KLA-CPPo6

Rhod-klaklakklaklak-GG-*N*pmb*N*lys*N*pcb*N*phe-NH_2

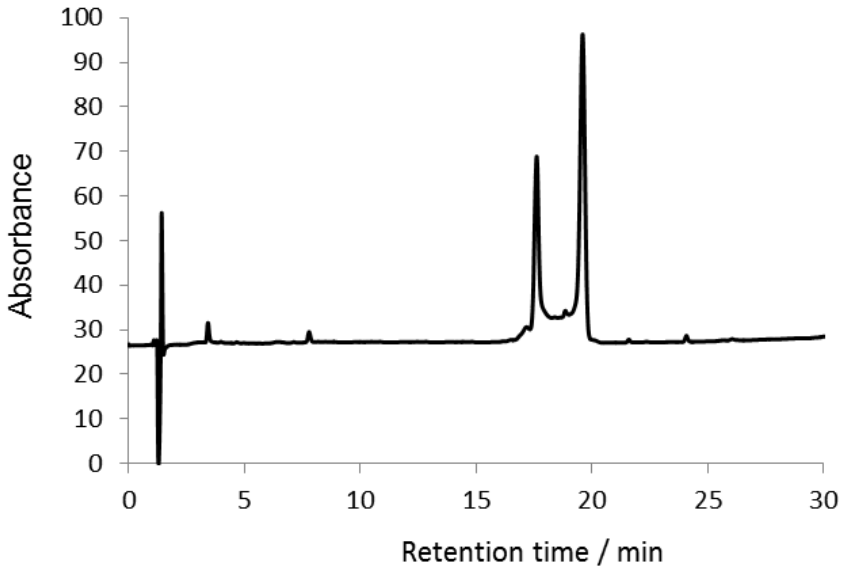

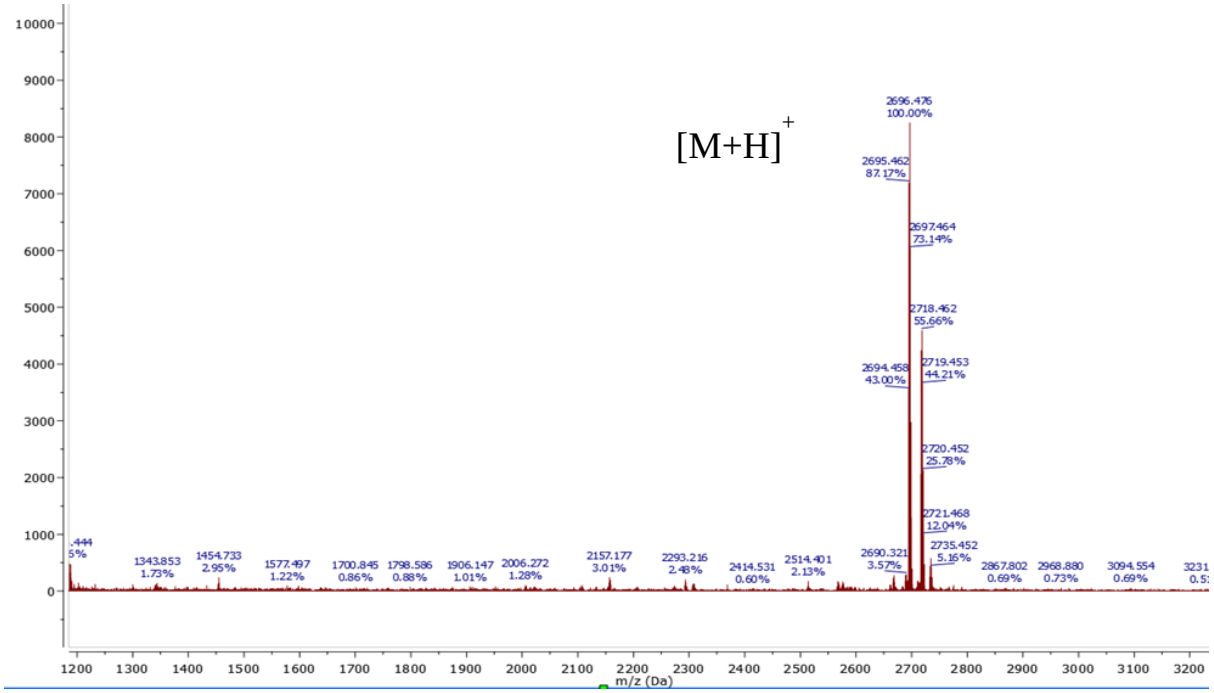

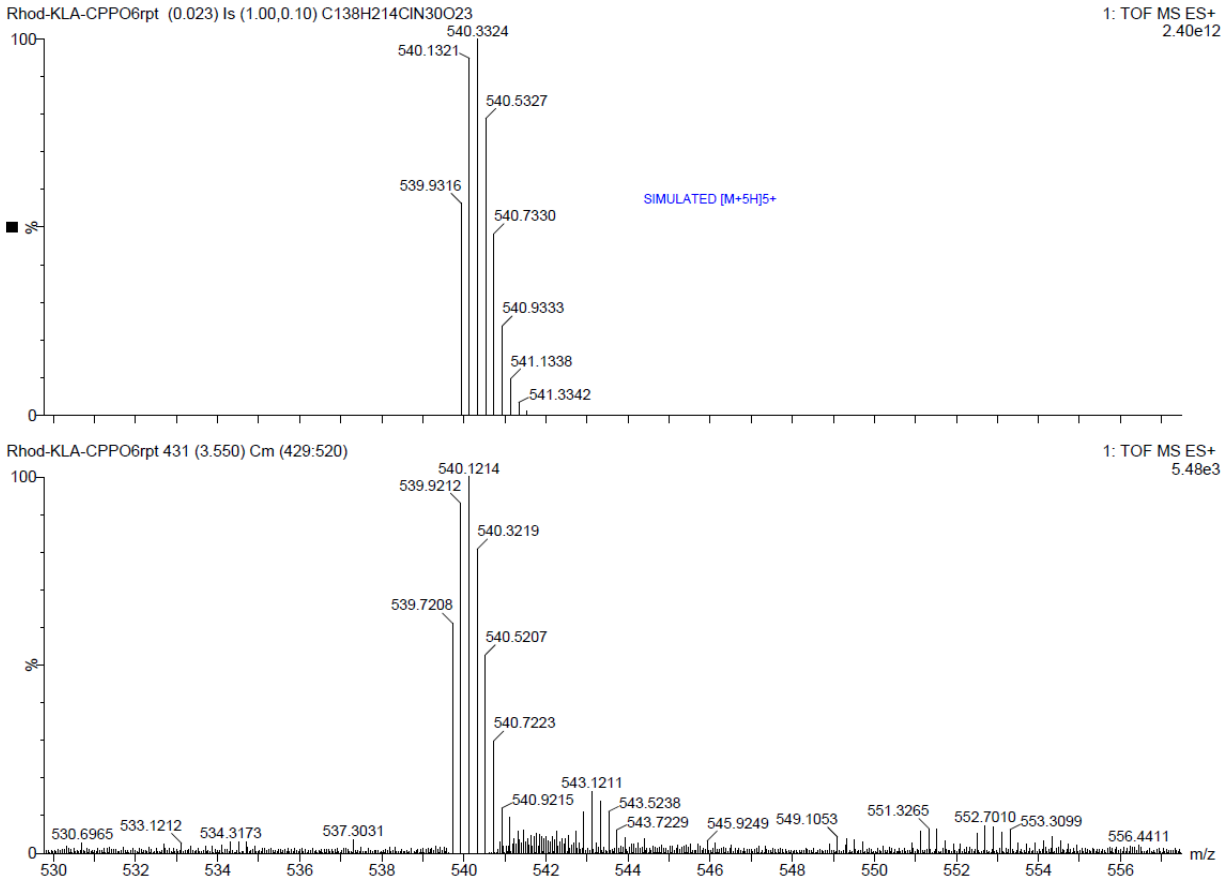

HRMS *m/z* (ESI) 540.3219, consistent with empirical formula $C_{138}H_{214}N_{30}O_{23}Cl$ with an accuracy of -3.8 ppm (accepted as $(M + 5H)^{5+}$).

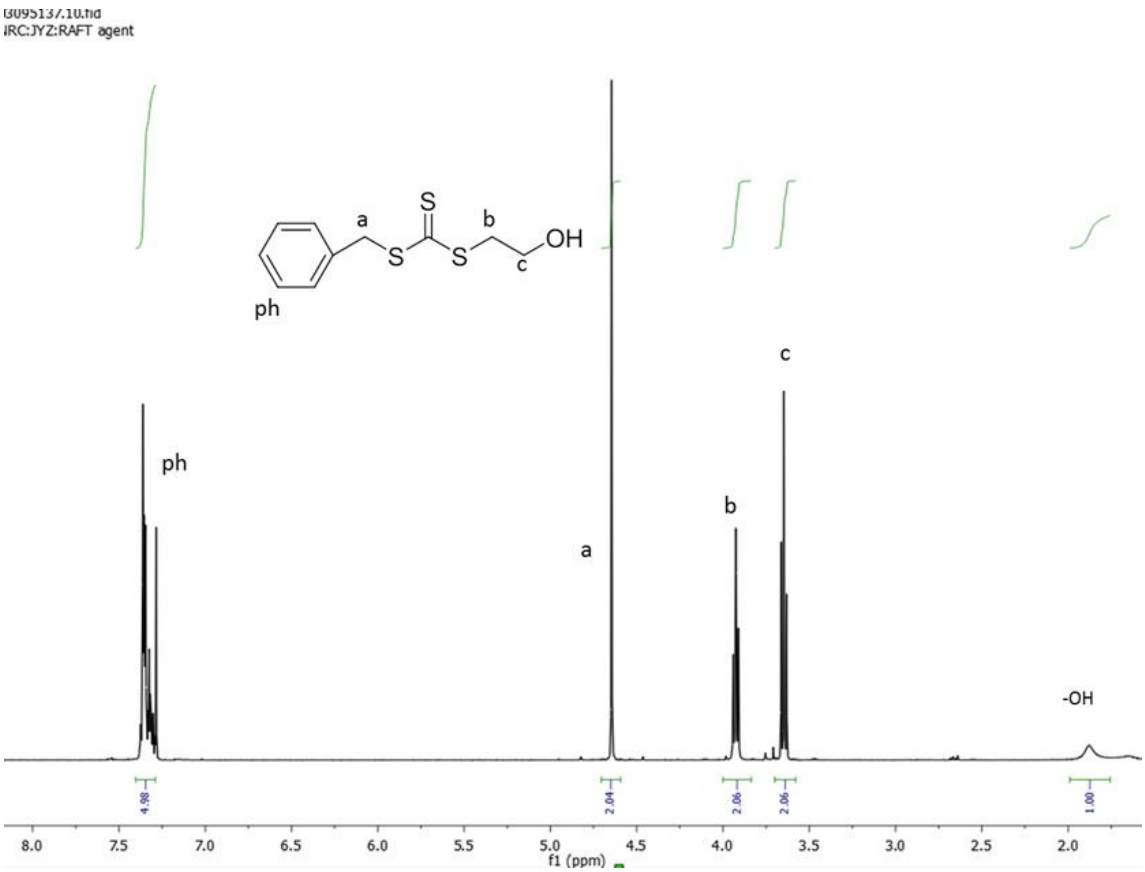

Appendix 6.1: ^{1}H NMR spectra of benzyl 2-hydroxyethyl carbonotrithioate (RAFT agent) (**15**) in solvent $CDCl_3$.